Entropic model for dose calculation in external beam radiotherapy and brachytherapy

Gabriele Birindelli

THÈSE

pour l'obtention du grade de

DOCTEUR DE l'UNIVERSITÉ DE BORDEAUX

École doctorale des sciences physiques et de l'ingénieur

Spécialité : **Astrophysique, Plasmas et Nucléaire**

présentée par

Gabriele BIRINDELLI

Entropic model for dose calculation in external beam radiotherapy and brachytherapy

Directeurs de thèse : Vladimir Tikhonchuk et Jean-Luc Feugeas

Co-Directeur de thèse : Philippe Nicolaï

Soutenue le 30 Avril 2019

Devant le jury composé de :

M. François Bochud	Professeur, CHUV Lausanne	Rapporteur
Mme. Marie Claude Bordage	Chargé de Recherche, INSERM Toulouse	Rapporteur
Mme. Catherine Dejean	Physicienne Medical, CAL Nice	Examinateur
M. Jean-Luc Feugeas	Ingénieur Chercheur, CEA, CELIA	Invité
M. Guy Kantor	Professeur, Université de Bordeaux	Examinateur
M. Philippe Nicolaï	Ingénieur Chercheur, CEA, CELIA	Invité
Mme. Laure Vieillevigne	Physicienne Medical, IUCT Toulouse	Examinateur
M. Olivier Saut	Directeur de Recherche, CNRS, IMB	Président
M. Vladimir Tikhonchuk	Professeur Emerite, Université de Bordeaux	Directeur

Titre : Modele entropique pour le calcul de dose en radiothérapie externe et curiethérapie

Résumé : ce travail est dédié au développement et à la validation d'un nouvel algorithme de résolution de l'équation de Boltzmann sur une grille cartésienne pour le transport et le dépôt d'énergie de particules énergétiques et de rayons X dans les tissus humains. Ce modèle basé sur une fermeture entropique fournit un outil mathématique efficace permettant de calculer la dose délivrée avec une précision comparable à celle des codes référents de Monte Carlo (MC) en un temps de calcul fortement réduit et sans exigence de puissance de calcul. Contrairement aux méthodes basées sur une discrétisation angulaire aux ordonnées discrètes de la solution, telles que le modèle développé dans le logiciel Acuros, le modèle entropique est basé sur l'écriture d'un nombre réduit d'équations aux moments pour les électrons et les photons dont la fermeture est assurée par le H-théorème de Boltzmann. En conservant une bonne précision de calcul, l'algorithme peut simuler différentes techniques de traitement telles que la radiothérapie externe - éventuellement en présence de champ magnétique pour la radiothérapie guidée par IRM - la curiethérapie ou la radiothérapie intra-opératoire. Le modèle a été comparé aux simulations MC en utilisant le code PENELOPE ; il a montré une excellente précision et de bonnes performances pour différents matériaux et structures géométriques. Le protocole de validation mis en place a consisté à simuler les distributions de doses dans des fantômes numériques complexes en termes de géométries (hétérogénéités) et de composition (os, poumons, air, prothèses). Pour la curiethérapie et la radiothérapie externe, des simulations réalistes basées sur des tomographies et utilisant l'espace de phase réel de la source ont été effectuées. Le code est capable de calculer des distributions de dose tridimensionnelles avec des voxels de 1 mm^3 sans incertitudes statistiques en quelques secondes au lieu de plusieurs minutes comme PENELOPE le propose. Dans les applications à la curiethérapie, nous montrons que les distributions de dose diffèrent significativement de celles calculées avec les approximations TG-43, grâce à une prise en compte plus précise des inhomogénéités et des compositions chimiques des matériaux ainsi que des forts gradients de densité. Pour les deux applications, le modèle entropique montre un excellent accord avec les calculs PENELOPE dans le critère de mesure d'erreur gamma-index 1 % / 1 mm. Cette thèse de doctorat présente les bases mathématiques et les différentes étapes d'optimisation et de validation du modèle entropique pour la radiothérapie. Les comparaisons avec les simulations MC démontrent une excellente précision et efficacité du modèle. Grâce au temps de calcul considérablement réduit et à sa précision, ce modèle est un candidat prometteur pour devenir un algorithme de calcul de dose en temps réel référent.

Mots-clés : Modele entropique; Calcul de dose; Équation de Boltzmann; Radiothérapie

Title : Entropic model for dose calculation in external beam radiotherapy and brachytherapy

Abstract : This work is dedicated to development of a completely new Grid-Based Boltzmann Solver (GBBS) for the transport and energy deposition by energetic particles and x-rays in human tissues. The entropic closure and structured mathematical formulation provide an efficient framework enabling calculations of the delivered dose with an accuracy comparable to Monte Carlo (MC) codes in a strongly reduced computational time and without any special processing power requirement. In contrast to discrete ordinates angular discretization methods, such as Acuros, the entropic model is based on a reduced number of moment equations for the electrons and photons closed with Boltzmann's H-theorem. Keeping a good accuracy of calculations, the algorithm can simulate different treatment techniques such as the external radiotherapy even in presence of magnetic field (e.g., MRI-guided radiotherapy), brachytherapy or intra-operative radiation therapy. The model has been compared with the full MC simulations by using the code PENELOPE and showed a good accuracy and performance for different materials and geometric structures. The validation procedure consisted in simulating dose distributions in complex numerical phantoms including a large number of heterogeneity shapes and materials such as bone, lung and air. For both, brachytherapy and external beam radiotherapy, simulations based on CT scans and using the real phase-space of the source, have been performed. The code is capable of calculating three-dimensional dose distributions with 1 mm^3 voxels without statistical uncertainties in a few seconds instead of several minutes like PENELOPE. In brachytherapy applications the calculated dose distributions significantly differ from the ones calculated with the TG-43 approximations, thanks to a more accurate account for the material inhomogeneities and strong density gradients. For both applications the entropic model shows an excellent agreement with PENELOPE calculations within the 1% / 1mm gamma-index criterion. This Ph. D. thesis presents the mathematical background and different steps of optimization and validation of the entropic model for the radiotherapy applications. Comparisons with the MC simulations demonstrates an excellent accuracy and efficiency of the model. Thanks to the significantly reduced computational time and its accuracy, this model is a promising candidate to become a real-time dose calculation algorithm.

Key words : Entropic model; Dose calculation; Boltzmann equation; Radiotherapy

Unité de recherche
[Centre Lasers Intenses et Applications - UMR 5107,
351 cours de la Libération, 33405 TALENCE cedex]

Acknowledgement

Firstly I would like to express my gratitude to my reviewers Marie-Claude Bordage and Francois Bochud, for accepting the onerous task of reading and reviewing my work in detail. I have deeply appreciated their useful comments and suggestions. I would like to thank also the others members of the jury Catherine Dejean, Laure Vieillevigne, Guy Kantor and Olivier Saut that honoured me with their presence at my defense.

I want to thank those who represented to me the real dream team: my advisors Vladimir Tikhonchuk, Jean-Luc Feugeas, Philippe Nicolaï and, even if unofficially, Bruno Dubroca. They never stopped supporting and helping me during my work, especially in the hard days that naturally come during a PhD. I'm grateful to them for the autonomy that they allowed me to have and, at the same time, for making me grow up as a person and as a scientist. Thanks to Vladimir for sharing during these years his impressive scientific knowledge and his care about my work. Thanks to Jean-Luc for his visionary and far-ranging spirit. Thanks to Philippe for teaching me the art of doubt as an inspiration and double-check. Thanks to Bruno for never giving up in explaining to me how "la mathematique" (as is written) is important in a physicist's life.

A special thank goes to the other PhD students I worked with, that have soon become new friends. Thanks to Teddy with whom we shared the final period of his PhD and the beginning of mine and with whom the exchanges have not ended. Thanks to Jonathan Page with whom we have shared almost the entire PhD by supporting each other and sharing numerous and unforgettable evenings. Thanks to Jerome Caron, my mentor in medical physics, who introduced me to this field sharing all his immense knowledge and willingness.

I would like to thank all the administrative and informatic staff of the CELIA laboratory composed by Sophie, Celine, Sonia, Richard and Gaetan. Without your patience everything would have been more difficult.

The "rue Jouis' merry gang" has been of primary importance in these years. It is thanks to them that I immediately found myself at home from the very first days in France. Thanks to Nicola Di Pietro for giving me his room, thanks to Giovanni Lazzarini for

his true friendship and immense culture and thanks to Dario Del Sorbo, to whom I am bounded by a very deep and long-time friendship but also by a cat that has his name and by the responsibility for his marriage. Thanks to Julien Moreau who, as a colleague, had the courage to become a "coloque" in Ritals' house. A true friend, I hope I have passed to him some love for Italy as well as countless recipes that he will hardly cook. Thanks to Sergio Corridore for bringing home his Sicilian touch without which everything would have been much more ordinary. Thanks to all the other frends that shared with me fantastic moments in these years: Claudio, Alice, Silvia, Federico, Daniele, Marina, Nadia, Giovanni, Sally, Alessandro "di giú" and Alessandro "di su", Gloria, Erwan, Pedro, Zaira, Donaldi, Jocelin, Catherine, David, Marine and Stephan. Many thanks to Luca Antonelli that luckily lost our bet.

A special thought goes to my father Giorgio, my mother Giuliana and my brother Matteo. They have always supported me with enthusiasm, even when my choices were not completely understood. Thank you for making me a free person, it's all because of you.

At last I would thank Emanuela, without her unconditional love and support this work would never seen the light. You have been my streght whenever it was abandoning me. Where this work ends, a bright future is beginning for us.

Table of acronyms

3DCRT: Three Dimensional Conformal Radiation Therapy
AAA: Anisotropic Analytical Algorithm
BT: Brachytherapy
CBCT: Cone Beam Computer Tomography CCC: Collapsed Cone Convolution
CEA: Commissariat à l'énergie atomique et aux énergies alternatives
CELIA: Centre Lasers Intenses et Applications
CSD: Continuous Slowing Down
CT: Computer Tomography
DICOM: Digital Imaging and Communications in Medicine
EBRT: External Beam Radiation Therapy
FWHM: Full Width Half Maximum
HDR: High Dose Rate
IGRT: Image Guided RadioTherapy
IMIT: Intensity Modulated Ion Therapy
IMPT: Intensity Modulated Proton Therapy
IMRT: Intensity–Modulated Radiation Therapy
LDR: Low Dose Rate
LINAC: Linear Accelerator
LBTE: Linear Boltzmann Transport Equation
MC: Monte Carlo
MDR: Moderate Dose Rate MLC: Multi-Leaf Collimator
MRI: Magnetic Resonance Imaging
MU: Monitor Unit
SBRT: Stereotactic Beam Radiation Therapy
TERMA: Total Energy Released per unit MAss
TPS: Treatment Planning System
US: Ultrasound
VMAT: Volumetric Modulated Arc Therapy

Table of acronyms

Contents

Introduction

Nowadays radiotherapy is among the most important and common techniques that are adopted for cancer treatment. The aim of radiotherapy consists in killing cancer cells with the use of ionizing radiations that are able to spare the healty tissue surrounding the tumor volume. The ionizing radiation consists in a beam of high energetic particles such as photons, electrons, protons, neutrons or ions. Specifically, two main techniques are widely used for the delivery of radiotherapy treatments: external beam radiotherapy and brachytherapy.

In external beam radiotherapy the ionizing particle beam is generated with the use of linear accelerators (LINAC). These machines accelerate to the desired energy a primary electron bunch that can be directly used or can be converted in x-ray photons for treatment. The external beam radiotherapy treatment has greatly improved in the last 40 years. The introduction of three dimensional imaging prompted the technological development of optimized delivery techniques. The first step of improvement consisted in the introduction of the three dimensional conformal radiation therapy (3DCRT). The particle beam is thus shaped in order to match the projected outline of the targeted tumor volume. Then, the introduction of Intensity–Modulated Radiation Therapy (IMRT) and of Image Guided RadioTherapy (IGRT) further increased the precision in the external beam radiotherapy treatments.

Brachytherapy is a type of radiotherapy in which sealed radioactive sources are placed directly inside the tumore or next to it. In brachytherapy, the precondition for clinical applications is given by the direct clinical tumor access and by a tumor volume of limited size. The low dose rate (LDR) brachytherapy is used as a permanent implantation. In this case the radioactive sources remain in the tissues and gradually become inactive as radioactivity decays over time. The main application of LDR brachytherapy is the prostate cancer treatment. On the contrary, the high dose rate (HDR) brachytherapy is used as a temporary implant mainly for gynecological cancer, breast cancer and prostate cancer. Today, the use of brachytherapy is in strong decline [46, 53, 81, 85] despite the presence of several studies showing a better overall survival of the treated patients [46, 53]. This is mainly due to the strong technological advances in external beam radiotherapy of the last decades.

In both external beam radiotherapy and brachytherapy, the dose is calculated using mathematical models that can predict the dose distribution in the patient starting from the beam configuration or the source disposition. This is done before the treatment delivery. Several models have been developed for dose calculation. The most common models are the kernel based models, which are based on a precalculated distribution of dose. This is released by an elemental photon beam incident in a medium (kernel). The main advantage of these models consists in their fast optimization of the dose distribution delivered with intensity modulated techniques. However, they show a lack of accuracy in heterogeneous media.

In principle, an exact dose calculation can be performed by solving the linear Boltzmann transport equation (LBTE). This equation describes the transport and the interactions of particles with the media. The linearity is an important property that results from the underlying assumptions that interactions between projectiles particles can be neglected and that the ambient medium properties are not modified by the interaction with the injected particles. Due to a high number of indipendent variables, i.e. a high dimensionality of the phase space, the solution of LBTE is extremely costly and difficult.

The Monte Carlo method is a statistical approach for the solution of the LBTE. The Monte Carlo method has been chosen as the gold standard for calculations in medical physics, due to its capability of accurately solving LBTE. However, this technique is very time consuming due to ithe intrinsic statistical approach. In the last decades, ad hoc Monte Carlo codes have been developed in order to speed up the dose calculation. However, due to some approximations used to improve the computational effort, these codes present some limitations of accuracy when used with new technological development such as the MRI-guided radiotherapy.

Deterministic solvers represent an alternative method with respect to the Monte Carlo codes for the solution of the LBTE. The deterministic models can be divided into two categories: those using the discrete ordinate and those using the moments. Discrete ordinates methods are based on the discretization of the LBTE in all its variables. Acuros (Varian Medical Systems) is the only deterministic code available in clinical context and it belongs to the family of discrete ordinates methods.

Angular moments methods represent an alternative to discrete ordinates methods. They are based on the solution of LBTE, but they require considerably less computational effort. This is due to the reduction of the degrees of freedom of the LBTE, which is obtained by integrating the equation over the direction variable. The entropic model developed at the CELIA laboratory belongs to the category of angular moments method.

This numerical code has been developed during the past years with the aim of solving different applications in plasma physics and astrophysics. Only in the last few years, the solution of applications to particle transport in cold matter and more specifically to radiotherapy has been approached with this code. These works were mainly focused on the mathematical properties of the model and only the principal physical cross sections were firstly implemented in the numerical code [20, 34, 108]. For these reasons, even showing good mathematical properties and a competitive performance in terms of calculation effort, the entropic model was far from a possible clinical implementation.

The aim of the present thesis is therefore the implementation, optimization and validation of the entropic model in its physical parameters, in order to calculate a dose distribution with an accuracy comparable to Monte Carlo codes despite the reduced number of degree of freedom. In this work, the model is applied to both external beam radiotherapy and brachytherapy applications.

This work is organized as follows.

The first Chapter is devoted to the presentation of the context and of the applications in medical physics of the present study. The main radiotherapy techniques are briefly presented, with a focus on external photon beam radiotherapy and brachytherapy. These latter techniques are the ones that will be resolved by the proposed model in the present work. Moreover, a brief revision of the numerical models present in literature for dose calculations in treatment planning is carried out.

The second Chapter is devoted to the presentation of the physical interactions taking place in the transport of electrons, positrons and photons in the radiotherapy energy regime. A first analysis of electrons and positrons is detailed, since these particles are responsible for the dose deposition. We focus on inelastic collisional and radiative scatterings and then on the elastic scattering that is responsible for the diffusion of charged particles. We also draw a presentation of the phenomena involving photons, by describing the three most probable processes in the energy range covered by the radiotherapy applications, i. e. the photoelectric scattering, the Compton scattering and the pair production in nuclear field.

In the third Chapter, the entropic model is presented and analyzed as it has been conceived for medical physics applications. The Boltzmann transport equation is derived in its linearized form. Thus, the entropic model is derived to model the coupled transport of photons and electrons. A detailed analysis is devoted to the beam initialization in the model, which is strictly dependent on the anisotropy of the beam. For this reason, a method to translate a phase-space initialization suitable for a Monte Carlo code into an

anisotropy distribution for entropic models is proposed. Moreover, in the last part of the chapter, the protocol of validation of the model with respect to the PENELOPE Monte Carlo code is presented.

Chapters 4 and 5 are dedicated to the validation of the M_1 model, i.e. the first member in the angular moments hierarchy of the entropic model, on external photon beam radiotherapy applications, thanks to a systematic comparison of our algorithm with the Monte-Carlo PENELOPE code. At first, homogeneous cases are resolved in order to analyse the impact of the anisotropy initialization on the solution of the Boltzmann equation. Moreover, on these simple tests, more realistic energy initialization corresponding to the bremsstrahlung process of photons generation. This requires the fact that primary and secondary particles need to be treated separately to avoid numerical issues. Other techniques for the optimization of the code and the accuracy preservation are proposed. Then, the validation on different heterogeneous cases is conducted in Chapter 5.

In Chapter 6, preliminary validation on brachytherapy applications is carried out. The model is tested on low dose rate brachytherapy applications. This choice is due to the fact that in this energy regime the photoelectric effect and the chemical composition of the different materials play an important role in the dose deposition.

In Conclusions we summarize the main results of this work showing the perspectives for the future developments.

Chapter 1

Context of the study

1.1 Radiotherapy

Radiation therapy or radiotherapy is one of the most important techniques used for cancer treatment. The aim of radiotherapy is to kill cancer cells and shrink tumors with the use of ionizing radiations. With the use of photons, electrons, protons, neutrons or ions, high radiation dose concentrations are reached in the tumor volume while the healthy tissues and organs receive as low dose concentration as possible. The absorbed dose, following the the International Bureau of Weights and Measures, is defined as mean energy imparted (by ionizing radiation) per unit mass. The unit of ionizing radiation absorbed dose is Gray (Gy), Gy = J / kg [100]. Depending on the delivery technique we can define two main types of radiotherapy:

- External beam radiotherapy: this type of radiotherapy is delivered using an external source of radiation;
- Brachytherapy: this type of radiotherapy is delivered using radioactive sealed sources directly into or next to the tumor.

Let us now describe more in detail the external beam radiotherapy and brachytherapy.

1.1.1 External beam radiotherapy

In external beam radiotherapy (EBRT) the ionizing radiation beam is directed to the patient from the external source. The tissues can be irradiated with different types of particles such as high energy photons, electrons, protons, α particles or carbon ions, see Figure 1.1.

In external electron or photon radiotherapy, the treatment unit is typically a linear accelerator (LINAC), see Figure 1.2. In a linear accelerator, electrons gain energy by interacting with a synchronized radio-frequency electromagnetic field. The accelerating waveguide consists of a long cylindrical tube, containing a series of circular baffles.

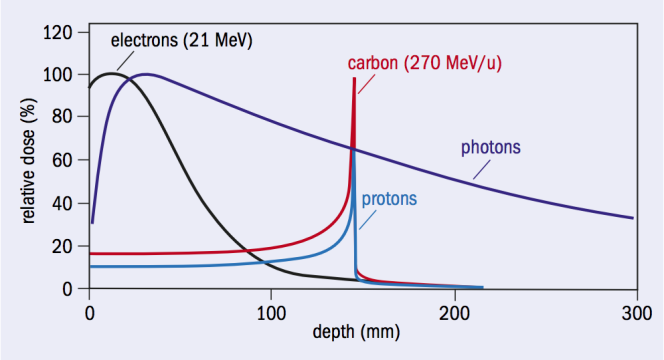

Figure 1.1: Bragg curves for elecron beam (black), carbon ions beam (red), photon beam (dark blue) and proton beam (light blue) used for external beam radiotherapy. Image from CERN Courier with permission.

Bunches of electrons generated by the electronic gun are injected into the guide in synchronism with pulsed microwave radiation. The accelerated bunch of electron is finally deflected with a magnetic field in order to be used for radiotherapy. This magnetic field is generated by a system of coils that is placed just before the head of the accelerator. Once the electron beam is created and bended in order to be perpendicular to the irradiated surface, it is narrow, tipically a few mm in diameter, and is essentially Gaussian in profile. This narrow pencil electron beam is not suitable for clinical use. If the electron beam is to be used for therapy, the originally narrow beam is broadened by a scattering foil. The electrons entering the patient skin are almost monoenergetic having the maximum energy achieved in the acceleration. The electron radiotherapy is mostly used for treatment of tumours up to about 70 mm deep (range in water on an electron beam with initial energy of $\simeq$ 14 MeV [9]).

Figure 1.2: Image of an Elekta Infinity linear accelerator. Image from Elekta with permission.

In photon radiotherapy, the source of electrons is focused onto a high atomic number target (generally tungsten), and their energy is converted into bremsstrahlung radiation. Due to this process the photon spectrum is broad with the maximum energy near to the

maximum energy of the electrons incident on the target.

The introduction in the 1980's of three dimensional imaging techniques, such as Computer Tomography (CT) and Magnetic Resonance Imaging (MRI), greatly improved the anatomy informations and prompted implementation of the Three Dimensional Conformal Radiation Therapy (3DCRT). From this moment each selected beam aperture would be designed to match the projected outline of the target, sparing the healthy tissues. In a first time, the beam aperture was shaped with the use of a high atomic number shielding. In a second time the Multi-Leaf Collimator (MLC) was implemented in the accelerator head. It consists of a large number of high atomic number leaves that can be moved individually as shown in Figure 1.3.

Figure 1.3: A Multi-Leaf Collimator (MLC) consists of a large number of highly absorbing tungsten leaves (on the order of 20–80 on each side) that can be positioned individually to create field openings with complex shapes. Image from Varian Medical Systems with permission.

A strong improvement of the treatment delivery is represented by the Intensity Modulated Radiation Therapy (IMRT). The definition of IMRT given by Bortfeld is the following [15]:

> IMRT is a radiation treatment technique with multiple beams in which at least some of the beams are intensity-modulated and intentionally deliver a non-uniform intensity to the target. The desired dose distribution in the target is achieved after superimposing such beams from different directions. The additional degrees of freedom are utilized to achieve a better target dose conformality and/or better sparing of critical structures.

In IMRT the particle beams are shaped and modulated in their intensity by the use of the multileaf collimator. This delivery technique reduces the dose in particularly sensitive critical organs and increase the dose in the target volume. In IMRT treatments several fields are used with a static or step-and-shoot technique [30, 110] or dynamically

[4, 84]. Another example of dynamic IMRT is the tomotherapy. Tomotherapy (i.e. "slice therapy") machines can be considered as a combination of a CT scanner and a linear accelerator that can deliver the radiation in a fan-shaped distribution, similar to CT imaging with a continuously rotating radiation source, while the patient is moved through the machine along the rotation axis.

Even if 3DCRT and IMRT give a high number of degrees of freedom in order to deliver precisely a high radiation dose to the planned location, uncertainties exist in many circumstances, such as tumor target definition, patient immobilization, and organ motion (morpological variations, breathing motion ...). In order to reduce these uncertainties the Image Guided RadioTherapy (IGRT) has been introduced [143]. Time-resolved (4D) imaging techniques for modeling intra-fraction organ motions are nowadays available. Moreover, the accelerator systems are equipped with diagnostic imaging sources as the Cone Beam Computer Tomography (CBCT) able to check the position of the tumor immediately before beam delivering. However the CBCT scan cannot be used during the treatment delivery. The most recent technology available on the market is the MRI-Linac for MRI guided radiotherapy. This machine combines a MRI scanner with a linear accelerator in a single system, as shown in Figure 1.4. With MR images it is possible to obtain high-quality soft tissue contrast, making the visualization of tumors in soft tissue areas (brain, liver, prostate, lung ...) simpler than with CT images. Thus, in principle it is possible to modify the treatment plan in order to adjust the beam configuration while the patient is on the treatment table. However, due to the presence of the magnetic field, the trajectories of the secondary electrons are modified inducing a modification in the planned dose distribution.

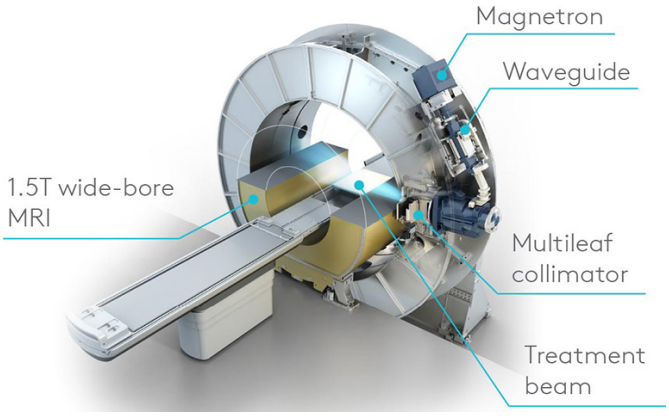

Figure 1.4: Scheme of the MRI-Linac Elekta. The system is the result of the collaboration between Elekta and at the University Medical Center Utrecht. The 1.5 T MRI scanner is integrated with a 6 MV radiotherapy accelerator. Image from Elekta with permission.

1.1.2 Brachytherapy

Brachytherapy is a type of radiotherapy in which sealed radioactive sources are placed directly into or next to tumor. Brachytherapy is characterized by a steep dose fall off with increasing distance to the radioactive source. The dose fall off is approximately proportional to $1/r^2$, where r is the distance to the source [94]. The precondition for clinical applications for brachytherapy is the direct clinical tumor access and limited size tumor volume. The most common sites for administration of brachytherapy nowadays are gynecologic and prostate cancers. Furthermore, brachytherapy is used for breast, skin, anus and rectum, sarcoma, head and neck, bladder, lung, esophagus, bile duct, liver and ocular malignancies [132].

Brachytherapy can be classified by the rate at which the dose is delivered. The dose rate has the units of Gray per hour [Gy/h]. The ICRU 38 Report refers to a dose rate of 0.4 to 2 Gy/h as a Low Dose Rate (LDR), 2 to 12 Gy/h as a Moderate Dose Rate (MDR), and greater than 12 Gy/h as a High Dose Rate (HDR) [26].

The LDR and HDR brachytherapy are used with different implantation techniques. The LDR brachytherapy is used with a permanent implantation. In this case the radioactive sources remain in the tissues and gradually become inactive as the radioactivity decays over time. The most important application of the LDR brachytherapy is the prostate cancer using permanently implanted ^{125}I seeds. This technique consists in the insertion of sources into the prostate gland using long needles via a transperineal approach combined with transrectal ultrasound guidance as shown in Figure 1.5. The ultrasound probe allows control of the needle position and seed loading within the prostate. The needles are guided by a template with a Cartesian grid.

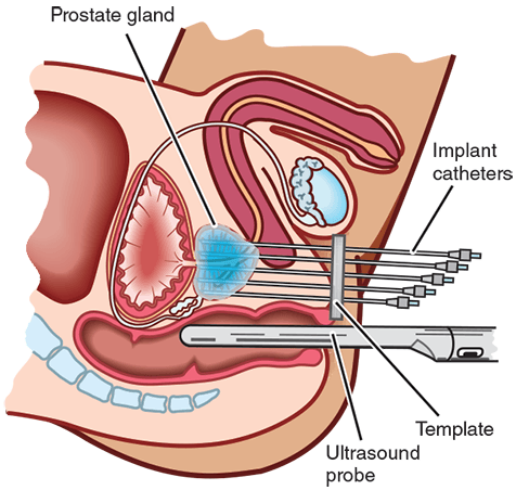

Figure 1.5: Prostate treatment scheme. The transrectal ultrasound probe gives a real time image of the prostate and of the inserted needles. Image from Prostate Cancer Foundation of Australia with permission.

On the other hand HDR brachytherapy is used with the temporary implantation. In

this case the radioactive sources are removed after the desired radiation dose is achieved. This technique is used especially for the treatment of gynecological cancer, breast cancer and prostate cancer. Among gynecologic brachytherapy applications, cervix cancer is the most common site, and the vast majority of all brachytherapy procedures worldwide are in locally advanced cervix cancer [50] treated definitely with a combination of external beam radiochemotherapy and brachytherapy. The radioactive source used for this kind of brachytherapy is generally ^{192}Ir. The source is contained in an afterloading system, see Figure 1.6, providing protection from radiation exposure by securing the radiation source in a shielded structure. Once the applicator or catheters are placed into or next the tissue with the cancer, they are connected to the afterloader. In a first step a dummy source, i.e. non radioactive source, is driven through the attached applicators and catheters in order to check for obstructions. Only after that the radioactive source exits the afterloader and travels through all the catheters stopping in all the planned positions.

Figure 1.6: Examples of afterloader systems. The radiation source is contained in a shielded afterloader and is driven in catheters through the connector disposal on the top. Image from Varian Medical Systems with permission.

In the last decades, the utilization of brachytherapy for the treatment of cervix cancer and prostate cancer is in decline [46, 53, 81, 85]. The reasons are not completely clear but could be attributed to the recent advances in surgery (laparoscopic and robotics techniques) and to the new EBRT technologies such as IMRT, Stereotactic Beam Radiation Therapy (SBRT) and heavy particle radiotherapy. Moreover these alternative techniques have higher reimbursement rates relative to brachytherapy and do not suffer from a lack of training of the medical staff [96, 106, 132]. However, there are clear indications that patients treated with combined EBRT and brachytherapy have significantly better overall survival than patients treated exclusively with EBRT [46, 53]. Several studies have been conducted on the dosimetric differences among external beam therapy versus brachytherapy for prostate and cervix cancer [42, 43]. The results of these studies demonstrate the superiority of brachytherapy in sparing the organ at risk and the tissues surrounding the tumor as shown in Figure 1.7.

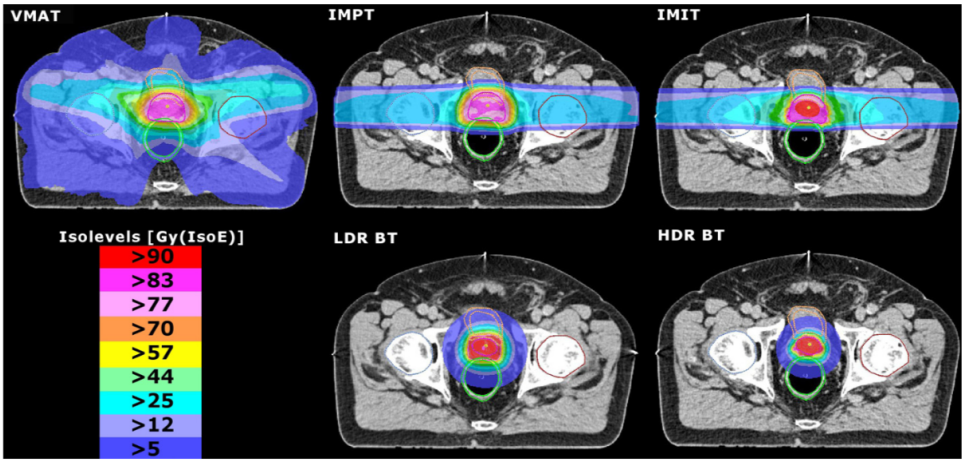

Figure 1.7: Dosimetric differences among volumetric modulated arc therapy (VMAT), intensity modulated proton therapy (IMPT), intensity modulated carbon-ion therapy (IMIT), low dose rate brachytherapy (LDR-BT) and high dose rate brachytherapy (HDR-BT). Brachytherapy techniques were superior in terms of bladder, rectum and normal tissue sparing. Image from Georg et al. [42] with permission.

Geometric deviations of few mm may have considerable impact on a given dose distribution due to the steep brachytherapy gradients [70]. The catheter implantation defines the volume which can be reached with a relevant dose, and therefore the quality of the implantation is of specific importance in brachytherapy. With real-time imaging it is possible to steer the catheters into place with a high accuracy and safety for the patient. Real-time imaging can in principle be performed with ultrasound (US), MRI, CT and endoscopy. MRI has a better soft tissue contrast with respect to US and CT. For both prostate and cervical cancer brachytherapy postimplant dosimetry seems to be more accurate when evaluated with MRI vs. CT/US [28, 130, 139] as shown in Figure 1.8.

With the advances in 3D imaging and image based target and organ definition, the grounds were laid for significant advances in treatment planning. The detailed assessment of the 3D dose distribution has allowed for new approaches in prescribing and reporting doses for the tumor targets as well as for organs at risk [132].

Developments in treatment delivery verification are therefore currently highly warranted. Several promising technologies have emerged during the last years opening a window to automation, real-time verification and improved verification of applicator geometry. Treatment planning is currently a process which takes e.g. 30 min - 2 h including image transfer, contouring and treatment planning. Since organ and catheter movements may occur on time scales of less than 1 h, the delivered dose may not be identical to planned dose [131]. If imaging is performed directly before treatment delivery these uncertainties can be reduced. Initiatives with on-board imaging such as flat-panel imaging are ongoing, and furthermore the first initiatives to build integrated MRI-delivery rooms are emerging [60].

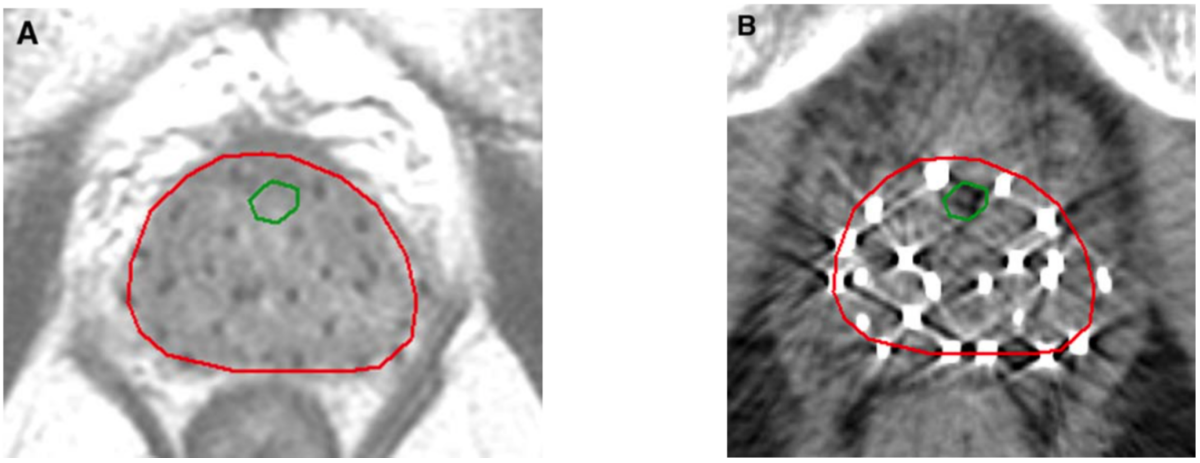

(a) (b)

Figure 1.8: LDR brachytherapy postimplant seed images: (A) MR image of mid-gland postimplant, and (B) corresponding CT slice. The MR image shows a better resolution of the soft tissues and avoids seed induced artifact typical of the CT image. Image from Crook et al. [28] with permission.

1.2 Treatment planning system and dose computation methods

Once a patient has been diagnosed with cancer, he undergoes to images aquisitions. Generally, in this step, computed tomography scan (CT-scan) and/or magnetic resonance imaging (MRI) are used to acquire the anatomical structures of the patient and the tumor localization. This sequence of images is imported in a software for treatment planification called Treatment Planning System (TPS). After a preliminary phase of contouring, the medical team, which is composed of dosimetrists, medical physicists and radiation oncologists, designs an individual treatment plan. The best alternatives for beam orientations, different field settings or better source placement in brachytherapy are chosen, in order to achieve the optimal dose distribution in the tumor volume sparing the neighbouring healthy tissues.

In the planning step, the dose calculation cannot be avoided in order to predict and visualise the dose distribution in the patient. The dose is calculated using mathematical models that can predict the dose distribution in the patient starting from the beam configuration. Several models have been developed for the dose calculation. Constant improvements have been proposed to increase the precision of these models and to fullfil the needs of radiotherapists. In the next sections we revise the most important models that are used in treatment planning for external photon beam radiotherapy and/or brachytherapy.

1.2.1 Kernel based models

The kernel based algorithms have a common root in the use of convolution/superposition technique.

The superposition method is based on the separation between the primary and the secondary particles. If we consider separately the primary photons and the secondary particles, the dose can be considered as the sum of the contributions of the secondary particles generated from primary photon interactions in distant voxels and deposing their energy in a small volume surrounding the point of interest. The dose calculated in a given point $P(x, y, z)$ reads:

$$D_P\,(x, y, z) = \int\int\int_V p\,(x', y', z')\; s\,(x, x', y, y', z, z')\; dV, \tag{1.1}$$

where D_P is the dose calculated in an element of volume surrounding P, which is determined by its position (x, y, z), V is the scattering volume, p is the fluence of the primary photons in the control volumes dV_1, dV_2 and dV_3 and s represents the energy fractions that are diffused in P by the control volumes per unit of primary fluence. This is sketched in Figure 1.9.

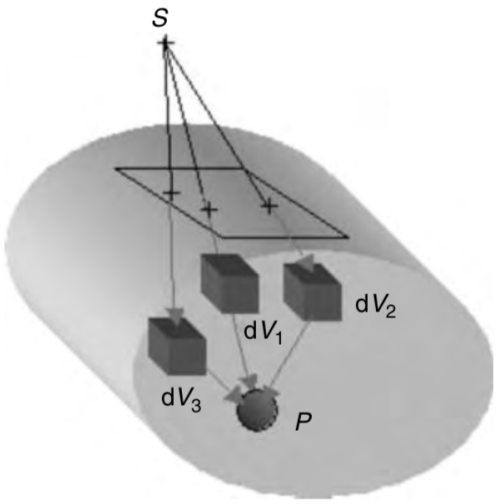

Figure 1.9: The superposition principle: the dose at P can be considered as the sum of the contributions of energy deposited in a small volume surrounding P by particles (electrons, photons) originating from primary photon interactions in distant volume elements dV_i. Image from Mayles et al. [86] with permission.

The energy deposition kernel is defined as a distribution of dose released in a medium due to an elementary photon beam incident at the origin of coordinates of the kernel. These kernels are normally pre-calculated with Monte Carlo simulations. Energy deposition kernels are categorized according to the geometry of the elementary beam that delivers the incident energy. Several kernels exist but we focus on the two most important: the point kernel and the pencil kernel. The point kernel is defined as the pattern

of energy deposited in an infinite medium around a primary photon interaction site. The pencil kernel is defined as the pattern of energy deposited in a semi-infinite medium from an infinitesimal and monodirectional beam. In Figure 1.10 the two kernel geometries are shown.

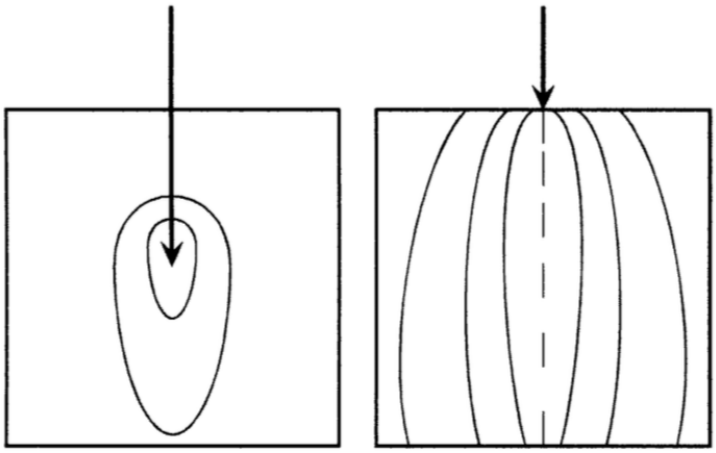

Figure 1.10: Irradiation geometries for point kernel (left) and pencil kernel (right). Image from Ahnesjo et al. [3] with permission.

1.2.1.1 Pencil beam algorithms

Pencil beam algorithms [3, 52, 74, 90, 129] are based on the pencil kernels. In the beginning they were derived for the transport of electron beams and then also for photons. This method assumes that any collimated photon beam incident on the patient is a conglomeration of lots of smaller pencil beams with an infinitesimal diameter. For this reason they are particularly adapted for dose calculations and optimization in IMRT technique.

The dose calculation at a given point is given by the sum of the contributions of every pencil beam that is part of the irradiation field. The dose calculated with the pencil beam kernel method in a point $P(x, y, z)$ is expressed by the relation:

$$D\left(x, y, z\right) = \frac{\mu}{\rho} \int \int \int_{V} \Psi\left(x', y', z'\right) K_{PB}\left(x - x', y - y', z - z'\right) dV, \tag{1.2}$$

where $P'(x', y', z')$ is the penetration point on the patient surface, μ/ρ is the mass attenuation coefficient, Ψ is the energy fluence, $\mu/\rho \cdot \Psi$ is the Total Energy Released per unit MAss (TERMA) from $P'(x', y', z')$, The K_{PB} factor represents the pencil beam kernel in a given point $P(x, y, z)$ that is the fractional energy deposition due to primary energy fluence entering in point $P'(x', y', z')$.

This type of algorithms are fast but they are accurate only in a homogeneous medium [27, 41, 148]. This is due to the fact that electrons travel a short path and contribute to the dose at points which have a distance of few mm to a couple of cm for higher energy

photon beams. In a homogeneous medium and for a sufficiently large field size, i.e. with lateral dimensions larger than the range of the secondary electrons in the medium, the electronic elquilibrium is achieved for most of the points inside the beam. This is not true at the interfaces between two different materials where electron disequilibrium occurs and should be taken into account.

1.2.1.2 Collapsed cone convolution algorithms

Differently from the pencil beam, the collapsed cone convolution algorithms are based on the point kernel. In point kernel models the source is built by summing the contributions coming from all other points of the kernel. The peculiarity of this method is the ability of imposing a dependence in space, which is not the case of the pencil beam methods.

According to Ahnesjo et al. [3], the propagation of the primary photons is computed by ray-tracing. In a second step the dose is calculated by superposition of appropriately weighted point kernels. The dose calculated at a given point r with the point kernel method can be expressed as:

$$D(\vec{r}) = \int\int\int_V T(\vec{s})h(\vec{r}-\vec{s})d^3s \tag{1.3}$$

where $T(\vec{s})$ is the TERMA from the primary photon energy fluence in the volume element $d^3\vec{s}$ and $h(\vec{r}-\vec{s})$ is the kernel calculated between the two points $\vec{r}$ and $\vec{s}$. The dose calculated with this method is exact for an arbitrary distribution of the fluence of monoenergetic photons incident in a parallel beam on an infinite medium. A direct application of kernel superposition is very time consuming because the integral (1.3) has to be calculated numerically with a loop over both $\vec{r}$ and $\vec{s}$.

In order to reduce the computational times, one could neglect the influence of the voxels that are far from the considered point and also to discretize in angles the contributions of the secondary electrons coming from a point kernel. This method inspires the Collapsed Cone Convolution (CCC) algorithms [2], which is widely implemented in several commercial TPSs. In these algorithms, the energy is transported along the cone axis, with the departure point corresponding to the center of the voxel where the TERMA is computed as shown in Figure 1.11.

The energies that are computed from the beam propagation in each voxel are then used by summing them for each neighbouring voxel in order to compute the dose deposition on the axis. Calculation times are of the order of minutes and a relatively accurate result is obtained in dense tissues. However, for the low-dense tissues, the algorithm shows some discrepancies when comparing it with the results of a Monte Carlo code [41].

The collapsed cone convolution methods are extensively used in clinical practice for both applications in external beam radiotherapy and brachytherapy.

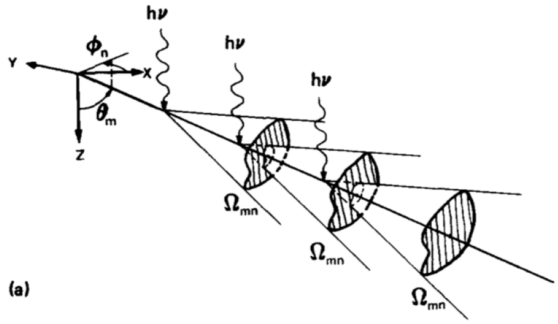

Figure 1.11: In the collapsed cone approximation, all energy released from primary photons at elements on a cone axis and flowing in coaxial cones is rectilinearly transported and deposited on the axis. Image from Ahnesjo et al. [2] with permission.

1.2.2 Monte Carlo methods

The Monte Carlo method is a statistical approach to the study of integro-differential equations [87]. The Monte Carlo algorithm can be considered as a probabilistic method of solution of a Boltzmann kinetic equation. The solution is found as an estimate of a parameter of a distribution or, more generally, of a given function of the parameter. Because of statistical nature in the Monte Carlo method the numerical solution has an uncertainty. For radiation transport problems, this technique simulates the tracks of individual particles, as shown in Figure 1.12, by sampling appropriate quantities from the probability distributions governing the individual physical processes, using machine-generated random numbers.

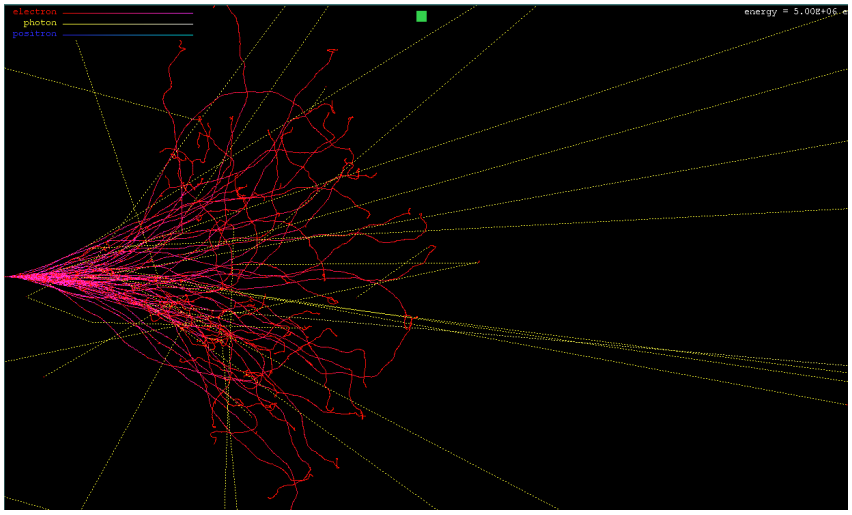

Figure 1.12: Simulation of an electron beam with initial energy of 5 MeV propagating in a water domain with a thickness of 5 cm. In red are represented the electron trajectories, in blue the positron trajectories and in yellow the photon trajectories. The simulation has been performed with the PENELOPE shower.exe program.

The range of applications of the Monte Carlo method is very broad. Due to its capability of accurately solve the linear Boltzmann transport equation (LBTE) that we describe in detail in Chapter 3, the Monte Carlo method has been chosen as the gold standard for calculations in medical physics. It can be applied to the dose calculations for the external beam radiotherapy or brachytherapy [22, 55, 126, 142], diagnostic x-ray applications [14, 146] or even for calibration of dosimetric instrumentation [16, 145].

Several general purpose Monte Carlo codes have been developed for radiation transport calculation, which are used in medicine, such as, EGSnrc [68], MCNP [17], ETRAN [125], GEANT4 [1], PENELOPE [121] and FLUKA [8]. Extensive efforts have been made to improve the Monte Carlo dose calculation algorithms used in the treatment planning systems to accurately reproduce all beam geometries and beam modification devices and to account for the effects of heterogeneities in the full three-dimensional (3D) patient geometry. In last decades several Monte Carlo toolkits based on general purposes codes have been developed. These toolkits, used for simulation of linear accelerators and dose calculation in the patient, are BEAMnrc[119], DOSXYZnrc [138], GATE [61] and PRIMO [116].

The general purpose codes have been designed for all application types and have not been optimized for clinical situations. The large number of particles that have to be simulated gives rise to extremely long calculations. For this reason, general purpose Monte Carlo codes are not integrated in the existing TPS. In the past decade, several fast Monte Carlo codes have been developed to improve the efficiency and decrease the calculation time. The most known fast Monte Carlo code is the Voxel Monte Carlo (VMC) code developed by Kawrakow and Fippel [66, 67]. The VMC code has been developed firstly for electron dose calculations and consequently extended to photon beam calculations. This code, based on the condensed history technique for the electron transport [64] and on the use of variance reduction techniques [65], has demonstrated a strong speed up in dose calculations up to 100 times a general purpose Monte Carlo code. Moreover this code has become the basis of the Nucletron electron beam dose calculation algorithm [29].

1.2.3 Deterministic methods

The deterministic solvers represent an alternative method with respect to the Monte Carlo codes for the solution of the LBTE. This method has been applied in different fields of physics but in the last two decades the interest for its applications for dose calculation in radiation therapy has consistently grown. The deterministic methods can be divided in two categories depending on the resolution method used for the solution of the LBTE. These two methods are the discrete ordinate methods and the moments methods.

The discrete ordinate methods are based on the discretization of all variables of the LBTE. More specifically with this method the direction variable is divided into a finite number of discrete angular intervals and is replaced by a discrete set of direction vectors.

Several academic works have been published on the solution of the LBTE demonstrating feasibility of this method for the dose distribution calculations [13, 44, 78, 97].

This method is suitable also for dose calculations in presence of an external magnetic field. In this case the trajectories of electrons can be deviated modifying the dose distribution in the patient. Thus, it is of great importance to have a model that is able to account for the Lorentz force. The discrete ordinate methods can simulate the dose deposited in a MRI-guided radiotherapy as shown in the works of St. Aubin et al. [6, 127, 144]. The results agreed within $2\% - 2$mm with the doses calculated with GEANT4 Monte Carlo code, even for strong magnetic fields as shown in Figure 1.13.

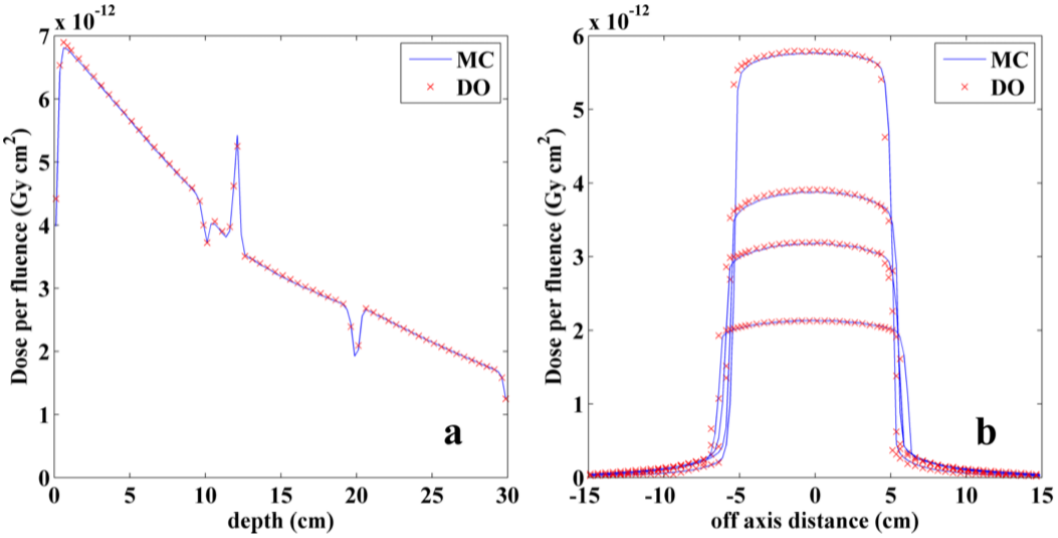

Figure 1.13: Monte Carlo and discrete ordinates formalism comparison. On the left: depth dose along the central axis. On the right: profiles at the center of the beam (x=0). A 10×10 cm^2 field propagates in a heterogeneous phantom composed by layers of materials with different density and chemical composition. The phantom used in this simulation consists in a slab of water in the first 10 cm, in a slab of bone ($\rho = 1.85$ g $\cdot$ cm^{-3}) between 10 and 12 cm in depth, in a slab of lung ($\rho = 0.26$ g $\cdot$ cm^{-3}) between 12 cm and 20 cm in depth and another slab of water between 20 cm and 30 cm. A magnetic field of 3 T is applied perpendicularly to the radiation beam. Image from St. Aubin et al. [127] with permission.

The first deterministic solver incorporated in a commercially available Treatment Planning System is Acuros® (Varian Medical Systems) [136, 137]. It has been derived from the Attila solver [140]. Acuros® has been developed for both external photon beam radiotherapy and brachytherapy. For brachytherapy applications has been named Acuros® BV and it has been developed exclusively for HDR ^{192}I brachytherapy applications [104, 107, 149, 150]. The same solver has been implemented for the external photon beam radiotherapy with the name of Acuros® XB [19, 35].

This model has been extensively validated in several publications. The first works comparing Acuros® XB algorithm against measurements, and also against the Anisotropic Analytical Algorithm (AAA) in water were performed by Fogliata et al. [38, 39, 40]. The model has been tested with different phantom geometries, beam sizes and energies. Similar studies were conducted by other groups [58, 111]. Acuros® XB is able to provide a high accuracy in different cases and also in presence of heterogeneities where the AAA algorithm fails as shown in Figure 1.14. Acuros® XB has been also compared with several Monte Carlo codes and it has been shown that this solver provides a comparable accuracy [19].

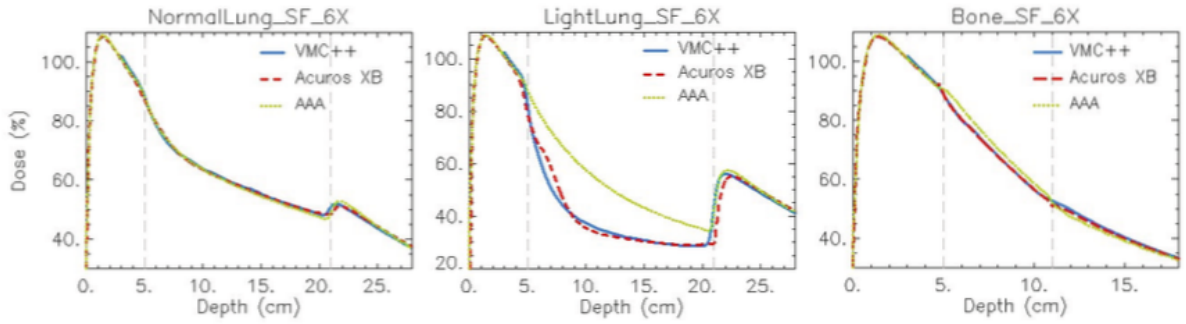

Figure 1.14: Depth dose curves for a photon 6MV beam calculated with VMC (in blue), Acuros XB version 10 (in red), and AAA (in yellow) in a heterogeneous phantom. The phantom consists in an insert, covering laterally only half of the entire phantom and positioned at 5 cm depth in water. Three different materials and thicknesses have been chosen for the insert. In the simulation on the left the heterogeneity is composed by normal lung ($\rho = 0.198$ g $\cdot$ cm^{-3}) 16 cm thick. In the simulation in the center the heterogeneity is composed by light lung ($\rho = 0.035$ g $\cdot$ cm^{-3}) 16 cm thick. In the simulation on the right the heterogeneity is composed by bone ($\rho = 1.798$ g $\cdot$ cm^{-3}) 6 cm thick. Image from Fogliata et al. [39] with permission.

The angular moments method is an alternative to the discrete ordinate methods for a deterministic solution of the LBTE. This methods consists in the reduction of the number of variables in the LBTE by taking moments over the direction variable. The details of this method are discussed in this work. In the past several works applied the moments method to the dose calculation for external beam radiotherapy with both electron and photon beam [57, 76, 34, 108]. These publications demonstrate the feasibility of this method for the dose distribution calculations but did not succeed reaching the precision required in the medical context. The last work on this model has been done by Page et al. where the Lorentz force has been introduced [103]. This work has demonstrated the possibility to implement the magnetic field effects in such a model obtaining good results in terms of precision as shown in Figure 1.15.

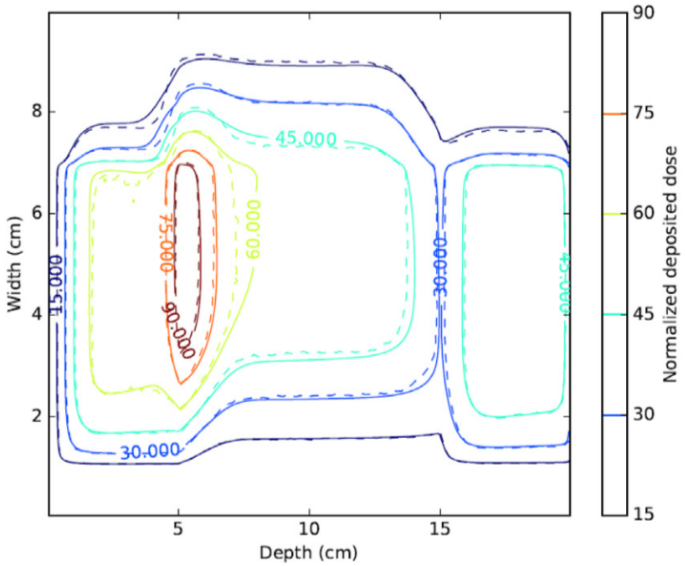

Figure 1.15: Comparison of dose distributions calculated with the Monte Carlo code FLUKA (dashed line) and the angular moments method M_1 (plain line). A 6 MeV monoenergetic photon beam propagates in a heterogeneous phantom. The numerical phantom consists in a slab of water in the first 5 cm , in a slab of lung ($\rho = 0.26$ g $\cdot$ cm^{-3}) between 5 and 15 cm in depth and another slab of water between 15 cm and 20 cm. A magnetic field of 1 T is defined perpendicularly to the beam propagation. Image from Page [103] with permission.

1.3 Conclusion

In this Chapter we have briefly introduced the context of this work recalling the techniques of radiotherapy. We focus on the external photon beam radiotherapy and brachytherapy that represent the main applications of our model. Moreover the main numerical models used for the dose calculations in treatment planning are presented. In the following Chapter we review the radiotherapy treatment related physics.

Chapter 2

Particle interactions in radiotherapy

2.1 Introduction

In this chapter we present a brief review of the most significant interactions taking place in the transport of electrons, positrons and photons in the radiotherapy energy range.

We first focus on electrons and positrons, which are responsible for the dose deposition. The first type of process to be described is the inelastic scattering. The inelastic collisions are those in which the primary particle experiences a loss of energy. In this sense we consider both the collisional and radiative processes as inelastic scattering. The collisional inelastic scattering for electrons is described with the Møller cross section [93] while for positrons we use the Bhabha formulation [11]. Radiative scattering is described using the Bethe-Heitler differential cross-section [10]. Then we describe the elastic scattering that is resposible for diffusion of charged particles. For description of this process the Mott formulation with the Mòliere screening is used [92]. At the end of this section the positron annihilation is described [56].

Regarding the photon interactions we focus on three most probable processes in the energy range covered by the radiotherapy applications. We first describe the photoelectric scattering that takes place at low energies. In water, taken as referent material in medical applications, this process is predominant in the energy range between 1 keV and 30 keV. In order to describe the photoelectric effect we use the simpler Sauter formulation [123] that in principle is valid only for the K-shell of the atom. Even if this formulation is not exact, it gives a more comprehensible view of the phenomenon combined with an acceptable precision. In the energy range between 30 keV and 26 MeV the most probable interaction for a photon is Compton scattering. For its description we use the Klein-Nishina cross section obtained in the approximation of a photon collision with a free electron at rest [72]. The last interactions that we present is the pair and triplet productions in field of a nuclei and in field of an atomic electron respectively. These scattering processes become predominant for energies higher than 26 MeV in water but produce a non-negligible contribution for photon energies higher than 10 MeV.

2.2 Electron and positron interactions

The most significant interactions of electrons and positrons in the energy range of radiotherapy include inelastic collisions on atomic electrons, bremsstrahlung interactions with nuclei, elastic nuclear scattering and positrons annihiliation. Our aim here is to summarize these interactions for reference in the subsequent sections of this work without any attempt to make a comprehensive review.

2.2.1 Inelastic scattering

The dominant energy loss mechanisms for electrons and positrons in the energy range of radiotherapy is inelastic scattering. The inelastic scattering can be divided into two main processes. The first one is the collisional scattering where electrons and positrons collide with an atomic electron producing electronic excitations and ionisation in the medium. If the energy transferred to the electron is lower than the binding energy, the latter is excited and then returns to its stable state. Otherwise, if the energy received by the target electron is sufficiently high to win the binding energy and to produce a discernible track, the ejected electron is called a secondary electron. The second process is the radiative scattering where electrons and positrons interacting with the electrostatic field of atomic nucleus convert a part of their energy in electromagnetic radiation. In sections 2.2.1.1 and 2.2.1.2 we revise the physical principles of these interactions.

2.2.1.1 Collisional scattering

The inelastic collision is the process where the electron or positron collides with an atomic electron producing excitations and ionisations in the medium. If after an inelastic collision two particles emerge, by convention, the particle with the higher energy is considered to be the primary electron or positron, while the less energetic one is considered to be the secondary particle. This type of interaction is the dominant energy loss mechanism for electrons and positrons with intermediate and low energies. In Figure 2.1 a scheme of the collisional process is reported.

Møller was the first one deriving the cross section for electron scattering on free electrons [93]. The Møller cross section can be written as differential in the energy loss, i.e. the knock-on electron energy. If E is the kinetic energy of the incident electron, W is the kinetic energy of the secondary electron and Z is the atomic number of the crossed medium, the Møller differential cross section in the energy of the secondary electron for the electron-electron inelastic scattering is given by:

$$\frac{d\sigma_{\mathrm{coll,e^-}}}{dW} = \frac{2\pi r_0^2 Z}{\beta^2}\frac{mc^2}{W^2}\left(1 + \left(\frac{W}{(E-W)}\right)^2 - \frac{W}{E-W} + \left(\frac{E}{E+mc^2}\right)^2\left(\frac{W}{E-W} + \frac{W^2}{E^2}\right)\right), \tag{2.1}$$

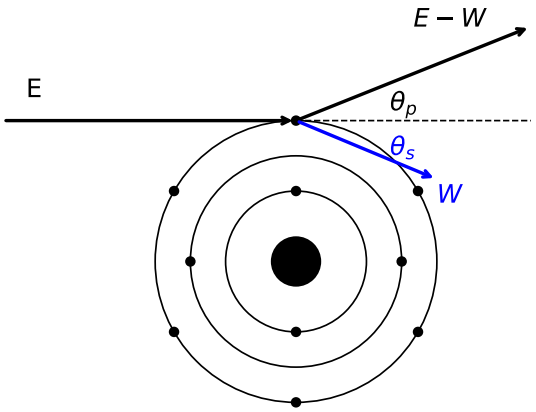

Figure 2.1: Scheme of an ionisation process. The incident electron with a kinetic energy E scatter on an atomic electron considered at rest. The most energetic electron emerging from the collision with an angle θ_p with respect to the impinging particle direction is called 'primary electron' (in black), while the less energetic one, emerging with an angle θ_s and energy W, is called 'secondary electron' (in blue).

where $r_0 = 2.817940326 \times 10^{-15}$m is the classical electron radius and $\beta = \frac{v}{c}$. The total cross section for collisional scattering is obtained by integrating over the energies at which the secondary electron can emerge. Due to the fact that the Møller cross section (2.1) is singular at $W = 0$, we have to impose a cut-off value for the knock-on electron. For this reason, the kinematical limits of the energy transfer are given by:

$$W_{\text{cut}} \leq W \leq \frac{E}{2}, \tag{2.2}$$

where the upper limit is due to the indistinguishability of the two electrons. Integrating Eq. (2.1) in the interval $[W_{\text{cut}}, \frac{E}{2}]$ we obtain the total cross section for the Møller scattering.

We define, by convention, the primary electron as the most energetic one emerging from the collision. The angles at which the primary and secondary electron emerge from the collision are given by the energy-momentum conservation. Calling θ_p and θ_s the angles of the primary and secondary electron with respect to the direction of the incident electron, they take the following formulation:

$$\begin{cases} \cos\theta_p &= \left(\dfrac{E-W}{E}\dfrac{E+2mc^2}{E-W+2mc^2}\right)^{\frac{1}{2}} \\ \cos\theta_s &= \left(\dfrac{W}{E}\dfrac{E+2mc^2}{W+2mc^2}\right)^{\frac{1}{2}}. \end{cases} \tag{2.3}$$

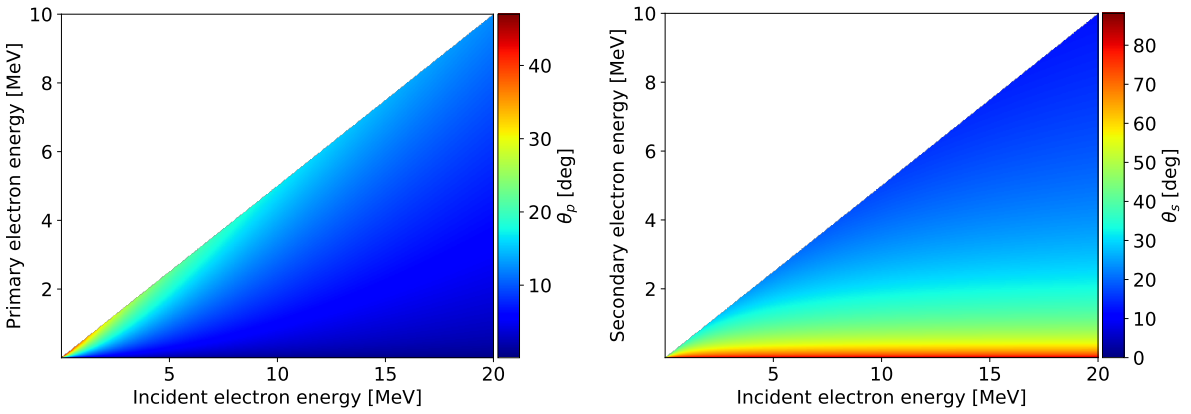

(a) (b)

Figure 2.2: 2D maps of the scattering angle for the primary electron, in panel (a), and for the secondary electron, in panel (b). The angular distribution of the primary electron in forward peaked especially for the higher energies. The secondary electron can emerge from the interaction with a larger angle.

As it can be noticed in Figure 2.2(a), the scattering angle of the primary particle is highly forward peaked relative to the direction of the incident electron. The angle of the secondary particle can be large for a small energy transfer. Due to the fact that the inelastic cross section is highly peaked for small energy transfer and due to the small range of the low energy electrons in water, we can infer that the inelastic collisional scattering is not the main cause of the diffusion of an electron beam. Moreover, the Møller cross section increases rapidly as $1/W^2$ at small energies of the secondary electron. That is why the inelastic scattering is usually divided into catastrophic and soft collisions. We consider as cathastrophic collisions those producing a secondary electron, while in soft collisions we take into account only the energy loss of the impinging particle and the electronic excitation.

Positrons are unstable particles that annihilate with electrons giving photons as described in Section 2.2.3. A positron does not interact with matter as a typical charged particle, since for high energy the competing process of annihilation followed by re-creation can cause the same transitions as direct scattering [120]. The differential cross section for binary collisions of positrons with free electrons at rest, is given by the Bhabha formula [11]:

$$\frac{d\sigma_{\text{coll,e}^+}}{dW} = \frac{2\pi r_0^2 Z}{\gamma - 1}\left(\frac{1}{\beta^2 W^2} - \frac{B_1}{W} + B_2 - B_3 W + B_4 W^2\right), \tag{2.4}$$

where:

$$\begin{aligned} \gamma &= \frac{E + mc^2}{mc^2} \\ y &= \frac{1}{\gamma + 1} \\ B_1 &= 2 - y^2 \\ B_2 &= (1 - 2y)(3 + y^2) \\ B_3 &= (1 - 2y)^2 + (1 - 2y)^3 \\ B_4 &= (1 - 2y)^3 \end{aligned} \tag{2.5}$$

For positron-electron collision the kinematical limit of the energy transfer is:

$$W_{\text{cut}} \leq W \leq E. \tag{2.6}$$

The relations that give the angles at which the incident positron and secondary electrons emerge relative to the direction of the incident particle are the same as for the electrons. This means that the positron inelastic scattering is also highly forward peaked.

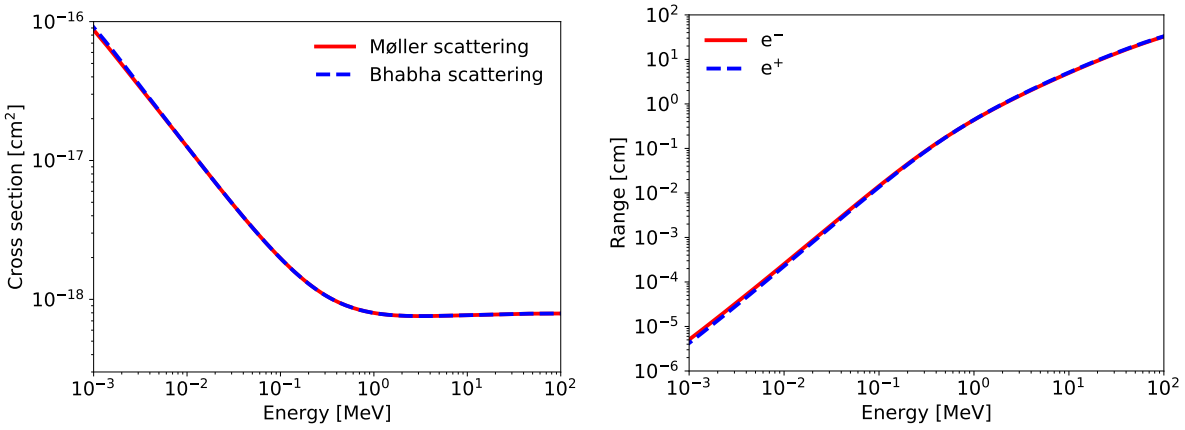

(a) (b)

Figure 2.3: (a) Møller (electron-electron) and Bhabha (positron-electron) total inelastic cross section in water, (b) electron and positron range in water. Data from the Monte Carlo code PENELOPE with permission.

In Figure 2.3(a) we plot the Møller and Bhabha total cross sections in water used in the Monte Carlo code PENELOPE [121]. As shown, the total cross sections do not differ significantly in the energy range of interest for medical applications. A slight difference can be noted for low energies where the range of the particles is of order of 10^{-5} cm (see Figure 2.3(b)), that is completely negligible with respect to the lengths of interest for dose calculation.

2.2.1.2 Radiative scattering

When fast electrons interact with the Coulombian field of the nucleus, as a result of the deflection caused by the electrostatic field a part of their energy can be converted into electromagnetic radiation as shown in Figure 2.4. This process is called the breaking radiation or bremsstrahlung.

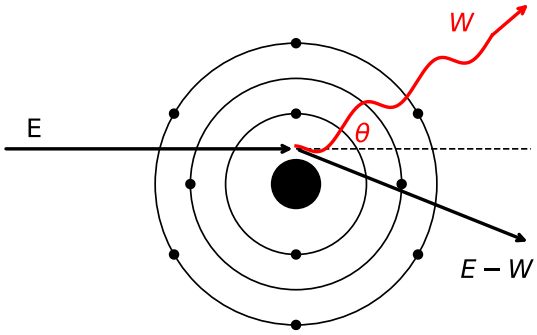

Figure 2.4: Scheme of electron bremsstrahlung scattering on an atomic nucleus. The electron is deviated and loses part of its kinetic energy that is converted in an emitted photon satisfying the conservation laws of energy and momentum.

The fraction of the electron energy converted into bremsstrahlung increases with the electron energy and, for a given electron energy, is larger for materials of high atomic number. In each bremsstrahlung event, an electron with kinetic energy E generates a photon of energy W, which takes values in the interval from 0 to E. For monoenergetic electrons that slow down and stop in a given material, the bremsstrahlung energy spectrum is continuous with a maximum energy that corresponds to the energy of the injected electrons.

The theory of bremsstrahlung was first formulated by Bethe and Heitler using second-order perturbation theory and the Born approximation [10]. Salvat et al. [122, 121] wrote a relatively simple formulation of the Bethe-Heitler differential cross-section for bremsstrahlung emission by electrons in the field of an atom of atomic number Z and screening radius R as tabulated value. This formulation reads:

$$\frac{d\sigma_{\text{rad}}}{dW} = r_0^2 \alpha Z(Z+\eta)\frac{1}{W}\left(\frac{W^2}{\gamma\, mc^2}\varphi_1(b) + \frac{4}{3}\left(1 - \frac{W}{\gamma\, mc^2}\right)\varphi_2(b)\right), \tag{2.7}$$

where α is the fine-structure constant, $\varphi_1(b)$ and $\varphi_2(b)$ are the screening functions defined

as:

$$\begin{aligned}\varphi_1(b) &= 4\ln(R\,mc/\hbar) + 2 - 2\ln(1+b^2) - 4b\arctan(b^{-1}),\\ \varphi_2(b) &= 4\ln(R\,mc/\hbar) + \frac{7}{3} - 2\ln(1+b^2) - 6b\arctan(b^{-1})\\ &\quad - b^2\left[4 - 4b\arctan(b^{-1}) - 3\ln(1+b^{-2})\right],\end{aligned} \tag{2.8}$$

where:

$$b = \frac{R\,mc}{2\gamma\,\hbar}\frac{W}{\gamma\,mc^2 - W}. \tag{2.9}$$

The radiative differential cross section for positrons reduces to that of electrons in the high-energy limit but is smaller for intermediate and low energies (see Figure 2.5). This behaviour has been studied by Kim et al. with the introduction of a scaling law to relate the electron bremsstrahlung cross section with the positron one [69].

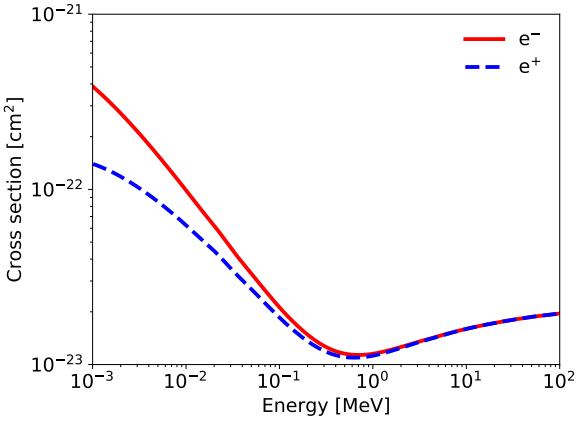

Figure 2.5: Total cross section for electron and positron bremsstrahlung in water. Data from the Monte Carlo code PENELOPE with permission.

2.2.1.3 Stopping power for electrons and positrons

The linear stopping power S for charged particles in a given absorber is defined as the differential energy loss within the material divided by the corresponding differential path length:

$$S(E) = -\frac{dE}{ds}. \tag{2.10}$$

For electrons and positrons propagating in matter the contribution to the stopping power is given both by the collisional and radiative scattering as follows:

$$S(E) = S_{\text{coll}}(E) + S_{\text{rad}}(E) = \mathcal{N}\int_0^{\frac{E}{2}} W\frac{d\sigma_{\text{coll}}}{dW}dW + \mathcal{N}\int_0^{E} W\frac{d\sigma_{\text{rad}}}{dW}dW, \tag{2.11}$$

where $\mathcal{N}$ is the number of atoms per unit volume. In Figure 2.6 we plot the stopping power calculated for electrons and positrons that propagate in water. As expected the energy loss do not differ significantly for the two particles.

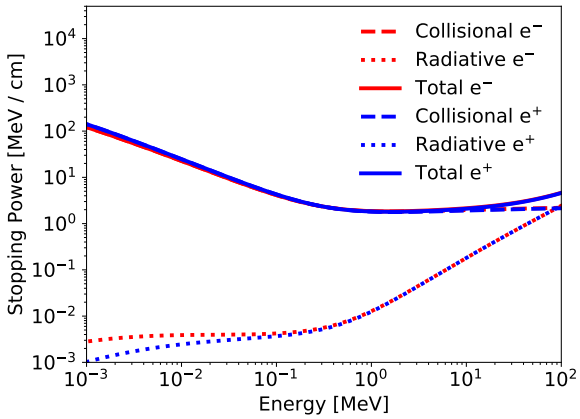

Figure 2.6: Stopping power for electrons and positrons propagating in water. The dashed lines represent the contribution of the collisional scattering to the total stopping power while the dotted lines represent the contribution of the radiative scattering. Red color is used for electrons while blue color is used for positrons. Data from the Monte Carlo code PENELOPE with permission.

2.2.2 Elastic scattering

The elastic interactions are those in which the initial and final quantum states of the target atom are the same, normally the ground state as shown in Figure 2.7. Because the mass of a target nucleus is much greater than that of the electron or positron, the energy lost by the projectile is negligible in this interaction.

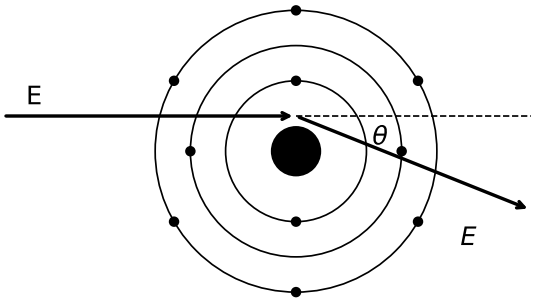

Figure 2.7: Scheme of electron elastic scattering on an atom. In the Mott formulation of the elastic scattering, the target atom is considered as a frozen charge distribution and the interaction with the projectile is assumed to reduce to the electrostatic interaction.

Elastic collisions of electrons and positrons with kinetic energies larger than a few hundred eV can be described as scattering of the projectile by the electrostatic field of the target [121]. The charge distribution of the target atom consists of the nucleus and the electron cloud. The differential cross section for the elastic scattering is derived by Mott from the Rutherford differential cross section and reads [147]:

$$\begin{aligned}\frac{d\sigma}{d\Omega} =& \frac{2\pi r_0^2 Z^2}{\left(1-\cos\theta+\frac{1}{2}\eta^2(E)\right)^2}\frac{(E+1)^2}{E^2(E+2)^2}\left(1+\frac{\alpha\pi Z}{\beta\sqrt{2}}\chi(E)\left(1-\cos\theta+\frac{1}{2}\eta(E)\right)^{\frac{1}{2}}\right.\\ &\left.+\left(R_{MR}-1-\frac{\alpha\pi Z}{2\beta}\chi(E)(1-\cos\theta)^{\frac{1}{2}}\right)\times\left(\frac{1-\cos\theta\,\frac{1}{2}\eta(E)}{1-\cos\theta}\right)^2\right)\end{aligned} \tag{2.12}$$

where:

$$\eta^2(E)=\left(\frac{(E+1)^2}{E(E+2)}-1\right)\left(\frac{\alpha Z^{\frac{1}{3}}}{0.885}\right)\left(1.13+3.76\frac{\alpha^2Z^2(E+1)^2}{E(E+2)}\right) \tag{2.13}$$

is the Moliere screening parameter. Moreover, R_{MR} is the ratio of Mott-to-Rutherford scattering determined from numerical calculations for high and low Z elements, and $\chi(E)$ is a tabulated function [32].

Elastic scattering has a prominent influence on the transport of fast electrons and positrons in matter. In elastic collisions, these particles may undergo large deflections and, as a result, the space distribution of dose from electrons and positrons depends strongly on the elastic scattering properties of the medium.

2.2.3 Electron-positron annihilation

When the photon energy exceeds twice the rest-mass energy of an electron, i.e. 1.022 MeV, the process of pair production is energetically possible, as it is explained in Section 2.3.3. The interaction takes place in the Coulomb field of the atom nucleus and the photon disappears being replaced by an electron-positron pair. All the excess energy above the 1.022 MeV goes into kinetic energy shared by the positron and the electron.

When the energy of positrons is very low, near the end of their range, they combine with the atomic electrons of the material. This process is called annihilation. The original positron and the atomic electron disappear and are replaced by two oppositely directed 0.511 MeV photons known as annihilation radiation as shown in Figure 2.8.

The annihilation in flight of a positron and electron is described by the cross section formula of Heitler [56]. Nelson has rewritten the Heitler formula translating it into the laboratory frame, integrating over azimuthal angle and changing from angle to energy variable [95]. Positrons with kinetic energy E penetrating a medium of atomic number Z can annihilate with free and at rest electrons by emission of two photons that may have different energies, say W_l and W_h. If the incident positron has a kinetic energy E, then the total energy is $\mathcal{W}_{e^+} = E + mc^2$. The total available energy is $\mathcal{W}_{\text{tot}} = \mathcal{W}_{e^+} + mc^2$.

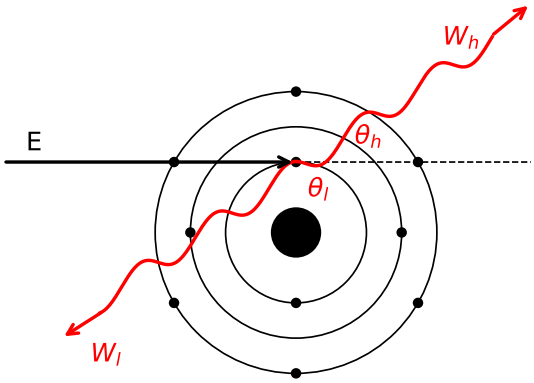

Figure 2.8: Scheme for electron-positron annihilation. The annihilation process have place when a propagating positron collides with an electron of the medium and the emission of two photons with energies W_l and W_h takes place.

The fraction of the total energy transferred to one photon (e.g. W_l) is:

$$\zeta = \frac{W_l}{E + 2mc^2}. \tag{2.14}$$

From the conservation of energy and momentum it follows that the two photons are emitted in directions with polar angles given by the following relations:

$$\begin{cases} \cos\theta_{\mathrm{l}} & = (\gamma^2 - 1)^{-\frac{1}{2}} \left(\gamma + 1 - \dfrac{1}{\zeta}\right), \\ \cos\theta_{\mathrm{h}} & = (\gamma^2 - 1)^{-\frac{1}{2}} \left(\gamma + 1 - \dfrac{1}{1-\zeta}\right). \end{cases} \tag{2.15}$$

The differential cross section for the positron annihilation is given by:

$$\frac{d\sigma}{d\zeta} = \frac{Z\pi\, r_0^2}{\gamma - 1} \frac{1}{\zeta} \left(1 + \frac{2\gamma}{(\gamma+1)^2} - \zeta - \frac{1}{(\gamma+1)^2} \frac{1}{\zeta}\right). \tag{2.16}$$

2.3 Photon interactions

In this Section, we consider the interactions of photons of energy E with atoms of atomic number Z. We limit our considerations to the energy range from 1 keV up to 100 MeV, where the dominant interaction processes are the photoelectric effect, incoherent (Compton) scattering and electron-positron pair production. Let us now introduce the first photon interaction that takes place in the low energy regime.

2.3.1 Photoelectric effect

In the photoelectric effect, a photon of energy E gives all its kinetic energy to a bounded electron of the medium, as shown in Figure 2.9. The photoelectric process can occur only if the photon has a kinetic energy greater than the binding energy of the electron. The direction of emission of the resulting photoelectron, relative to that of the absorbed photon, is defined by the polar and azimuthal angles, respectively θ_e and φ_e. Due to the fact that the incident photon is not polarised the angular distribution of photoelectrons is independent of φ_e. After a photoelectric collision, due to the vacancy in the original electron shell, the atom is in an excited state. The vacancy can be filled by an higher orbital electron with a consequent emission of an X-ray. If the energy released by the outer electron is given to another electron in a higher shell the latter is ejected as an Auger electron.

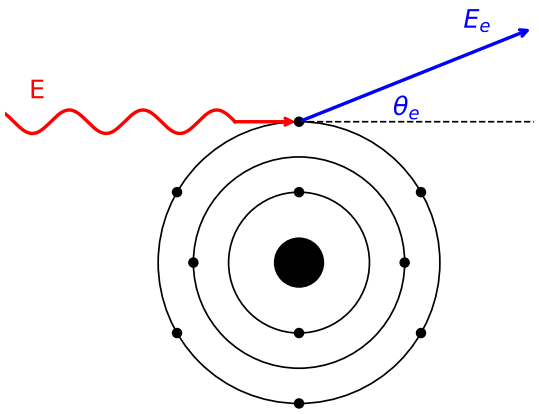

Figure 2.9: Scheme for photoelectric effect. A photon of energy E is absorbed by the atom and an orbital electron is ejected with an energy E_e and an angle θ_e with respect to the direction of the impinging photon. In this process, the entire energy of the photon is absorbed by the atom and then transferred to the atomic electron.

In first approximation, the polar angle θ_e can be sampled from the K-shell cross section derived by Sauter [123]. The Sauter differential cross section in the energy of the photoelectron can be written as:

$$\frac{d\sigma}{d\Omega} = \alpha^4 r_0^2 \left(\frac{Zmc^2}{E}\right)^5 \frac{\beta^3}{\gamma} \frac{\sin^2\theta_e}{(1-\beta\cos\theta_e)^4} \left(1 + \frac{1}{2}\gamma(\gamma-1)(\gamma-2)(1-\beta\cos\theta_e)\right). \quad (2.17)$$

The Sauter cross-section is adequate only for ionisation of the K-shell by high energy photons. Nevertheless, no appreciable errors are introduced when Sauter's distribution is used to describe any photoionisation event. The reason is that the emitted photoelectron

immediately interacts with the medium, and its direction of motion is strongly altered after travelling a path length much shorter than the photon mean free path. Due to the strong dependence on the atomic number of the material, the photoelectron cross section varies significantly even if the variation of Z is small. In Figure 2.10 the plot of the photoelectric total cross section for water and bone equivalent materials is reported. As it can be noted, despite to the small difference between the equivalent atomic number of water and bone, the two cross sections consistently differ. Moreover, in the low-energy region, discontinuities in the curve of bone appear at photon energies. These discontinuities correspond to the binding energies of electrons in the various shells of the 'equivalent atom' of bone material. The edge lying highest in energy corresponds to the binding energy of the K-shell electron.

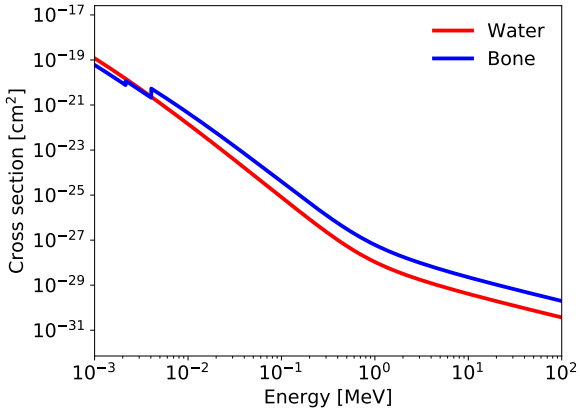

Figure 2.10: Total cross sections for photoelectric effect in water ($\rho = 1.0$ g $\cdot$ cm^{-3}, $Z_{\text{eq}} = 7.22$) and bone ($\rho = 1.85$ g $\cdot$ cm^{-3}, $Z_{\text{eq}} = 10.63$) equivalent materials. The two discontinuities in the bone curve correspond to the K-shell edges. Data from the Monte Carlo code PENELOPE with permission.

2.3.2 Incoherent scattering

In the Compton effect, the incident photon with energy E collides with an atomic electron and gives some of its energy to that electron as shown in Figure 2.11. After the collision the incident photon energy and direction are changed according to the conservation of the energy and momentum. The electron, that can be considered at rest before the collision, has now kinetic energy E_{e}. The Compton effect is the dominant scattering process for energies between 30 keV and 26 MeV in water and is the main cause of the energy loss of photons in radiotherapy applications.

It is worthwhile for a better comprehension to derive the kinematics of the Compton process from the laws of conservation of the energy and momentum. We introduce the relativistic energy-momentum 4-vector defined as follows:

$$\vec{P} = \left(\mathcal{W}c^{-1}, \vec{p}\right) = \left(\mathcal{W}c^{-1}, p_x, p_y, p_z\right), \tag{2.18}$$

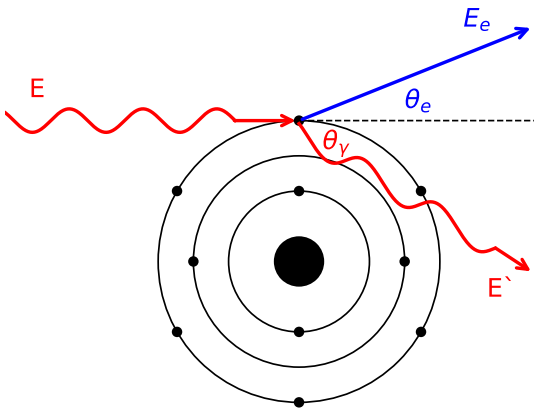

Figure 2.11: Scheme of photon scattering on an atomic electron. The kinematics of the Compton scattering consists in the binary collision between a photon (projectile) and an atomic electron at rest (target). The energies E_e and E', and the propagation angles θ_e and θ_γ of the knock-on electron and of the scattered photon respectively are correlated by the conservation of energy and momentum.

where $\mathcal{W} = E + mc^2$ is the total energy, including the rest energy of the electron $mc^2 = 0.511$ MeV and $\vec{p}$ is the momentum. Let us now analyse the kinematics of a two body reaction, in which a projectile labelled with the index 1 collides with a target labelled with the index 2 initially at rest in the laboratory frame of reference. Particles 3 and 4 are the particles after the collision. The energy-momentum 4-vectors of the involved particles are:

$$\begin{aligned}
\vec{P_1} &= \left(\mathcal{W}_1 c^{-1}, 0, 0, p_1\right), \\
\vec{P_2} &= \left(\mathcal{W}_2 c^{-1}, 0, 0, 0\right) = \left(m_e c, 0, 0, 0\right), \\
\vec{P_3} &= \left(\mathcal{W}_3 c^{-1}, p_3 \sin\theta_3, 0, p_3 \cos\theta_3\right), \\
\vec{P_4} &= \left(\mathcal{W}_4 c^{-1}, p_4 \sin\theta_4, 0, p_4 \cos\theta_4\right).
\end{aligned} \tag{2.19}$$

The momentum and energy conservation is expressed as follows:

$$\vec{P_1} + \vec{P_2} = \vec{P_3} + \vec{P_4}. \tag{2.20}$$

The square length of the energy-momentum vector is invariant:

$$\vec{P} \cdot \vec{P} = \mathcal{W}^2 c^{-2} - \vec{p}^2 = (mc)^2, \tag{2.21}$$

which gives the following expression

$$\begin{aligned}(m_4c)^2 = \vec{P}_4 \cdot \vec{P}_4 &= \left(\vec{P}_1 + \vec{P}_2 - \vec{P}_3\right)\left(\vec{P}_1 + \vec{P}_2 - \vec{P}_3\right) \\ &= \vec{P}_1\vec{P}_1 + \vec{P}_2\vec{P}_2 + \vec{P}_3\vec{P}_3 + 2\vec{P}_1\vec{P}_2 - 2\vec{P}_1\vec{P}_3 - 2\vec{P}_2\vec{P}_3 \\ &= (m_1c)^2 + (m_2c)^2 + (m_3c)^2 + 2\mathcal{W}_1\mathcal{W}_2c^{-2} - 2\left(\mathcal{W}_1\mathcal{W}_3c^{-2} - p_1p_3\cos\theta_3\right) - 2\mathcal{W}_2\mathcal{W}_3c^{-2}.\end{aligned} \tag{2.22}$$

After some algebraic manipulations, we obtain an expression for the exiting angle of the particle 3:

$$\cos\theta_3 = \frac{(m_4c)^2 - (m_1c)^2 - (m_2c)^2 - (m_3c)^2 - 2\mathcal{W}_1\left(\mathcal{W}_3 - \mathcal{W}_2\right)c^{-2} + \mathcal{W}_2\mathcal{W}_3c^{-2}}{2p_1p_3}. \tag{2.23}$$

The magnitude of the momentum is given by

$$(cp)^2 = E\left(E + 2mc^2\right). \tag{2.24}$$

Recalling the definition of $\mathcal{W}$ and substituting in the previous equation, we obtain:

$$c^2p^2 = \left(\mathcal{W} - mc^2\right)\left(\mathcal{W} + mc^2\right) = \left(\mathcal{W}^2 - m^2c^4\right), \tag{2.25}$$

which gives:

$$cp = \sqrt{\mathcal{W}^2 - m^2c^4}. \tag{2.26}$$

With these expressions, we can rewrite relation (2.23) in the following way:

$$\cos\theta_3 = \frac{m_4^2c^4 - m_3^2c^4 - m_2^2c^4 - m_1^2c^4 - 2\mathcal{W}_1\left(\mathcal{W}_3 - \mathcal{W}_2\right) + \mathcal{W}_2\mathcal{W}_3}{2\sqrt{\mathcal{W}_1^2 - m_1^2c^4}\sqrt{\mathcal{W}_3^2 - m_3^2c^4}}. \tag{2.27}$$

By symmetry, an analogous expression for $\cos\theta_4$ is derived:

$$\cos\theta_4 = \frac{m_3^2c^4 - m_4^2c^4 - m_2^2c^4 - m_1^2c^4 - 2\mathcal{W}_1\left(\mathcal{W}_4 - \mathcal{W}_2\right) + \mathcal{W}_2\mathcal{W}_4}{2\sqrt{\mathcal{W}_1^2 - m_1^2c^4}\sqrt{\mathcal{W}_4^2 - m_4^2c^4}}. \tag{2.28}$$

We introduce the particles mass and energy values for the case of the Compton scattering

$$\begin{cases} m_1 = 0 \\ m_2 = m_e \\ m_3 = 0 \\ m_4 = m_e \end{cases} \qquad \begin{cases} \mathcal{W}_1 = E \\ \mathcal{W}_2 = m_ec^2 \\ \mathcal{W}_3 = E' \\ \mathcal{W}_4 = m_ec^2 + E - E' \end{cases} . \tag{2.29}$$

By using these values in Eqs. (2.27) and (2.28) we obtain expressions for the exiting angles of the secondary photon $\theta_\gamma = \theta_3$ and of the produced electron $\theta_\mathrm{e} = \theta_4$:

$$\begin{cases} \theta_\gamma = \arccos\left(\dfrac{mc^2}{E}\left(\dfrac{E}{mc^2} + 1 - \dfrac{E}{E'}\right)\right) \\ \theta_\mathrm{e} = \arccos\left(\left(\dfrac{E}{mc^2} + 1\right)\left(\dfrac{1 - \frac{E}{E'}}{\frac{E}{mc^2}\left[2 + \frac{E}{mc^2}\left(1 - \frac{E}{E'}\right)\right]}\right)^{1/2}\right). \end{cases} \tag{2.30}$$

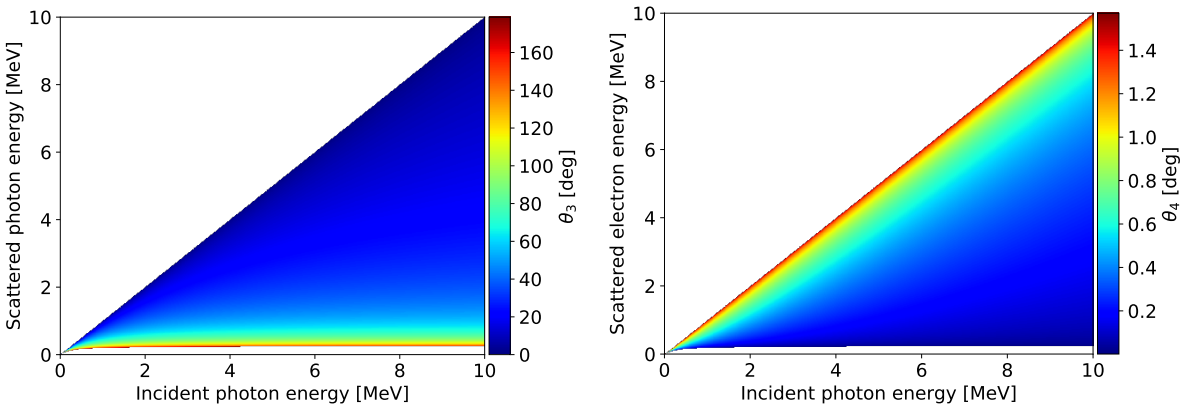

(a) (b)

Figure 2.12: Two dimensional maps of the angles of the exiting particles (a) photons (b) electrons, as functions of the incident photon energy E and the scattered photon energy E_{p}.

We now plot the angles expressed in (2.30) as functions of the incident photon energy E and the scattered photon energy E' in Figure 2.12. As shown in Figure 2.12 the angular distribution of the emitted photon is forward peaked for a small energy loss and for photons of higher energy. For lower energy photons the angular distribution of the emitted photon is more isotropic. The relation between the exiting energy of the photon and its deviation with respect to the initial direction follows from the expression (2.30) for the angle θ_γ:

$$E' = \frac{E}{1 + \frac{E}{mc^2}(1 - \cos\theta_\gamma)}. \tag{2.31}$$

The differential cross section for the Compton scattering on a free electron at rest is given by the Klein-Nishina formula [72]:

$$\frac{d\sigma}{d\epsilon} = \pi r_0^2 \frac{Zmc^2}{E}\left(\frac{1}{\epsilon} + \epsilon\right)\left(1 - \frac{\epsilon \sin^2\theta_\gamma}{1 + \epsilon^2}\right), \tag{2.32}$$

where $\epsilon = E'/E$ and θ_γ is the scattering angle of the photon. As it can be seen in Eq. (2.32), the Compton scattering depends linearly on Z. This simple formulation represents an approximation for the Compton interaction. In reality, the atomic electrons are bounded with an ionisation energy of the active shell. The ionization energy can be neglected in the medical physics application due to the high energy of the incident particles. Moreover, atomic electrons are not at rest, but move with a certain momentum distribution, which gives rise to the so-called Doppler broadening of the Compton line.

2.3.3 Pair production

Electron-positron pairs can be created by absorption of a photon following the interaction with the Coulomb field as shown in Figure 2.13. The most probable interaction takes

place in the field of the atomic nucleus but for higher energy can occur in the field of an atomic electron. The massive particle absorbs energy and momentum so that these two quantities are conserved. If the interaction takes place in the field of an atomic electron is called 'triplet production' because the initial electron at rest obtains also kinetic energy and thus two electrons and one positron have produced with a significant amount of kinetic energy. The threshold energy for pair production in the field of a nucleus (assumed of infinite mass) is $2mc^2$.

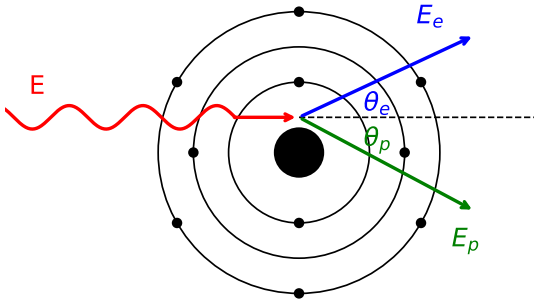

Figure 2.13: Scheme of pair production in nuclear field. The photon of energy E interacts with the electromagnetic field of an atomic nucleus and gives up all its energy in the process of creating a pair consisting of an electron and a positron with energy E_e and E_p respectively.

The Bethe-Heitler differential cross section for a photon of energy E to create an electron-positron pair [10], in which the electron has a kinetic energy $E_\mathrm{e} = \epsilon E - mc^2$, can be expressed as

$$\frac{d\sigma}{d\epsilon} = r_0^2 \alpha Z(Z+\eta)\left((\epsilon^2+(1-\epsilon)^2)(\Phi_1 - 4f_C) + \frac{2}{3}\epsilon(1-\epsilon)(\Phi_2 - 4f_C)\right), \tag{2.33}$$

where ϵ is the fraction of the photon energy taken by the secondary electron, η is the triplet contribution, Φ_1 and Φ_2 are screening functions of the nucleus reading

$$\begin{aligned}\Phi_1(b) &= 2 - 2\ln(1+b^2) - 4b\arctan(b^{-1}) + 4\ln(Rmc/\hbar)\\ \Phi_2(b) &= 4\ln(Rmc/\hbar) + \frac{4}{3} - 2\ln(1+b^2) + 2b^2\left[4 - 4b\arctan(b^{-1}) - 3\ln(1+b^{-2})\right],\end{aligned} \tag{2.34}$$

where

$$b = \frac{mc^2}{2E}\frac{1}{\epsilon(1-\epsilon)}\frac{Rmc}{\hbar}, \tag{2.35}$$

and f_C is the Coulomb correction for high-energy given by

$$f_C = a^2[(1+a^2)^{-1} + 0.202059 - 0.03693a^2 + 0.00835a^4 - 0.00201a^6 + 0.00049a^8 - 0.00012a^{10} + 0.00003a^{12}]. \tag{2.36}$$

coheretly to Salvat et al. [121].

2.4 Conclusion

In this chapter we presented a brief review of the most important interactions that electrons, positrons and photons can experience crossing a material in the radiotherapy energy regime. The knowledge of the scattering cross section is fundamental in order to understand the physical processes that take place during the propagation of a particle beam. In the following sections we use the physics described in this chapter in order to justify and better understand the numerical strategies that we adopt in our model. In Figure 2.14 we show the plot of the total cross sections for photons and electrons in water.

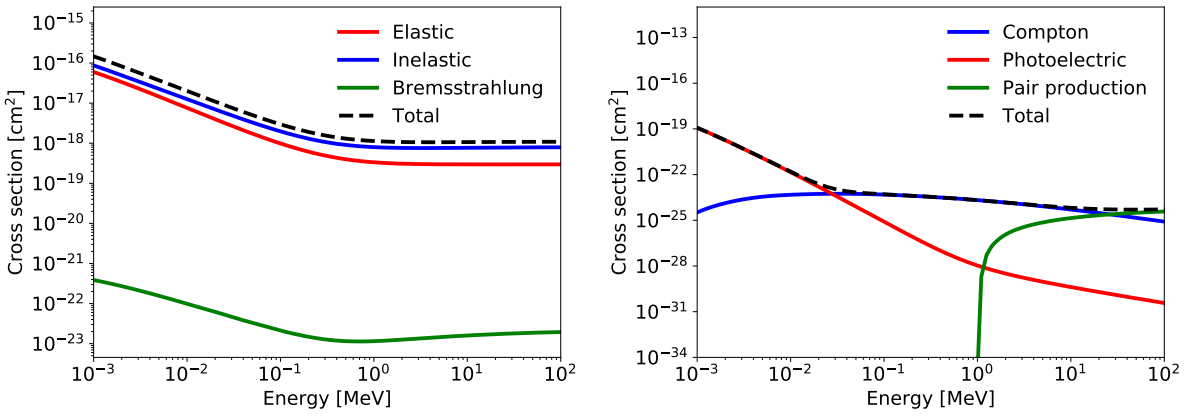

(a) (b)

Figure 2.14: (a) Electron cross sections in water: the dashed black line represents the total cross section, the blue line represents the collisional inelastic scattering contribution, the red line represents the elastic scattering contribution and the green line represents the radiative scattering contribution. (b) Photon cross sections in water: the dashed black line represents the total cross section, the red line represents the photoelectric scattering contribution, the blue line represents the Compton scattering and the green line represents the pair production. Tables of data from the Monte Carlo code PENELOPE.

Chapter 3

Moments method for the Boltzmann transport equation solution

3.1 Introduction

This chapter is devoted to the presentation of the entropic model as it has been conceived for medical physics applications. In the first part of this chapter we introduce the Boltzmann transport equation, in its linearized form. We present an heuristic derivation of the equation in order to allow the reader to better understand the equation and the moments method that is built on it.

Once the linear Boltzmann transport equation is written in its general form for the coupled transport of photons, electrons and positrons we introduce the entropic model. The first member of the hierarchy, the M_1 model, has been developed by Dubroca and Feugeas [33] in 1999. Moreover we study some structural limitations of this model as the simultaneous treatment of two opposite beams or the numerical issues due to the treatment of the secondary particles. At the end of this section we introduce the second member of the hierarchy, the M_2 model.

An important part of this chapter is devoted to the beam initialization in the M_1 model. The M_1 model is a mesoscopic model so the kinetic description is partially lost. In this sense, instead of initialize a phase-space as in a Monte Carlo code, for the M_1 model the initialization is strictly dependent on the anisotropy of the beam. For this reason we propose a method to translate a phase-space initialization suitable for a Monte Carlo code into an anisotropy distribution for M_1.

In the last part of this chapter we describe the method used for the validation of the M_1 model with respect to the PENELOPE Monte Carlo code. Multiple techniques of comparisons are used in this work in order to analyse precisely the differences and define the degree of discrepancy between the two codes for the external photon beam radiotherapy and brachytherapy.

3.2 Boltzmann transport equation

3.2.1 Introduction

The equation that describes the transport and the interactions of particles with the media is the Boltzmann transport equation that under its linearized form, i.e. when only the interaction of projectile particles with the ambient atoms is considered and interactions between the projectile particles are neglected, reads [7, 21]:

$$\frac{1}{v}\frac{\partial\psi(\vec{r},E,\widehat{\Omega},t)}{\partial t}+\widehat{\Omega}\cdot\nabla\psi(\vec{r},E,\widehat{\Omega},t)+\sigma_t(\vec{r},E)\psi(\vec{r},E,\widehat{\Omega},t)= \int_0^\infty dE'\int_{S^2}d\widehat{\Omega}'\,\sigma_s(\vec{r},E'\to E,\widehat{\Omega}'\to\widehat{\Omega})\psi(\vec{r},E',\widehat{\Omega}',t)+Q(\vec{r},E,\widehat{\Omega},t) \tag{3.1}$$

where $\overrightarrow{r}\in\mathbb{R}^3$ is the position vector, E is the particle energy, $\widehat{\Omega}$ is a unitary vector defining the direction of particle propagation, S^2 is the unit sphere in 3-dimensional Euclidean space, ψ is the particle flux, σ_t is the total cross-section, σ_s is the differential scattering cross-section and Q is the source term. This equation describes the transport of particles in a given medium and it can be used for calculating the dose deposition for medical purposes. Equation (3.1) has seven independent variables: three spatial variables $\vec{r}=[x,y,z]^T$, two angular variables $\widehat{\Omega}=[\cos\theta,\cos\phi\sin\theta,\sin\phi\sin\theta]^T$, energy E and time t. Due to a high number of independent variables, i.e. a high dimensionality of the phase space, the solution of this equation is extremely costly and difficult.

The domain of application of the linearized Boltzmann transport equation is defined by specifying in Eq. (3.1) expressions for the cross sections. In order to describe the transport of photons, electrons and positrons we need a system of coupled transport equations. This is due to the fact that the incident particles can produce particles of a other species. As described in Chapter 2 photons produce electrons, electrons produce photons, photons can produce positron-electron pairs or these pairs produce photons.

For medical applications such as dose calculations the linearized form of the Boltzmann equation is justified and a simpler equation with respect to Eq. (3.1) can be formulated under two main assumptions:

1. The first assumption is related to the propagation of the particle beam in a medium. As experimentally measured in [47], the average value of the number of electrons emitted by an accelerator (a Varian 21Ex in the specific case) in the electron radiotherapy configuration is $(1.68\pm0.08)\times10^{11}$ per steradian [sr^{-1}] and per Monitor Unit [MU^{-1}]. This number is very small compared to the electron density of water, which can be considered as material of reference in medical physics applications, that is 3.34×10^{23} electrons per gram [g^{-1}]. From this consideration two important consequences arise. The first consequence consists in the fact that the binary collisions among the beam particles can be neglected. Moreover, electromagnetic field

produced by particles can be neglected. The second consequence is that the physical characteristics of the ambient medium (e.g. temperature, density, composition) are not modified by the interaction with the injected particles. This means that the cross sections governing the collision of the transported particles are defined at the beginning of the simulation and do not change. This consideration justifies the use of the linearized Boltzmann kinetic equation for radiological purposes.

2. The second assumption is related to the kinetic energy of the injected particles. The injected particles are relativistic and the energy range considered for the simulations goes from 1 keV to 20 MeV. This means that the velocity of the medium particles and the rapidity of the biological response are negligible if compared to the speed of particles. Moreover, the time required for slowing down the particles is negligible if compared to the time of irradiation. These assumptions imply that the flux of injected particles can be considered as constant in time and the equation describing the transport of particles is time independent.

For a better understanding of the LBTE, we present a heuristic derivation of the system of coupled photon-electron-positron transport equations and an explaination of each term in the equations.

3.2.2 Heuristic derivation of the transport equation

The probability to find a particle (photon, electron and positron in our case) in the phase space is described by the distribution function $f(\vec{r}, E, \widehat{\Omega})$. It presents the number of particles in the infinitesimal volume element $d\vec{r}$ about the point $\vec{r}$ with energies in dE about E and with directions in $d\widehat{\Omega}$ about $\widehat{\Omega}$. The distribution function is related to the particle flux according to the relation $\psi(\vec{r}, E, \widehat{\Omega}) = vf(\vec{r}, E, \widehat{\Omega})$, where v is the particle velocity.

When a particle undergoes an interaction with the electrons or the atomic nuclei that compose the ambient medium, two reactions may take place: the particle can be either scattered, or absorbed, or produce a particle of other species. Each interaction is considered to be local in space and instantaneous in time. Between two interactions, in absence of an external electromagnetic field, the particle is assumed to propagate in a straight line. The probability of interaction of the particle with the ambient medium is governed by cross sections.

We now define more precisely the meaning of different types of cross sections:

- The absorption cross section $\sigma_a(\vec{r}, E)$ can be defined as the probability that a particle is absorbed (disappears) over a unit pathlength and another different species of particle is created. Such a cross section has unit of inverse length and depends on the particle kinetic energy E and on the spatial position $\vec{r}$.

- The scattering cross section $\sigma_s(\vec{r}, E)$ is defined as the probability that a particle is scattered over a unit pathlength. Such cross section has units of inverse length and depends on the particle kinetic energy E and on its spatial position $\vec{r}$. The probability that a particle with energy E' and direction of flight $\widehat{\Omega}'$ emerges from an interaction with a given energy E and direction $\widehat{\Omega}$ is defined by the differential scattering cross section. Assuming that the scattering does not depend on the azimuthal angle ϕ, we define $\mu = \widehat{\Omega} \cdot \widehat{\Omega}'$ as the cosine of the collision angle, i.e. the angle at which a secondary particle comes out of a collision, with respect to the direction of the colliding particle. The differential cross section is defined as:

$$\sigma_s(\vec{r}, E', E, \mu) = \frac{d\sigma(\vec{r}, E', E, \mu)}{dE\, d\mu} \tag{3.2}$$

  The differential scattering cross sections have units of inverse length inverse energy and inverse steradian. Moreover, the scattering differential cross sections can be represented by a Legendre expansion in the following way:

$$\sigma(E' \to E, \mu) = \sum_{L=0}^{\infty} \frac{2L+1}{4\pi}\, \sigma_L(E' \to E)\, P_L(\mu), \tag{3.3}$$

  where $P_L(\mu)$ are the Legendre polynomials defined by the Rodrigues' formula as

$$P_L(\mu) = \frac{1}{2^L\, L!} \frac{d^L}{d\mu^L}(\mu^2 - 1)^L, \tag{3.4}$$

  and

$$\sigma_L(E' \to E) = \int d\widehat{\Omega}\, P_L(\mu)\sigma(E' \to E, \mu) = 2\pi \int_{-1}^{1} d\mu\, P_L(\mu)\sigma(E' \to E, \mu), \tag{3.5}$$

  are the expansion coefficients.

- The total cross section $\sigma_t(\vec{r}, E) = \sigma_a(\vec{r}, E) + \sigma_s(\vec{r}, E)$ can be defined as the probability that a particle undergoes any interaction per unit pathlength. Such a cross section has unit of inverse length and depends on the particle kinetic energy E and on its spatial position $\vec{r}$.

These absorption, scattering and total cross sections are macroscopic cross sections. These cross sections are related to the microscopic cross sections introduced in Chapter 2, i.e. the cross sections defined for an element, through the following relation:

$$\sigma_{\mathrm{ma}} = \frac{N_A\, \rho}{A} \sigma_{\mathrm{mi}} \tag{3.6}$$

where N_A is the Avogadro's constant, ρ is the mass density of the material and A is gram-atomic weight of an element.

The transport equation can be defined as a balance relation describing the motion of particles in the phase space. The phase space consists of three variables (six dimensions) $\vec{r}$, $\widehat{\Omega}$, and E. A differential volume of the phase space is given by:

$$dP = d^3\vec{r}\, d\widehat{\Omega}\, dE. \tag{3.7}$$

Let P be the volume in phase space, in its most basic form the particle balance equation reads:

$$[\text{change rate in P}] = [\text{flux of particles entering P}] - [\text{flux of particles leaving P}]. \tag{3.8}$$

In order to determine the number of particles in a volume P, we have to integrate $f = f(\vec{r}, E, \widehat{\Omega})$ over the spatial volume ΔV, the range of directions $\Delta\widehat{\Omega}$ and energy range ΔE. We define the term that takes into account the particles entering P as the "gain" term and the term that takes into account particles exiting P as the "loss" term. Let us now derive the balance relation describing distribution of particles in the phase space by analysing the gain and loss terms.

Gains: Particles can enter the phase volume P in two different ways:

1. **Source**: the source term describes the number of particles entering the phase volume due to a specified external source. The source is defined as input data and does not vary during the simulation. The source is defined by:

   $$Q(\vec{r}, E, \widehat{\Omega}) = \frac{\#\,\text{particles}}{\text{cm}^3 \cdot \text{MeV} \cdot \text{sr}} \tag{3.9}$$

   The number of particles entering in a phase differential volume due to the external source is given by

   $$\int_{\Delta V} d^3\vec{r} \int_{\Delta E} dE \int_{\Delta\widehat{\Omega}} d\widehat{\Omega}\, Q(\vec{r}, E, \widehat{\Omega}) \tag{3.10}$$

2. **Inscatter**: This refers to the particles that scatter into the phase volume. This term takes into account the contributions given by all scattering processes to produce particles in a given phase volume. It is defined by:

   $$\int_{\Delta V} d^3\vec{r} \int_{\Delta E} dE \int_{\Delta\widehat{\Omega}} d\widehat{\Omega} \int_E^\infty dE' \int_{S^2} d\widehat{\Omega}'\, \sigma_s(\vec{r}, E' \to E, \widehat{\Omega}' \to \widehat{\Omega}) \psi(\vec{r}, E', \widehat{\Omega}') \tag{3.11}$$

Losses: Particles can exit the phase volume P in two different ways:

1. **Absorption**: When a particle undergoes collisions, it is possible that a process of absorption takes place. The number of particles absorbed per unit volume can be written as follows:

   $$\sigma_a(\vec{r}, E)\, \psi(\vec{r}, E, \widehat{\Omega}). \tag{3.12}$$

   Therefore, the number of particles absorbed within the phase volume P is given by

   $$\int_{\Delta V} d^3\vec{r} \int_{\Delta E} dE \int_{\Delta\widehat{\Omega}} d\widehat{\Omega}\, \sigma_a(\vec{r}, E)\, \psi(\vec{r}, E, \widehat{\Omega}) \tag{3.13}$$

2. **Outscatter**: The term outscattering refers to the loss of particles from a phase volume due to a scattering interaction. We can describe the rate at which particles outscatter as follows

$$\int_{\Delta V} d^3\vec{r} \int_{\Delta E} dE \int_{\Delta\widehat{\Omega}} d\widehat{\Omega}\, \sigma_s(\vec{r}, E)\, \psi(\vec{r}, E, \widehat{\Omega}). \tag{3.14}$$

Transport: Let us now consider some arbitrary surface dS with unit normal vector $\vec{e}_n$. We can describe the net rate at which particles cross the surface dS having energies within dE and traveling in directions within $\mathrm{d}\widehat{\Omega}$ by

$$\widehat{\Omega} \cdot \vec{e}_n\, \psi(\vec{r}, E, \widehat{\Omega})\, dS\, dE\, d\widehat{\Omega}. \tag{3.15}$$

The rate at which particles leave the phase volume is given by

$$\int_{S_{\Delta V}} dS \int_{\Delta E} dE \int_{\Delta\widehat{\Omega}} d\widehat{\Omega}\, \widehat{\Omega} \cdot \vec{e}_n\, \psi(\vec{r}, E, \widehat{\Omega}), \tag{3.16}$$

where $S_{\Delta V}$ denotes the surface of ΔV. Applying the divergence theorem, we obtain:

$$\int_{\Delta V} d^3\vec{r} \int_{\Delta E} dE \int_{\Delta\widehat{\Omega}} d\widehat{\Omega}\, \widehat{\Omega} \cdot\, \nabla\psi(\vec{r}, E, \widehat{\Omega}). \tag{3.17}$$

By using all the introduced terms, it is possible to write the Boltzmann transport equation in the following form :

$$\begin{aligned}\int_{\Delta V} d^3\vec{r} \int_{\Delta E} dE \int_{\Delta\widehat{\Omega}} d\widehat{\Omega}\, \Big(\widehat{\Omega} \cdot\, \nabla\psi(\vec{r}, E, \widehat{\Omega}) + \sigma_s(\vec{r}, E)\, \psi(\vec{r}, E, \widehat{\Omega}) + \sigma_a(\vec{r}, E)\, \psi(\vec{r}, E, \widehat{\Omega})\Big) = \\ \int_{\Delta V} d^3\vec{r} \int_{\Delta E} dE \int_{\Delta\widehat{\Omega}} d\widehat{\Omega} \int_0^\infty dE' \int_{S^2} d\widehat{\Omega}'\, \Big(\sigma_s(\vec{r}, E' \to E, \widehat{\Omega}' \to \widehat{\Omega})\psi(\vec{r}, E', \widehat{\Omega}') + Q(\vec{r}, E, \widehat{\Omega})\Big)\end{aligned} \tag{3.18}$$

Since ΔV, ΔE and $\Delta\widehat{\Omega}$ are all arbitrary, the two integrands are equivalent everywhere. Moreover we can write the total cross section as $\sigma_t = \sigma_a + \sigma_s$. Substituting these quantities into the transport equation yields the following integro-differential equation:

$$\begin{aligned}\widehat{\Omega} \cdot\, \nabla\psi(\vec{r}, E, \widehat{\Omega}) + \sigma_t(\vec{r}, E)\, \psi(\vec{r}, E, \widehat{\Omega}) = \\ \int_0^\infty dE' \int_{S^2} d\widehat{\Omega}'\, \sigma_s(\vec{r}, E' \to E, \widehat{\Omega}' \to \widehat{\Omega})\psi(\vec{r}, E', \widehat{\Omega}') + Q(\vec{r}, E, \widehat{\Omega})\end{aligned} \tag{3.19}$$

Equation (3.19) is a generic form of a linear Boltzmann transport equation that describe the transport of one particle species. In our work we describe propagation of a photon beam that can interact with the medium generating secondary particles of other

species. The system of coupled Boltzmann equations for the transport of photons, electrons and positrons is given by:

$$
\begin{aligned}
\widehat{\Omega}\cdot\nabla\psi^{\gamma}(\vec{r},E,\widehat{\Omega})+\sigma_t^{\gamma}(\vec{r},E)\,\psi^{\gamma}(\vec{r},E,\widehat{\Omega}) &= \int_0^{\infty}dE'\int_{S^2}d\widehat{\Omega}'\,\sigma_s^{\gamma,\gamma}(\vec{r},E'\to E,\widehat{\Omega}'\to\widehat{\Omega})\psi^{\gamma}(\vec{r},E',\widehat{\Omega}')\\
&+\int_0^{\infty}dE'\int_{S^2}d\widehat{\Omega}'\,\sigma_s^{e,\gamma}(\vec{r},E'\to E,\widehat{\Omega}'\to\widehat{\Omega})\psi^{e}(\vec{r},E',\widehat{\Omega}')\\
&+\int_0^{\infty}dE'\int_{S^2}d\widehat{\Omega}'\,\sigma_s^{p,\gamma}(\vec{r},E'\to E,\widehat{\Omega}'\to\widehat{\Omega})\psi^{p}(\vec{r},E',\widehat{\Omega}')\\
&+Q^{\gamma}(\vec{r},E,\widehat{\Omega}),\\
\widehat{\Omega}\cdot\nabla\psi^{e}(\vec{r},E,\widehat{\Omega})+\sigma_t^{e}(\vec{r},E)\,\psi^{e}(\vec{r},E,\widehat{\Omega}) &= \int_0^{\infty}dE'\int_{S^2}d\widehat{\Omega}'\,\sigma_s^{e,e}(\vec{r},E'\to E,\widehat{\Omega}'\to\widehat{\Omega})\psi^{e}(\vec{r},E',\widehat{\Omega}')\\
&+\int_0^{\infty}dE'\int_{S^2}d\widehat{\Omega}'\,\sigma_s^{\gamma,e}(\vec{r},E'\to E,\widehat{\Omega}'\to\widehat{\Omega})\psi^{\gamma}(\vec{r},E',\widehat{\Omega}')\\
&+\int_0^{\infty}dE'\int_{S^2}d\widehat{\Omega}'\,\sigma_s^{p,e}(\vec{r},E'\to E,\widehat{\Omega}'\to\widehat{\Omega})\psi^{p}(\vec{r},E',\widehat{\Omega}'),\\
\widehat{\Omega}\cdot\nabla\psi^{p}(\vec{r},E,\widehat{\Omega})+\sigma_t^{p}(\vec{r},E)\,\psi^{p}(\vec{r},E,\widehat{\Omega}) &= \int_0^{\infty}dE'\int_{S^2}d\widehat{\Omega}'\,\sigma_s^{p,p}(\vec{r},E'\to E,\widehat{\Omega}'\to\widehat{\Omega})\psi^{p}(\vec{r},E',\widehat{\Omega}')\\
&+\int_0^{\infty}dE'\int_{S^2}d\widehat{\Omega}'\,\sigma_s^{\gamma,p}(\vec{r},E'\to E,\widehat{\Omega}'\to\widehat{\Omega})\psi^{\gamma}(\vec{r},E',\widehat{\Omega}'),
\end{aligned}
\tag{3.20}
$$

where ψ^e, ψ^γ and ψ^p are the particles flux for electron, photon and positron respectively and σ_t^e, σ_t^γ and σ_t^p are the total cross section for electron, photon and positron interactions respectively. The eight differential cross sections that appear in the Boltzmann transport equations take into account all the possible interactions and couple the system of equations. More in detail:

- $\sigma_s^{e,e}$ is the electron-to-electron differential cross section and includes collisional scattering, knock-on production, radiative scattering, elastic scattering and Auger production following impact ionization;
- $\sigma_s^{\gamma,e}$ is the photon-to-electron differential cross section and includes Compton electron production, photoelectric production, pair electron production and Auger production following photoionization;
- $\sigma_s^{p,e}$ is the positron-to-electron differential cross section and includes knock-on production and Auger production following impact ionization;
- $\sigma_s^{\gamma,\gamma}$ is the photon-to-photon differential cross section and includes Compton scattering and fluorescence production following photoionization;
- $\sigma_s^{e,\gamma}$ is the electron-to-photon differential cross section and includes bremsstrahlung production and fluorescence production following impact ionization;

- $\sigma_s^{p,\gamma}$ is the positron-to-photon differential cross section and includes bremsstrahlung production, fluorescence production following impact ionization and annihilation radiation;

- $\sigma_s^{p,p}$ is the positron-to-positron differential cross section and includes collisional scattering, radiative scattering and elastic scattering;

- $\sigma_s^{\gamma,p}$ is the photon-to-positron differential cross section and includes only the pair positron production.

The system of coupled equations (3.20) written in a condensed notation and neglecting the source term reads:

$$\widehat{\Omega}\cdot\nabla\psi^i(\vec{r},E,\widehat{\Omega})+\sigma_t^i(\vec{r},E)\psi^i(\vec{r},E,\widehat{\Omega}) = \sum_{p=[i,j]}\int dE' \int_{S^2} d\widehat{\Omega}\,\sigma_s^{p,i}(\vec{r},E'\rightarrow E,\widehat{\Omega}'\rightarrow\widehat{\Omega})\psi^p(\vec{r},E',\widehat{\Omega}), \tag{3.21}$$

where i,j are the species of the transported particles, $\vec{r}$ is the position vector, E the particle energy, $\widehat{\Omega}$ the flight direction, $\psi(\vec{r},E,\widehat{\Omega})$ is the particle angular flux, σ_t and σ_s the total and the differential cross section.

3.2.3 Boltzmann-CSD equations for charged particles

As shown in Sections 2.2.1.1 and 2.2.1.2 both the collisional and radiative inelastic cross sections rapidly increase as the energy loss becomes small. Thus, an accurate discretization of these cross sections on an energy grid would require an excessive number of narrow-width mesh. This would make the cost of the computation unaffordable. For this reason an alternative treatment of charged particles inelastic interactions is required. As introduced in Section 2.2.1.1, inelastic interactions (both collisional and radiative) can be divided into two classes: catastrophic interactions, resulting in large-energy losses with the production of a secondary electron and soft interactions, resulting in small-energy losses without the production of a secondary particle. Catastrophic interactions are represented by macroscopic cross sections for which a discretization can be applied with a sufficiently small number of energy groups. A different approach is required for soft interactions. Due to the fact that a small-energy loss kinematically results in a small deviation, the cumulative effect of many soft interactions can be approximated by the continuous energy loss of a charged particle without angular deflection and without production of secondary particles. This approach is called the restricted continuous slowing-down (CSD) approximation [7]. In the context of this approximation, the electron or positron flux satisfies the Boltzmann-CSD equation. By dividing all inelastic interactions into soft and catastrophic events and by applying the CSD approximation to the former ones, the

electron and positron transport equations become:

$$\begin{aligned}
\widehat{\Omega}\cdot\nabla\psi^e(\vec{r},E,\widehat{\Omega})+\sigma_t^e(\vec{r},E)\psi^e(\vec{r},E,\widehat{\Omega}) &= \int dE'\int_{S^2} d\widehat{\Omega}'\,\sigma_*^{e,e}(\vec{r},E'\to E,\widehat{\Omega}'\to\widehat{\Omega})\psi^e(\vec{r},E',\widehat{\Omega}') \\
&+\frac{\partial}{\partial E}\left(R_e^{\text{coll}}(E)\,\psi^e(\vec{r},E,\widehat{\Omega})\right)+\frac{\partial}{\partial E}\left(R_e^{\text{rad}}(E)\,\psi^e(\vec{r},E,\widehat{\Omega})\right) \\
&+\int dE'\int_{S^2} d\widehat{\Omega}'\,\sigma^{\gamma,e}(\vec{r},E'\to E,\widehat{\Omega}'\to\widehat{\Omega})\psi^\gamma(\vec{r},E',\widehat{\Omega}') \\
&+\int dE'\int_{S^2} d\widehat{\Omega}'\,\sigma^{p,e}(\vec{r},E'\to E,\widehat{\Omega}'\to\widehat{\Omega})\psi^p(\vec{r},E',\widehat{\Omega}') \\
\widehat{\Omega}\cdot\nabla\psi^p(\vec{r},E,\widehat{\Omega})+\sigma_t^p(\vec{r},E)\psi^p(\vec{r},E,\widehat{\Omega}) &= \int dE'\int_{S^2} d\widehat{\Omega}'\,\sigma_*^{p,p}(\vec{r},E'\to E,\widehat{\Omega}'\to\widehat{\Omega})\psi^p(\vec{r},E',\widehat{\Omega}') \\
&+\frac{\partial}{\partial E}\left(R_p^{\text{coll}}(E)\,\psi^p(\vec{r},E,\widehat{\Omega})\right)+\frac{\partial}{\partial E}\left(R_p^{\text{rad}}(E)\,\psi^p(\vec{r},E,\widehat{\Omega})\right) \\
&+\int dE'\int_{S^2} d\widehat{\Omega}'\,\sigma^{\gamma,p}(\vec{r},E'\to E,\widehat{\Omega}'\to\widehat{\Omega})\psi^\gamma(\vec{r},E',\widehat{\Omega}')
\end{aligned} \tag{3.22}$$

where $\sigma_*^{e,e/p,p}(E\to E',\Omega\to\Omega')$ is the electron-electron / positron-positron differential cross sections that do not include soft inelastic interactions. $R_{e/p}^{\text{coll}}(E)$ and $R_{e/p}^{\text{rad}}(E)$ are the restricted collisional and radiative stopping powers for electrons that represent the continous slowing-down due to soft interactions.

3.3 Entropic model

The moments method has been adopted in a very large range of applications in physics as one of efficient methods for solving the transport equation. The application of this method covers astrophysics (see for example the work of Chandrasekhar [23]), radiative transfer starting from the works of Chandrasekhar [24] and Pomraning [109]. Other fields of application are the fluid dynamics of rarefied gases (see e.g. [48]) and plasma physics with applications to the inertial or magnetic confinement fusion [82, 83, 51].

In the present work we adopt the angular moments method with entropic closure introduced in 1977 in the work by Minerbo [89] on the radiative transport. It is by questioning the most probable form of the radiative intensity distribution that he has introduced the argument of maximization of the entropy. In his work the closure relation of the first member was not presented in an analytical form in the Bose-Einstein formalism, assuming that the photons obey to the Maxwell-Boltzmann one.

An analytical formulation of the angular closure relation has been introduced for the first time in 1999 by Dubroca and Feugeas [33]. The model has been further developed by CEA researchers in CELIA laboratory and it created the basis of a rich scientific production, with applications in different fields such as transport of charged particles in plasma [31, 134, 112] and more recently in radiotherapy [20, 102]. Moreover important

collaborations have been developed over the years at the national and European level, for example by Olbrand et al. [101], Duclous et al. [34] and Pichard et al. [108] with the University of Aachen.

3.3.1 Angular moments of the LBTE

The M_1 model was first derived by Dubroca and Feugeas [33] for simulations of the radiation transport in plasmas and then adapted for the relativistic electron transport by Duclous et al. [34]. In this section, we revise the principal elements of the angular moments algorithm. The moment method replaces the LBTE by a reduced number of moment equations of lower dimension. Such an approach allows reducing the number of degrees of freedom, i.e. the number of variables, while keeping a good accuracy of calculations. The moments are defined as integrals on the unit sphere in the phase space of the flux function $\psi(\vec{r}, E, \widehat{\Omega})$. As those moments depend on fewer variables $(\vec{r}, E)$ than the fluences $(\vec{r}, E, \widehat{\Omega})$, their computation requires less numerical efforts. The first three angular moments of the distribution function are:

$$\begin{aligned}
\psi_0(\vec{r}, E) &= \int_{S^2} \psi(\vec{r}, E, \widehat{\Omega})\, d\widehat{\Omega}\,, \\
\vec{\psi}_1(\vec{r}, E) &= \int_{S^2} \widehat{\Omega}\, \psi(\vec{r}, E, \widehat{\Omega})\, d\widehat{\Omega} = (\psi_1^x, \psi_1^y, \psi_1^z)^T\,, \\
\vec{\vec{\psi}}_2(\vec{r}, E) &= \int_{S^2} (\widehat{\Omega} \otimes \widehat{\Omega}) \psi(\vec{r}, E, \widehat{\Omega})\, d\widehat{\Omega} = \begin{bmatrix} \psi_2^{x,x} & \psi_2^{x,y} & \psi_2^{x,z} \\ \psi_2^{y,x} & \psi_2^{y,y} & \psi_2^{y,z} \\ \psi_2^{z,x} & \psi_2^{z,y} & \psi_2^{z,z} \end{bmatrix},
\end{aligned} \tag{3.23}$$

where ψ_0 is a scalar, $\vec{\psi}_1$ is a vector and $\vec{\vec{\psi}}_2$ is a tensor. These angular moments do not have just a mathematical meaning. Through an integration over the energy variable, important physical quantities can be derived:

$$\begin{aligned}
n(\vec{r}) &= \int_0^{+\infty} \frac{1}{v} \psi_0(\vec{r}, E)\, dE\,, \\
E(\vec{r}) &= \frac{1}{n(\vec{r})} \int_0^{+\infty} \frac{E}{v} \psi_0(\vec{r}, E)\, dE\,, \\
\vec{F}(\vec{r}) &= \int_0^{+\infty} E\, \vec{\psi}_1(\vec{r}, E)\, dE\,,
\end{aligned} \tag{3.24}$$

where $n(\vec{r})\,[\mathrm{cm}^{-3}]$ is the particle density (number of particle per unit volume), $E(\vec{r})\,[\mathrm{J}]$ is the mean energy of the particles and $\vec{F}(\vec{r})\,[\mathrm{J} \cdot \mathrm{s}^{-1} \cdot \mathrm{cm}^{-2}]$ is the energy flux of particles. Finally the deposited dose can be calculated. The dose in radiotherapy is defined as the total deposited energy by the particles in a unit mass [Gy = J/kg]. With the moments model the dose rate can be calculated as:

$$\frac{dD(\vec{r})}{dt} = \frac{1}{\rho(\vec{r})} \int E \sigma_{\mathrm{dep}} \psi_0(\vec{r}, E) dE \tag{3.25}$$

where $\rho(\vec{r})$ is the density of the medium and σ_{dep} is the macroscopic energy deposition cross section defined as the net energy deposited in the medium due to the interactions of particles with a given energy per unit pathlength [77]. This cross sections have units of energy per distance.

We define the zero-moment of the of coupled Boltzmann equations (3.21), by integrating the latter over the unit sphere:

$$\int_{S^2} d\widehat{\Omega}\left[\widehat{\Omega}\cdot\nabla\psi^i(\vec{r},E,\widehat{\Omega})+\sigma_t^i(\vec{r},E)\psi^i(\vec{r},E,\widehat{\Omega})\right]= \int_{S^2} d\widehat{\Omega}\left[\sum_{p=[i,j]}\int dE'\int_{S^2} d\widehat{\Omega}'\,\sigma_s^{p,i}(\vec{r},E'\to E,\widehat{\Omega}'\to\widehat{\Omega})\psi^p(\vec{r},E',\widehat{\Omega})\right]. \tag{3.26}$$

Generically, the kinetic linear Boltzmann gain term can be written as:

$$G(\psi)(\widehat{\Omega})=\int_{S^2}\sigma(\widehat{\Omega}'\to\widehat{\Omega})\psi(\widehat{\Omega}')\,d\widehat{\Omega}', \tag{3.27}$$

where $\vec{r}$ and E variables are omitted because they can be seen as parameters in this equation. Recalling the definition of moments, we can calculate the zero-moment of the gain term as:

$$\begin{aligned} G_0(\psi)(\widehat{\Omega}) &= \int_{S^2}\int_{S^2}\sigma(\widehat{\Omega}'\to\widehat{\Omega})\,\psi(\widehat{\Omega}')\,d\widehat{\Omega}'d\widehat{\Omega} \\ &= \int_{S^2}\int_{S^2}\sigma(\widehat{\Omega}'\to\widehat{\Omega})\,d\widehat{\Omega}\,\psi(\widehat{\Omega}')\,d\widehat{\Omega}'=\sigma_0\psi_0. \end{aligned} \tag{3.28}$$

where σ_i are the i-order moments of scattering cross section. The zero-moment and first moment of the scattering differential cross section are defined as:

$$\begin{aligned} \sigma_0 &= 2\pi\int_{-1}^{1}\mu^0\sigma(\mu)\,d\mu, \\ \sigma_1 &= 2\pi\int_{-1}^{1}\mu^1\sigma(\mu)\,d\mu. \end{aligned} \tag{3.29}$$

Substituting the zero-moment of the gain term in Eq. (3.26) we obtain:

$$\nabla\vec{\psi}_1^i(\vec{r},E)+\sigma_t^i(E)\psi_0^i(\vec{r},E)=\sum_{p=[i,j]}\int\sigma_0^{p,i}(\vec{r},E'\to E)\psi_0^p(\vec{r},E')dE'. \tag{3.30}$$

The zero moment equation gives ψ_0 as a function of ψ_1 which is given by the first moment equation. In order to obtain the first moment equation we have to integrate (3.21) as:

$$\int_{S^2} d\widehat{\Omega}\,\widehat{\Omega}\left[\widehat{\Omega}\cdot\nabla\psi^i(\vec{r},E,\widehat{\Omega})+\sigma_t^i(\vec{r},E)\psi^i(\vec{r},E,\widehat{\Omega})\right]= \int_{S^2} d\widehat{\Omega}\,\widehat{\Omega}\left[\sum_{p=[i,j]}\int dE'\int_{S^2} d\widehat{\Omega}'\,\sigma_s^{p,i}(\vec{r},E'\to E,\widehat{\Omega}'\to\widehat{\Omega})\psi^p(\vec{r},E',\widehat{\Omega})\right]. \tag{3.31}$$

By using the change of variable $\widehat{\Omega}'' = R^T\widehat{\Omega}$ where the operator of rotation R is such that $\widehat{\Omega}'R = \vec{e}_1$, the first-moment of the gain term reads:

$$\begin{aligned} G_1(\psi)(\widehat{\Omega}) &= \int_{S^2}\int_{S^2} \widehat{\Omega}\,\sigma(\widehat{\Omega}'\to\widehat{\Omega})\,\psi(\widehat{\Omega}')\,d\widehat{\Omega}'d\widehat{\Omega} \\ &= \int_{S^2}\int_{S^2} \widehat{\Omega}\,\sigma(\widehat{\Omega}'\to\widehat{\Omega})\,d\widehat{\Omega}\,\psi(\widehat{\Omega}')\,d\widehat{\Omega}' \\ &= \int_{S^2} R\int_{S^2} \widehat{\Omega}''\,\sigma(\widehat{\Omega}''\vec{e}_1)\,d\widehat{\Omega}''\,\psi(\widehat{\Omega}')\,d\widehat{\Omega}' \\ &= \int_{S^2} R\,\vec{e}_1\,\sigma_1\,\psi(\widehat{\Omega}')\,d\widehat{\Omega}' \\ &= \int_{S^2} \widehat{\Omega}'\,\sigma_1\,\psi(\widehat{\Omega}')\,d\widehat{\Omega}' = \sigma_1\psi_1. \end{aligned} \tag{3.32}$$

Substituting the first-moment of the gain term in (3.31) we obtain:

$$\nabla\vec{\psi}_2^i(\vec{r},E) + \sigma_t^i(E)\vec{\psi}_1^i(\vec{r},E) = \sum_{p=[i,j]}\int \sigma_1^{p,i}(\vec{r},E'\to E)\vec{\psi}_p^i(\vec{r},E')dE'. \tag{3.33}$$

In this equation the first moment depends on the second moment. Stopping the developpement at the first two moments we can build the following system of two equations:

$$\begin{cases} \nabla\vec{\psi}_1^i(\vec{r},E) + \sigma_t^i(E)\psi_0^i(\vec{r},E) &= \sum_{p=[i,j]}\int \sigma_0^{p,i}(\vec{r},E'\to E)\psi_0^p(\vec{r},E')dE'\,, \\ \nabla\vec{\psi}_2^i(\vec{r},E) + \sigma_t^i(E)\vec{\psi}_1^i(\vec{r},E) &= \sum_{p=[i,j]}\int \sigma_1^{p,i}(\vec{r},E'\to E)\vec{\psi}_1^p(\vec{r},E')dE'\,. \end{cases} \tag{3.34}$$

This system is not closed because it has more unknowns than equations. In order to have a unique solution to the moments problem, the system has to be closed. This closure consists in adding relations in order to have as many unknowns as equations. Commonly, this closure consists in expressing ψ_{N+1} as a function of the lower order moments $(\psi_0, ..., \psi_N)$.

3.3.2 Entropic closure

A closed and isolated system evolves to equilibrium, moving to more probables states, due to the collisions between particles. The second law of thermodynamics asserts that the entropy attains its maximum, as the system reaches the state of equilibrium. This law finds its statistical interpretation in the H-theorem that has been extensively described in literature [59]. The angular entropy of our system of moments is defined as:

$$H(\psi) = -\int_{S^2}(\psi\ln\psi - \psi)\,d\widehat{\Omega} \tag{3.35}$$

The originality of our approach comes from the use of the entropy maximization principle (Boltzmann's H-theorem) to close the system of moment equations (3.34) over the angular variable. The higher moment $\vec{\psi}_2$ is expressed as a function of ψ_0 and $\vec{\psi}_1$. The underlying

distribution function ψ^i_{ME} that maximizes the entropy under the constraint of the two first moments definition has the form:

$$\psi^i_{ME}(\vec{r}, E, \widehat{\Omega}) = a_0 e^{\widehat{\Omega}\cdot\vec{a}_1}, \tag{3.36}$$

where a_0 and $\vec{a}_1$ are Lagrange multipliers of the constraints minimisation problem, $a_0 \geq 0$ is a scalar, and $\vec{a}_1 \in \mathbb{R}^3$ is a vector. This Maxwell-Boltzmann-type distribution provides relations of a_0 and $\vec{a}_1$ to the angular moments as follows [33]:

$$\begin{aligned} \psi^i_0 &= 4\pi a_0 \frac{\sinh|\vec{a}_1|}{|\vec{a}_1|}, \\ \vec{\psi}^i_1 &= 4\pi a_0 \frac{\sinh|\vec{a}_1|(|\vec{a}_1|\coth|\vec{a}_1| - 1)}{|\vec{a}_1|^2}\vec{a}_1. \end{aligned} \tag{3.37}$$

The combination of these two equations leads to the definition of the anisotropy factor:

$$|\alpha| = \frac{|\psi^i_1|}{\psi^i_0} = \frac{1 - |a_1|\coth|a_1|}{|a_1|}. \tag{3.38}$$

By using expression (3.36) one can explicitly relate the second angular moment ψ^i_2 to the lower moments through the Eddington factor χ according to the following equation:

$$\psi^i_2 = \psi^i_0 \left(\frac{1 - \chi(\alpha)}{2} \mathrm{I} + \frac{3\chi(\alpha) - 1}{2} \frac{\psi^i_1}{|\psi^i_1|} \otimes \frac{\psi^i_1}{|\psi^i_1|} \right). \tag{3.39}$$

The Eddington factor is related to the anisotropy factor by the following interpolation relation:

$$\chi(\alpha) = \frac{1}{3}(1 + \alpha^2 + \alpha^4). \tag{3.40}$$

The anisotropy factor is bounded in the interval $[0, 1]$. It means that the Eddington factor χ assumes values between $[\frac{1}{3}, 1]$. The M_1 model is able to treat various regimes of non-equilibrium, from the mono directional pencil beam case ($\alpha = 1$), i.e. external radiotherapy, to the isotropic case ($\alpha = 0$), i.e. brachytherapy.

3.3.3 Limitations of the M_1 model

The moments method provides an approximate LBTE solution with only two angle-averaged quantities instead of the distribution function. The M_1 model is the first member in the angular moments (M) hierarchy. The main limitation of the M_1 is that it accounts for only one direction of particle propagation for a given energy. This limitation is not too restrictive in case of a single beam but it may cause problems when multiple beams propagate in a given domain crossing each others. In this section we explain mathematically this limitation and describe its effects. Let us consider a simplified LBTE equation in one spatial dimension:

$$\mu \frac{\partial \psi(x, E, \mu)}{\partial x} = \sigma \left(\frac{1}{2} \int_{-1}^{+1} \psi(x, E, \mu)\, d\mu - \psi(x, E, \mu) \right) \tag{3.41}$$

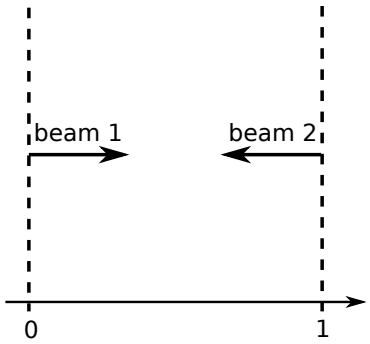

Figure 3.1: Two opposite beams interaction in a closed domain.

where μ is the cosine of the direction of flight, i.e. the first component of the three-dimentional vector $\widehat{\Omega}$, and x is the space variable.

We consider the situation schematically drawn in Figure 3.1 where two particle beams propagate in the domain in opposite directions. We define the two beams with boundary conditions in the following way:

$$\begin{cases} \psi(0,\mu) = \delta_{\{\mu=1\}} & \text{if} \quad \mu \geq 0 \\ \psi(1,\mu) = \delta_{\{\mu=-1\}} & \text{if} \quad \mu \leq 0 \end{cases} \tag{3.42}$$

where $\psi(0,\mu)$ is the flux function of the beam propagating from the left to the right and $\psi(1,\mu)$ is the flux function of the beam propagating in the opposite direction. It is evident that the general solution of equation (3.41) is given by $\psi \equiv 1$. Due to the linearity of the problem, we can apply the superposition principle splitting the problem into two fluxes. Hence, we can rewrite conditions (3.42) as:

1.
$$\begin{cases} \psi(0,\mu) = \delta_{\{\mu=1\}} & \text{if} \quad \mu \geq 0 \\ \psi(1,\mu) = 0 & \text{if} \quad \mu \leq 0 \end{cases} \tag{3.43}$$

which gives as solution

$$\psi(x,\mu) = \delta_{\{\mu=1\}}, \tag{3.44}$$

2.
$$\begin{cases} \psi(0,\mu) = 0 & \text{if} \quad \mu \geq 0 \\ \psi(1,\mu) = \delta_{\{\mu=-1\}} & \text{if} \quad \mu \leq 0 \end{cases} \tag{3.45}$$

which gives as solution

$$\psi(x,\mu) = \delta_{\{\mu=-1\}}. \tag{3.46}$$

Once we compute the sum of solutions (3.44) and (3.46)

$$\psi(x,\mu) = \delta_{\{\mu=1\}} + \delta_{\{\mu=-1\}}, \tag{3.47}$$

we obtain the initial problem with solution $\psi \equiv 1$. Applying the moment model to the previous problem we cannot use the superposition principle because of a nonlinear closure relation. This can be easily shown by computing the moments of solution (3.47):

$$\begin{aligned} \psi_0 &= \int_{-1}^{1} \psi(x,\mu)\, d\mu = 2, \\ \psi_1 &= \int_{-1}^{1} \mu\, \psi(x,\mu)\, d\mu \\ &= \int_{-1}^{1} \mu\, \delta_{\{\mu=1\}}\, d\mu + \int_{-1}^{1} \mu\, \delta_{\{\mu=-1\}}\, d\mu = 0. \end{aligned} \tag{3.48}$$

Since the first moment is equal to zero the two opposite fluxes annihilate each other. Moreover, the moments (3.48) are identical to the moments of an isotropic distribution. This means that the first moment approximation is not able to treat at the same time two or more fluxes with exactly the same energy that cross each other in a given domain.

The system of moments equations Eq. (3.34) has been discretized as explained in Section 3.4 and written as a numerical M_1 code. In the following paragraphs we present two more pathological cases obtained while running the M_1 numerical code.

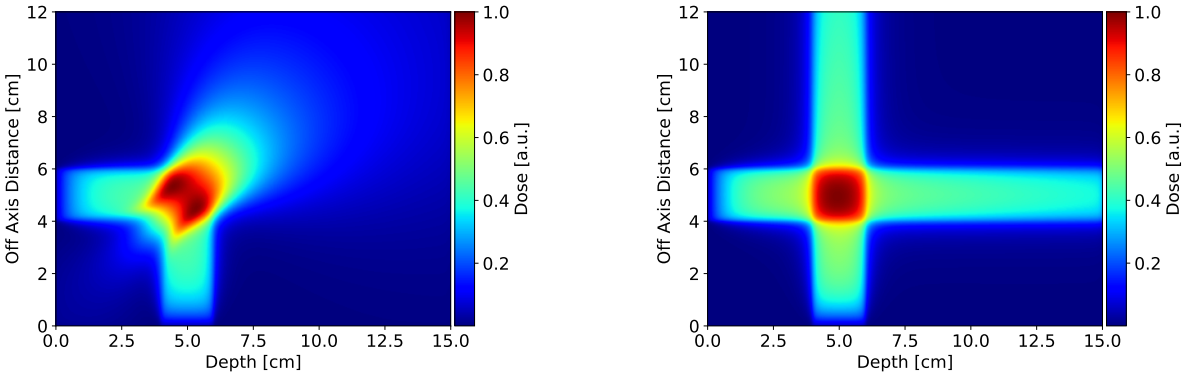

(a) (b)

Figure 3.2: Two orthogonal photon beams injected on the left and on the lower boundary of a water phantom. (a) the averaging effect of the M_1 model is shown in the case where the two beams are treated simultaneously while it disappears if the two beams are treated separately as in panel (b).

In order to give another example of this limitation we present the result of simulation of the dose deposition of two orthogonal photon beams injected from the left and from the lower boundary in a water phantom. As shown in Figure 3.2(a), when two beams cross each other an interaction seems to take place and the two entering beams fuse in a single exiting beam propagating in the mean direction. This is a numerical effect due to the M_1 closure and it occurs every time when two or more fluxes of particles enter in the same phase volume at different angles. In order to overcome this problem, the

linearity of the solution of the LBTE have to be used and the two beams have to be treated independently. In Figure 3.2(b), we show the result obtained by propagating the two beam separately and adding the deposited doses.

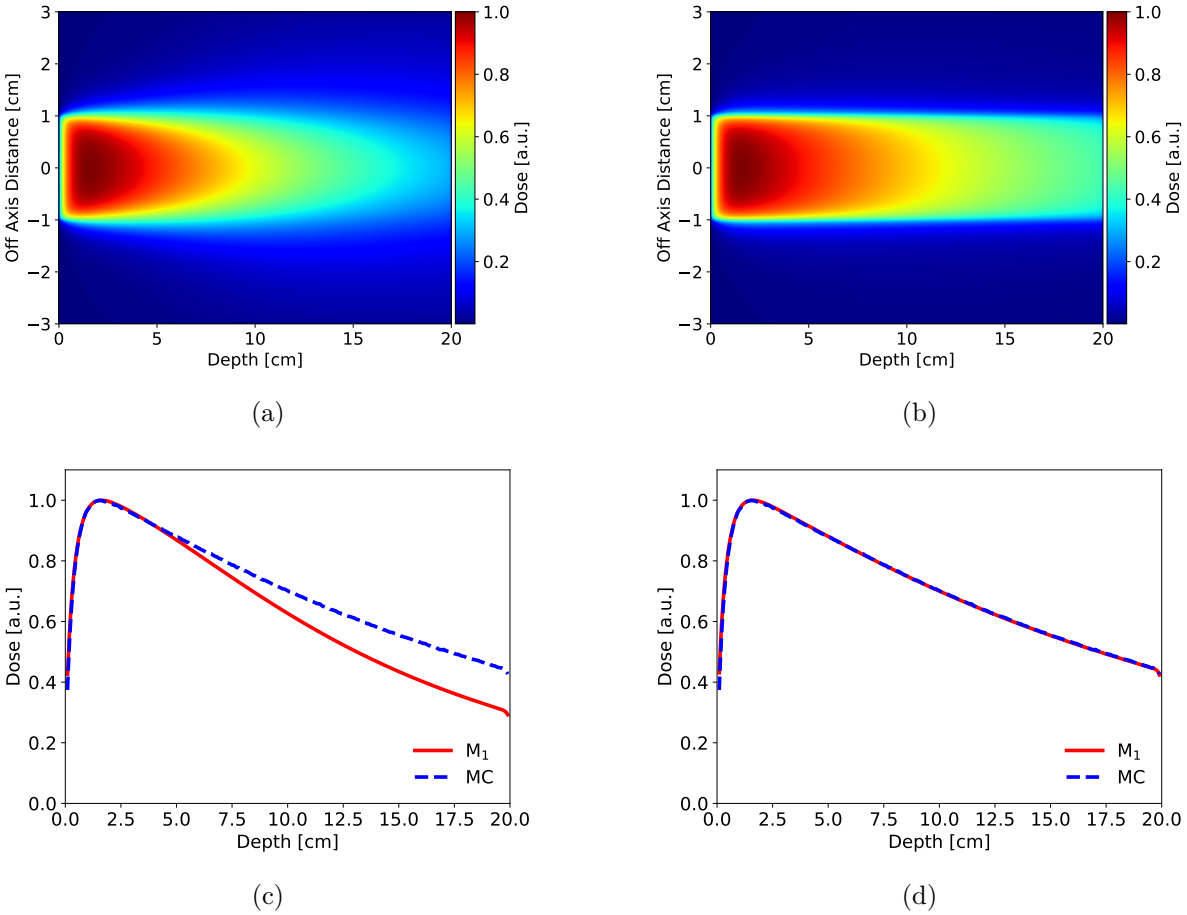

Figure 3.3: 6 MV photon beam coming from the left in a homogeneous water phantom. In panels (a) and (b) the 2D maps of the dose distribution calculated without and with the primary and secondary particles splitting is shown. In panels (c) and (d) the comparison of the respective depth dose distribution calculated with M_1 and the Monte Carlo (MC) code PENELOPE are shown.

This numerical effect can also appear in modeling the propagation of a single photon beam initialized with a bremsstrahlung spectrum. This comes from the fact that all the photons are initialized with a given anisotropy. This anisotropy is preserved by the photons that propagate without interacting with the medium. These photons can be called 'primary photons'. On the other hand the photons scattering in the medium loose their energy and change their anisotropy. These photons can be called 'secondary photons'. Considering the primary and secondary photons in the same population, the flux averaging takes place as explained above. On the contrary if the two populations are modeled separately the stability and the accuracy of the method are consistently

improved. In Figure 3.3 a comparison between M_1 with and without the particle populations splitting and a simulation performed with the Monte Carlo code PENELOPE is shown. Introduction of the splitting procedure is described in detail in Section 4.4.2. It allows a succesful use of the M_1 model for realistic simulations in external photon beam radiotherapy without considering the next member of the hierarchy. However, for brachytherapy applications we need to consider the M_2 model due to the issues related to the volume source initialization.

3.3.4 M_2 model

For a better accuracy and flexibility of the entropic model, one can consider the next member in the hierarchy, the M_2 model [108], to get closer to the exact solution. In M_2 we introduce a new system of equations where $\psi_3(\vec{r}, E)$ is function of $\psi_2(\vec{r}, E)$. The third angular moment is defined as:

$$\vec{\vec{\psi}}_3(\vec{r}, E) = \int_{S^2} \widehat{\Omega} \otimes \widehat{\Omega} \otimes \widehat{\Omega}\, \psi(\vec{r}, E, \widehat{\Omega})\, d\widehat{\Omega} \tag{3.49}$$

Due to the fact that the equation for $\psi_0(\vec{r}, E)$ is redundant with the equation for $\psi_2(\vec{r}, E)$ (the trace of $\psi_2(\vec{r}, E)$ is equal to $\psi_0(\vec{r}, E)$) the system for the M_2 model consists of two equations as follows:

$$\begin{cases} \nabla \vec{\vec{\psi}}_2^{\,i}(\vec{r}, E) + \sigma_t^i(E)\vec{\psi}_1^i(\vec{r}, E) & = \sum_{p=[i,j]} \int \sigma_1^{p,i}(E' \to E)\vec{\psi}_1^p(\vec{r}, E')dE' \,, \\ \nabla \vec{\vec{\psi}}_3^{\,i}(\vec{r}, E) + \sigma_t^i(E)\vec{\psi}_2^i(\vec{r}, E) & = \sum_{p=[i,j]} \int \sigma_2^{p,i}(E' \to E)\vec{\psi}_2^p(\vec{r}, E')dE' \,. \end{cases} \tag{3.50}$$

where σ_2 is the second moment of the scattering differential cross sections.

The closure of the M_2 model is different from the closure of the first member of the hierachy presented in Section 3.3.2. The closure problem for M_2 has been developed by Pichard [108]. The M_2 model overcomes the M_1 limitations despite to a higher number of variables and a higher computational effort.

In this work we demonstrate that the M_1 model reaches a high level of accuracy in external beam radiotherapy applications. However, for brachytherapy simulations, the M_2 model is needed.

3.4 Discretization of the kinetic equation

In general, one cannot solve numerically equations (3.21) in a continuous form. For this reason the LBTE has to be discretized in space, directions and energy. The technique for discretizing the phase space variables of the complete LBTE is based on the discrete-ordinates method [44, 45]. In this approach, all particles are split in several energy groups and the transport equation is written for every energy group and for a finite number of directions. The set of directions and corresponding weights is commonly referred to as

a quadrature set of the order N (corresponding to $N^2 + 2N$ directions). Space is also discretized in volume elements raising the number of calculation operations to $N_\Omega \times N_V \times N_E$, where N_V is the number of voxels in the three-dimensional domain, N_Ω is the number of directions and N_E is the number of energy groups. To ensure the convergence to the solution, the number of angles has to be sufficiently large, otherwise detrimental numerical "ray-effect" arises producing oscillations in the solution. Sophisticated computational techniques are required to mitigate it [44, 45]. However, thanks to the moments method, we do not need to solve the LBTE equation in its original form but we focus on the system of coupled equations (3.34). This implies that only discretizations in energy and space are required. Considering moments $\psi_0(\vec{r}, E)$ and $\vec{\psi_1}(\vec{r}, E)$ we have 4 unknowns, thus the number of calculation operations for a three dimensional case can be estimated as proportional to $4 \times N_V \times N_E$, where N_V is the number of voxels in the three-dimensional domain and N_E is the number of energy groups. We can compare the computational efforts, by assuming that for the two methods the spatial and energy discretization are the same. It is clear that the number of degrees of freedom when adopting the discrete-ordinates method is consistently higher with respect to the moment method, if the number of moments studied is lower than N_Ω.

3.4.1 Spatial discretization

The spatial domain is discretized using a uniform orthogonal discretization using a cubic grid. The spatial discretization is performed using the finite volume scheme based on the HLL (from A. Hartem, P.D. Lax and B. Van Leer [54]) approximate Riemann solver. This numerical scheme is commonly used for the moment method equations due to its capability to preserve the realizability from one energy step to another. Since a systematic study and improvement of the numerical discretization of the domain are out the scope of the present thesis, we have used the numerical scheme implemented in the previous version of the code [20, 108].

Two different grids are used depending on the considered application. For all the applications in external photon beam radiotherapy a spatial discretization of $0.5 \times 0.5 \times 0.5$ mm^3 is used. In brachytherapy, instead, a finer mesh has to be used. The reason is that in a deterministic code the accuracy of the calculation is inherently related to the chosen grid resolution. For example, in order to correctly resolve the boundary of a brachytherapy source, that in this work has been modeled as a sphere with a diameter of 2 mm, one needs at least 9 cells. For this reason a voxel of $0.25 \times 0.25 \times 0.25$ mm^3 is used.

An optimization of the spatial discretization scheme is clearly needed in order to improve the computational performance in terms of time and memory allocation. To this end, in the future, a non-uniform mesh refinement can be implemented. This technique allows a strong reduction of the number of grid cells where the problem exhibits a smooth behavior and also a strongly localized increase of the number of cells in areas needing

more accuracy. An example of non-structured mesh with refinement is shown in Figure 3.4 Similar technique can be implemented in the M_1 code.

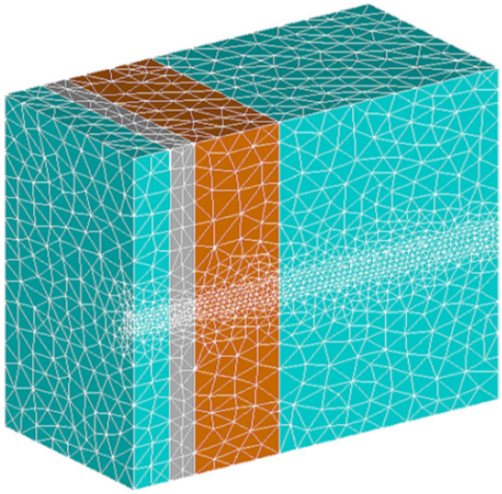

Figure 3.4: An example of non-uniform discretization scheme. This scheme used in Acuros is based on a discretization of the domain in tetrahedral elements. Image from Gifford et al. [44] with permission.

3.4.2 Energy discretization

A numerical code based on the entropic model has been developed at the CELIA laboratory during the past years, with the aim of solving LBTE for different applications in plasma physics and astrophysics. These works were mainly focused on the mathematical properties of the model with an order of magnitude precision. For these reasons, only the principal physical cross sections were implemented in the numerical code. In the last few years, the applications related to particle transport in cold matter and more specifically to radiotherapy have been approached with this code. The works by Caron [20] and Duclous [34] were the starting point for medical physics problems but the physical cross sections were limited to the electron scattering. The Mott formulation for elastic scattering was implemented while the inelastic scattering was derived from the Møller formula. Due to the considered energy regime of the electrons the bremsstrahlung process was neglected. Then, in the work of Pichard [108] a version of the coupled photon-electron entropic model for radiotherapy was developed for the first time. The main focus of that work was on a study of the mathematical properties of higher order entropic closure, thus the implementation of the photon cross sections was limited to the Compton scattering.

The very first purpose of this thesis consisted in improvement of the physical description in order to have a more complete model permitting a few percent accuracy required for medical applications. Our entropic model is based on the multigroup method for the cross sections discretization. This method consists in discretization of the particle energy

domain into energy intervals, that are called groups, as follows:

$$\Big|_{E_1} \quad group \quad 1 \quad \Big|_{E_2} \quad group \quad 2 \quad \Big|_{E_3} \quad \cdots\cdots \quad \Big|_{E_G} \quad group \quad G \quad \Big|_{E_{G+1}} \tag{3.51}$$

where $E_1 > E_2 > E_3 > \cdots \quad E_{G+1}$, E_1 is the maximum energy and E_{G+1} is the cutoff energy. The problem is solved numerically by starting from the highest energy group till to the lowest one. This is motivated by the fact that collision processes lead to reduction of the particle energy but not to its increase. By convention, the higher group numbers are associated with lower particle energies.

In the multigroup approximation, all particles in the same energy group are assumed to interact with each other with the same probability. The multigroup approximation is sufficiently accurate only if the cross sections do not significantly vary in energy within a group. Hence, the structure of the energy grid may have an impact on the accuracy of the simulation. For instance, the photoelectric cross section varies strongly near the shell binding energy. This behaviour has a greater impact in presence of materials with a high atomic number such as silver (see Figure 3.5). In order to accurately calculate the distribution of photoelectrons, the group structure should have a fine resolution in the proximity of the shell binding energies.

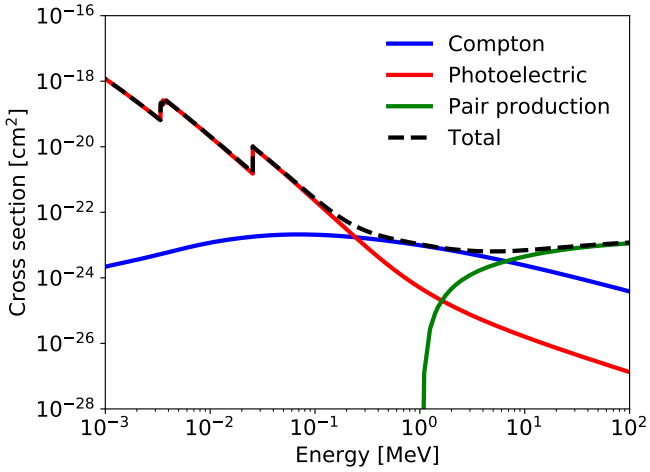

Figure 3.5: Plot of the photon total cross sections for silver calculated with the Monte Carlo code PENELOPE [121]. The discretization of the energy variable in proximity of the binding energies of the atomic shells must be adapted to avoid errors in the calculation of the cross sections.

Let us now introduce discrete notation in the LBTE formalism. The group particle flux, $\psi_g(r, \Omega)$, is defined as:

$$\psi_g(\vec{r}, \widehat{\Omega}) = \int_{E_{g+1}}^{E_g} \psi(\vec{r}, E, \widehat{\Omega})\, dE, \tag{3.52}$$

where $\psi(\vec{r}, E, \widehat{\Omega})$ is the particle flux. Integrating the LBTE over the g-th group and taking into account the definition of the group particle flux (3.52), the coupled system of

mutigroup transport equations reads:

$$\widehat{\Omega}\cdot\nabla\psi_g(\vec{r},\widehat{\Omega})+\sigma_{t,g}(\vec{r})\,\psi_g(\vec{r},\widehat{\Omega})= \sum_{g'=1}^{G}\int_{S^2}d\widehat{\Omega}'\,\sigma_{s,g'\to g}\left(\vec{r},\widehat{\Omega}'\to\widehat{\Omega}\right)\psi_{g'}(\vec{r},\widehat{\Omega}')+Q_{ext}(\vec{r},\widehat{\Omega}). \tag{3.53}$$

As shown in Section 3.3.1, the differential scattering cross section can be represented by a Legendre expansion. Moreover, as shown in Eqs. (3.29), the coefficients of the differential cross sections at the zero-th and first order of the Legendre expansion the same as the moments of the differential cross section calculated in the gain term in Eq. (3.34).

The multigroup-Legendre expansion coefficients for the cross sections describing scattering and production interactions are stored in transfer matrices. For a differential cross section, the expansion coefficients that are stored in the transfer matrix of L^{th}-order read:

$$\sigma_{g'\to g,L}=\frac{\displaystyle\int_{E_{g'+1}}^{E_{g'}}dE'\int_{E_{g+1}}^{E_g}\sigma_L(E'\to E)\,dE}{E_{g'}-E_{g'+1}}. \tag{3.54}$$

In the present work, the M_1 model, based on a multigroup energy approach, uses the cross sections calculated with the CEPXS code [77]. This code is valid over the energy range from 1 keV to 100 MeV and it provides the calculation of the transfer matrices with a consistent and complete physical model. The detailed description of the multigroup Legendre expansion coefficients calculation is presented in the CEPXS user manual [77]. Here, for sake of completeness we list all the physical interactions that are taken into account in our model.

Photon cross sections

1. **Compton scattering**: the Klein-Nishina [72] cross section is used for Compton incoherent scattering and electron production;

2. **Photoelectric effect**: the Biggs-Ligthill [12] cross sections are used for photoelectric absorption. The angular distributions devised by Sauter [123] are used for the emitted electrons;

3. **Pair interaction**: The Biggs-Lighthill [12] cross sections are used for the absorption of photons by pair production. The energy distribution of the charged secondaries in pair production is obtained from Bethe-Heitler theory [10].

Electron/positron cross sections

1. **Elastic scattering**: the cross section of Riley et al. [114] is used at non-relativistic energies (<256 keV). The Mott cross section with Moliere screening is used at relativistic energies (>256 keV) [147];
2. **Inelastic scattering**: the Moller [147] cross section is used for large-energy loss collisions. For other collisions, the restricted CSD approximation is used;
3. **Secondary electron production**: the Moller [147] cross section is used to determine the production of secondary electrons with energies down to the cutoff energy. Secondaries production and impact ionization are not correlated in CEPXS;
4. **Bremsstrahlung photon production**: The bremsstrahlung cross section is based on a formulation involving Born-approximation cross sections described by Koch and Motz [73]. This cross section is used to describe both bremsstrahlung photon production and the slowing down of an electron by radiative emission that results in large-energy losses. For small-energy loss radiative events, the restricted CSD approximation is used;
5. **Impact ionization**: The Gryzinski [49] impact ionization cross sections are used for the K, L1, L2, L3 and M shells.

As described in Section 4.5, in order to optimize the memory allocation and at the same time to keep a good accuracy in the simulations, the energy variable in the M_1 code is discretized with a non-uniform grid. The energy grids have been calibrated in a way that the total cross section variation between two adjacent groups is small. Thus, we impose an upper threshold on the total cross section gradient between two groups. In external photon beam simulations, the energy grid for simulations in the energy range between 10 keV and 7.2 MeV is composed by 21 energy groups while for simulations in energy range between 10 keV and 18 MeV the energy grid is composed by 39 energy groups. With the aim of reducing the memory allocation we merged the transport of positrons and electrons. This was achieved by partial coupling between the photon and electron grids. This is possible thanks to the following approximations:

- Bremsstrahlung and fluorescence following impact ionization are not taken into account;
- The energy that would have been transferred to photons produced by charged secondaries is deposited locally;
- Both particles exiting a pair production are assumed to be electrons.

In this work we apply the entropic model also to low dose rate brachytherapy simulations. In this regime the particle energy is low (less than 50 keV) and only photon transport is taken into account. The secondary electrons, due their range smaller than 0.1 mm, are assumed to deposit their energy locally. In brachytherapy applications the energy variable is discretized with a linear grid composed by 5 energy groups.

3.5 Beam initialization

Dose calculations for treatment planning in radiotherapy require a model of the particle beam injected in the patient. In external beam radiotherapy, the source model must be general enough to cover all common irradiation techniques including the intensity modulated radiation therapy (IMRT).

Simulation of particle transport with Monte Carlo methods is the most accurate way to determine the absorbed dose, especially in regions where tissue interfaces and heterogeneities play an important role [71, 113]. Monte Carlo simulations have become a common method for modeling linear accelerators, starting from the early days of their application to medical physics problems, such as external beam radiotherapy. The first simplified models for transport of particles produced with accelerators were reported from the late 1970s till the 1990s [25, 98, 99, 105, 117]. Usually the Monte Carlo particle transport is divided into three different parts: a source part, a beam modifier part and a patient part. The first part deals with the patient-independent components of the linear accelerator which is presented in Figure 3.6. After being accelerated, the primary electron beam emerges from the waveguide with a narrow energy, angular and spatial distribution. This electron beam is directed on a high-Z metal target where the bremsstrahlung photons are created. The bremsstrahung photons are then collimated initially by a primary collimator and the photon fluence is differentially attenuated by the flattening filter to produce a flat dose distribution at the patient surface. The second part handles all the beam modifications between the accelerator and the patient. These are obtained with the use of devices such as jaws, multi-leaf collimators, wedges, blocks etc. Finally, the beam entering the patient is initialized in the phase-space by using the output generated in the first two steps.

One of the difficulties related to the clinical implementation of Monte Carlo dose calculations is the characterisation of the radiation source. A possible strategy consists in performing full Monte Carlo simulations. In the external beam radiotherapy it consists in simulating the transport through the full accelerator head, while for brachytherapy it consists in the simulation of the source encapsulation. These simulations generate a the phase-space output that consists in a very large file, where the state variables of particles traversing the phase-space scoring plane are recorded. Typically, each line represents a particle and the following quantities are reported: type of particle, energy of the particle, position of the particle in space, direction of flight of the particle in terms of director cosine, the particle statistical weight and other complementary information. This phase-space data provide accurate particle distributions in the phase-space plane and thus can be used directly as source model.

The direct use of a phase-space file in Monte Carlo simulations for treatment planning presents some limitations. One limitation concerns mostly the external beam radiotherapy and is related to the lack of flexibility in adjusting the data for accelerators with slightly different outputs. The second limitation is the introduction of a systematic error

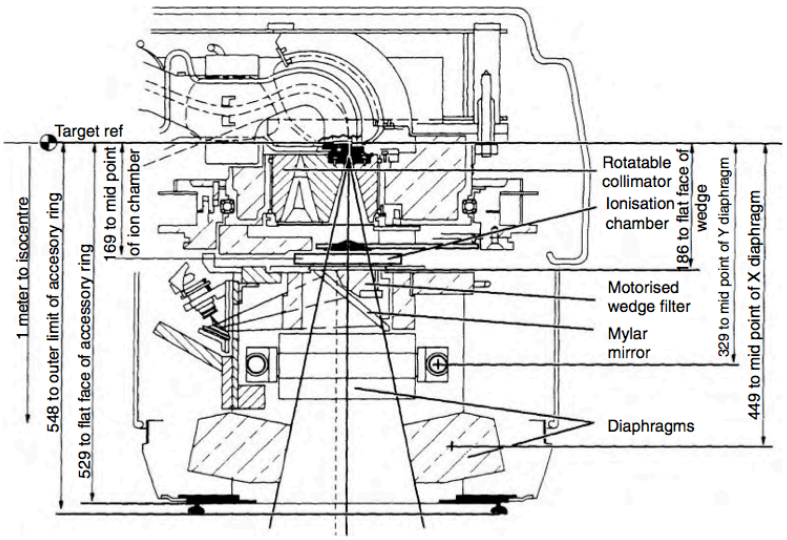

Figure 3.6: Diagram of an Elekta SL series accelerator. As it can be noticed in this diagram, the particle beam exiting from the accelerator head interacts with different componets of the structure. Scattered secondary particles are created in the end of the accelerator head, where the beam is shaped with the use of diaphragms and of the multileaf collimator. Image from Mayles et al. [86] with permission.

due to the limited size of the phase-space file, which results in a finite variance of the calculated dose. In order to overcome such limitations, two different approaches can be adopted: the first one is analytical characterization of the beam [36, 62], whereas the second one consists in creating a histogram-based source model, based on the phase-space data [37, 80, 124].

The M_1 model is a mesoscopic model, where the kinetic description that characterizes the Monte Carlo method is partially lost. In this sense, the beam initialization describing the beam injected in the domain have to be calculated in a different way with respect to the phase-space data. Specifically, for the M_1 model we have to define the anisotropy of each particle species. As mentioned before, the M_1 model has to be solved at the discrete level. This means that the anisotropy has to be calculated in each boundary voxel for each energy group.

The aim of this section is to develop a direct method to calculate the beam initialization starting from a phase-space file. This method guarantees that the M_1 and the Monte Carlo simulations have the same initial conditions, thus they can be considered as equivalent. Specifically, no matter the method chosen for the Monte Carlo initialization, the equivalent M_1 initialization can be found. In the present work, we adopt simple boundary conditions and we do not take into account accelerator models. In the next section, a method that translates the phase-space data into the M_1 initialization is presented in the most general case.

3.5.1 Phase-space initialization

As introduced in Section 3.2.2, the particle flux is defined as:

$$\psi = v(E) f(x, y, z, E, \widehat{\Omega}), \tag{3.55}$$

where the direction vector is defined as follows:

$$\widehat{\Omega} = \left[\cos\theta, \cos\phi \sin\theta, \sin\phi \sin\theta\right]^T. \tag{3.56}$$

Let us define a volume element of the phase space as

$$V_{i,j,k,l} = [x_i, x_i + \Delta x] \times [y_j, y_j + \Delta y] \times [z_k, z_k + \Delta z] \times [E_l, E_l + \Delta E]. \tag{3.57}$$

The 0-th moment can be written as follows:

$$\begin{aligned} \psi_{0,i,j,k,l} = \frac{1}{\Delta x\, \Delta y\, \Delta z\, \Delta E} \int_{x_i}^{x_i+\Delta x} \int_{y_j}^{y_j+\Delta y} \int_{z_k}^{z_k+\Delta z} \int_{E_l}^{E_l+\Delta E} \\ \int_{S^2} v(E) f(x, y, z, E, \widehat{\Omega})\, dx\, dy\, dz\, dE\, d\widehat{\Omega}, \end{aligned} \tag{3.58}$$

where the sum of all particles present in volume (3.57) is

$$f = \sum_{p=1}^{N} w_p\, \chi_{[x_i, x_i+\Delta x]} \chi_{[y_j, y_j+\Delta y]} \chi_{[z_k, z_k+\Delta z]} \chi_{[E_l, E_l+\Delta E]} \delta(\widehat{\Omega} - \widehat{\Omega}_m). \tag{3.59}$$

Here w_p is the weight of particle p, χ is an indicator function in the considered interval and δ is the Kroenecker function that selects the direction $\widehat{\Omega}_m$. After substituting (3.59) in (3.58), we obtain:

$$\begin{aligned} \psi_{0,i,j,k,l} = \frac{1}{V_{i,j,k,l}} \sum_{p=1}^{N} w_p \int_{V_{i,j,k,l}} v(E_l) \chi_{[x_i, x_i+\Delta x]} \chi_{[y_j, y_j+\Delta y]} \chi_{[z_k, z_k+\Delta z]} \chi_{[E_l, E_l+\Delta E]}\, dx\, dy\, dz\, dE \\ \int_{S^2} \delta(\widehat{\Omega} - \widehat{\Omega}_m)\, d\widehat{\Omega}, \end{aligned} \tag{3.60}$$

where

$$\int_{V_{i,j,k,l}} \chi_{[x_i, x_i+\Delta x]} \chi_{[y_j, y_j+\Delta y]} \chi_{[z_k, z_k+\Delta z]} \chi_{[E_l, E_l+\Delta E]} \begin{cases} = 1 & \text{if} \quad (x_i, y_j, z_k, E_l) \in V_{i,j,k,l} \\ = 0 & \text{elsewhere} \end{cases} \tag{3.61}$$

and, by definition:

$$\int_{S^2} \delta(\widehat{\Omega} - \widehat{\Omega}_m) d\widehat{\Omega} = 1. \tag{3.62}$$

In this way, the numerical approximation of the 0-th moment in a given differential volume of the phase space reads as follows:

$$\psi_{0,i,j,k,l} = \frac{1}{V_{i,j,k,l}} \sum w_p v(E_l). \tag{3.63}$$

In an analogous way, one can obtain the following numerical approximation of the first moment:

$$\vec{\psi}_{1,i,j,k,l} = \frac{1}{V_{i,j,k,l}} \sum_{p=1}^{N} w_p \int_{V_{i,j,k,l}} v(E_l) \chi_{[x_i,x_i+\Delta x]} \chi_{[y_j,y_j+\Delta y]} \chi_{[z_k,z_k+\Delta z]} \chi_{[E_l,E_l+\Delta E]} \, dx \, dy \, dz \, dE$$

$$\int_{S^2} \widehat{\Omega} \delta(\widehat{\Omega} - \widehat{\Omega}_m) \, d\widehat{\Omega} = \frac{1}{V_{i,j,k,l}} \sum_{p=1}^{N} w_p \widehat{\Omega}_m v(E_l). \tag{3.64}$$

Recalling the definition of anisotropy (3.38) and using the results obtained for (3.63) and (3.64), we can now calculate the anisotropy factor for each direction in each boundary voxel as follows:

$$\begin{aligned} \alpha^x_{i,j,k,l} &= \frac{\psi^x_{1,i,j,k,l}}{\psi_{0,i,j,k,l}}, \\ \alpha^y_{i,j,k,l} &= \frac{\psi^y_{1,i,j,k,l}}{\psi_{0,i,j,k,l}}, \\ \alpha^z_{i,j,k,l} &= \frac{\psi^z_{1,i,j,k,l}}{\psi_{0,i,j,k,l}}. \end{aligned} \tag{3.65}$$

The anisotropy factor α is the norm of this vector. Several works have been dedicated to modeling of the architecture of clinical accelerators. This modeling is done with Monte Carlo algorithms, such as PENELOPE [121], Geant4 [1] and EGSnrc [68], and it provides the phase-space at a given plane at the exit of the accelerator as an output. A large number of phase spaces calculated for photon linac, electron linac or Co-60 source of different companies are available at the International Atomic Energy Agency website (www-nds.iaea.org/phsp). In Figure 3.7, an example of application of the described method to a real phase-space is shown. Here we have taken the phase-space data generated and validated for a Varian Clinac 600C [18].

The anisotropy distributions in this case can be fitted with simple polynomial surfaces. With this method we can avoid to recalculate at every simulation the anisotropy distributions with a considerable gain in term of computational effort. Moreover only storage of the fitting parameters is needed.

3.5.2 Simplified numerical initialization

For a preliminary validation of the M_1 code, we have performed several simulations taking into account square beams of different dimensions with a homogeneous distribution of particles and Gaussian energy spectra.

With a Monte Carlo code such as PENELOPE, it is possible to define the numerical sources by specifing some parameters such as the energy spectrum, the shape and the position of the beam, the direction of emission of the particles and the rotation of the

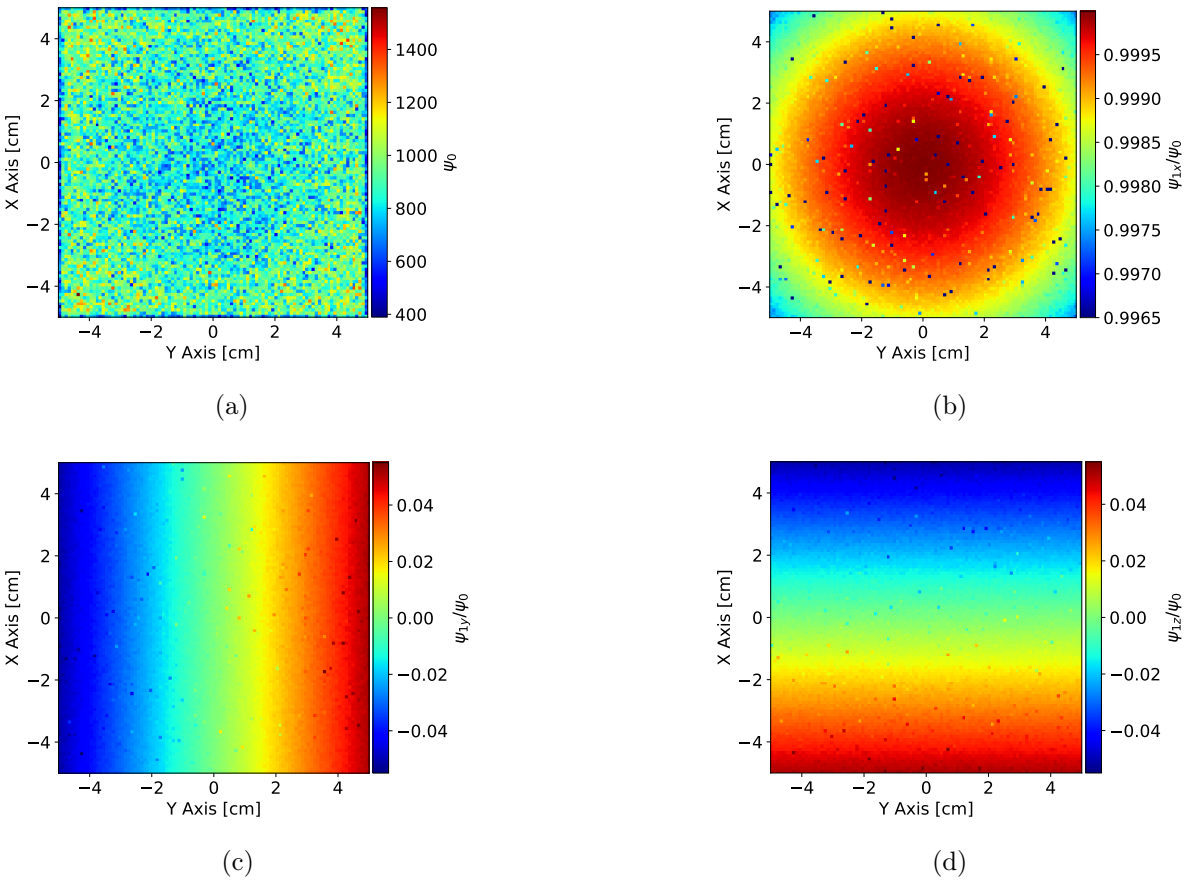

Figure 3.7: Anisotropy distribution calculated for a Varian Clinac 600C. The phase space data file has been discretized following the method described in Section 3.5.1. In panel (a) the particles distribution ψ_0 inside the beam is represented. In panel (b) the anisotropy distribution α^x parallel the propagation axis of the beam is represented. In panels (c) and (d) are represented the anisotropy distributions in the transversal directions of the beam, α^y and α^z respectively.

beam with respect to the direction of propagation. It is possible to define the direction of emission of the particles isotropic within a cone. This latter is defined as the part of a sphere limited by polar and azimuthal angle intervals, $[\theta_0, \theta_1]$ and $[\phi_0, \phi_1]$, respectively. The polar interval $[\theta_0, \theta_1]$ given in degrees satisfies the following constraints: $\theta_0 \leq \theta_1$ and $\theta_0,\ \theta_1 \in [0°, 180°]$. The azimuthal interval, instead, respects the following constraints: $\phi_0 \in [0, 360)$ and $\Delta\phi \in [0, 360]$.

In these preliminary simulations, we consider square sources where the emission direction of homogeneously distributed particles is sampled within a cone of a given aperture. The base of the cone, perpendicular to the propagation direction, can be seen as a particular case of a spherical trapezoid with $\theta_0 = 0$, θ_1 equal to the cone angular semi-aperture (angle between the cone axis and its generatrix) and $\Delta\phi = 360°$. A semi-aperture $\theta_1 = 180°$ defines a fully isotropic emission. Let consider as an exam-

ple a homogeneous square beam, where each particle is isotropically emitted in a cone with the axis parallel to the propagation direction ($\mu_0 = \cos(\theta_0) = 1$) and with a given semi-aperture $\mu_1 = \cos(\theta_1)$ with respect to the propagation axis.

We can then define the particle flux as the product of two functions as:

$$\psi(E, \mu) = f(E)C(\mu) \tag{3.66}$$

where $f(E)$ is the distribution function in energy and $C(\mu)$ is the angular distribution function. We define the characteristic function as:

$$C(\mu) \begin{cases} = 1 & \text{if} \quad \mu \in [\mu_1, 1], \\ = 0 & \text{elsewhere.} \end{cases} \tag{3.67}$$

Recalling the definition of zeroth and first moments (3.23) and the definitition of the direction vector (3.56) we obtain:

$$\begin{aligned}
\psi_0 &= \int_{S_2} w\, f(E)\, C(\mu)\, d\widehat{\Omega} = w\, f(E) \int_0^{2\pi} d\phi \int_{\mu_1}^1 d\mu = 2\pi\, w\, f(E)\, (1 - \mu_1), \\
\vec{\psi}_1 &= \int_{S_2} \widehat{\Omega}\, w\, f(E)\, C(\mu)\, d\widehat{\Omega} \\
&= w\, f(E) \int_0^{2\pi} \begin{bmatrix} 1 \\ \cos(\phi) \\ \sin(\phi) \end{bmatrix} d\phi \cdot \int_{\mu_1}^1 \begin{bmatrix} \mu \\ \sqrt{1-\mu^2} \\ \sqrt{1-\mu^2} \end{bmatrix} d\mu \\
&= \frac{1}{2}\, w\, f(E) \begin{bmatrix} \phi \\ \sin(\phi) \\ -\cos(\phi) \end{bmatrix}_0^{2\pi} \cdot \begin{bmatrix} \mu^2 \\ \mu\sqrt{1-\mu^2} + \arcsin(\mu) \\ \mu\sqrt{1-\mu^2} + \arcsin(\mu) \end{bmatrix}_{\mu_1}^1 \\
&= \frac{1}{4}\, \alpha\, f(E) \begin{bmatrix} 2\pi \\ 0 \\ 0 \end{bmatrix} \cdot \begin{bmatrix} 1 - \mu_1^2 \\ \pi/2 - (\mu_1\sqrt{1-\mu_1^2} + \arcsin(\mu_1)) \\ \pi/2 - (\mu_1\sqrt{1-\mu_1^2} + \arcsin(\mu_1)) \end{bmatrix},
\end{aligned}$$

where w is the particle weight. This formulation is obtained assuming that the beam propagates in x direction. By using the definition of anisotropy (3.38), we get:

$$\begin{aligned}
\alpha^x &= \frac{\psi_1^x}{\psi_0} = \frac{1 + \mu_1}{2}, \\
\alpha^y &= \frac{\psi_{1,}^y}{\psi_0} = 0, \\
\alpha^z &= \frac{\psi_1^z}{\psi_0} = 0.
\end{aligned} \tag{3.68}$$

In order to have a proof that the proposed projection method is correct, we record the phase space of a square beam of $10 \times 10\,\mathrm{cm}^2$ with a Gaussian energy spectrum and an isotropic emission in a cone with a semi-aperture of 5°. Following the definition of

the anisotropy factor along the axis given in (3.68), for this specific case we find the following values: $\alpha^x = 0.9981$ and $\alpha^y = \alpha^z = 0$. For this result, we show in Fig. 3.8 a comparison between the method of anisotropy calculation presented in Section 3.5.1 and the analytical calculation presented above. The two methods are equivalent and the only difference is due to the statistical variation of the Monte Carlo simulation.

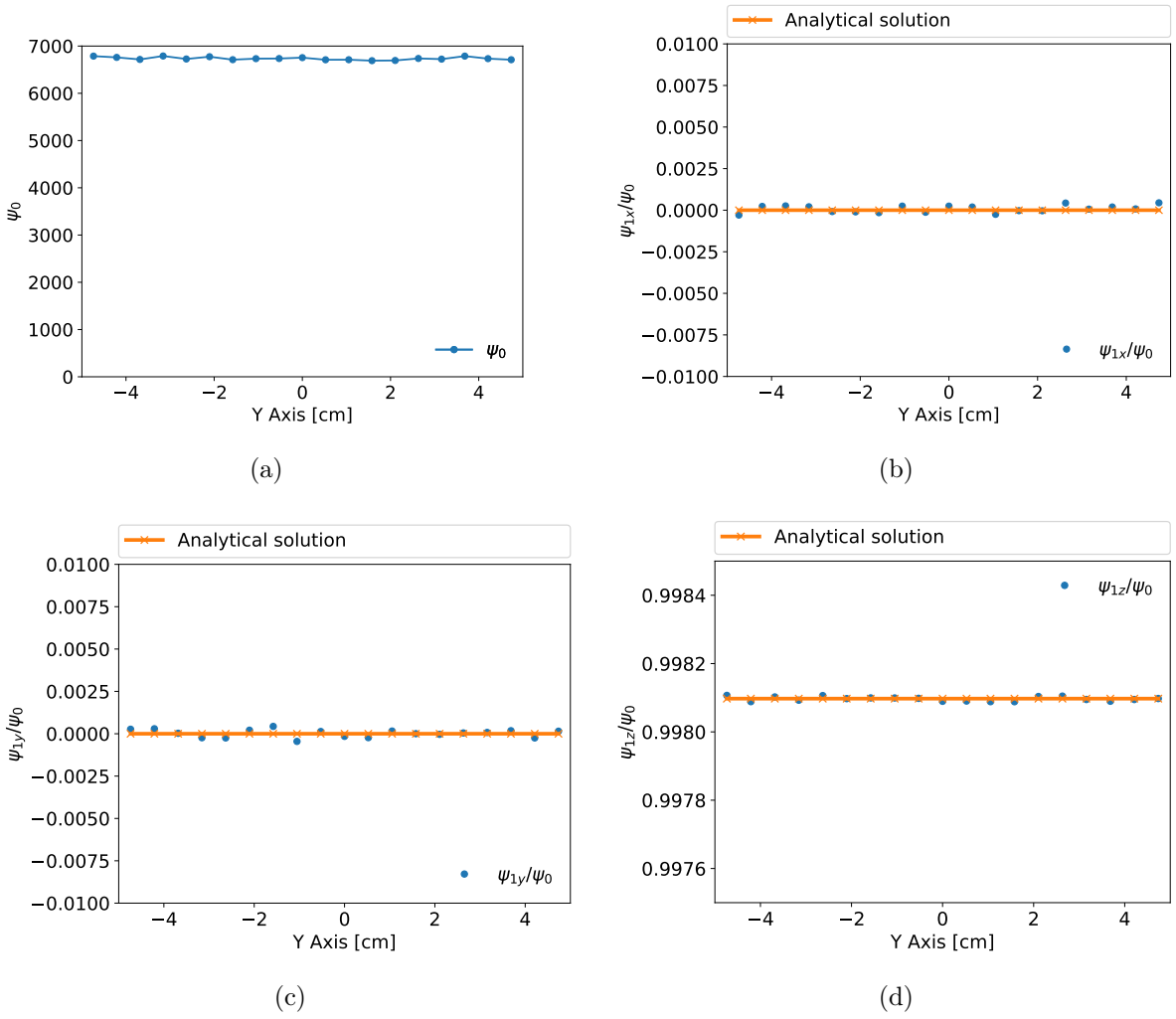

Figure 3.8: (a) The flux function ψ_0 of the beam. (b) anisotropy distribution α^x parallel the propagation axis of the beam is represented. (c) and (d) anisotropy distributions in the transverse directions of the beam, α^y and α^z respectively. The analytical solution is plotted in orange while the result obtained with the discretization of a phase space data file is plotted in blue. The two methods of beam initialization are equivalent.

3.6 Validation method for the numerical comparison

In this section we propose the methodology used for comparison of the dose distributions calculated with the moments method and the referent Monte Carlo code PENELOPE.

3.6.1 Isodose maps and dose profiles

The dose distributions calculated with our model and the Monte Carlo code are compared in multiple ways. The dose distributions are normalized to the maximum value in water for external beam simulations, while in brachytherapy calculations the dose distributions are nomalized at 0.5 cm from the center of the source.

The degree of agreement in measured by overlaying the isodose contours from the two simulations for selected dose levels. Although the overlay provides information along the isodose contour only, this method is useful for visually evaluating the compared dose distributions and identifying localized dose differences in the regions where hot or cold spots occur. The discrepancies between two isodose maps can be strong in regions where the dose gradient is small but this has a small impact on the overall accuracy of the calculation. As example of the methods of comparison described above we refer to the case presented in Section 5.4. In this test case a photon beam of 18 MV propagates in a water domain with a half lung insert placed betewen 5 and 15 cm. In Figure 3.9 the two dimensional isodose maps are compared.

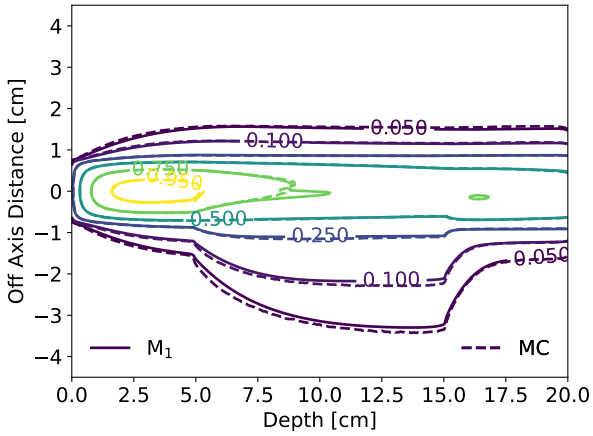

Figure 3.9: Example of comparison between two dimensional isodose maps at $z = 0$ in the xy plane. A discrepancy between the 75% isodoses (in green) is observed on the central axis of the beam between 8 and 10 cm in depth.

The superposition of isodose contours shows a local disagreement in the lung region, at 8-10 cm depth. A more quantitative comparison of dose profiles can be acquired along a line passing through the area of the disagreement. Typically the dose profiles cuts are taken at the center of the beam along the propagation axis, called the depth dose profile, and perpendicularly to the propagation axis at different depths in order to evaluate the

beam straggling. With reference to the test shown in Figure 3.9, an example of the use of the cuts diagnostics is shown in Figure 3.10.

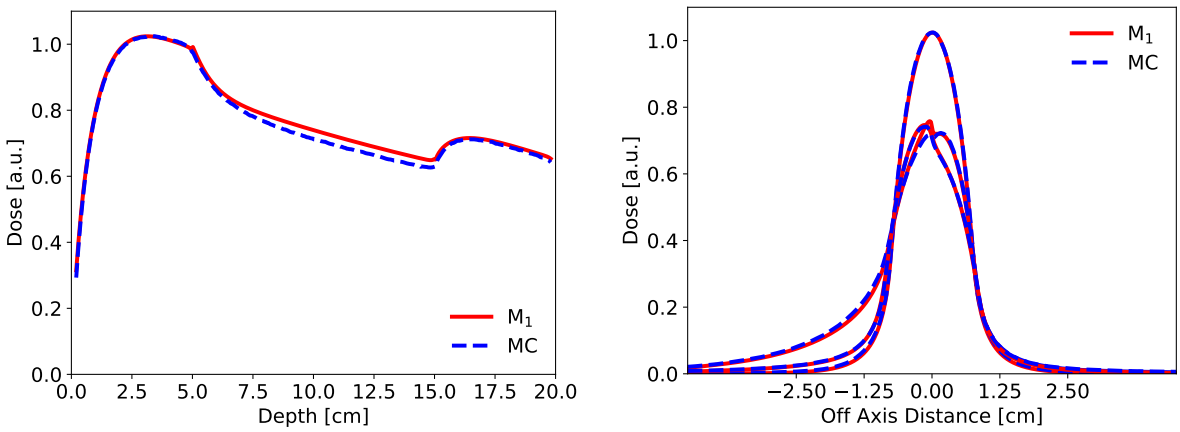

(a) (b)

Figure 3.10: Examples of dose profiles: (a) depth dose distribution along the central axis, (b) transverse dose profiles at the center of the beam ($z = 0$) taken at depths of 3.2, 10 and 17 cm. The depth dose profile shows that the discrepancy between the two calculations is present in all the lung region. On the other hand, the lateral dose profile taken at 10 cm depth shows that the discrepancy is limited along the interface between water and lung.

3.6.2 Dose difference and percentage dose difference

The preceding two methods provide a qualitative two dimensional or one-dimensional evaluation. For the quantitative evaluation we introduce the dose difference diagnostic that measures the discrepancy between the two calculated distributions.

For the external beam simulations we introduce the dose difference between the two distributions. It is calculated for each pair of voxels i as:

$$\Delta D_{i,\%_{abs}} = \left(\frac{D_{M_1,i}}{D_{M_1,\max}} - \frac{D_{MC,i}}{D_{MC,\max}} \right) \times 100\%. \tag{3.69}$$

In Figure 3.11 we show the difference between the two dose distributions calculated for the test case presented in Figure 3.9.

For brachytherapy simulations we introduce the percentage dose difference diagnostic. This definition accounts for the fact that in brachytherapy simulations the dose has maximum at the center of the volume source and decreases rapidly (approximately as $1/r^2$) outside the source. It means that the in the region of interest the absolute dose values are very small and a more precise diagnostic is needed. The percentage dose

difference is calculated for each pair of points of both distributions according to:

$$\Delta D_{i,\%_{rel}} = \left(\frac{D_{M_1,i}}{D_{MC,i}} - 1 \right) \times 100\%. \tag{3.70}$$

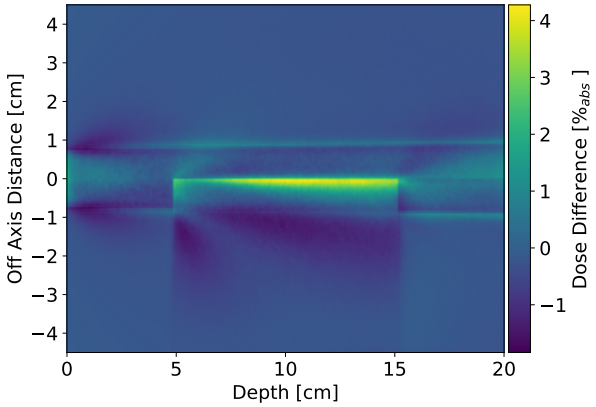

Figure 3.11: Spatial distribution of the dose difference between the Monte Carlo and M_1 simulations. This diagnostic is useful for quick quantitative visualization of the degree of discrepancy, its shape and its extension.

The main advantage of this diagnostics is that, the image offers a quick quantitative evaluation. The dose difference image can be used for further quantitative analysis in terms of the average dose difference / percentage dose difference distribution. This provides additional information regarding the average dose difference / percentage dose difference and the standard deviation of a dose difference / percentage dose difference distribution. These two quantities are defined as:

$$\begin{aligned} \overline{\Delta D} &= \frac{1}{N} \sum_{i=1}^{N} \Delta D_i, \\ \sigma(\Delta D) &= \sqrt{\frac{\sum_{i=1}^{N} (\Delta D_i - \overline{\Delta D})^2}{N}}. \end{aligned} \tag{3.71}$$

where N is the number of voxels in the domain. The same formulation is valid for $\Delta D_{\%}$. Considering the dose difference distribution shown in Figure 3.11, the calculated mean dose difference is $0.42\% \pm 0.42\%$.

3.6.3 Gamma index

The gamma index was first introduced by Low and Dempsey [79] as a metric that combines features of both dose difference and distance-to-agreement, while performing robustly in the regions where those are prone to failure. Conceptually, the gamma index is very similar to dose difference and distance-to-agreement, but combines them into a metric

resembling a distance. In this way both dose difference and distance-to-agreement are taken into account for every point compared.

The gamma index can be explained as follows: we want to estimate the degree of agreement of two dose distributions $D_a(\vec{r})$ and $D_b(\vec{r})$. For sake of simplicity we consider the dose distributions as two dimensional and we focus on the dose at a given point $D_a(\vec{r}_a)$. The degree of accuracy can be estimated in principle with two different criteria. The first criterion is the dose difference between the two distributions D_a and D_b evaluated at a given point $\vec{r_a}$. The passing parameter Δ_{DD} is introduced and the agreement criterion is defined as follows: if the distributions satisfies the condition $|D_b(\vec{r}_a) - D_a(\vec{r}_a)| \leq \Delta_{DD}$, the dose difference test is passed at the point $\vec{r_a}$. The second criterion is the distance-to-agreement between the referent dose value $D_a(\vec{r}_a)$ and $D_b(\vec{r}_b)$. The distance to agreement criterion, Δ_{DTA} , is represented by a disk in the spatial domain with a radius equal to Δ_{DTA}. If the difference between the distribution $D_b(\vec{r}_b)$, for $\vec{r}_b$ being within the disk, and $D_a(\vec{r}_a)$ falls within the acceptance criterion, the DTA test passes at that point. Combining the two criteria we obtain a global acceptance criterium. This γ-index has the form:

$$\gamma(\vec{r}_a) = \sqrt{\frac{|\vec{r} - \vec{r}_a|^2}{\Delta^2_{DTA}} + \frac{|D_b(\vec{r}) - D_a(\vec{r}_a)|^2}{\Delta^2_{DD}}}. \tag{3.72}$$

If $\gamma(\vec{r}_a) \leq 1$ the test is passed otherwise it is failed. In Figure 3.12 we show the result of the γ-index calculated with $\Delta_{DTA} = 1$mm and $\Delta_{DD} = 1\%$. In this example the test failed to pass in the zone of the water-lang interface between the depth of 5 to 15 cm.

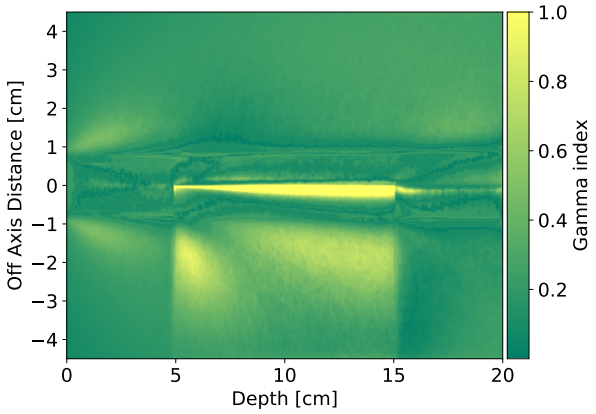

Figure 3.12: γ-index map showing the results of the 1%/1 mm criterion. The test failed the region of water-lung interface between 5 and 15 cm.

3.7 Conclusion

In this chapter the linear Boltzmann transport equation and the M_1 model have been presented. This model is based on a reduced number of equations for the angular moments,

allowing to reduce the number of degrees of freedom with respect to standard models. Some intrisic limitations of the model have been evidenced and the adopted solutions to improve the results have been proposed. Moreover, we have introduced the discretization methods for the energy and the spatial variables. The methodology of the validation process is defined with respect to the Monte Carlo code which is considered as a reference in order to optimize the code and obtain accurate solutions. The entire validation process is presented in the following chapters for both external beam radiotherapy and brachytherapy.

Chapter 4

Setup for external photon beam simulations

4.1 Introduction

In this chapter we present the validation of the M_1 model described above. The validation is made comparing our algorithm with the Monte Carlo PENELOPE-2014 code [121]. In this chapter all the test cases are run in a homogeneous phantom in order to reduce the complexity of the analysis.

Firstly we consider a photon beam with a Gaussian energy spectrum centered at 6 MeV. This choice allows to test the accuracy of the model in a standard energy regime for the external beam radiotherapy. Moreover, in this preliminary step we analyse the impact of the anisotropy initialization on the solution of the Boltzmann equation. In the end we demonstrate that for simulating a realistic beam divergence one needs to choose an appropriate anisotropy distribution.

Once the model is validated for a Gaussian spectrum we introduce a more realistic energy initialization corresponding to a bremsstrahlung spectrum. In this case the needed accuracy of the M_1 method can be achieved by introducing a split between the primary and secondary particles. The primary and secondary particles need to be treated separately otherwise numerical issues can appear.

As a results of test cases presented in this chapter we optimize the physical parameters of the code. Firstly we demonstrate that a solution of a fully-coupled problem, i.e. all transported particles can produce secondary particles of the other species taken into account, is not necessary. The solution of the M_1 equation with a partially-coupled physics allows to save memory allocation and computational time without affecting the precision of the model. As a last step we introduce a non-uniform energy grid that is crucial to optimize the M_1 algorithm.

4.2 Protocol of comparison

In order to validate the M_1 model for the external photon beam radiotherapy applications, we conduct a comparison of all test cases with the Monte Carlo code PENELOPE-2014 [121]. In the present section we describe the protocol of comparison for the two methods, by analyzing the parameters that control the precision of the simulations. These parameters include the model to describe the entering beam, the calculation geometry and the discretization parameters.

4.2.1 Source model

We begin by describing the model of the source used for the first validation step. A source of particle is described here by two parameters: the energy spectrum and the direction of propagation.

4.2.1.1 Energy spectrum

In order to test the accuracy of the M_1 model in the standard energy regime of the external beam radiotherapy, a photon beam with Gaussian spectrum (Full Width at Half Maximum = 10% of the mean energy E_0) centred at $E_0 = 6$ MeV is considered, see Figure 4.1. Although this spectrum represents the mean energy of the clinical bremsstrahlung spectrum with nominal energy of 18 MeV, this initialisation is not representative of a real phase-space of the beam exiting the linear accelerator. However, this academic case is a convenient starting point to test the accuracy in reproducing the Compton scattering that is the most probable photon interaction in the radiotherapy energy regime (see Section 2.3.2).

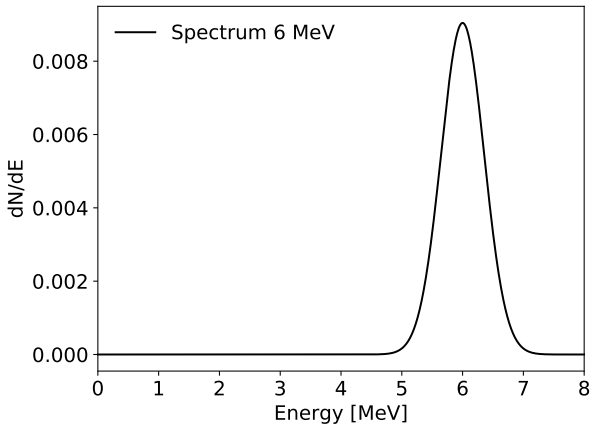

Figure 4.1: Photon beam initialisation with a Gaussian spectrum centered at 6 MeV with FWHM of 0.6 MeV.

As a second step, the more realistic 6 MV and 18 MV photon beam spectra shown in Figures 4.2(a) and 4.2(b) are used in adequation with standards of current accelerators.

These spectra are obtained by the analysis of two different phase-space files available on the International Atomic Energy Agency website (www-nds.iaea.org/phsp). More specifically, to obtain the 6 MV spectrum we use the phase-space generated for the Varian Clinac 600C [18] while for the 18 MV spectrum the phase-space generated for the Elekta Precise is used [133]. The contaminant electrons and positrons are not taken into account, thus the spectrum represents a photon beam distribution only.

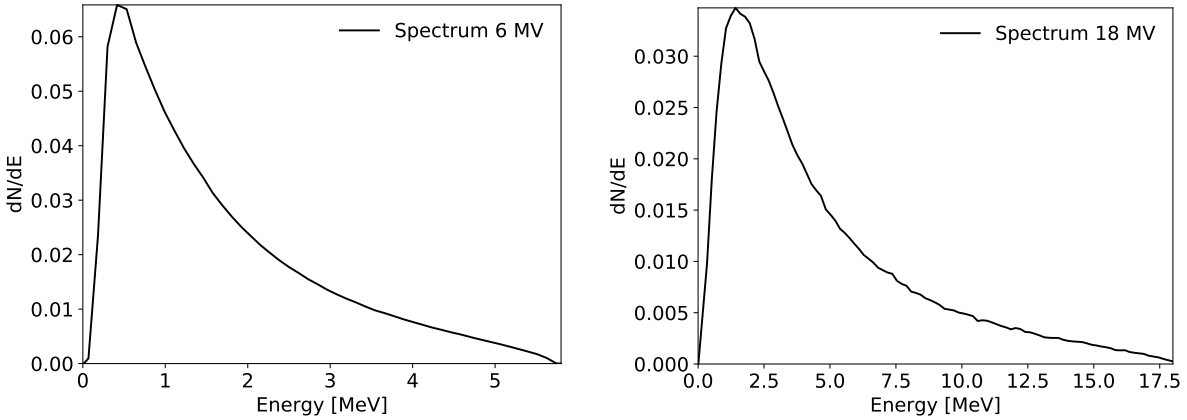

(a) (b)

Figure 4.2: Realistic initialisation using bremsstrahlung spectra: (a) spectrum of the Varian Clinac 600C at the nominal energy of 6 MeV and (b) spectrum of the Elekta Precise at the nominal energy of 18 MeV.

4.2.1.2 Direction initialization

In this preliminary validation of the M_1 code, we perform several simplified simulations taking into account square beams of different dimensions with a homogeneous particles distribution. In order to not increase the number of parameters in the initialization, we consider photon beams that propagate only along one direction. Such a beam is easy to initialize because only the anisotropy parameter along the propagation axis has to be defined while the intensity of the beam is assumed to be constant. As explained in Section 3.5.2, this means that in every point of the beam the particles are emitted within a given cone aperture with respect to the propagation axis and isotropically with respect to the azimuthal angle. Since the realizability domain of the M_1 model is defined as

$$\begin{aligned}\mathcal{A} &= \left\{ \psi = [\psi_0, \psi_1]^T \, : \exists \, \bar{\psi} \geq 0 \, | \, \psi_0 = \int_{S^2} \bar{\psi} \, d\Omega \, , \, \psi_1 = \int_{S^2} \Omega \, \bar{\psi} \, d\Omega \right\} \\ &= \left\{ \frac{\psi}{\psi_0} \geq 0 \, , \, ||\psi_1|| < \psi_0 \right\} , \end{aligned} \tag{4.1}$$

it implies that the anisotropy $\alpha = ||\frac{\psi_1}{\psi_0}|| < 1$. The initialization of the beam without an angular spread represents a singularity in the M_1 model. For this reason, two different

values of the cone aperture are chosen: the first corresponds to a very small aperture with respect to the propagation axis of 0.05°, the second value is 5°. A sketch of these initializations is presented in Figure 4.3(a).

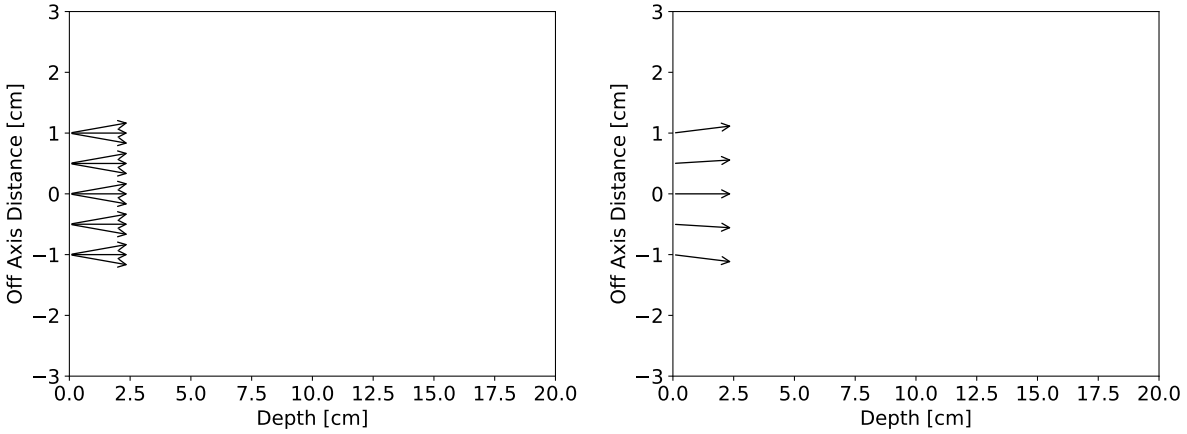

(a) (b)

Figure 4.3: Direction initializations used for the external photon beam validation: (a) initialization of the beam with only one anisotropy and (b) initialization of a realistic beam.

Such a direction initialization is useful in order to test the accuracy of the model in a simplified configuration with a few parameters. However such beam does not correspond to reality where the beam is generated in interaction of a narrow electron beam with a high-Z metal target placed at a certain distance from the patient surface. Such a beam, in a first approximation, can be considered as generated by a point source at a given distance from the phantom surface. In this work we set a source-to-surface distance (SSD) of 100 cm. In this way the particles entering the phantom do not have the same direction and a geometrical aperture of the beam has to be defined. In Figure 4.3(b) a scheme of this initialization is given.

4.2.2 Calculation geometry

In the present chapter, the homogeneous water phantom sketched in Figure **??** is used. This configuration simplifies the analysis of the discrepancies between the reference Monte Carlo code and the M_1 model. The calculation domain is defined by a $6 \times 6 \times 20$ cm^3 phantom.

For this first setup simulations we only consider cases with water. Heterogeneous test cases with several materials are presented in the next chapter.

4.2.3 Numerical parameters of simulations

In this section the parameters used in the M_1 and Monte Carlo simulations are presented. These parameters concern the spatial discretization of the domain, the energy range and its discretization used in M_1 and the cut-off energy imposed in the PENELOPE code.

4.2.3.1 M1 parameters

As introduced in Chapter 3, the M_1 model requires discretization in both space and energy. In all simulations proposed in this Chapter a uniform orthogonal spatial discretization is adopted with a cubic mesh of $0.5 \times 0.5 \times 0.5$ mm^3. The spatial discretization may evolve in the future with introduction of the adaptive mesh refinement technique that optimize the number of meshes in the regions of interest. Moreover higher order numerical schemes may be introduced in the code in order to allow the convergence to the solution on a larger mesh grid.

Regarding the energy variable, different discretizations are employed. We first consider the cases with the initial energy spectrum of 6 MeV. For those presented in Sections 4.3, 4.4.1 , 4.4.2 and 4.5.1 a uniform discretization with 100 groups is used. In Section 4.5.2 we adopt two different non-uniform optimized grids for photons and electrons. This method reduces the number of energy groups to 21 for both types of particles. In all these cases the energy range is set between 10 keV and 7.2 MeV. For the simulation with an energy of 18 MeV presented in Section 4.5.1 a uniform discretization with 300 groups is used, whereas in the case presented in Section 4.5.2 the number of energy groups is reduced to 39 for both types of particles. In all 18 MeV cases the energy range is set between 10 keV and 18.5 MeV.

4.2.3.2 PENELOPE parameters

The dose depositions calculated by the M_1 model are compared to the Monte Carlo simulations performed with the code PENELOPE [121]. This code simulates coupled electron-photon transport in the energy range from 100 eV to 1 GeV. The numerical phantoms are created with the 'pengeom' package. The absorbed dose distribution are tallied using a uniform orthogonal grid with $0.5 \times 0.5 \times 0.5$ mm^3 voxels. The typical number of tested particles in the Monte Carlo calculations was 2×10^9, which allowed us to obtain the deposited dose maps with a statistical uncertainty below 1% in all voxels. The absorption energy parameters are set to $\mathrm{EABS}(1,\mathrm{M}) = \mathrm{EABS}(2,\mathrm{M}) = \mathrm{EABS}(3,\mathrm{M}) = 0.01\mathrm{MeV}$ for electrons, photons and positrons in all simulations. The elastic scattering parameters are set to $\mathrm{C1(M)} = \mathrm{C2(M)} = 0.01$. The cut-off energy losses parameters for inelastic collisions and bremsstrahlung emission are set respectively to $\mathrm{WCC(M)} = \mathrm{EABS}(1,\mathrm{M})$ and $\mathrm{WCR(M)} = \mathrm{EABS}(2,\mathrm{M})$.

4.3 Dose distribution with a Gaussian spectrum

The accuracy of the M_1 model by taking into account the most relevant physical phenomena occurring in a radiotherapy treatment is evaluated here. To this end, we use a Gaussian spectrum centered at 6 MeV as energy initialization. In water, in this energy regime, photons mostly interact following the Compton scattering.

In this section we also conduct a study on the direction initialization, by analyzing how the anisotropy initialization impacts the solution of the Boltzmann equation. As a first step, in Section 4.3.1 we use a small diffusion parameter (i.e. an anisotropy factor near to the unity) along the propagation axis in order to approximate a monodirectional beam. Then, in Section 4.3.2 we adopt a constant and larger diffusion parameter (i.e. a smaller anisotropy factor), observing that this initialization presents an incorrect behaviour due to the M_1 angular approximation. This test clearly shows that this initialization is not suitable for reproducing a realistic beam. As a last example, in Section 4.3.3 a realistic anisotropy distribution is employed. This initialization results in a better accuracy of M_1 in reproducing the Monte Carlo simulations.

4.3.1 Small diffusion initialization

In order to analyse the M_1 model accuracy in reproducing a Monte Carlo simulation in a standard case, we consider a very simple initialization: a photon beam propagating along one direction with a very small divergence. As zero divergence represents a singularity for M1, see Section 4.2.1.2, we initialize an entering flux with a single propagation direction and a small diffusion parameter of 0.05°. This corresponds to an anisotropy factor along the propagation axis $\alpha_x = 0.99999981$. In the discretized computational domain for the M_1 code, this configuration produces an upper/lower shift of the beam of only one grid cell at the right domain boundary. We call that beam monodirectional (with zero divergence). In PENELOPE, the equivalent configuration is obtained by initializing an emitting surface perpendicular to the propagation axis. In this surface the particles are homogeneously distributed and they are emitted in every point within a cone with a semi-aperture of 0.05° (see Figure 4.3(a)).

The results are shown in Figure 4.4 in Cartesian coordinates with the x-axis in the beam propagation direction and y-axis along the beam width. In particular, panels 4.4(a) and 4.4(b) show the depth dose distribution along the central axis $y = z = 0$ and the transverse profiles at $z = 0$ taken at the depths of 2.5, 10.0 and 17.0 cm. The last panel 4.4(c) presents the superposition of the two dimensional (2D) isodose maps at the beam axis $z = 0$ in the xy plane. In Figure 4.5 we plot two diagnostics in order to analyse the discrepancies between the two solutions. Panel 4.5(a) presents the γ-index map with 1%/1 mm criterion. A more strict diagnostic showing the dose differences between the two calculations is presented in panel 4.5(b).

As shown in Figures 4.4 and 4.5, the M_1 model accurately reproduces the Monte

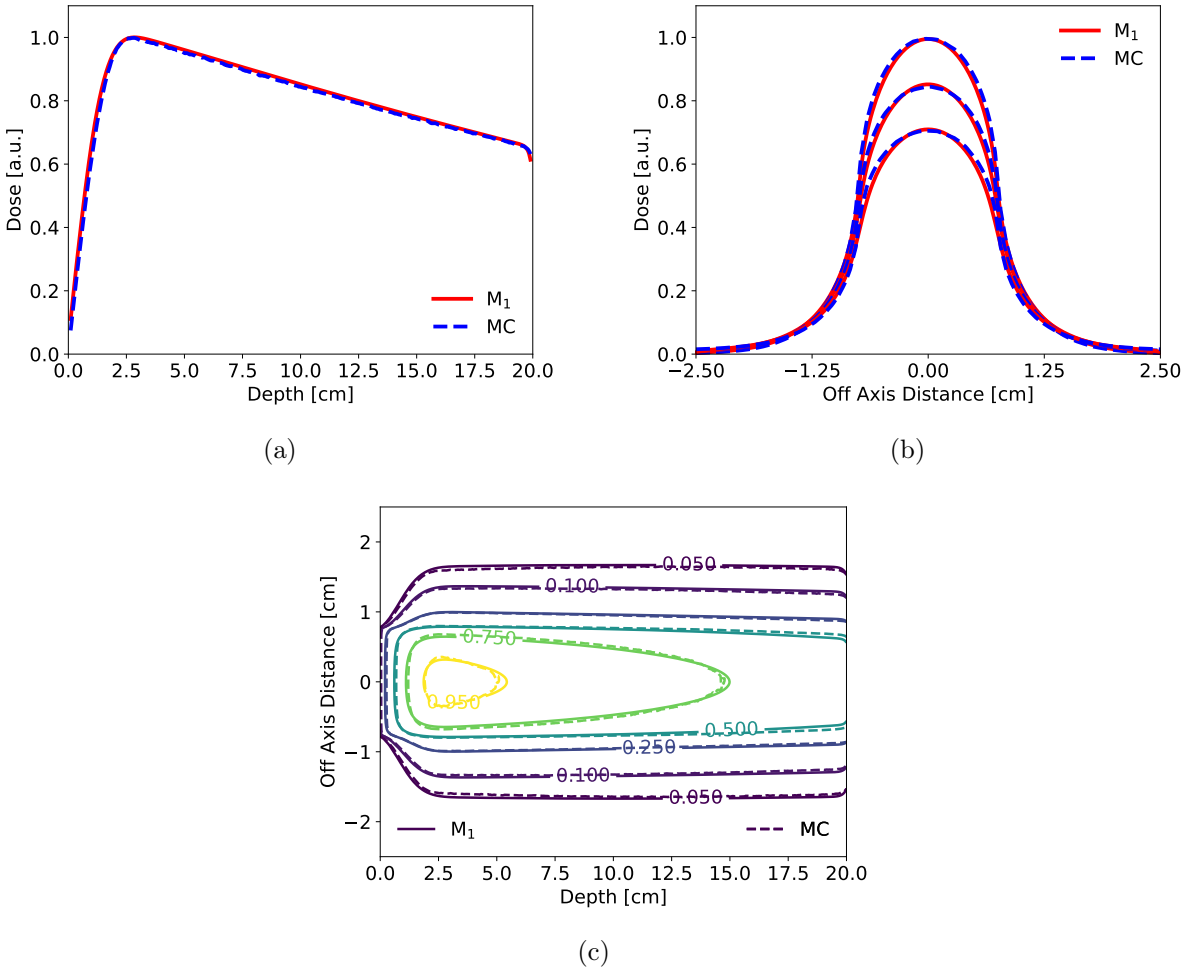

Figure 4.4: Direction initialisation with a small diffusion parameter. A 6 MeV photon beam coming from the left in a homogeneous water phantom: (a) depth dose distribution along the central axis, (b) transverse dose profiles at the center of the beam ($z = 0$) taken at depths of 2.5, 10 and 17 cm, (c) 2D isodose map at $z = 0$ in the xy plane.

Carlo simulation. A statistical analysis of the dose difference shows that the mean dose difference between the two simulations is $0.78\% \pm 0.98\%$. The γ-index success rate is 100%. In Figure 4.5(b), the major differences can be observed in the build-up region at 1 cm from the entrance plane and on the edges of the beam. Both regions are characterized by a strong electronic disequilibrium. In order to explain these discrepancies, we resort to the Compton scattering described in Section 2.3.2 and we plot in Figure 4.6(a) the Klein-Nishina cross section (2.32) expressed as a function of the incident photon energy E and its scattering angle.

For a photon energy of 6 MeV, we can see that the most probable emission direction for the secondary photon has a small angle with respect to the direction of the incident photon. However, a small number of photons can be emitted perpendicularly to the

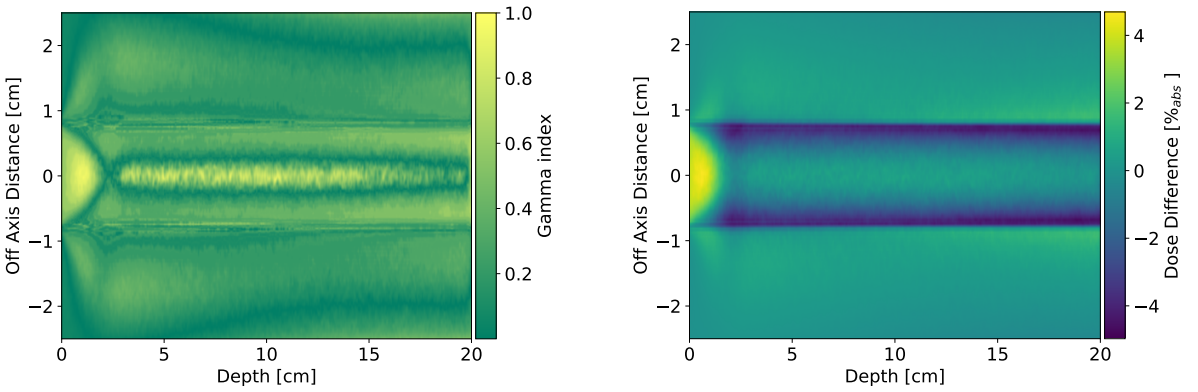

(a) (b)

Figure 4.5: Direction initialisation with a small diffusion parameter. A 6 MeV photon beam coming from the left in an homogeneous water phantom: (a) γ-index map showing the results of the 1%/1 mm criterion, (b) spatial distribution of the dose differences, see Section 3.6.2, between the Monte Carlo and M_1 simulations. The γ-index criterion is satisfied for all the points of the domain. However the differences between the dose distributions can be of the order of 4% in certain regions of the domain. The stronger discrepancies can be observed in the build-up region and on the edges of the beam.

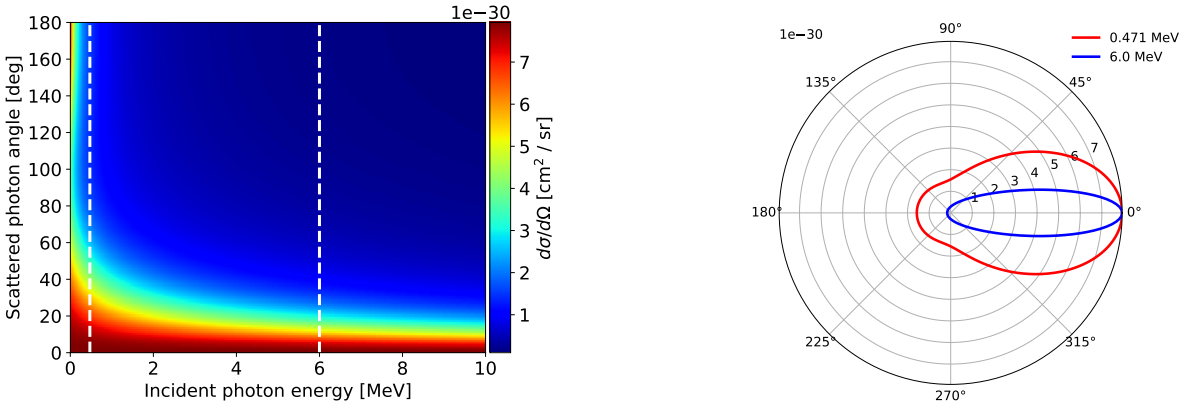

(a) (b)

Figure 4.6: Klein-Nishina cross section: (a) 2D map of the Klein-Nishina cross section as a function of the incident photon energy E and the angle of the scattered secondary (b) polar plot of the Klein-Nishina for a 6 MeV and a 0.471 MeV photons.

propagation direction or can be even backscattered. Analysing the Figure 2.12(a), we observe that the photons emitted perpendicularly have an energy of 0.471 MeV. These photons in turn, interacting with a higher probability, emit electrons with an energy up to 0.305 MeV. Figure 4.5(b) shows that the maximum dose difference on the edges of the beam. The difference is negative, this means that the M_1 model underestimates the dose

in these regions. If we measure the width of this region, we see that it is comparable to the range of electron with an energy of 0.3 MeV. Hence, we can conclude that the lack of energy comes from the fact that these electrons have not been generated. This is due to the flux annihilation intrinsically performed by the M_1 model inside the beam in the low energy groups. This also explains the dose difference in the build-up region where M_1 averages the backscattered photons with the small-angle scattered ones.

4.3.2 Large diffusion initialization

The test case presented in the previous section has shown that M_1 has a good accuracy in reproducing a Monte Carlo simulation in an highly anisotropic case. Nevertheless, in clinical applications, particle beams with zero divergence do not exist. Therefore, we now consider a test case where the photon beam is initialized with an anisotropy factor calculated with a larger diffusion in order to mimic a divergent beam. With this aim we employ an anisotropy factor $\alpha_x = 0.9981$, which corresponds to a semi-aperture of the emission cone of 5°.

The results are shown in Figures 4.7 and 4.8. The statistical analysis of the dose difference shows that the mean dose difference between the two simulations is $0.99\% \pm 0.77\%$, i. e. the precision of the M_1 model in this case is lower than before. In particular, in panel 4.7(a) we observe a discrepancy between the two simulations in the interval between 10 and 17 cm. This difference is manifested in the fact that the γ-index with $1\%/1\,\text{mm}$ criterion is not satisfied in this region (see Figure 4.8(a)) and its global success rate goes down to 97.77%.

In the dose difference map in panel 4.8(b) we can observe that an overdose artefact appears. These two shadows start from the left border of the domain at the top and bottom of the beam. Their profiles follow the solution of the following system of equations:

$$\begin{cases} y = -0.75 + x \cdot \tan 5^\circ & \text{lower line} \\ y = 0.75 - x \cdot \tan 5^\circ & \text{upper line} \end{cases} \tag{4.2}$$

In Figure 4.8(b) the curves representing Eq. (4.2) are plotted, with the crossing point located at $x \simeq 8.57\,\text{cm}$. In Figure 4.7(a) the crossing point is indicated by the dashed line. This structure can be explained as follows: as discussed above, in M_1 model an average on the particle flux has place inside the beam. However, the voxels on the upper and lower boundaries of the beam are not subject to this kind of averaging. This origins two flows of photons following the cone aperture that cross each other in the center of the beam. Once the two flows cross each other, the average takes place and a resulting flow along the propagation axis is generated as schematically shown in Figure 4.9.

The energy that is lost in this average is deposited locally with two important consequencies: a reduction of the photon flux and the consequent overdose observed at the beam axis between 10 and 17 cm (Figure 4.7(a)).

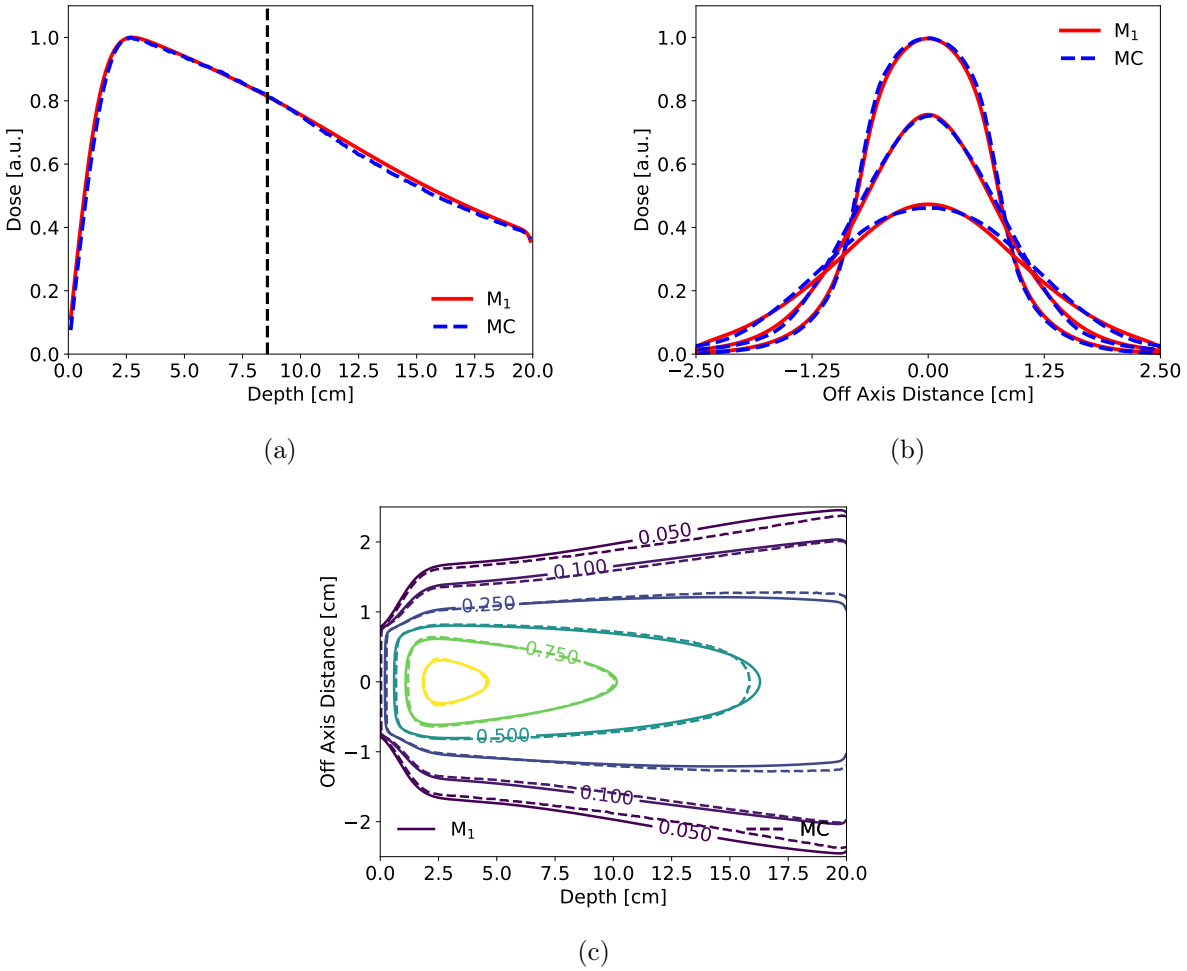

Figure 4.7: Direction initialisation with a large diffusion parameter. Is shown a 6 MeV photon beam coming from the left in an homogeneous water phantom: (a) depth dose distribution along the central axis, (b) transverse dose profiles at the center of the beam ($z = 0$) taken at depths of 2.5, 10 and 17 cm and (c) 2D isodose map at $z = 0$ in the xy plane.

4.3.3 Realistic anisotropy distribution

In the section above, we have shown that the beam initialization with a single value for the anisotropy factor can lead to a pathological behaviour of the M_1 model. To overcome this problem being more adherent to the reality we adopt an initialization that takes into account a real anisotropy distribution. The method is explained in Section 3.5.1. We consider the point source at 100 cm from the phantom surface. Since the beam has a width of 1.5 cm, it produces an aperture of 0.43° at the edges and a zero divergence in the center.

The results are shown in Figures 4.10 and 4.11. The statistical analysis of the dose difference shows that in this case the M_1 model is more accurate than in the previous cases with a mean dose difference between the two simulations of $0.55\% \pm 0.61\%$. This

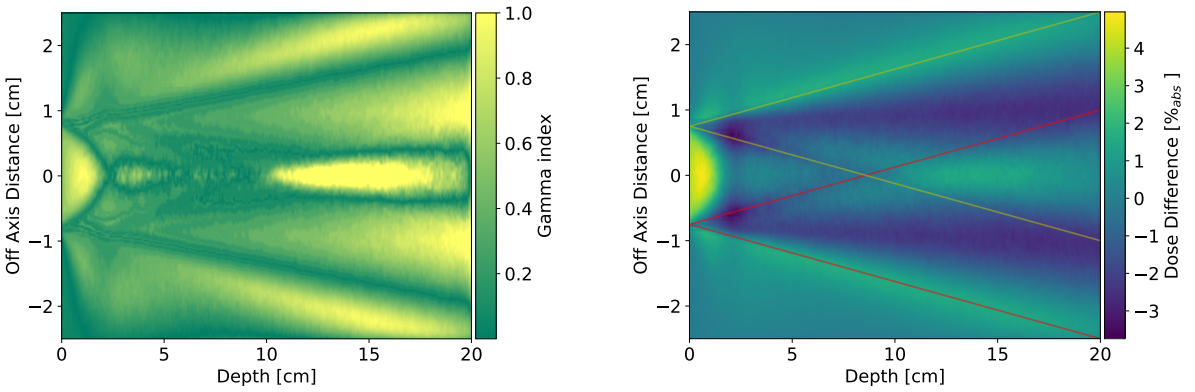

(a) (b)

Figure 4.8: Direction initialisation with a large diffusion parameter. A 6 MeV photon beam coming from the left in an homogeneous water phantom: (a) γ-index map showing the results of the 1%/1 mm criterion, (b) spatial distribution of the dose differences between the Monte Carlo and M_1 simulations. The γ-index fails in a limited region of the domain between 10 and 17 cm in depth. On the dose difference map two overdose artefact appears at the top and bottom of the beam at the entrance and propagate in the first centimiters of the domain. The solutions of the system (4.2) are plotted in red and yellow lines.

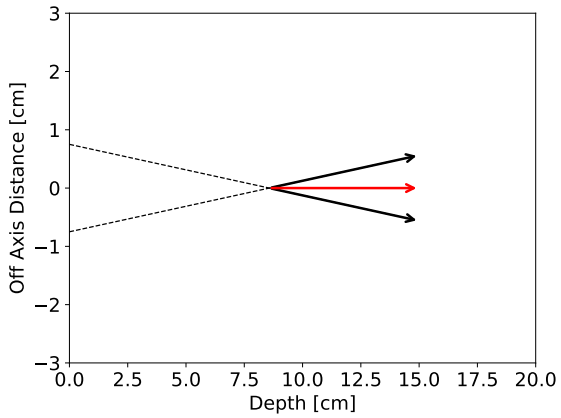

Figure 4.9: Schematic representation of the averaging process for voxels on the upper and lower boundaries of the beam. The particle flux exiting the numerical interaction (in red) has the propagation direction parallel to the beam axis.

improvement in accuracy is due to the fact that in a geometrically divergent beam the averaging effect of the M_1 model is less important, especially in the transverse direction. For this reason the dose difference at the edges of the beam is smaller than in the first case while the difference in the build-up region remains almost the same.

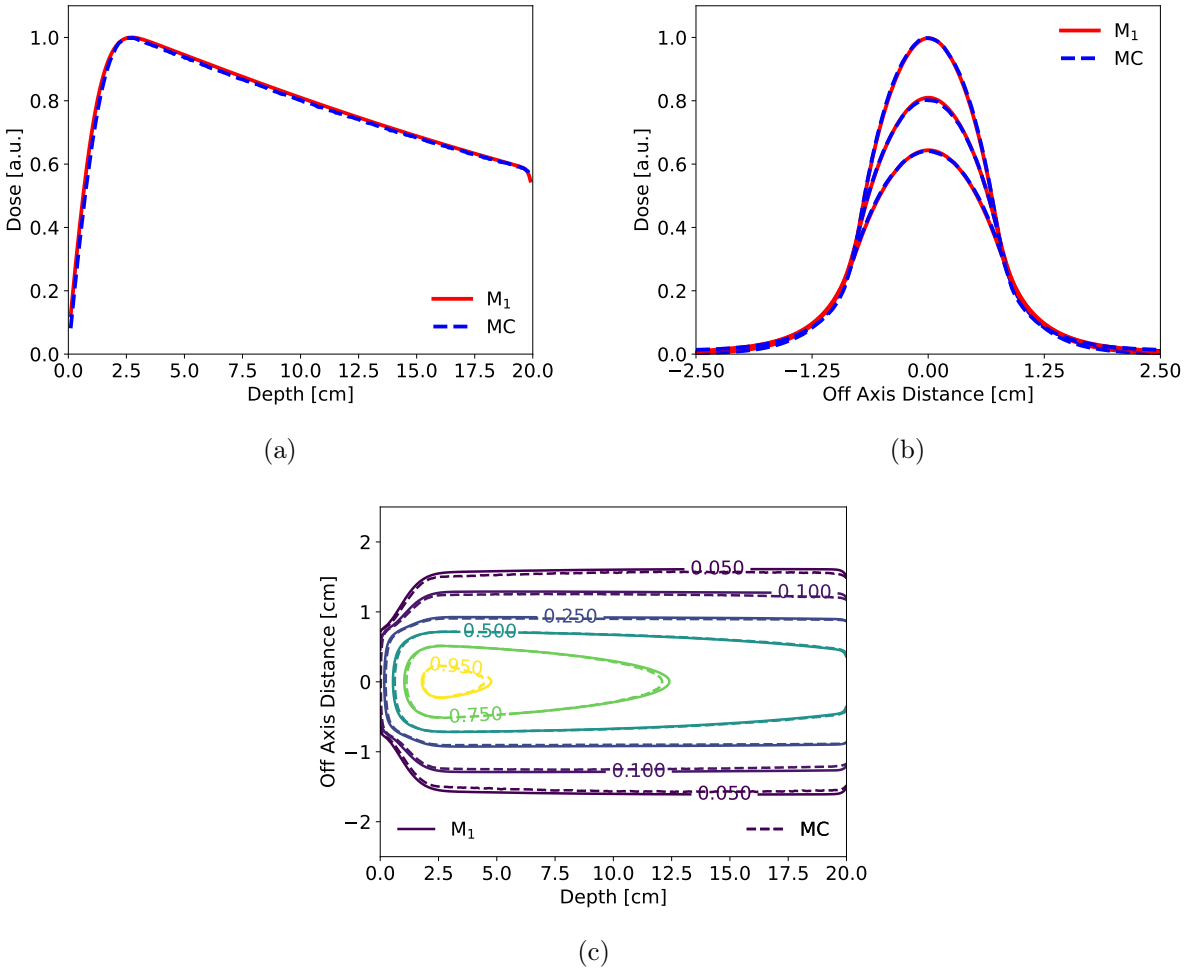

Figure 4.10: Initialisation with a realistic anisotropy distribution. A 6 MeV photon beam coming from the left in an homogeneous water phantom: (a) depth dose distribution along the central axis, (b) transverse dose profiles at the center of the beam ($z = 0$) taken at depths of 2.5, 10 and 17 cm and (c) 2D isodose map at $z = 0$ in the xy plane.

4.4 Dose distribution with a bremsstrahlung spectrum

As a next step in validation of the M_1 model, we study a more realistic case of a bremsstrahlung spectrum. To this end, we adopt a 6 MV spectrum for the injected photons. The direction initialization is the one introduced in Section 4.3.3. In this configuration, we analyse other limitations of the M_1 model and we propose some solutions to improve the precision and to reduce the computational effort.

4.4.1 Dose distribution without secondary particles populations

As a first case, we test the precision of the M_1 model considering a 6 MV bremsstrahlung spectrum. For this spectrum, the Compton scattering remains the most probable inter-

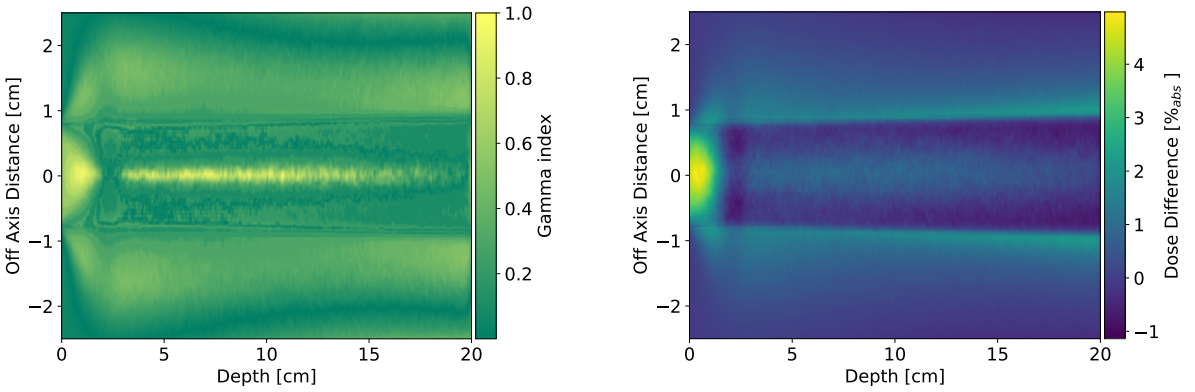

(a) (b)

Figure 4.11: Initialisation with a realistic anisotropy distribution. A 6 MeV photon beam coming from the left in an homogeneous water phantom: (a) γ-index map showing the results of the 1%/1 mm criterion, (b) spatial distribution of the dose differences between the Monte Carlo and M_1 simulations. The γ-index is satisfied in every point of the domain. Moreover, the dose differences on the edges of the beam are strongly reduced. However, the dose difference in the build-up region remains of the same order of the previous calculations.

action of photons with the ambient medium. Thus, we expect an accuracy comparable with the one obtained in the test of Section 4.3.3. As above, all the energy groups are initialized with the method presented Section 3.5.1.

The M_1 model does not reproduce the Monte Carlo simulation in this case, as it can be observed in Figures 4.12 and 4.13. A statistical analysis of the dose difference shows that the mean dose difference between the two simulations is $5.88\% \pm 5.28\%$. The γ-index success rate is 29.60%.

This low accuracy is clearly related to the shape of spectrum, due to some limitations of the M_1 model. This mismatch can be related to the fact that M_1 does not distinguish the primary and scattered photons. Specifically, the anisotropy initialization is the same for all energy groups. Moreover, in a deterministic algorithm, the solution of the Boltzmann equation is performed by starting from the energy group with highest energy and by decreasing of one energy group at every iteration, until the lowest energy group is reached. As Eq. (3.53) shows, the solution for a given energy group takes into account all particles that are scattered from the higher energy groups, according to the gain term. Thus, when considering a single population for primary (more collimated) and secondary (more scattered) photons, especially in a bremsstrahlung spectrum, M_1 averages their anisotropy. This process produces the very diffusive solution that is shown in Figures 4.12 and 4.13.

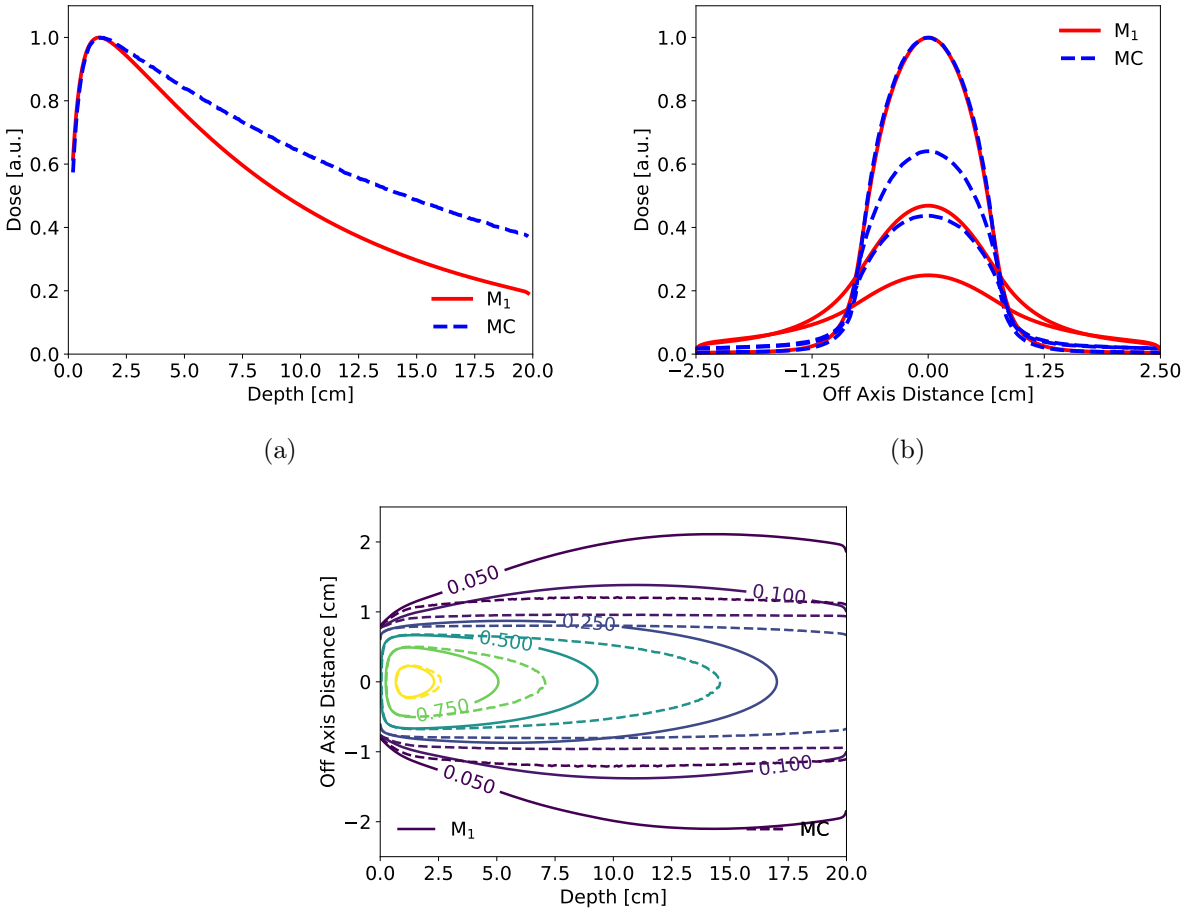

Figure 4.12: 6 MV photon beam coming from the left in an homogeneous water phantom: (a) depth dose distribution along the central axis, (b) transverse dose profiles at the center of the beam ($z = 0$) taken at depths of 1.4, 10 and 17 cm and (c) 2D isodose map at $z = 0$ in the xy plane. The dose distributions calculated with M_1 and the Monte Carlo codes strongly differ. The depth and lateral dose profiles show that the M_1 model is consistently more diffusive with respect to the Monte Carlo simulation. The diffusive behaviour is even more evident in the isodose map.

4.4.2 Dose distribution with secondary particles populations

In order to improve the results according to the analysis shown in the previous section, we split the calculation of Equation (3.53) in two consecutive steps by introducing the population of secondary particles. With this splitting we avoid the angular averaging between the primary and secondary particles in every energy group performed by the M_1 model .

We define $\psi_{[0]}$ the flux of the primaries and $\psi_{[1]}$ the flux of the secondaries. Using the argument that particles of the same type scattered $(n-1)$-times can only act as a source

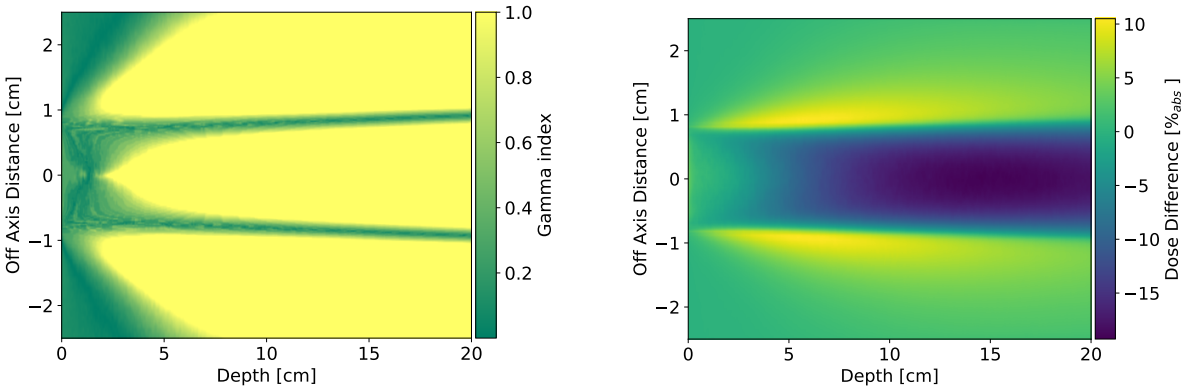

(a) (b)

Figure 4.13: 6 MV photon beam coming from the left in an homogeneous water phantom: (a) γ-index map showing the results of the 1%/1 mm criterion, (b) spatial distribution of the dose differences between the Monte Carlo and M_1 simulations. The γ-index fails for mostly the point of the domain. The strong diffusive behaviour of the M_1 model has an impact on the dose differences that are consistent for both inside and outside regions of the photon beam.

for particles that are scattered n-times, we can decompose the LBTE of each particle into a system of differential equations and one integro-differential equation. Doing so the coupled LBTE Eqs. (3.21) take the following form:

$$\begin{cases} \widehat{\Omega}\cdot\nabla\psi^i_{[0]}(\vec{r},\epsilon,\widehat{\Omega}) + \sigma^i_t(\vec{r},\epsilon)\psi^i_{[0]}(\vec{r},\epsilon,\widehat{\Omega}) = 0, \\ \widehat{\Omega}\cdot\nabla\psi^i_{[1]}(\vec{r},\epsilon,\widehat{\Omega}) + \sigma^i_t(\vec{r},\epsilon)\psi^i_{[1]}(\vec{r},\epsilon,\widehat{\Omega}) = \displaystyle\int d\epsilon' \int_{S^2} d\widehat{\Omega}'\, \sigma^{i,i}_s(\epsilon'\to\epsilon,\widehat{\Omega}'\to\widehat{\Omega})\psi^i_{[0]}(\vec{r},\epsilon',\widehat{\Omega}') \\ \qquad\qquad + \displaystyle\int d\epsilon' \int_{S^2} d\widehat{\Omega}'\, \sigma^{i,i}_s(\epsilon'\to\epsilon,\widehat{\Omega}'\to\widehat{\Omega})\psi^i_{[1]}(\vec{r},\epsilon',\widehat{\Omega}') \\ \qquad\qquad + \displaystyle\int d\epsilon' \int_{S^2} d\widehat{\Omega}'\, \sigma^{j,i}_s(\epsilon'\to\epsilon,\widehat{\Omega}'\to\widehat{\Omega})\psi^j_{[1]}(\vec{r},\epsilon',\widehat{\Omega}'). \end{cases} \tag{4.3}$$

where in the last equation $\psi^i_{[1]}$ takes into account all photons that are scattered more than once and $\psi^j_{[1]}$ takes into account the contribution to the i-species coming from the scattering of the other types of particles. In order to better clarify this point, we can take as an example the interaction of a photon beam. The first homogeneous differential equation of the system describes the absorption of the injected particles, i.e. the primaries. On the other hand, the second equation describes the transport of all the scattered particles. The first integral of the right term takes into account the secondaries produced by the primary photons. The second integral takes into account all the scattered secondary photons that are reinjected in the same population $\psi^i_{[1]}$ and the third equation takes into account the contribution from the $e - /p \to \gamma$ scattering.

As shown in Figures 4.14 and 4.15 the M_1 model with splitting on primary and secondary particles reproduces accurately the Monte Carlo simulation. A statistical analysis

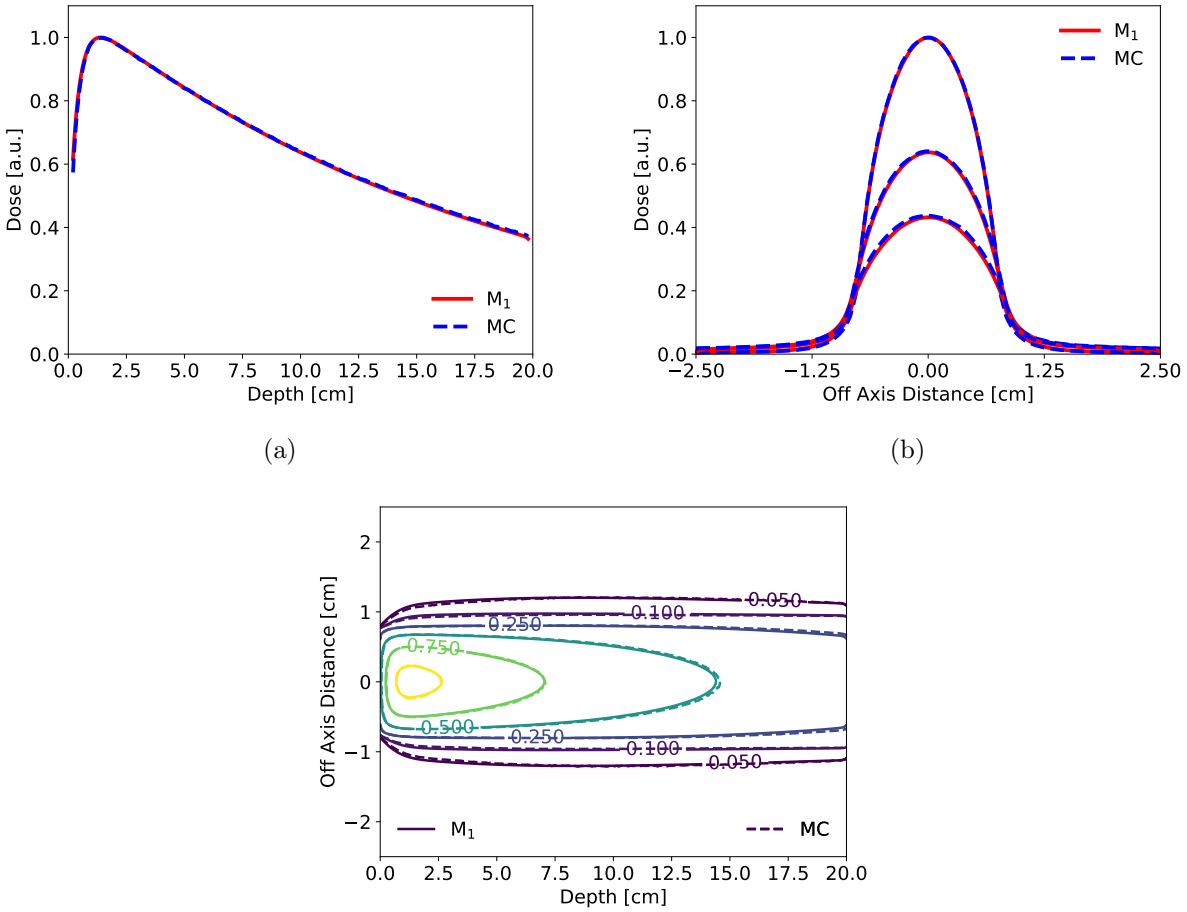

Figure 4.14: 6 MV photon beam coming from the left in an homogeneous water phantom: (a) depth dose distribution along the central axis, (b) transverse dose profiles at the center of the beam ($z = 0$) taken at depths of 1.4, 10 and 17 cm and (c) 2D isodose map at $z = 0$ in the xy plane. The secondary particle splitting allows to obtain a very accurate result with the M_1 model.

of the dose difference shows that the mean dose difference between the two simulations is $0.40\% \pm 0.36\%$. The γ-index success rate is 100.%.

The splitting method provides a higher accuracy without affecting the stability of the model because the convergence is reached with the same number of interations. The number of scattered populations can be extended to 2-times, 3-times...N-times. In our case the first scattered population is sufficient to reach a desired accuracy. A direct consequence of this method is the increase of memory allocation needed for the solution of the Boltzmann equation. Indeed, three more populations, i.e. secondary electrons-photons-positrons, have to be taken into account.

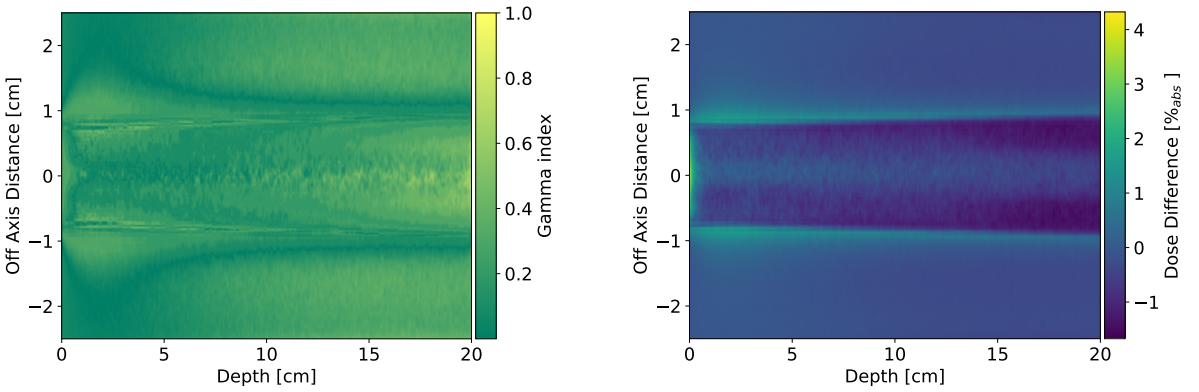

(a) (b)

Figure 4.15: 6 MV photon beam coming from the left in an homogeneous water phantom: (a) spatial distribution of the dose differences between the Monte Carlo and M_1 simulations and (b) 2D isodose map at $z = 0$ in the xy plane. The γ-index is respected for all the voxels in the domain. Despite to all the previous cases, the dose differences are very small also in the build-up region. Differences of the order of 4% are reached only in the first millimiters of the domain.

4.5 Optimization of the M_1 model

In this section we describe the optimization of the physical parameters of the M_1 model. The deterministic models are very costly in terms of memory occupation. This is due to the fact that the distribution functions have to be stored for each voxel of the domain and for each energy group. This leads to the impossibility to run simulations on a standard computer. For this reason we have to reduce the memory needed for the calculation by introducing some simplifications in the model. In this section we propose two approximations that allow to consistently reduce the computational effort.

The first approximation consists in the introduction of the partial coupling, which reduces the number of species of the transported particles and consequently the physical effects taken into account. This approximation does not affect the accuracy of the model but it produces an important gain in term of memory allocation.

The second approximation consists in the introduction of a non-unifomly optimized energy discretization. This approximation allows to consistently reduce the number of energy groups without affecting the precision of the calculation. The simulations of this section are conducted for both bremsstrahlung spectra at 6 MV and 18 MV.

4.5.1 Dose distribution with partial coupling

Equation (3.21) describes the particle cascade in which every transported particle can produce particles of the other species. In such a cascade, the particle species are fully coupled to each other. However fully-coupled problems are expensive to run while suf-

ficiently accurate solutions can be obtained with simpler coupling schemes that entail a lower computational effort. In the energy regime of the external beam photon radiotherapy some physical effects make a very small contribution and can be neglected without loss in the accuracy of the solution.

With this aim we can introduce a notion of partial-coupling. According to Figure 2.14 for the total cross sections, the contribution of bremsstrahlung and pair production is very small. Correspondingly for the equation for photons the bremsstrahlung effect and the fluorescence following impact ionization can be neglected. Moreover, the energy that would have go to the photons produced by charged secondaries is deposited locally. In addition, due to a small difference in electron and positron cross sections both pair secondaries can be considered electrons. These approximations are justified from a physical point of view below.

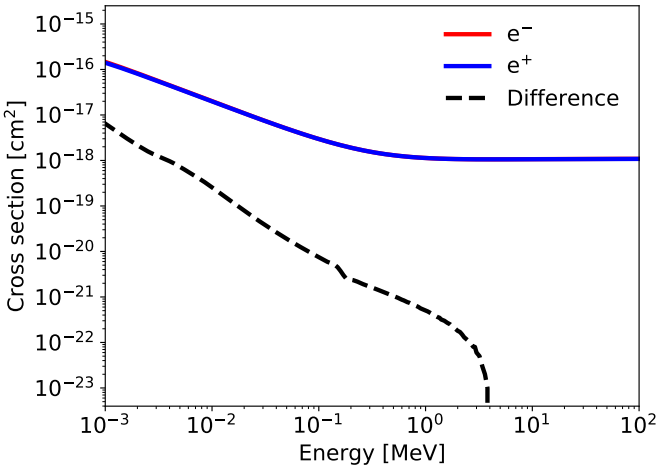

Figure 4.16: Total cross sections for electrons (red) and positrons (blue) in water and the difference between them (dashed black).

As a first step we focus on the assimilation of the positron population with the electron population. This means that in the case of a pair production reaction, we assume that instead of an electron and a positron two electrons are created. This approximation does not induce a considerable error in the dose deposition calculation. This is due to the fact that the electron and positron cross sections have a negligible difference in the energy range considered for our applications. As shown in Figure 4.16, only in the energy range between 0.001 MeV and 0.1 MeV the difference is larger then one percent. For these energies electrons and positrons in water have a range smaller than 0.5 mm which is a typical voxel size. This means that the positrons and electrons can be considered in the same population without introducing a noticible error in the dose deposition calculation.

This hypotesis has one more consequence. Without positrons the annihilation process is not taken into account. In order to make an estimation on the impact of annihilation process we conducted a numerical experiment with the PENELOPE code.

In order to estimate the fraction of the initial photon energy converted in electron and positron, we set a photon point source with a 6 MV or 18 MV spectrum that injects a parallel beam of photons in a wire of a very small thickness. In our case the wire is made of water, it is 20 cm long and its thickness is 10^{-5} cm. The thickness has been chosen considering the range of the less energetic elecrons in water, in order to avoid their re-absorption. Thus, all secondary particles can escape from the wire. This system is embedded in a spherical vacuum chamber with a perfectly absorbing wall. In this way we use the chamber as a detector. All the primary photons that do not interact with the wire are filtered out and not taken into account in the detection.

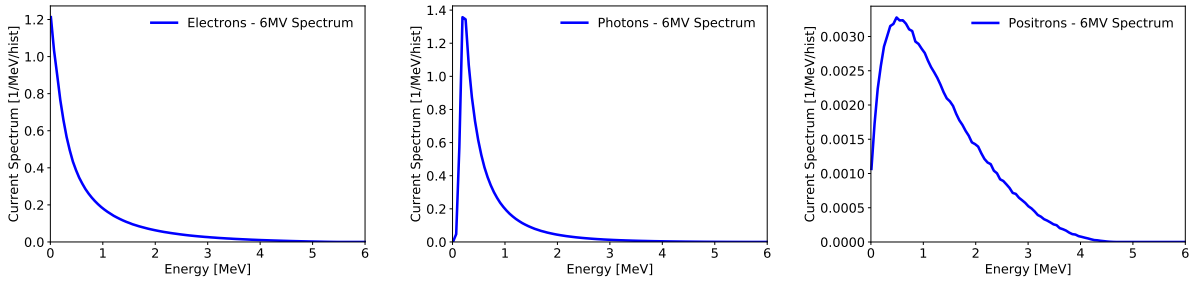

(a) (b) (c)

Figure 4.17: Spectra of the secondary particles produced by a photon beam of 6 MV: a) electrons, b) photons, c) positrons. We consider only the secondaries produced after the first interaction of the primary photon. Simulation perfomed with the PENELOPE code.

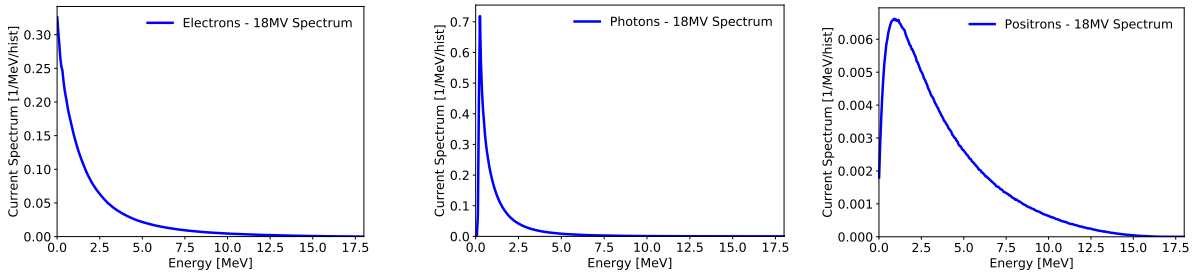

(a) (b) (c)

Figure 4.18: Spectra of the secondary particles produced by a photon beam of 18 MV: a) electrons, b) photons, c) positrons. We consider only the secondaries produced after the first interaction of the primary photon. Simulation perfomed with the PENELOPE code.

In Figures 4.17 and 4.18 the detected spectra of the secondary particles are shown. These spectra are in units of MeV on the abscissa axis and in 1/MeV/hist on vertical axis. This unit describe the energy detected per primary photon (history) injected in

the simulation. Due to the fact that we detect only the secondaries generated by the first interaction of the primary photons, these spectra represent the energy distribution of the first generated secondary particles. If we integrate numerically these spectra over the energy variable we obtain the number secondary particles produced by one primary photon:

$$\begin{aligned}\mathcal{N}_{6MV} &= \int_{E_{min}}^{E_{max}} \frac{dN}{dE} dE = \begin{cases} 0.684 & e^-/\text{hist} \\ 0.693 & \gamma\ /\text{hist} \\ 0.006 & e^+/\text{hist} \end{cases} \\ \mathcal{N}_{18MV} &= \int_{E_{min}}^{E_{max}} \frac{dN}{dE} dE = \begin{cases} 0.532 & e^-/\text{hist} \\ 0.503 & \gamma\ /\text{hist} \\ 0.032 & e^+/\text{hist} \end{cases} \end{aligned} \tag{4.4}$$

These numbers give us an important information. Positrons represent less than 0.6% in the first example and about 3% in the second example of the total number of secondary particles. Neglecting the positron population we neglect also the annihilation process that has place in the end of the positron propagation. This means that a part of the positron energy is not converted into the two annihilation photons. Assuming that all the positrons experience the annihilation process when their energy is equal to their rest energy, the energy carried by the annihilation photons can be estimated multipling the number of positrons with the double of the electron energy at rest. With this simple calculation we obtain that for the 6 MV spectrum, the missed energy is approximately 6 keV, while for the 18 MV spectrum is approximately 32 keV.

With the previous calculation we estimated the energy carried by the annihilation photons per history. We can also estimate the total energy that is carried by each type of secondary particle. For doing that we have to solve:

$$\begin{aligned}\mathcal{E}_{6MV} &= \int_{E_{min}}^{E_{max}} E\,\frac{dN}{dE} dE = \begin{cases} 0.528 & \text{MeV} \cdot e^-/\text{hist} \\ 0.486 & \text{MeV} \cdot \gamma\ /\text{hist} \\ 0.008 & \text{MeV} \cdot e^+/\text{hist} \end{cases} \\ \mathcal{E}_{18MV} &= \int_{E_{min}}^{E_{max}} E\,\frac{dN}{dE} dE = \begin{cases} 1.201 & \text{MeV} \cdot e^-/\text{hist} \\ 0.679 & \text{MeV} \cdot \gamma\ /\text{hist} \\ 0.118 & \text{MeV} \cdot e^+/\text{hist} \end{cases} \end{aligned} \tag{4.5}$$

Comparing now the energy of the annihilation photons with the total energy of the secondaries, we conclude that it contains less than 3% of the initial energy and can be neglected without introducing a strong error in the simulation of dose deposition.

Another approximation in the partial-coupling consists in neglecting bremsstrahlung photons produced by charged secondaries. As shown in Figure 4.17, this approximation is completely justified for a 6 MV photon beam, because no charged secondaries are

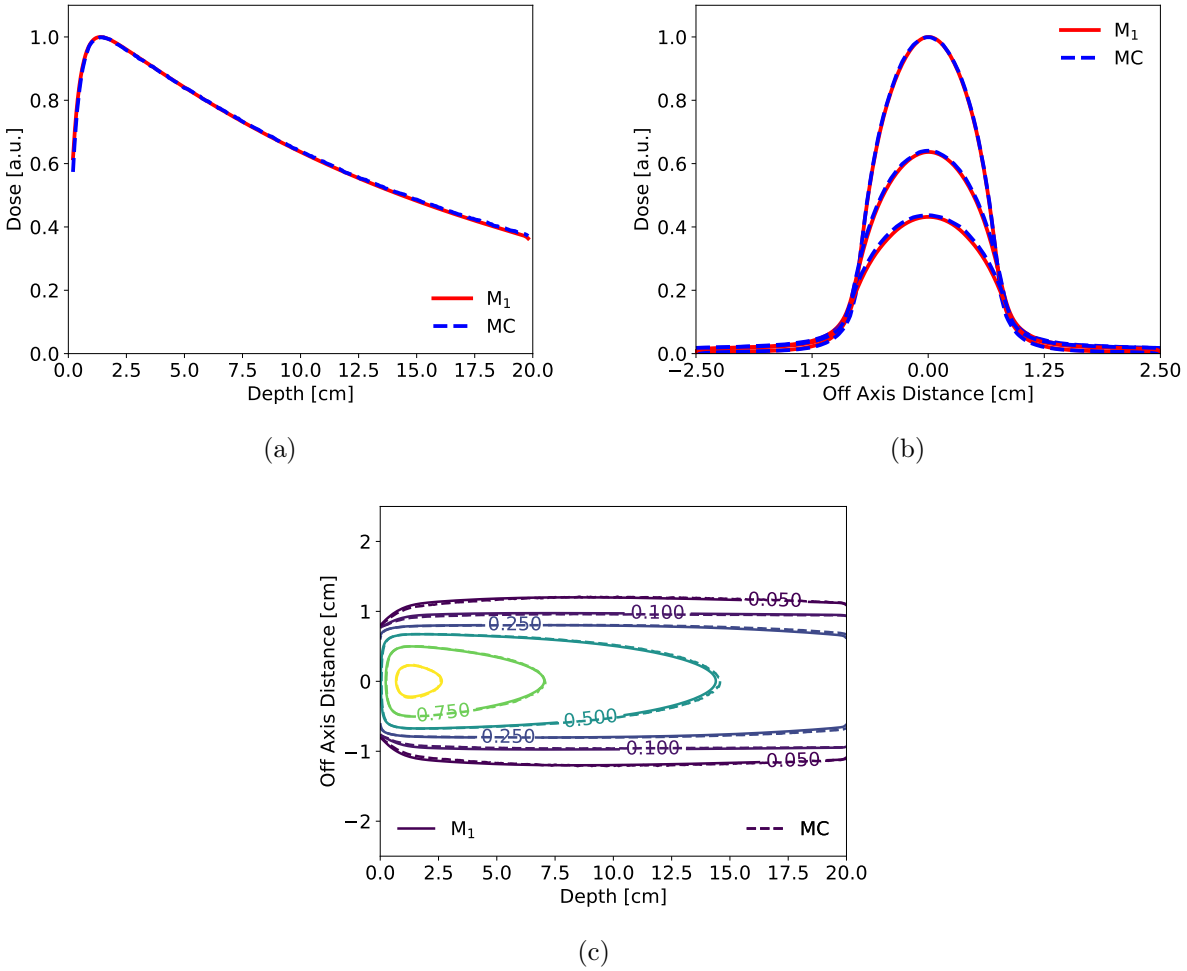

Figure 4.19: Dose calculation performed with the LBTE partial coupling. 6 MV photon beam coming from the left in an homogeneous water phantom: (a) depth dose distribution along the central axis, (b) transverse dose profiles at the center of the beam ($z = 0$) taken at depths of 1.4 cm, 10 cm, 17 cm and (c) 2D isodose map at $z = 0$ in the xy plane. The dose distribution is calculated with a higher accuracy.

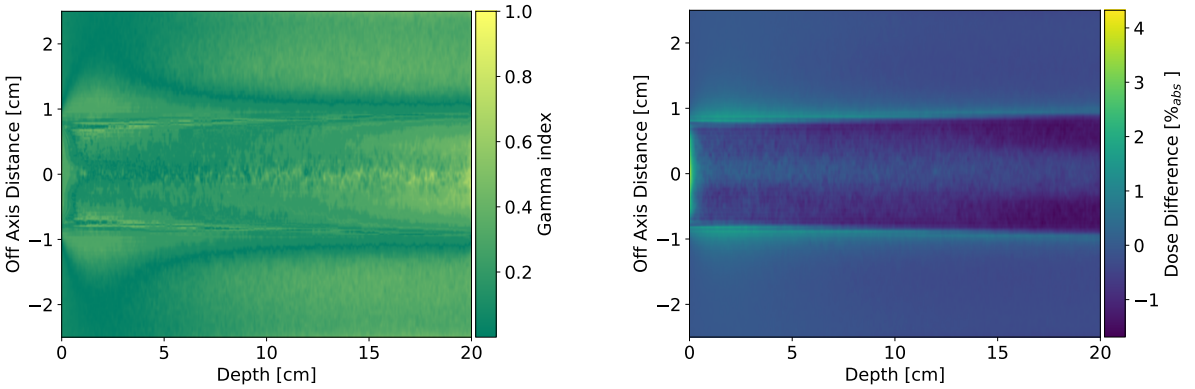

(a) (b)

Figure 4.20: Dose calculation performed with the LBTE partial coupling. 6 MV photon beam coming from the left in an homogeneous water phantom: (a) γ-index map showing the results of the 1%/1 mm criterion and (b) spatial distribution of the dose differences between the Monte Carlo and M_1 simulations. The γ-index is respected in the whole domain. The map of dose differences shows that the level of accuracy of the partial coupled solution is comparable with the full coupled solution.

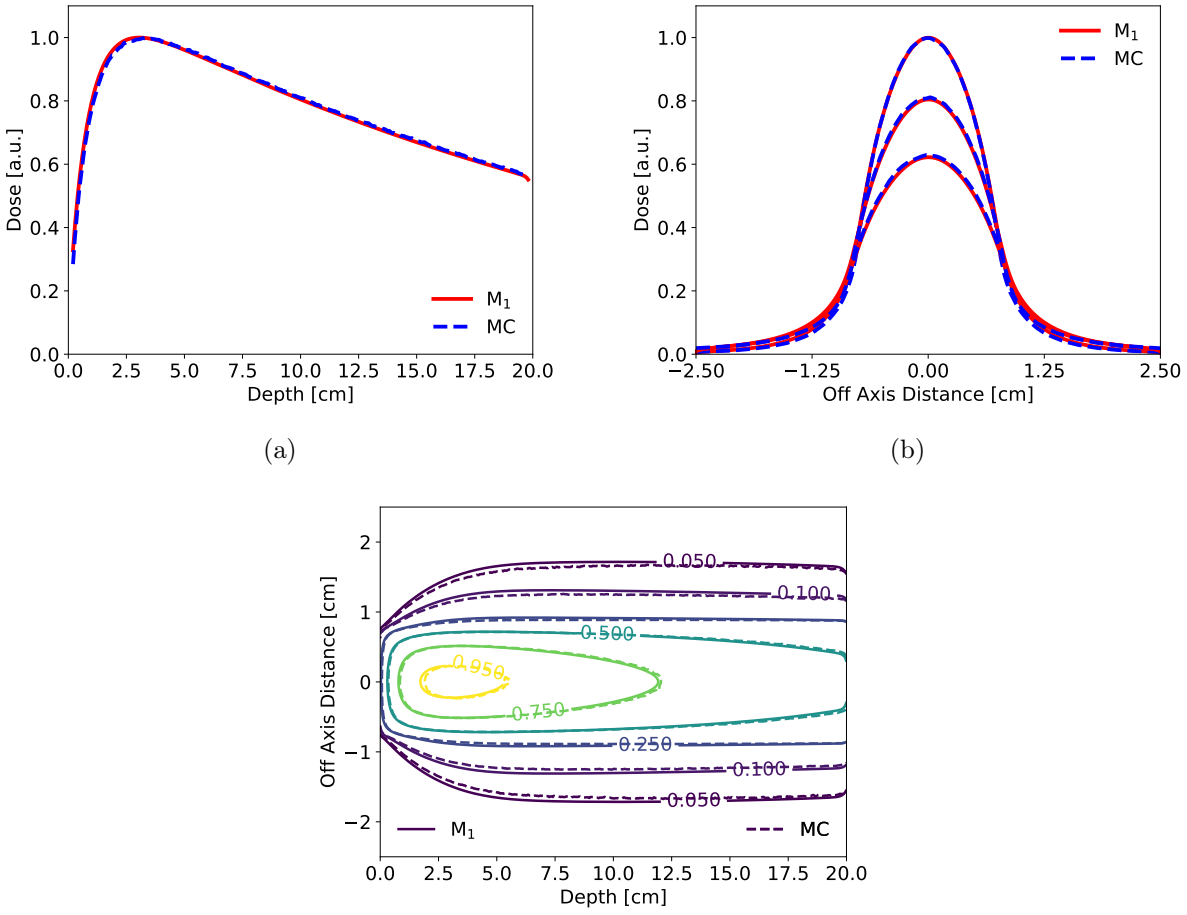

Figure 4.21: Dose calculation performed with the LBTE partial coupling. 18 MV photon beam coming from the left in an homogeneous water phantom: (a) depth dose distribution along the central axis, (b) transverse dose profiles at the center of the beam ($z = 0$) taken at depths of 3.2 cm, 10 cm, 17 cm and (c) 2D isodose map at $z = 0$ in the xy plane.

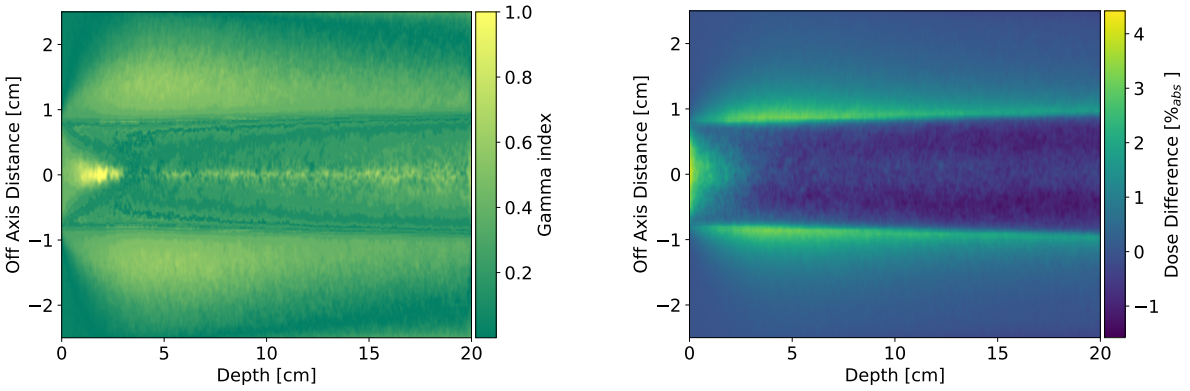

(a) (b)

Figure 4.22: Dose calculation performed with the LBTE partial coupling. 18 MV photon beam coming from the left in an homogeneous water phantom: (a) γ-index map showing the results of the 1%/1 mm criterion and (b) spatial distribution of the dose differences between the Monte Carlo and M_1 simulations. The partial coupling approximation do not affect the precision of the M_1 simulations even for high energy photon beam.

sufficiently energetic to produce bremsstralhung radiation. For a 18 MV photon beam, as shown in Figure 4.18, only a small part of the electron and positron population has sufficient energy to produce bremsstralhung radiation.

As shown in Figures 4.19 and 4.20 for the 6 MV spectrum and in Figures 4.21 and 4.22 for the 18 MV spectrum, these approximations do not affect the accuracy of the calculation. For the 6 MV spectrum, a statistical analysis of the dose difference shows that the mean dose difference between the two simulations is $0.41\% \pm 0.36\%$. The γ-index success rate is 100.%. For the 18 MV spectrum, a statistical analysis of the dose difference shows that the mean dose difference between the two simulations is $0.66\% \pm 0.63\%$. The γ-index success rate is 99.96%. These examples justify the use of simplified cross sections for acceleration of the dose calculation with M_1 code.

4.5.2 Dose distribution with non-uniform energy mesh

In order to push forward the optimization of M1, we investigated the possibility of reduction of the number of energy groups, while preserving the same accuracy in dose calculation. In order to do that, we recall that energy discretization based on the multi-group approach relies on the hypothesis that the total cross sections, see Figure 2.14, remain approximately constant within a group. This means that the total cross section for each particle varies slowly between contigous groups.

Here we propose a non uniform discretization for the energy variable. The energy grids have been calibrated in a way that the total cross section variation between two adjacent groups has to be small. Thus, we impose an upper threshold on the total cross section gradient between two groups. Thanks to this technique we are able to discretize the energy variable is with 21 energy groups for the 6 MV simulations and with 39 energy groups for the 18 MV simulations. This reduction of energy groups represents a strong optimization of the code. For the simulation of the 6 MV spectrum, it allows to reduce the computational time of a factor 14 and the memory allocation of a factor 3.

The results with this optimized non-uniform energy mesh are presented in Figures 4.23 and 4.24 for 6 MV spectrum and in Figures 4.25 and 4.26 for 18 MV spectrum. We observe that the accuracy is preserved for both cases. For 6 MV spectrum, a statistical analysis of the dose difference shows that the mean dose difference between the two simulations is $0.52\% \pm 0.26\%$. The γ-index success rate is 100.%. For 18 MV spectrum, a statistical analysis of the dose difference shows that the mean dose difference between the two simulations is $0.42\% \pm 0.19\%$. The γ-index success rate is 99.91%.

4.6 Conclusion

In this chapter the M_1 model has been validated and optimized by considering a homogeneous phantom. The accuracy of the model has been tested on some specific issues,

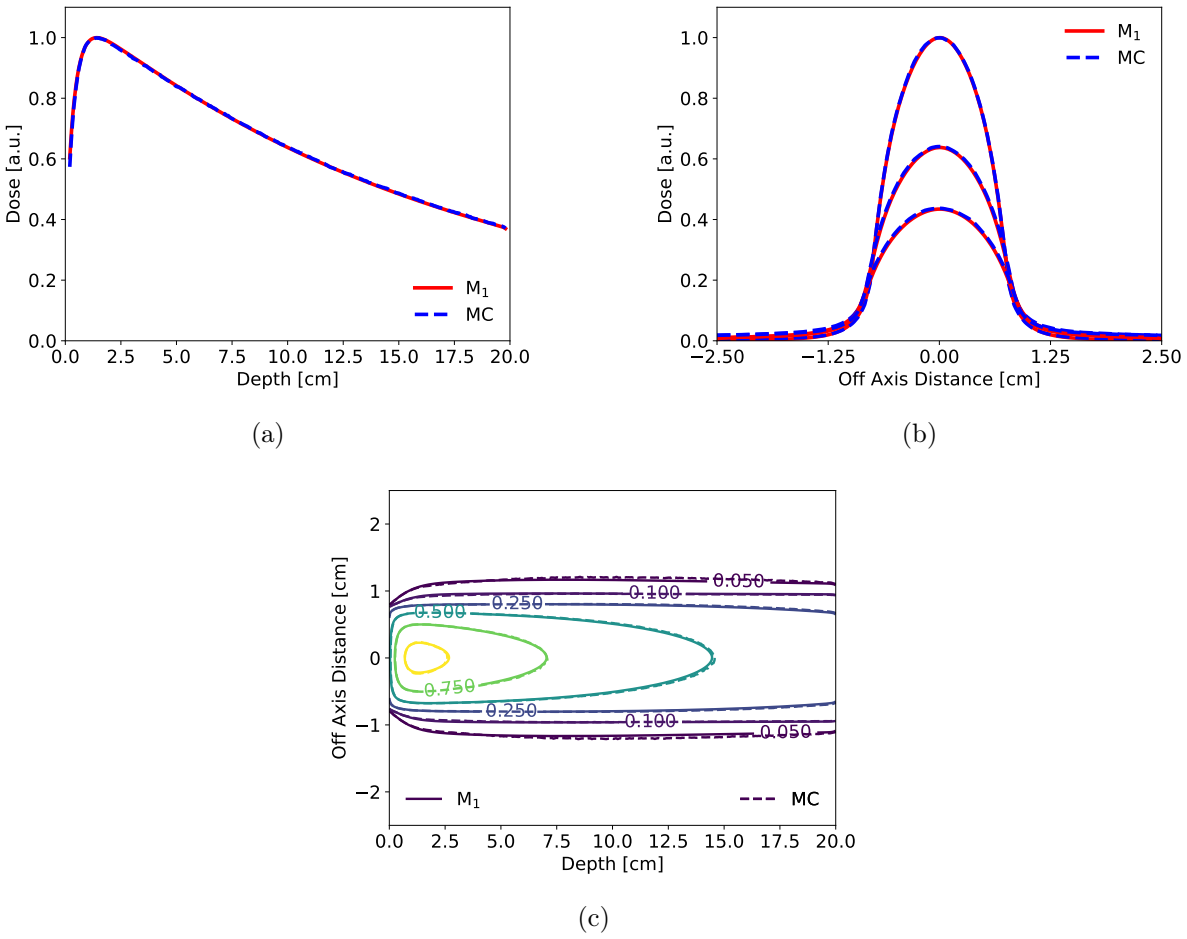

(a)

(b)

(c)

Figure 4.23: Dose calculation performed with non-uniform energy grid. 6 MV photon beam coming from the left in an homogeneous water phantom: (a) depth dose distribution along the central axis, (b) transverse dose profiles at the center of the beam ($z = 0$) taken at depths of 1.4 cm, 10 cm, 17 cm and (c) 2D isodose map at $z = 0$ in the xy plane.

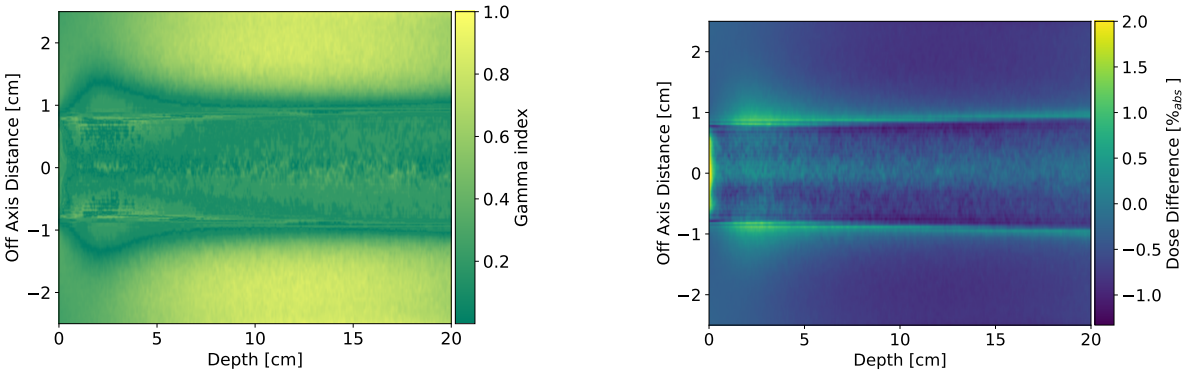

(a) (b)

Figure 4.24: Dose calculation performed with non-uniform energy grid. 6 MV photon beam coming from the left in an homogeneous water phantom: (a) γ-index map showing the results of the 1%/1 mm criterion and (b) spatial distribution of the dose differences between the Monte Carlo and M_1 simulations.

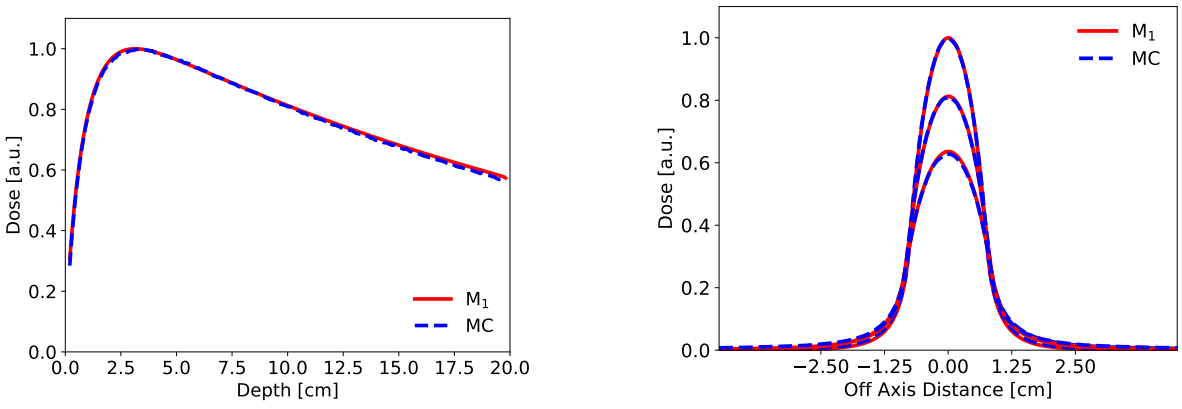

(a) (b)

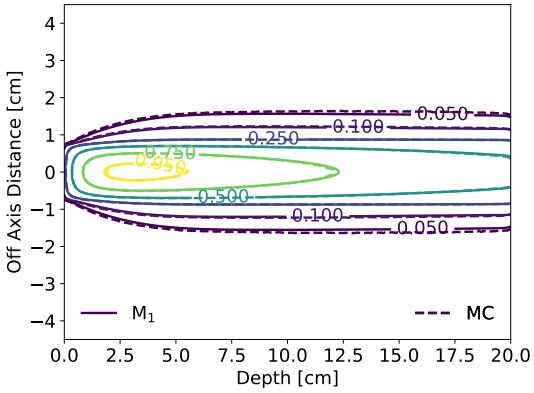

(c)

Figure 4.25: Dose calculation performed with non-uniform energy grid. 18 MV photon beam coming from the left in an homogeneous water phantom: (a) depth dose distribution along the central axis, (b) transverse dose profiles at the center of the beam ($z = 0$) taken at depths of 3.2 cm, 10 cm, 17 cm and (c) 2D isodose map at $z = 0$ in the xy plane.

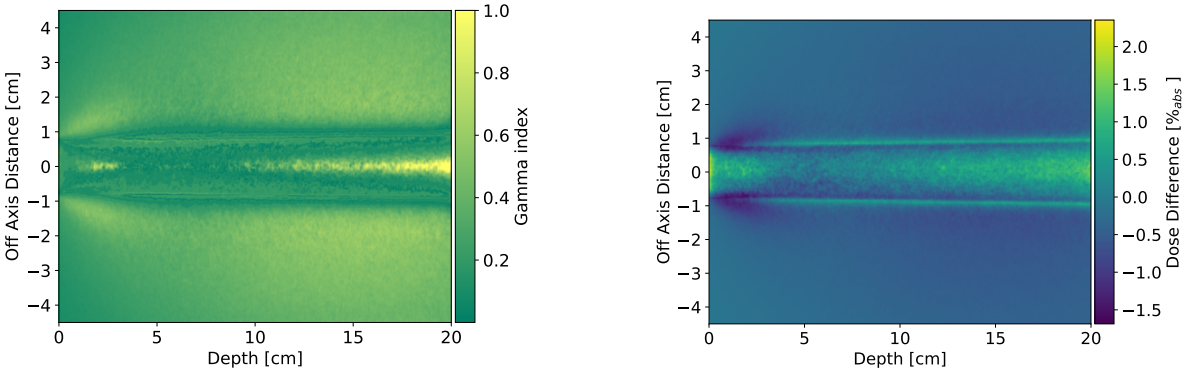

(a) (b)

Figure 4.26: Dose calculation performed with non-uniform energy grid. 18 MV photon beam coming from the left in an homogeneous water phantom: (a) γ-index map showing the results of the 1%/1 mm criterion and (b) spatial distribution of the dose differences between the Monte Carlo and M_1 simulations.

starting from the beam initialization. The analysis has shown that a single anisotropy initialization is not suitable for the description of a realistic beam. The solution of this problem is the initialization of an anisotropy distribution that is directly calculated starting from a Monte Carlo phase-space file. The second important topic is the need of introducing the secondary particle population in order to accurately solve the propagation of a realistic photon beam with a bremsstrahlung spectrum. In the end of the chapter we presented the optimized discretization of the M_1 model. With the introduction of the partial-coupling approximation the model has to be solved for less physical interactions and type of particles. As a last step we have introduced a non-uniform mesh for the energy variable. These optimizations have strongly improved the memory allocation and the calculation time, with a reduction of a factor of ~ 3 and of ~ 14 respectively.

Chapter 5

Validation of the entropic model in heterogeneous phantoms

5.1 Introduction

In the previous chapter we have validated the M1 model in a homogeneous domain, optimizing the memory allocation and the calculation time by adopting the partial-coupling approximation and using a non-uniform energy mesh. In this chapter the model is employed on more complex heterogeneous phantoms. All validation tests are conducted for both 6 MV and 18 MV spectra.

The first phantom geometry is composed of a heterogeneous layer placed in the center of the water phantom, in order to cover the entire beam aperture. This phantom is used to test the accuracy of the model in presence of different materials and simple interfaces. This model is used to consider such materials as water, aluminium, bone and lung.

Once the model is validated on this simple geometry, we introduce more complex configurations. One example is inspired by a work by Fogliata et al. [41] and it is useful to test the accuracy of the M1 model in conditions of a strong lateral electron disequilibrium.

Two more geometries are used to test M1 in more complicated numerical conditions. The first one is inspired by a benckmark for fast Monte Carlo codes [118] and presents a steep density gradient as well as a strong difference in the atomic numbers between two adjacent layers. The last phantom geometry is the most challenging and realistic, since it represents an entire thorax.

5.2 Protocol of comparison

We present here a comparison of the results obtained with M1 model and with the Monte Carlo code PENELOPE. We conduct a study with several test cases, with heterogeneous materials and different geometries.

5.2.1 Source model

We use the source model described in Section 4.5. The M1 model is here validated with both the 6 MV and 18 MV spectra shown in Figure 4.2. In all the test cases, the anisotropy distribution is initialized as explained in Section 4.2.1.2.

5.2.2 Calculation geometry

Here we validate the optimized M1 model for external beam radiotherapy by considering multiple heterogeneous phantom geometries. With this aim, we define more complex geometries, taking inspiration from other works on the validation of medical codes [128, 41, 118, 19]. The calculation domain is defined by a $6 \times 6 \times 20$ cm^2 phantom for the 6 MV spectrum and by a $9 \times 9 \times 20$ cm^2 phantom for the 18 MV spectrum.

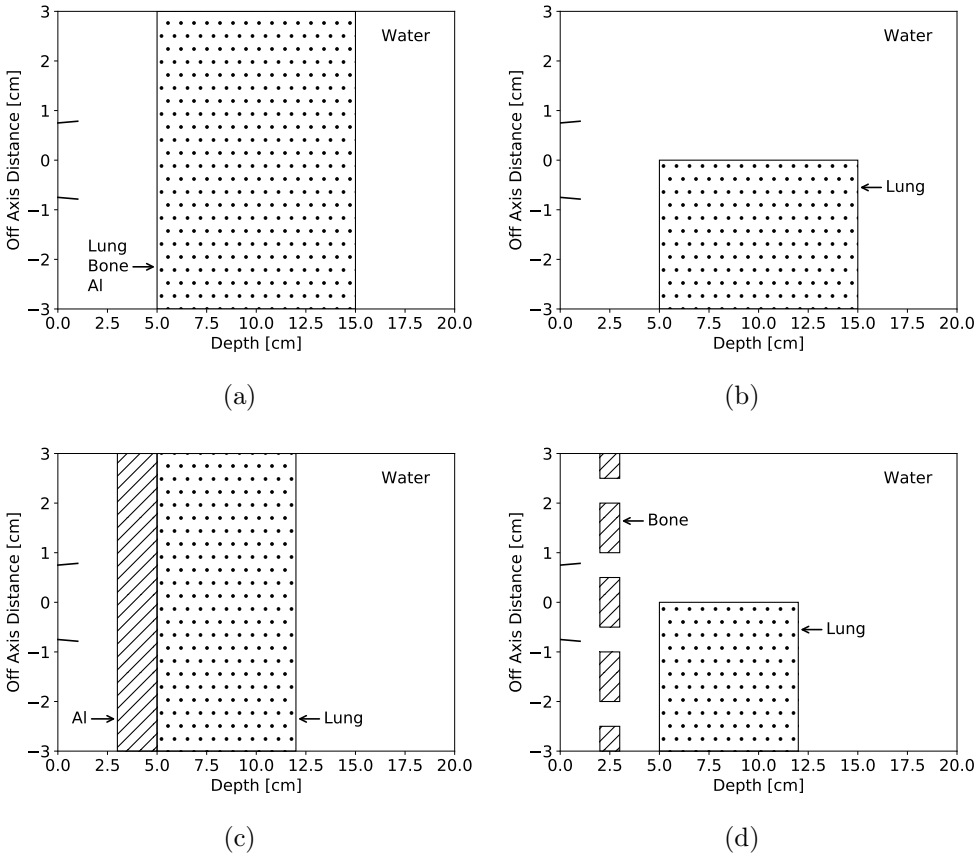

Figure 5.1: Phantoms used for the external photon beam validation: (a) phantom with a single entire heterogeneous slab, (b) phantom with a single half heterogeneous slab, (c) phantom with two heterogeneous slabs and (d) phantom with several heterogeneous slabs.

The first heterogeneity is presented in Figure 5.1(a). It consists of a slab of a material which is different with respect to water in its chemical composition and density and which

covers the entire beam aperture. The slab is 10 cm thick and lies in water between 5 cm and 15 cm in depth. This phantom geometry is useful to verify the ability of the model in accurately solving the transport in different collisional regimes and in handling a discontinuity in the density profile. This test is analyzed in the case of slab made of lung, bone and aluminium.

The second heterogeneity is shown in Figure 5.1(b). It consists in a slab of lung that covers a half of the beam aperture. The slab is 10 cm thick and lies between 5 cm and 15 cm in depth. This phantom allows to verify the accuracy of the M1 model in the case of a strong lateral electron disequilibrium. In particular, in lung the production rate of electrons is lower than in water. At the interface this difference causes an electronic disequilibrium that is difficult to resolve for the models currently used in clinical practice.

The third geometry is presented in Figure 5.1(c). It consists of a slab of water between 0 cm and 3 cm in depth, a slab of aluminium between 3 cm and 5 cm in depth, a slab of lung between 5 cm and 12 cm in depth and another slab of water between 12 cm and 20 cm. The interest in the study of this test is in the sharp gradient of density and in the difference of equivalent atomic numbers between aluminium and lung. This phantom has been proposed at the early stage of the development of optimized Monte Carlo algorithm as benchmark with the full Monte Carlo codes [118].

The last geometry that we consider is the most challenging one, since it collects all the difficulties of the previous cases. It is composed of a water phantom where a spinal is simulated with several bone inserts of 1 cm^3 is placed at 2.5 cm in depth and with a distance of 2 cm from the half lung slab.

Here we focus on several specific materials commonly used in the radiotherapy applications. The biological materials, water (1.0 g/cm^3), lung (0.26 g/cm^3) and bone (1.85 g/cm^3) are defined with their proper chemical composition. As an example of non-biological materials, used for prosthesis implants, aluminium (2.7 g/cm^3) is considered. In Table 5.1 the complete list of these materials with their chemical composition in terms of fraction by weight of each element and density is reported.

	Composition [fraction by weight]	Density [$g \cdot cm^{-3}$]
Water	H 0.111898, O 0.888102	1.
Cortical Bone (ICRU-44)	H 0.034000, C 0.155000, N 0.042000, O 0.435000, Na 0.001000, Mg 0.002000, P 0.103000, S 0.003000, Ca 0.225000	1.85
Lung (ICRU-44)	H 0.103000, C 0.105000, N 0.031000, O 0.749000, Na 0.002000, P 0.002000, S 0.003000, Cl 0.003000, K 0.002000	0.26
Aluminium	Al 1.	2.7

Table 5.1: Table of the materials with their chemical composition and density [141].

5.2.3 Numerical parameters of simulations

For the simulations that are analysed in the present chapter, the M1 model is solved by adopting the same spatial discretization of the domain and the same energy range and discretization introduced in Section 4.2.3.1. Also the cut-off energy imposed in the Monte Carlo code is the one discussed in Section 4.2.3.2.

5.3 Dose distribution in presence of a single insert

We begin our analysis by analyzing three different tests for both 6 MV and 18 MV spectra with the simple heterogeneous geometry shown in Figure 5.1(a). These tests allow us to verify the capability of the M1 model to treat the transport of particles and the dose deposition in different collisional regimes. Moreover, they represent a first validation of the model ability in handling a simple discontinuity in the density profile. We simulate all the three materials used for heterogeneities, i. e. lung, bone and aluminium.

5.3.1 Lung slab

As a first step in the validation process, we test an heterogeneity composed by lung (for its chemical compostition and density see Table 5.1). The main interest of this case is related to the strong density gradients occurring at the interfaces. Moreover, in the lung, the mean free path of the electrons generated by the photon beam is longer than in water. For this reason, this case is useful to test precision of the model in handling the transport of the charged particles in a low density material.

The M1 code is able to accurately calculate the transport of the particles and the consequent spreading of dose deposition in lung as shown in Figures 5.2(b) and 5.2(c) for the 6 MV spectrum and in Figures 5.4(b) and 5.4(c) for the 18 MV spectrum. Moreover, M1 well captures the second build-up that is present after the insert as shown in Figures 5.2(a) and 5.4(a). In 18 MV case M1 model overestimates the dose deposition on the beam axis in the lung heterogeneity. However an underestimation of the dose is observed off the primary beam in lung.

The deficit of dose in the heterogeneity shown in Figures 5.2(a) and 5.4(a) is well known in literature [75, 88, 135]. With decreasing material density, the range and the lateral spread of the secondary electrons are increased. Moreover, especially for small field size, a consistent number of secondary electrons travel outside the geometrical limits of the photon beam. This causes the enlargement of the beam penumbra in the underdense material as shown in Figures 5.2(c) and 5.4(c). Further, for higher energy beam the electron disequilibrium is stronger due to the higher energy of the charged secondaries. This results in a stronger lack of dose on the beam axis. Moreover, the lack of scattering for primary photons in lung results in a new build-up when radiation penetrates through the water region after the lung slab.

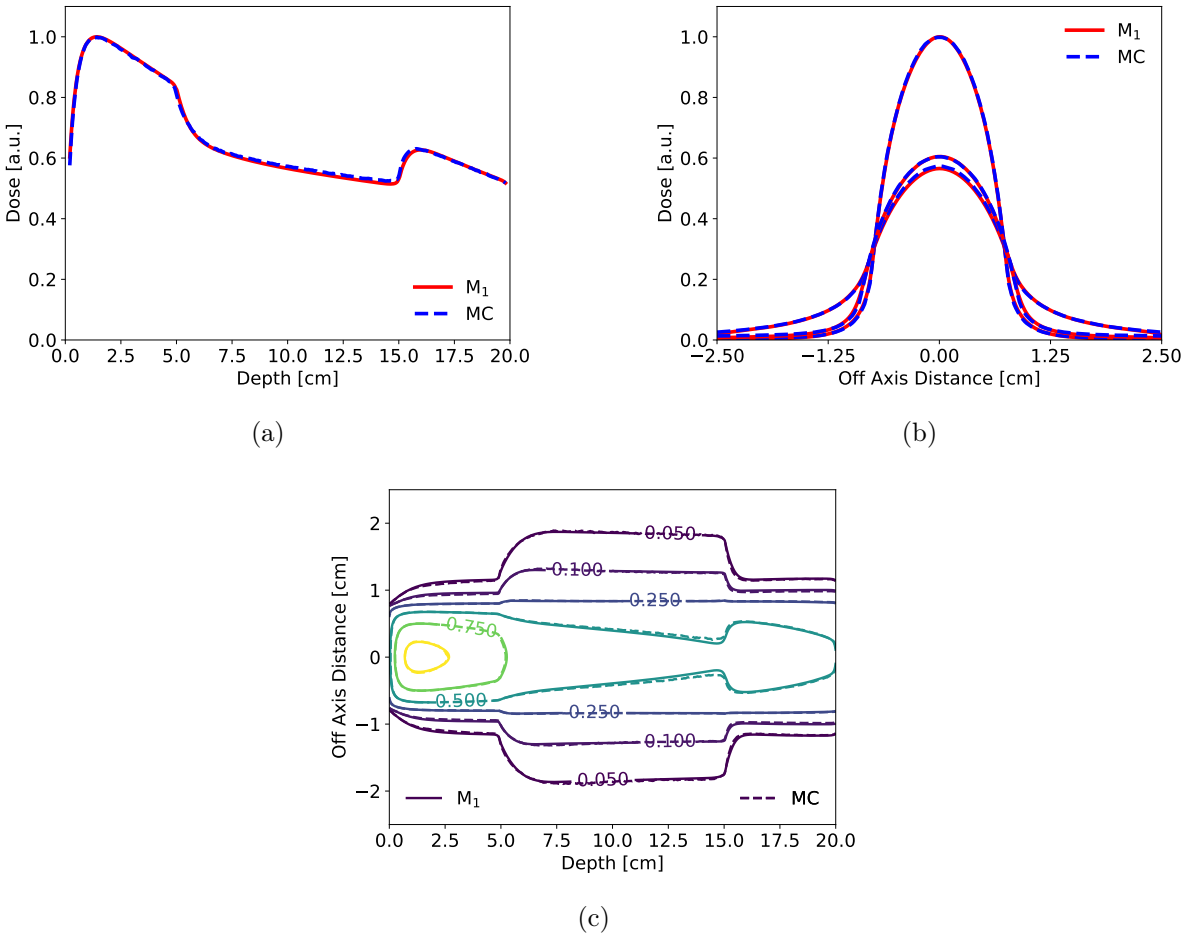

Figure 5.2: 6 MV photon beam coming from the left in a water phantom with a lung insert between 5 cm and 15 cm: (a) depth dose distribution along the central axis, (b) transverse dose profiles at the center of the beam ($z = 0$) taken at depths of 1.4, 10 and 17 cm and (c) 2D isodose map at $z = 0$ in the xy plane. The M1 model reproduces with high accuracy the dose deposition calculated by the Monte Carlo simulation. The lack of dose on the beam axis and the enlargement of beam penumbra due to the spread of electrons in lung is reproduced with precision. The second build-up in last water layer is accurately resolved.

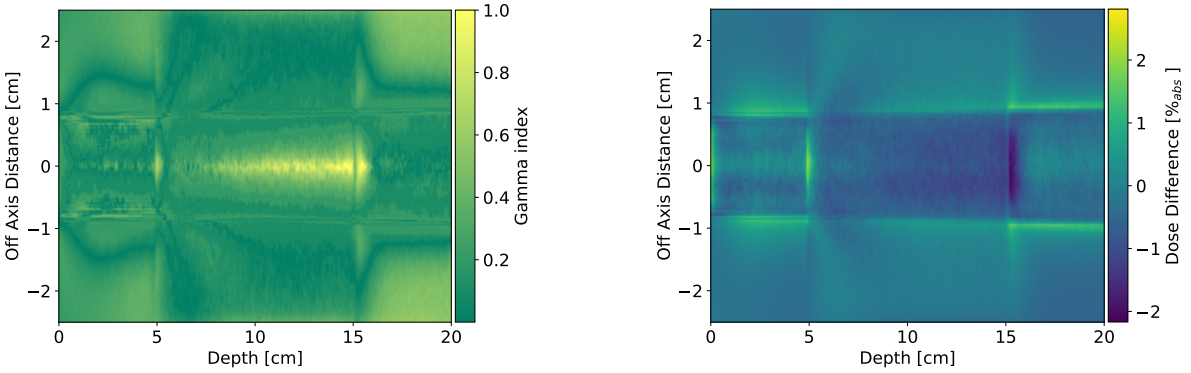

(a) (b)

Figure 5.3: 6 MV photon beam coming from the left in a water phantom with a lung insert between 5 cm and 15 cm: (a) γ-index map showing the results of the 1%/1 mm criterion and (b) spatial distribution of the dose differences between the Monte Carlo and M1 simulations. The γ-test is respected for the 99.98% of the points in the domain. The dose difference map shows that the maximum of the discrepacies is reached at the heterogeneity interfaces. The dose differences remain in the range of 3% in whole domain.

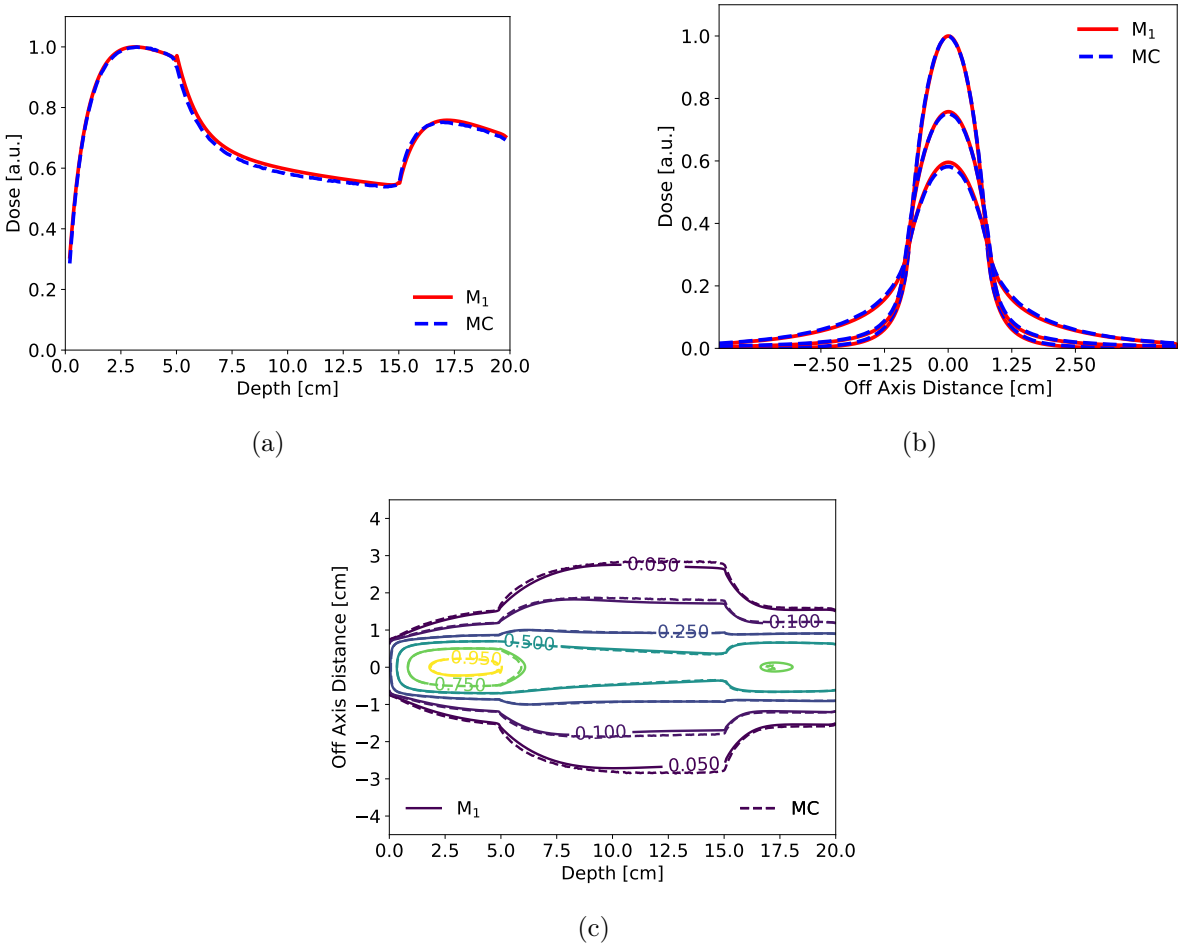

Figure 5.4: 18 MV photon beam coming from the left in a water phantom with a lung insert between 5 cm and 15 cm: (a) depth dose distribution along the central axis, (b) transverse dose profiles at the center of the beam ($z = 0$) taken at depths of 3.2, 10 and 17 cm and (c) 2D isodose map at $z = 0$ in the xy plane. M1 keeps a good accuracy in the calculation of dose deposition as shown in the 2D isodose map. However, in lung, it slightly overestimates the dose deposition on the beam axis. At this overdose on beam axis corresponds an underestimation on the lateral dose deposition in lung.

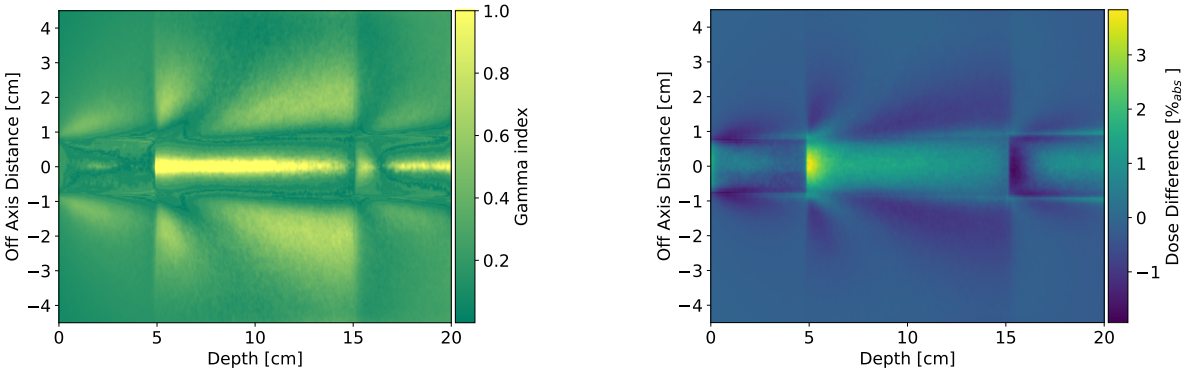

(a) (b)

Figure 5.5: 18 MV photon beam coming from the left in a water phantom with a lung insert between 5 cm and 15 cm: (a) γ-index map showing the results of the 1%/1 mm criterion and (b) spatial distribution of the dose differences between the Monte Carlo and M1 simulations. The γ-test is respected for 98.91% of the points in the domain. The most important discrepancy appears at the first interface between lung and water where the dose difference reach 3.7%.

In case of a 6 MV beam, the 99.98% of the points in the domain respect the γ-index criterion for $1\% - 1\,\text{mm}$ (see Figure 5.3(a)), whereas for the 18 MV beam, the γ-index success rate is 98.91% (see Figure 5.5(a)). For the 6 MV spectrum, a statistical analysis of the dose difference (see Figure 5.3(b)) shows that the mean dose difference between the two simulations is $0.34\% \pm 0.30\%$, whereas for the 18 MV spectrum is $0.41\% \pm 0.36\%$ (see Figure 5.5(b)).

5.3.2 Bone slab

We now present the second test case, in which the heterogeneity is represented by a 10 cm bone insert. As for the test of the previous section, we have to deal with two simple interfaces. However, the physical phenomena occurring during the simulation are different.

In Figures 5.6 - 5.7 and 5.8 - 5.9 the results are shown respectively for the 6 MV and 18 MV spectra. As shown in Figures 5.6(c) and 5.8(c), the M1 model accurately simulates the lack of lateral diffusion in the insert. This phenomenon is mainly due to the higher density of the bone. An interesting behaviour of the dose deposition appears at the first interface of the heterogeneity. In Figures 5.6(a) and 5.8(a), we can observe a peak of dose reaching the maximum at the interface. Moreover, for the 18 MV spectrum, we can observe in Figure 5.8(a) a new build up in the heterogeneity. Let us now explain in detail these phenomena appearing before and after the interface.

In this case, as in the previous one, the material interface is represented by a strong difference in the density. Moreover, the two materials are different in their equivalent atomic number. Since we are dealing with cold matter and since the particles have a relativistic energy, we can consider the materials as a compound of atoms. We consider a compound composed by N elements in which the molecules consist of x_i atoms of element X_i, for i=1,..,N. The number of electrons per molecule is $Z_M = \sum_{i=1}^{N} x_i Z(X_i)$ and the molar mass is $A_M = \sum_{i=1}^{N} x_i A(X_i)$, where $Z(X_i)$ is the atomic number of element X_i and $A(X_i)$ is its atomic weight. By considering an equivalent single element material with the same mass density as the actual medium, the atomic number Z_{eq} is given by the following relation [121]:

$$Z_{eq} = \frac{\sum_{i=1}^{N} x_i Z(X_i) A(X_i)}{A_M}. \tag{5.1}$$

This means that the equivalent atomic number is the mass average of the atomic numbers of the constituent atoms. Thus we get that $Z_{eq,H2O} \simeq 7.22$ and $Z_{eq,Bone} \simeq 10.63$. The difference between equivalent atomic numbers of these two materials is more prominent with respect to the materials considered in the test case of Section 5.3.1, where $Z_{eq,Lung} \simeq 7.14$.

In order to explain the behaviour of the dose before the interface it is important to take into account this difference. Indeed, the difference of the two materials Z_{eq} has an impact on the cross section of photons. Specifically the photoelectric cross section is a

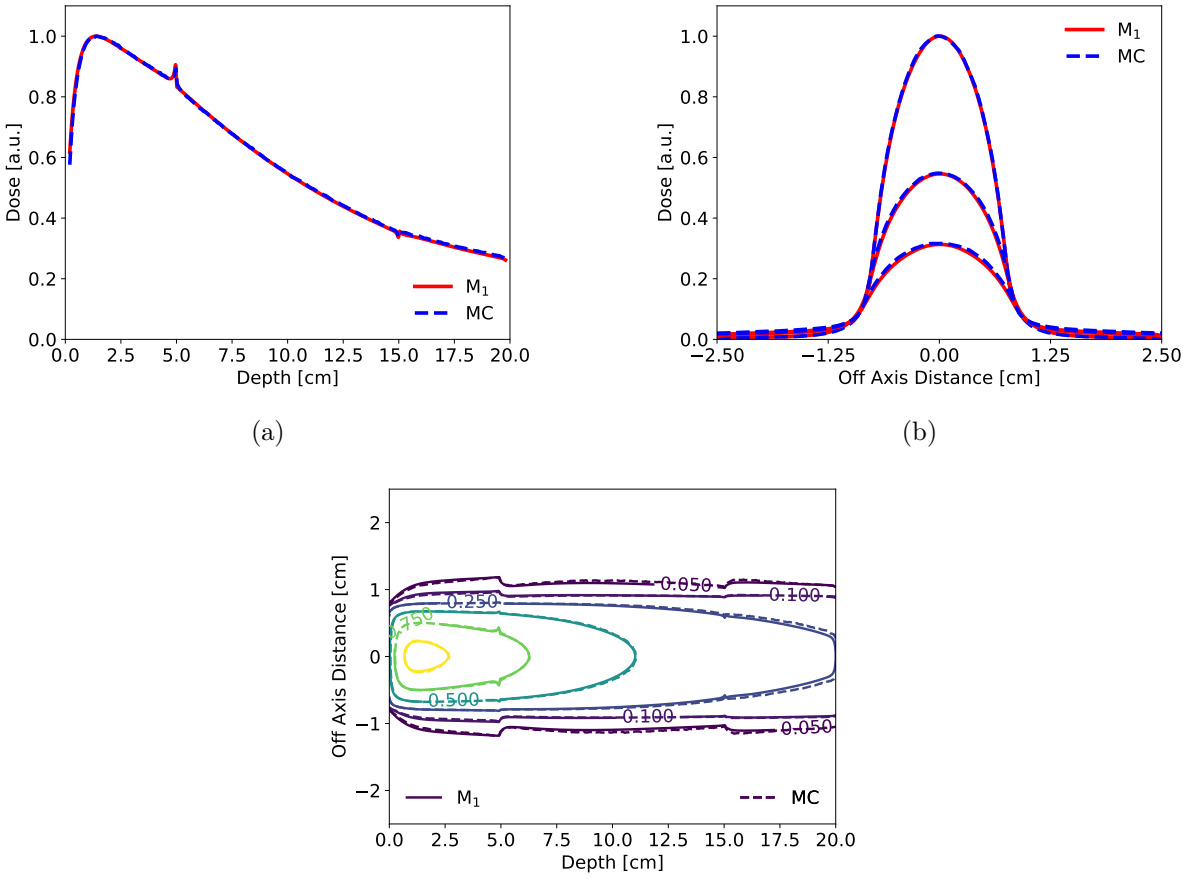

Figure 5.6: 6 MV photon beam coming from the left in a water phantom with a bone insert between 5 cm and 15 cm: (a) depth dose distribution along the central axis, (b) transverse dose profiles at the center of the beam ($z = 0$) taken at depths of 1.4, 10 and 17 cm and (c) 2D isodose map at $z = 0$ in the xy plane. The M1 model reproduces with a high accuracy the dose distribution in the whole domain. On the depth dose profile we can notice that our model correctly reproduces the changement of the slope in bone. This is due to the higher absorption coefficient of bone with respect to water. Moreover the discontinuities at the heterogeneity interfaces are correctly reproduced.

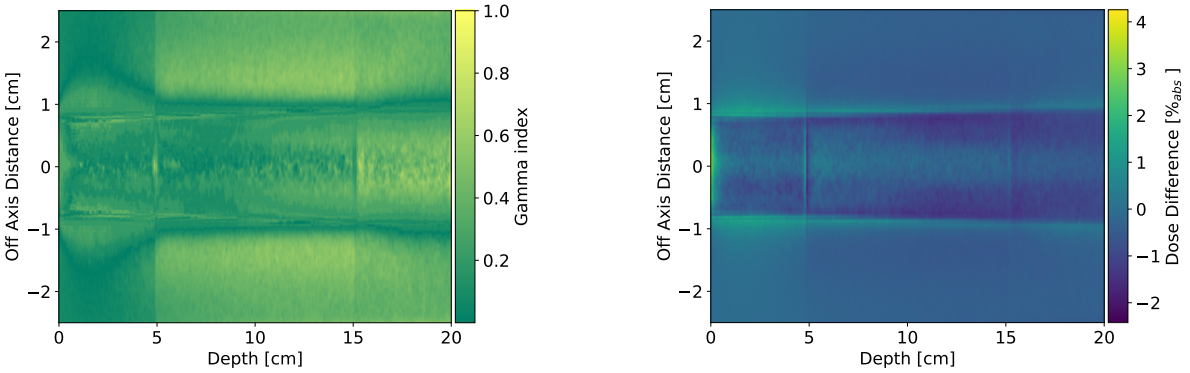

(a) (b)

Figure 5.7: 6 MV photon beam coming from the left in a water phantom with a bone insert between 5 cm and 15 cm: (a) γ-index map showing the results of the 1%/1 mm criterion and (b) spatial distribution of the dose differences between the Monte Carlo and M1 simulations. The γ-test is satisfied in the whole domain. The dose difference map show a high agreement between the two curves with exception of the first millimiters where the dose difference reach the 4%.

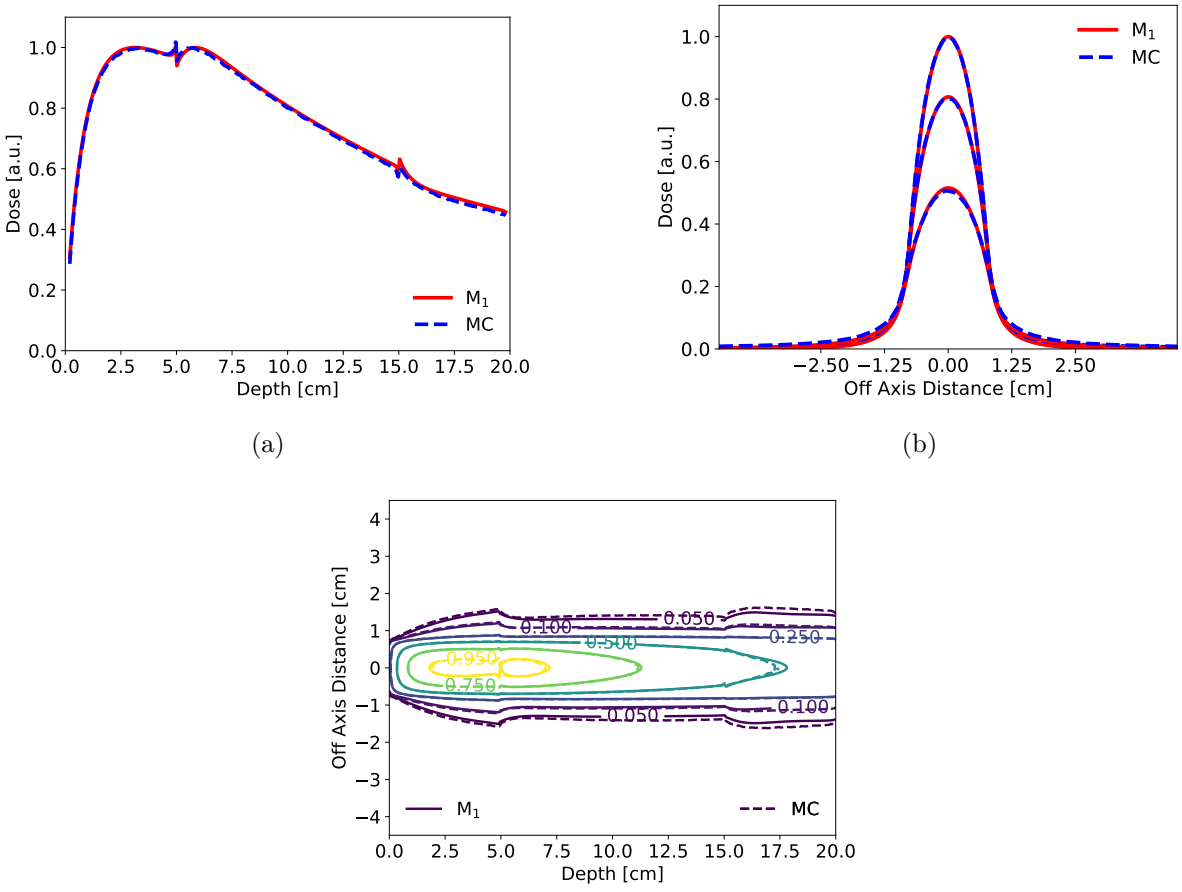

Figure 5.8: 18 MV photon beam coming from the left in a water phantom with a bone insert between 5 cm and 15 cm: (a) depth dose distribution along the central axis, (b) transverse dose profiles at the center of the beam ($z = 0$) taken at depths of 3.2, 10 and 17 cm and (c) 2D isodose map at $z = 0$ in the xy plane. In this case the M1 model is slightly less diffusive than the Monte Carlo code. In depth dose profile our model reproduces the second build-up after the first interface in bone but overestimates the discontinuity at the second interface.

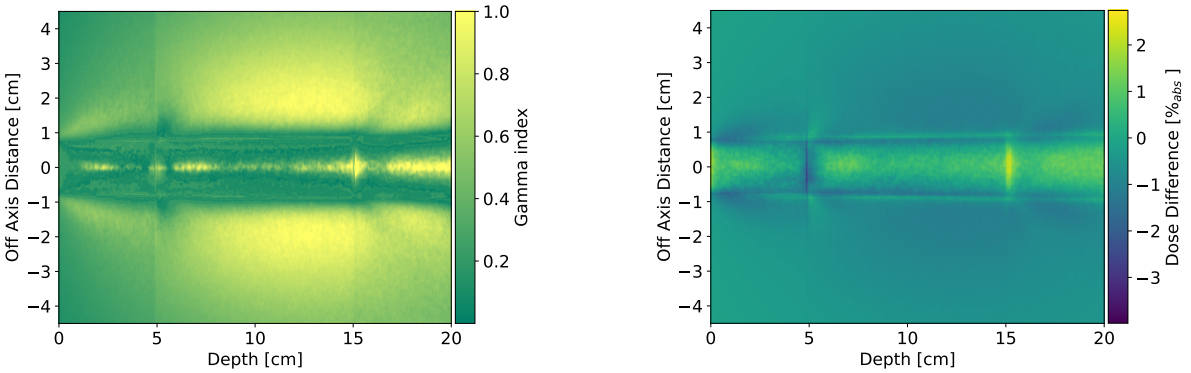

(a) (b)

Figure 5.9: 18 MV photon beam coming from the left in a water phantom with a bone insert between 5 cm and 15 cm: (a) γ-index map showing the results of the 1%/1 mm criterion and (b) spatial distribution of the dose differences between the Monte Carlo and M1 simulations.

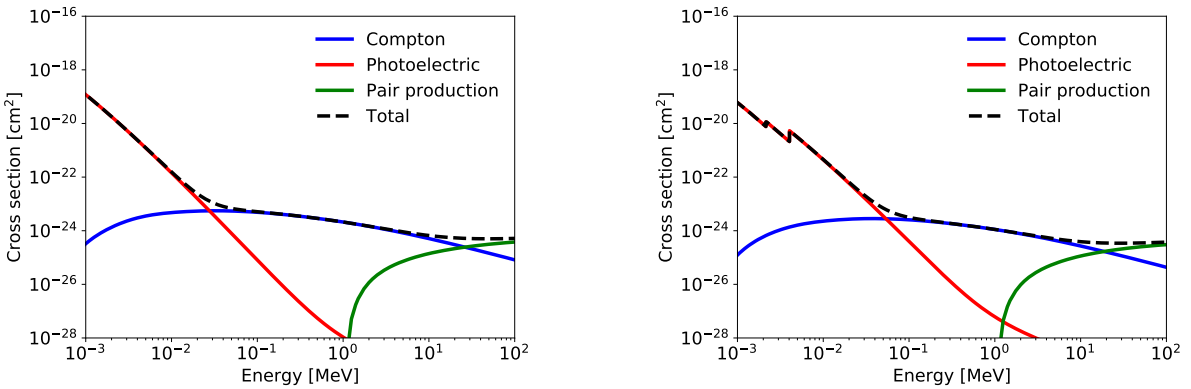

(a) Total cross section for photons in water

(b) Total cross section for photons in bone

Figure 5.10: Plots of the total cross section for photons in water (a) and in bone (b). Data from the Monte Carlo code PENELOPE with permission.

function of Z^5 (see Equation (2.17)). Comparing the cross sections calculated for the two materials, see Figures 5.10(a) and 5.10(b), we can observe that the photoelectric effect becomes significant for higher energies in bone with respect to water. Such an effect is characterized by a quasi-isotropic emission of photoelectrons. This means that a part of those photoelectrons that are generated at the bone surface can be backscattered in water. This is the reason of the peak of dose generated before the interface. The opposite behaviour is observed at the second interface. Here, a lack of secondary electrons coming from the water layer causes a depletion of the dose just behind the interface.

Another interesting phenomenon is the build-up that can be observed in Figure 5.8(a). This effect can be explained as follows. As explained in Chapter 2, the macroscopic cross section is related to the microscopic cross section through the relation $\sigma_{\text{ma}} = \frac{N_A \rho}{A} \sigma_{\text{mi}}$. If we consider the total cross section, this quantity is commonly called 'attenuation coefficiant'. The attenuation coefficient gives also an information on the production rate of electrons, due to the fact that all the interactions taken into account produce charged secondaries. The production rate of electrons in the bone is larger than in water. For this reason, the condition of equilibrium in the bone is reached only after 1 cm for the 18 MV photon beam, due to the high energy of the produced electrons.

Concerning the results presented in Figures 5.7 and 5.9, in the case of 6 MV beam, the 100% of the points in the domain respect the γ-index criterion for $1\% - 1\,\text{mm}$ (see Figure 5.7(a)), whereas for the 18 MV beam, the γ-index success rate is 99.65% (see Figure 5.9(a)). For the 6 MV spectrum, a statistical analysis of the dose difference (see Figure 5.7(b)) shows that the mean dose difference between the two simulations is $0.46\% \pm 0.32\%$, whereas for the 18 MV spectrum is $0.63\% \pm 0.28\%$ (see Figure 5.9(b)). The M1 model simulate with high accuracy all the physical processes described above for both spectra. A small overestimation of the dose at the second interface can be observed for the 18 MV spectrum. The lack of lateral diffusion of secondary electrons in bone correctly reproduced.

5.3.3 Aluminium slab

We now solve the same test with a non-biological insert, aluminium. The difference of the equivalent atomic number between the two materials in this geometry, is here even more pronounced, since $Z_{al} = 13$. For this reason, this case presents an amplification of the peaks at the interfaces, a stronger gradient on the dose deposition and smaller lateral spread of the dose in the aluminium (see Figures 5.11 - 5.12 and 5.13 - 5.14).

In the case of the 6 MV beam, the 100% of the points in the domain respect the γ-index criterion for $1\% - 1\,\text{mm}$ (see Figure 5.12(a)), whereas for the 18 MV beam, the γ-index success rate is 90.92% (see Figure 5.14(a)). For the 6 MV spectrum, a statistical analysis of the dose difference (see Figure 5.12(b)) shows that the mean dose difference between the two simulations is $0.41\% \pm 0.30\%$, whereas for the 18 MV spectrum is $0.73\% \pm 0.38\%$ (see Figure 5.14(b)). The 18 MV case fails the γ-test mostly in regions outside the primary

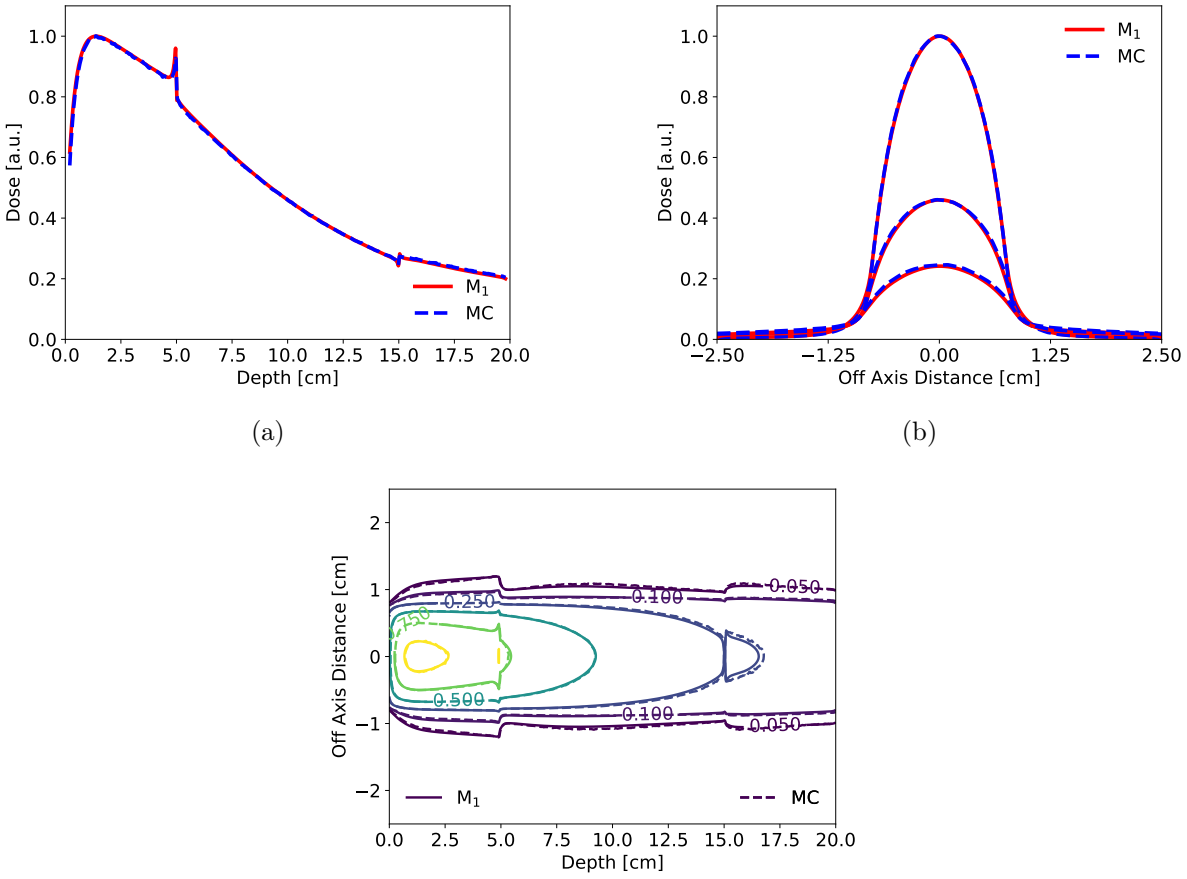

Figure 5.11: 6 MV photon beam coming from the left in a water phantom with a aluminium insert between 5 cm and 15 cm: (a) depth dose distribution along the central axis, (b) transverse dose profiles at the center of the beam ($z = 0$) taken at depths of 1.4, 10 and 17 cm and (c) 2D isodose map at $z = 0$ in the xy plane. This simulation is characterized by the presence of a strong density gradient and a higher difference in equivalent atomic number between water and the insert. The M1 model reproduces with a high precision the dose distribution calculated with PENELOPE. Only at the first interface an overestimation of dose can be noticed.

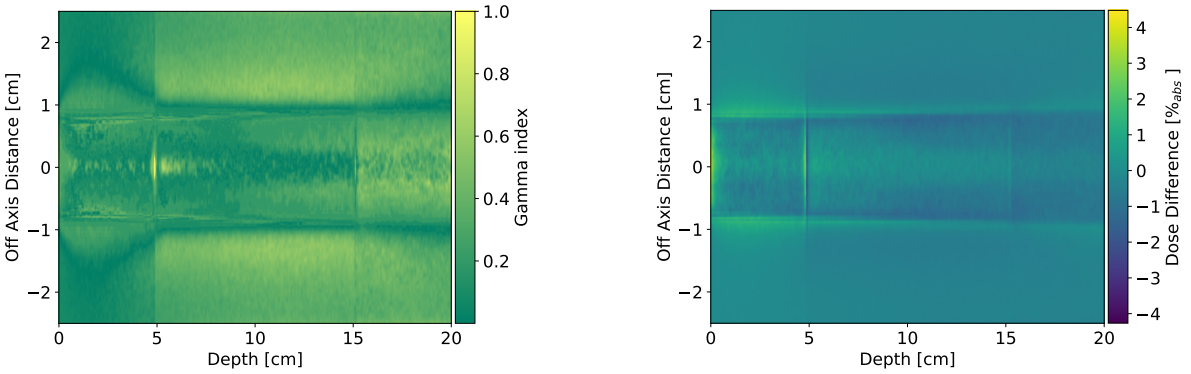

(a) (b)

Figure 5.12: 6 MV photon beam coming from the left in a water phantom with a aluminium insert between 5 cm and 15 cm: (a) γ-index map showing the results of the 1%/1 mm criterion and (b) spatial distribution of the dose differences between the Monte Carlo and M1 simulations. The γ-test is respected in 100% of the points in the domain.

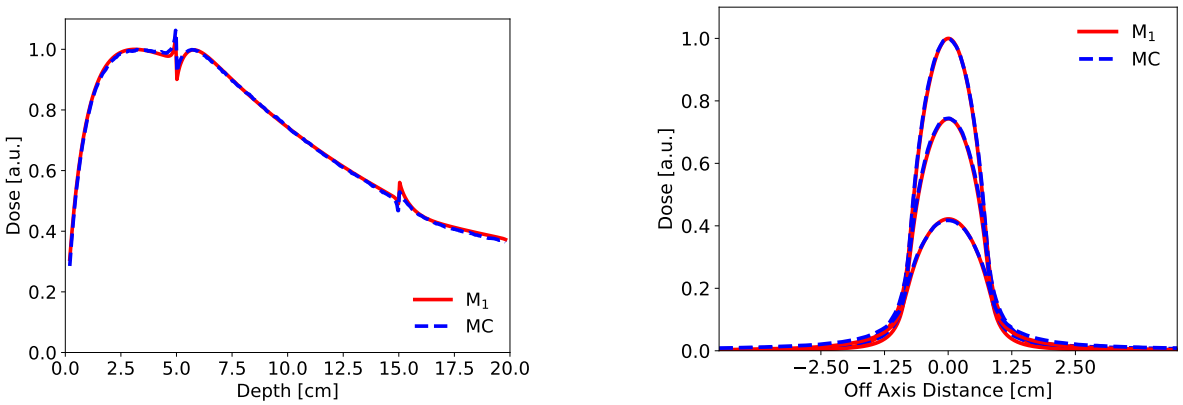

Figure 5.13: 18 MV photon beam coming from the left in a water phantom with a aluminium insert between 5 cm and 15 cm: (a) depth dose distribution along the central axis, (b) transverse dose profiles at the center of the beam ($z = 0$) taken at depths of 3.2, 10 and 17 cm and (c) 2D isodose map at $z = 0$ in the xy plane.

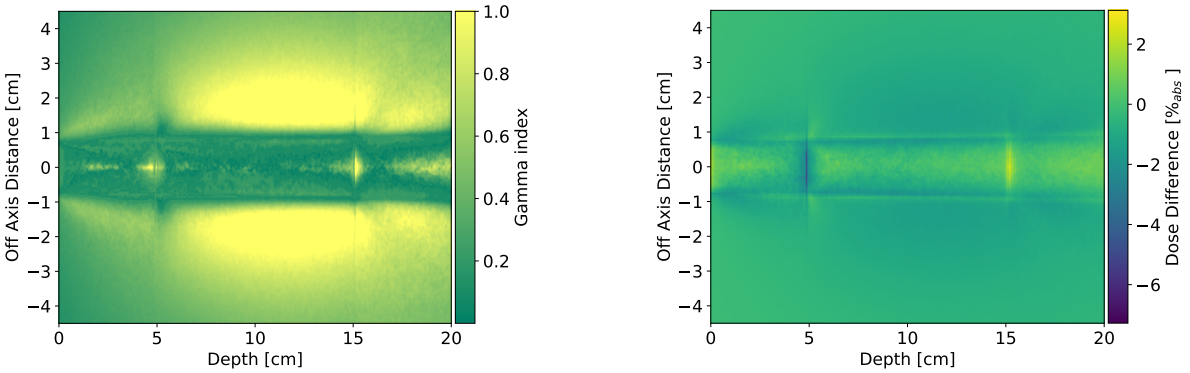

(a) (b)

Figure 5.14: 18 MV photon beam coming from the left in a water phantom with a aluminium insert between 5 cm and 15 cm: (a) γ-index map showing the results of the 1%/1 mm criterion and (b) spatial distribution of the dose differences between the Monte Carlo and M1 simulations. In this case the γ-test is respected only for 90.92% of the points. It can be noticed that the regions where the test fails are in the aluminium insert and outside the geometrical aperture of the beam where the contribution of more diffused secondaries is important. Probably a better discretization of the energy variable would solve this problem. However it is worthwhile to notice that for a dosimetric viewpoint, this dose difference in aluminium would not have an impact on the quality of the treatment.

beam aperture in aluminium. This discrepancy is mainly due to a lack of precision in treatment of secondaries for higher atomic number materials. A better discretized energy domain could improve the result. However, this discrepancy do not have an impact on the precision outside the heterogeneity.

5.4 Dose distribution in presence of a half width insert

We now analyse a test with a single half width insert of lung. This test demonstrates the behaviour of the M1 model in presence of an interface along the beam axis. At the interface the lateral electron disequilibrium is considerable and the model has to handle along the beam propagation two different physical regimes. In lung the production rate of secondary electrons is three-times lower than in water. Moreover the mean free path of electrons in lung is larger than in water. For this reason, the charged particles flux in voxels near the interface is not compensate and electron disequilibrium is strong.

In the 6 MV case the model accurately reproduces the dose distribution that has been calculated with PENELOPE as shown in Figures 5.15 and 5.16. However, for the 18 MV spectrum a non negligible dose difference is present at the interface along the beam axis as it follows by observing Figures 5.17 and 5.18. In the case of 6 MV beam, the 100% of the points in the domain respect the γ-index criterion for $1\% - 1\,\text{mm}$ (see Figure 5.16(a)), whereas for the 18 MV beam, the γ-index success rate is 98.93% (see Figure 5.18(a)). For 6 MV spectrum, a statistical analysis of the dose difference (see Figure 5.16(b)) shows that the mean dose difference between the two simulations is $0.38\% \pm 0.25\%$, whereas for 18 MV spectrum is $0.42\% \pm 0.42\%$ (see Figure 5.18(b)).

5.5 Dose distribution in presence of a double heterogeneity insert

In this section we present a test case where the two materials with the largest difference in atomic number and density are adjacent. Even if this case cannot represent a realistic configuration, it is of interest in order to analyse possible limitations of the M1 model. These limitations can rise at the interface between aluminium and lung due to the strongly different physical regimes in these materials. Indeed, aluminium is characterized to be a diffusive material for the photon population while the electrons have a range between 10^{-5} cm and 1.5 cm. On the other hand in the lung material, having a lower Z_{eq}, a lower diffusion of photons occurs and the electrons have a larger range.

For both the 6 MV and 18 MV spectra the treatment of the aluminium/lung interface shows an overdose with respect to the Monte Carlo simulation. This can be due to a numerical oscillation that can be reduced with more advanced numerical techniques. Despite this difference, M1 accurately reproduces the Monte Carlo simulation in the rest

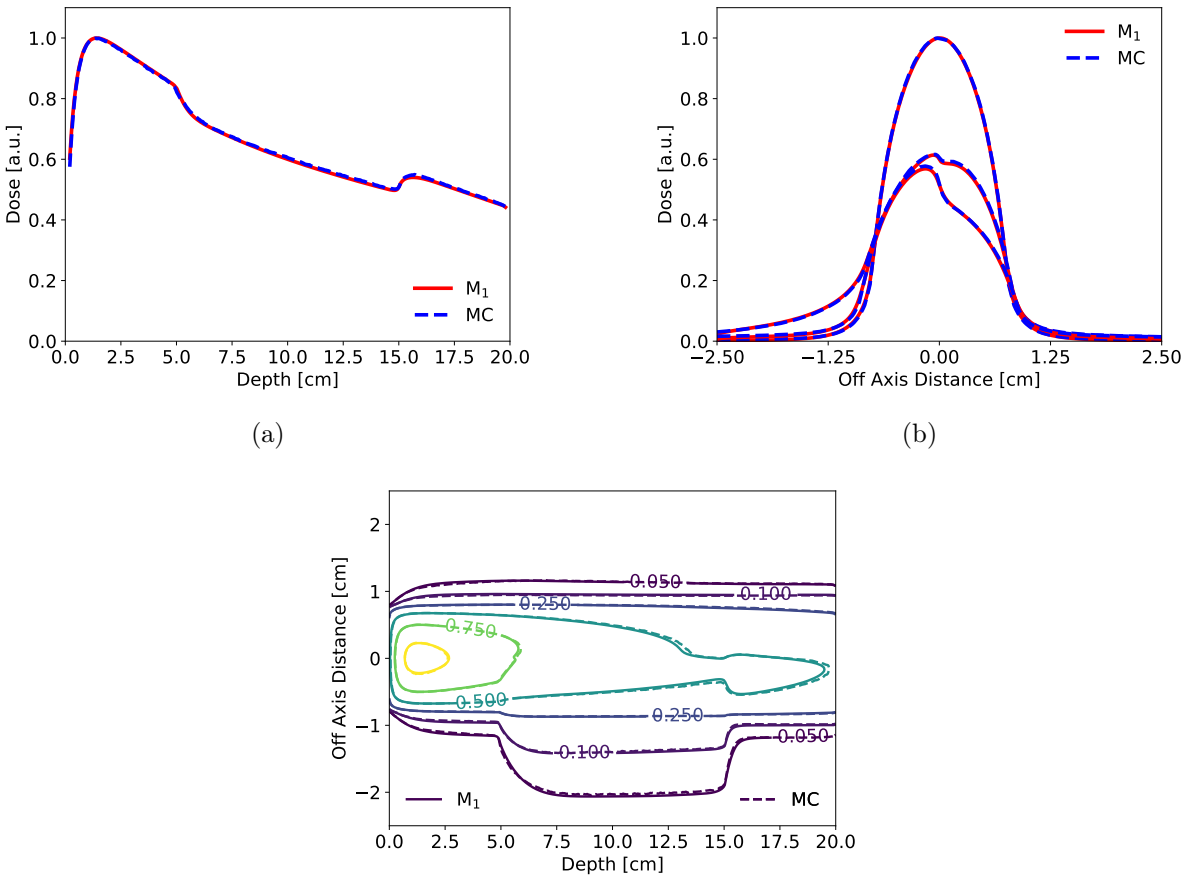

Figure 5.15: 6 MV photon beam coming from the left in a water phantom with a half lung insert between 5 cm and 15 cm: (a) depth dose distribution along the central axis, (b) transverse dose profiles at the center of the beam ($z = 0$) taken at depths of 1.4, 10 and 17 cm and (c) 2D isodose map at $z = 0$ in the xy plane. The M1 model preserve the accuracy demostrated in case of entire slab. The depth dose profile shows a high accuracy even along the heterogeneity interface.

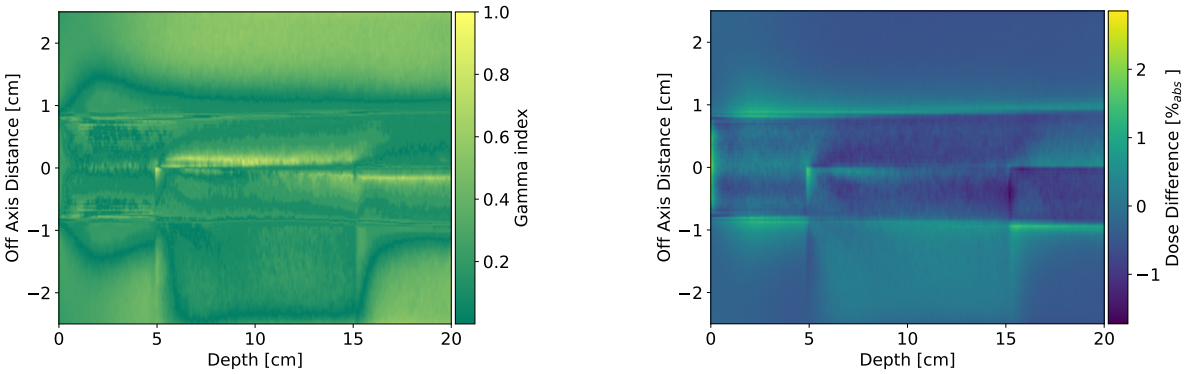

(a) (b)

Figure 5.16: 6 MV photon beam coming from the left in a water phantom with a half lung insert between 5 cm and 15 cm: (a) γ-index map showing the results of the 1%/1 mm criterion and (b) spatial distribution of the dose differences between the Monte Carlo and M1 simulations.

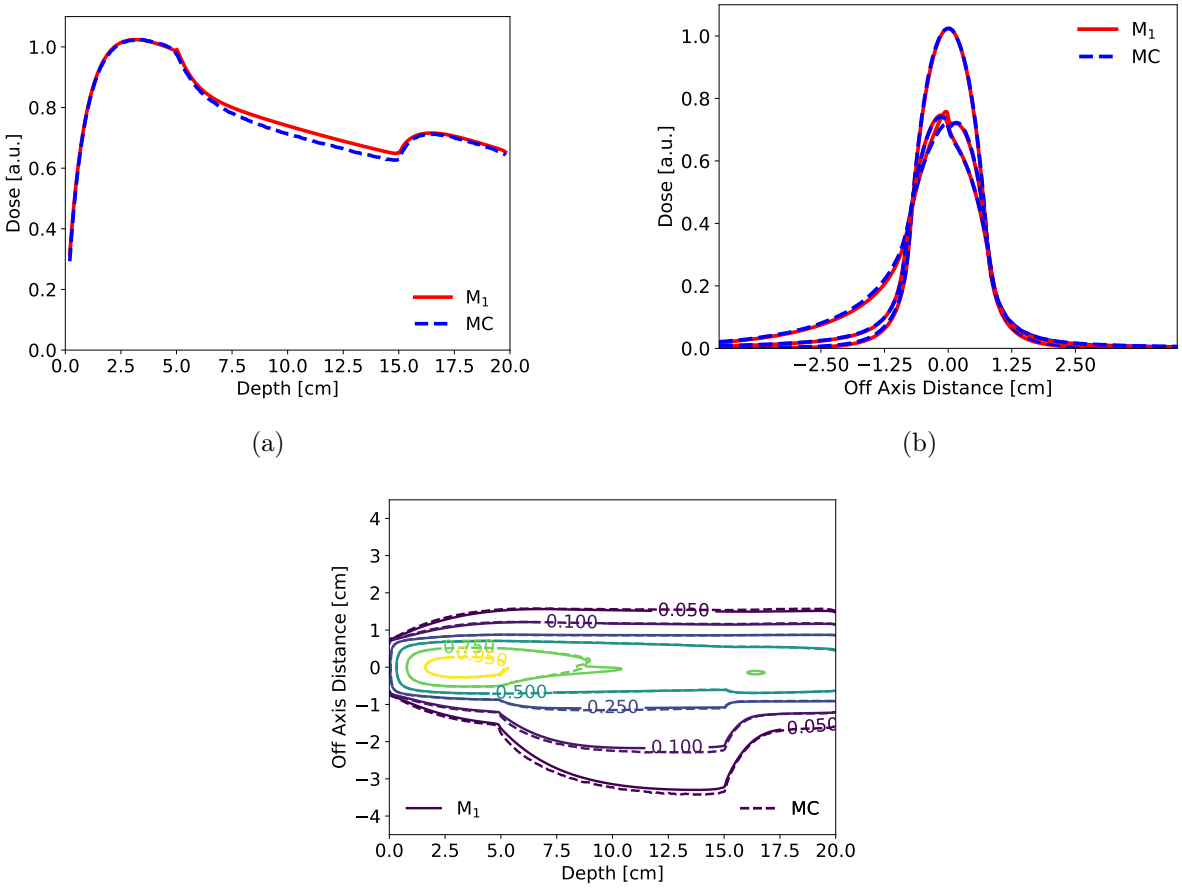

Figure 5.17: 18 MV photon beam coming from the left in a water phantom with a half lung insert between 5 cm and 15 cm: (a) depth dose distribution along the central axis, (b) transverse dose profiles at the center of the beam ($z = 0$) taken at depths of 3.2, 10 and 17 cm and (c) 2D isodose map at $z = 0$ in the xy plane. In this case the M1 simulation shows a discrepancy in the depth dose profile along the heterogeneity interface. However, as shown on the lateral profiles, this discrepancy is limited to the region of the interface and do not affect the rest of the domain.

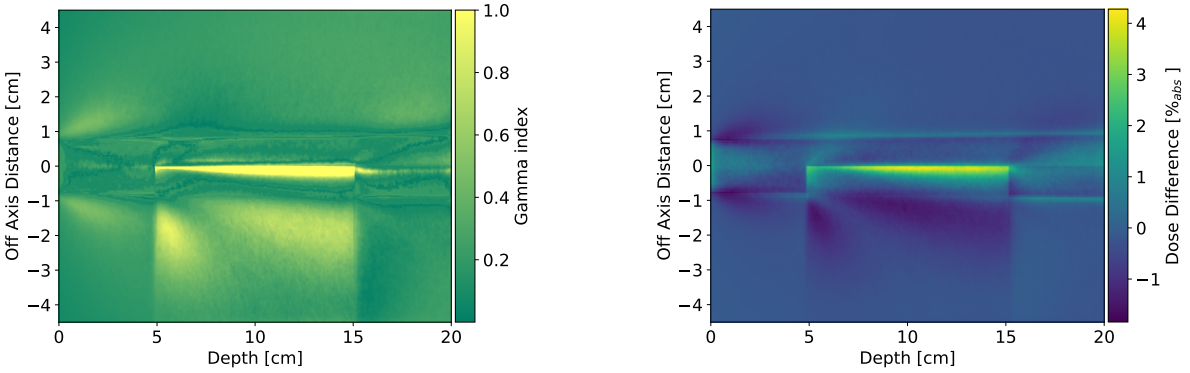

(a) (b)

Figure 5.18: 18 MV photon beam coming from the left in a water phantom with a half lung insert between 5 cm and 15 cm: (a) γ-index map showing the results of the 1%/1 mm criterion and (b) spatial distribution of the dose differences between the Monte Carlo and M1 simulations. The γ-test fails along the interface on the central axis of the beam where the dose difference is stronger. Probably a better discretization of the energy variable would increase the precision of the M1 model.

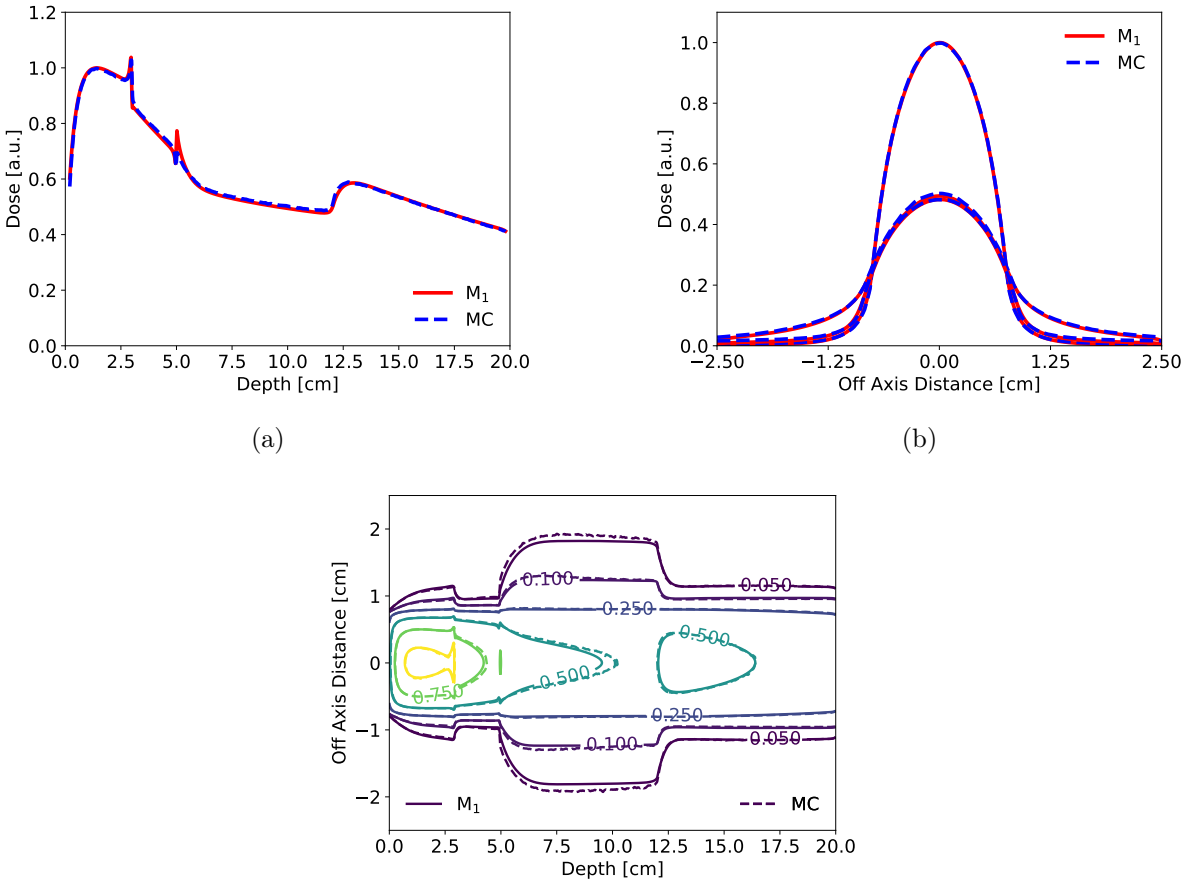

Figure 5.19: 6 MV photon beam coming from the left in a water phantom with a double heterogeneity made of aluminium between 3 cm and 5 cm and lung between 5 cm and 12 cm: (a) depth dose distribution along the central axis, (b) transverse dose profiles at the center of the beam ($z = 0$) taken at depths of 1.4, 10 and 17 cm and (c) 2D isodose map at $z = 0$ in the xy plane. In this case the density gradient is emphasised at the interface between aluminium and lung inserts. The M1 model calculates with a good accuracy the dose distribution in all the domain but demonstrates some difficulties in the resolution of this interface. An improved numerical scheme would increase the precision on the resolution of this kind of interface.

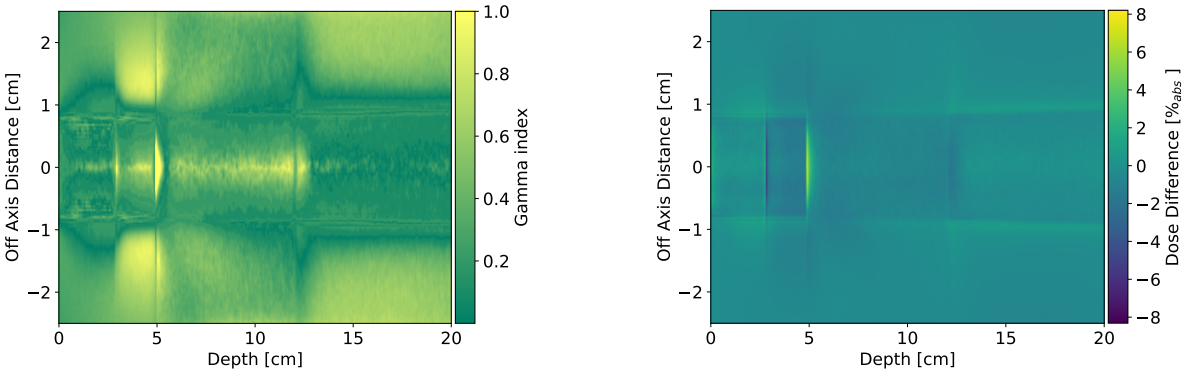

(a) (b)

Figure 5.20: 6 MV photon beam coming from the left in a water phantom with a double heterogeneity made of aluminium between 3 cm and 5 cm and lung between 5 cm and 12 cm: (a) γ-index map showing the results of the 1%/1 mm criterion and (b) spatial distribution of the dose differences between the Monte Carlo and M1 simulations. The γ-test is satisfied for 99.85% of the points in the domain.

of the domain, as shown in Figures 5.19 - 5.20 and 5.21 - 5.22. In the case of 6 MV beam, the 99.85% of the points in the domain respect the γ-index criterion for $1\% - 1\,\text{mm}$ (see Figure 5.20(a)), whereas for the 18 MV beam, the γ-index success rate is 99.66% (see Figure 5.22(a)). For 6 MV spectrum, a statistical analysis of the dose difference (see Figure 5.20(b)) shows that the mean dose difference between the two simulations is $0.53\% \pm 0.41\%$, whereas for 18 MV spectrum is $0.46\% \pm 0.56\%$ (see Figure 5.22(b)).

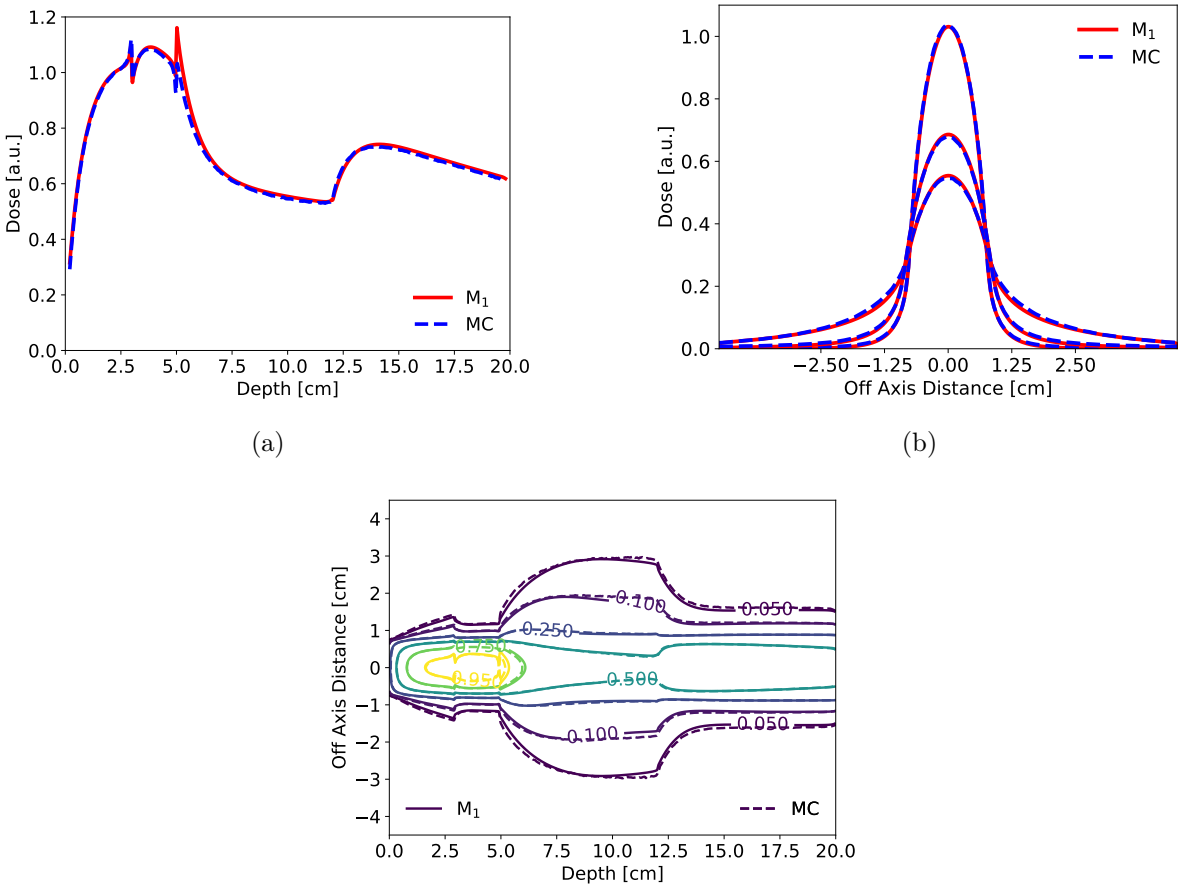

Figure 5.21: 18 MV photon beam coming from the left in a water phantom with a double heterogeneity made of aluminium between 3 cm and 5 cm and lung between 5 cm and 12 cm: (a) depth dose distribution along the central axis, (b) transverse dose profiles at the center of the beam ($z = 0$) taken at depths of 3.2, 10 and 17 cm and (c) 2D isodose map at $z = 0$ in the xy plane. The aluminium-lung interface as in the previous case represents a difficulty for our model. The difference in the treatment of this interface between the two codes is grater than before. This fact suggests that the problem could be attributed a bad treatment of secondary electrons at the interface.

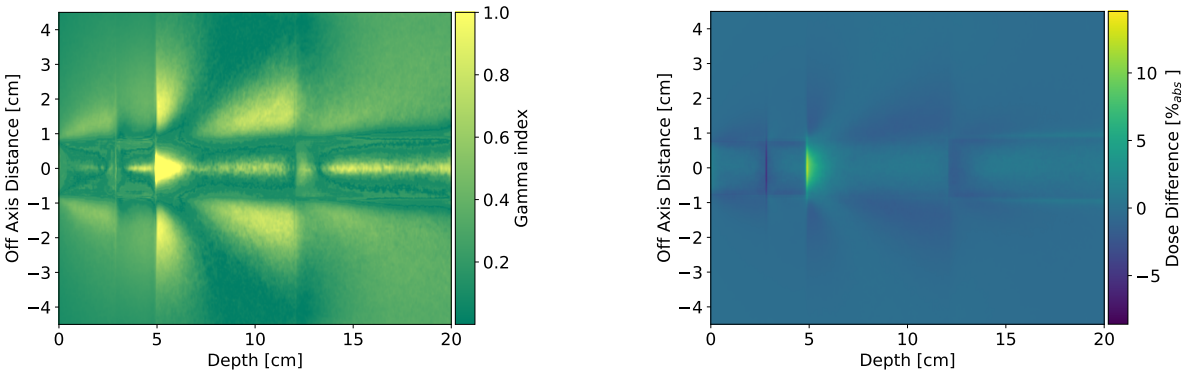

(a) (b)

Figure 5.22: 18 MV photon beam coming from the left in a water phantom with a double heterogeneity made of aluminium between 3 cm and 5 cm and lung between 5 cm and 12 cm: (a) γ-index map showing the results of the 1%/1 mm criterion and (b) spatial distribution of the dose differences between the Monte Carlo and M1 simulations. The success rate of γ-test is 99.66%.

5.6 Dose distribution in a complex geometry

The last test we perform consists in a geometry where all the difficulties of the previous cases are included. Due to the presence of the spinal heterogeneity composed by cubes smaller than the field size, the model has to handle interfaces that have a complex shape. As expected, the model reproduces with a good accuracy the dose distribution calculated with PENELOPE with the same discrepancies analyzed in the previous sections. In the case of 6 MV beam, the 99.96% of the points in the domain respect the γ-index criterion for $1\% - 1\,\text{mm}$ (see Figure 5.24(a)), whereas for the 18 MV beam, the γ-index success rate is 99.57% (see Figure 5.26(a)). For 6 MV spectrum, a statistical analysis of the dose difference (see Figure 5.24(b)) shows that the mean dose difference between the two simulations is $0.51\% \pm 0.32\%$, whereas for 18 MV spectrum is $0.60\% \pm 0.50\%$ (see Figure 5.26(b)).

5.7 Conclusion

In this chapter the M1 model has been validated in heterogeneous tests. We have shown that the model is accurate in all the proposed configurations. In all 6 MV beam simulations the M1 results are in very good agreement with the PENELOPE simulations, whereas for the 18 MV cases the accuracy can still be improved especially at the interfaces with lung. In particular, improvements of the energy variable discretization and the introduction of more accurate numerical schemes for the spatial discretization could reduce the highlighted discrepancies . However, all the presented results confirm that M1

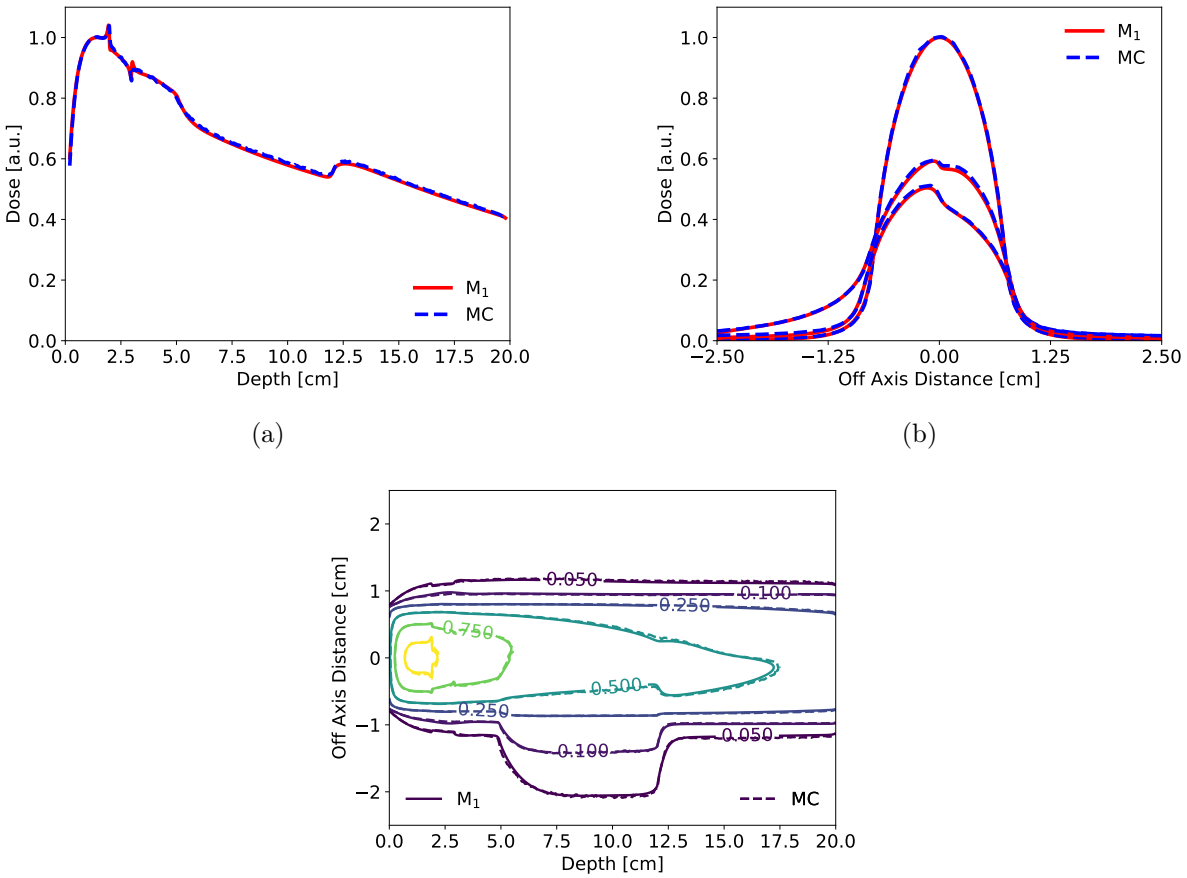

Figure 5.23: 6 MV photon beam coming from the left in a water phantom with cubic bone inserts between 2 cm and 3 cm and a half lung insert between 5 cm and 12 cm: (a) depth dose distribution along the central axis, (b) transverse dose profiles at the center of the beam ($z = 0$) taken at depths of 1.4, 10 and 17 cm and (c) 2D isodose map at $z = 0$ in the xy plane.

model can reach the accuracy of a Monte Carlo code with a reduced number of degree of freedom. This validation represents a first step towards a possible integration of the M1 model in a clinical Treatment Planning System.

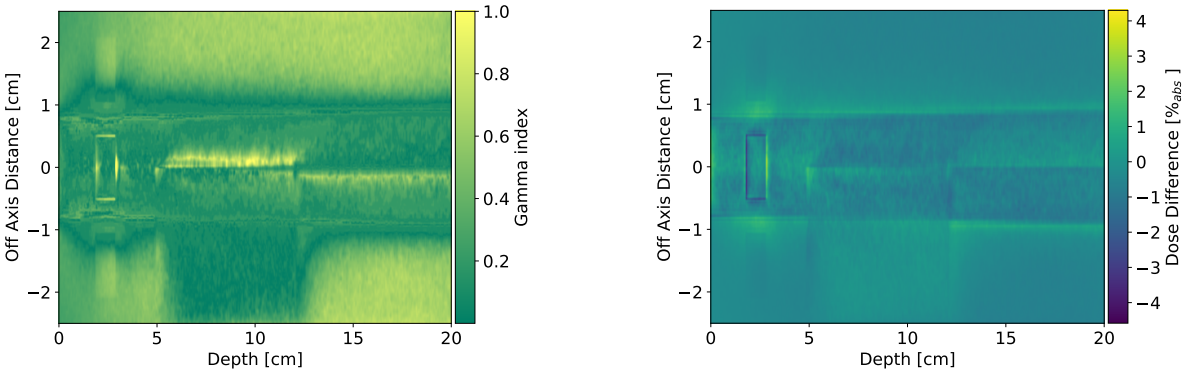

(a) (b)

Figure 5.24: 6 MV photon beam coming from the left in a water phantom with cubic bone inserts between 2 cm and 3 cm and a half lung insert between 5 cm and 12 cm: (a) γ-index map showing the results of the 1%/1 mm criterion and (b) spatial distribution of the dose differences between the Monte Carlo and M1 simulations.

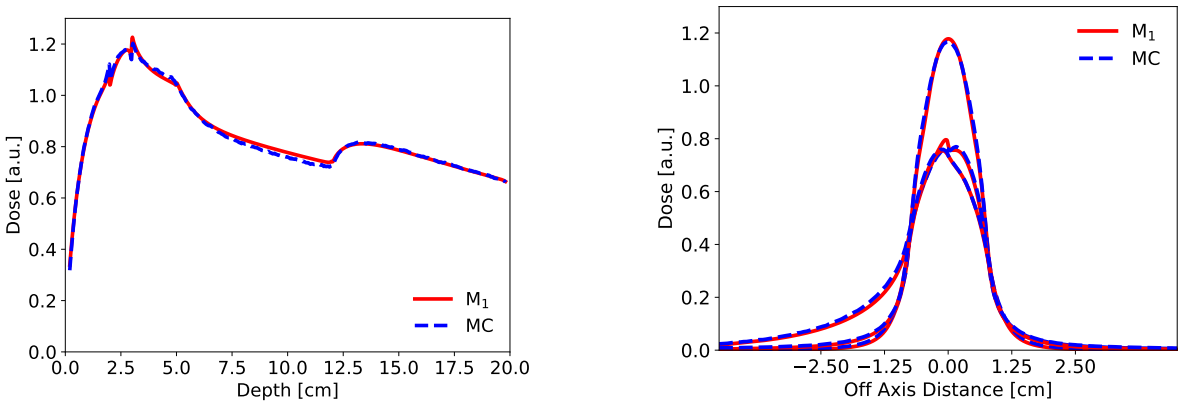

(a) (b)

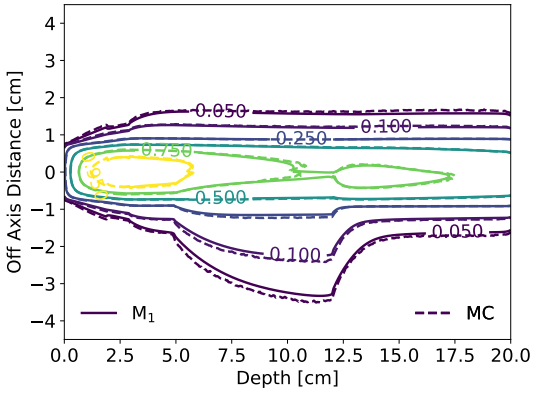

(c)

Figure 5.25: 18 MV photon beam coming from the left in a water phantom with cubic bone inserts between 2 cm and 3 cm and a half lung insert between 5 cm and 12 cm: (a) depth dose distribution along the central axis, (b) transverse dose profiles at the center of the beam ($z = 0$) taken at depths of 3.2, 10 and 17 cm and (c) 2D isodose map at $z = 0$ in the xy plane.

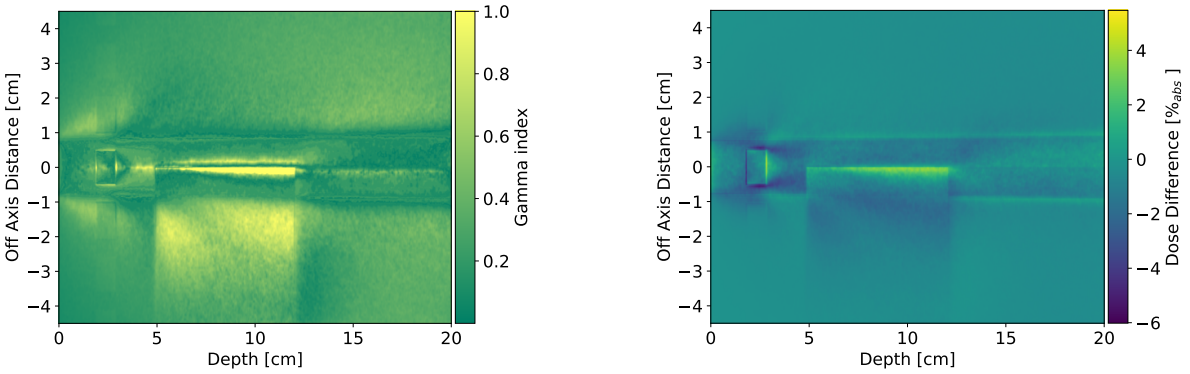

(a) (b)

Figure 5.26: 18 MV photon beam coming from the left in a water phantom with cubic bone inserts between 2 cm and 3 cm and a half lung insert between 5 cm and 12 cm: (a) γ-index map showing the results of the 1%/1 mm criterion and (b) spatial distribution of the dose differences between the Monte Carlo and M1 simulations.

Chapter 6

Entropic model for brachytherapy applications

6.1 Introduction

In this chapter we present a preliminary validation on brachytherapy applications of the entropic model introduced in Chapter 3. As in the case of external radiotherapy (see Chapters 4 and 5), the validation is conducted by comparing the results obtained with our algorithm and with the Monte-Carlo code PENELOPE [121].

The model is here tested on low dose rate brachytherapy applications. This choice is explained by the fact that in this energy range the photoelectric effect and chemical composition of the different materials play an important role in the dose deposition. Thus, the calculations that nowadays are performed in clinical practice neglecting these parameters following the TG-43 recommendations [115], could be improved with the use of our model. In order to simplify the calculations, we perform the comparison in a two dimensional domain, with a Gaussian energy spectrum centered at 0.03 MeV and with isotropic sources.

As a first step, we use a homogeneous phantom, in order to test the accuracy of our model in a simple configuration. In this preliminary phase, we demonstrate that our model does not provide the required accuracy to simulate a dose distribution because a single preferential direction in the M_1 model is not compatible with an isotropic source. For this reason, we introduce the M_2 model that has been mathematically developed by Teddy Pichard [108] and is capable to account for multiple directions. The M_2 model overcomes the limitations of the M_1 model and assures a better accuracy in the dose calculations.

Once the model is validated in a homogeneous case, we introduce more realistic phantoms including heterogeneities. The first phantom geometry is composed by a water phantom with three inserts of lung, bone and air. This geometry is useful to test the behaviour of our model in presence of different materials and chemical compositions. The

second geometry is a patient-equivalent mathematical phantom for the upper thoracic esophageal brachytherapy treatment. This geometry has been already used in literature for the validation of treatment planning systems in ^{192}Ir high dose-rate brachytherapy.

As a last case, we present a realistic calculation made with multiple sources, mimicking a treatment of prostate brachytherapy. Simulations are conducted taking into account first the density of different tissues present in the CT scan and then also the chemical composition of the tissues.

6.2 Protocol of comparison

In order to validate the entropic model, we conduct a comparison with the Monte Carlo code PENELOPE [121] for all test cases. In the present section, we describe the protocol of comparison by analyzing the different parameters that are adopted to conduct the simulations.

6.2.1 Source model

This chapter is a preliminary study on the feasibility in applying the entropic model to brachytherapy simulations. For this reason, we use a simple model of the source with respect to real brachytherapy seeds in order to reduce the number of considered parameters.

Figure 6.1: Geometry of a Nucletron SelectSeed brachytherapy source. In red the cylindrical silver rod coated with a silver halide layer (AgCl/AgI) and in blue the titanium encapsulation. Image from CLRP TG-43 Parameter Database for Brachytherapy, with permission.

The first approximation is performed on the geometry of the source. Instead of using the realistic source shown in Figure 6.1, the source is represented by a water sphere of 1 mm radius homogeneously filled with a radioactive isotope. This approximation allows to avoid a precise description of the seed which is extremely demanding for our algorithm. Indeed, in order to correctly resolve the geometry of all components of the source, a very fine grid is necessary. With a uniform grid implemented at the moment in our code, the simulations would require a high memory allocation and a long time. The use of a spherical geometry of the source seed allows to consider an isotropic photon emission.

The second approximation concerns the spectrum of the emitted photons. In a real brachytherapy the seed contains a radioisotope emitting photons with a broad characteristic spectrum. We apply our model to a low dose-rate brachytherapy where the iodine-125

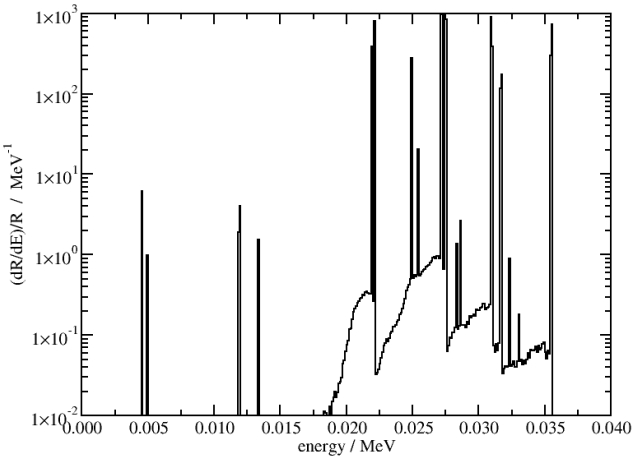

Figure 6.2: Spectrum of photons exiting the Nucletron SelectSeed brachytherapy source. Image from CLRP TG-43 Parameter Database for Brachytherapy, with permission.

(^{125}I) isotope is mostly used. This isotope decays by electron capture in an excited state of tellurium-125 (^{125}Te), by emitting X-rays at 35 keV, 31 keV, 27.4 keV and 27.2 keV [63]. The emission spectrum is shown in Figure 6.2, for the Nucletron SelectSeed source containing ^{125}I. In order to correctly resolve this spectrum one would need a large number of energy groups. For validation purposes we decided to use a simplified photon spectrum with a Gaussian distribution (Full Width at Half Maximum = $0.1\,E_0$) centred at E_0 = 30 keV.

6.2.2 Calculation geometry

As for the external beam applications, we validate the entropic model on multiple phantom geometries. All heterogeneous geometries are tested in two different approximations. The first test is perfomed by considering the heterogeneities as water for the chemical composition, but with the appropriate density of the considered material. In the second test, instead, we also take into account the real chemical composition.

Five different materials are considered in the present chapter: air (0.0012 g·cm^{-3}), lung (0.26 g·cm^{-3}), adipose (0.95 g·cm^{-3}), water (1. g·cm^{-3}) and bone (1.85 g·cm^{-3}). In Table 6.1 the complete list of these materials with their chemical composition in terms of fraction by weight of each element and density is reported.

We start the validation with a homogeneous phantom. This configuration simplifies the analysis of the discrepancies between the reference Monte Carlo code and the entropic model. The calculation geometry is defined by a 8×8 cm^2 phantom.

In order to test the model in presence of heterogeneities we consider two different geometries. The first heterogeneous domain is shown in Figure 6.3(b). It is composed by a water phantom where three inserts of 1 cm^2 made of lung, bone and air are placed at 1 cm from the center of the source. This geometry is also defined by a 8×8 cm^2 phantom.

	Composition [fraction by weight]	Density [g·cm^{-3}]
Water	H 0.112, O 0.888	1.
Cortical Bone (ICRU-44)	H 0.034, C 0.155, N 0.042, O 0.435, Na 0.001, Mg 0.002, P 0.103, S 0.003, Ca 0.225	1.85
Lung (ICRU-44)	H 0.103, C 0.105, N 0.031, O 0.749, Na 0.002, P 0.002, S 0.003, Cl 0.003, K 0.002	0.26
Adipose (ICRU-44)	H 0.114, C 0.598, N 0.007, O 0.278, Na 0.001, S 0.001, Cl 0.001	0.95
Air	H 0.112, O 0.888	0.0012

Table 6.1: Table of the materials with their chemical composition and density [141].

The second geometry is a patient-equivalent mathematical phantom for a upper thoracic esophageal brachytherapy treatment. This geometry has been used in literature to study the effect of patient inhomogeneities surrounding the esophagus on the dosimetry planning of a HDR ^{192}Ir brachytherapy [5, 104]. The sketch of this phantom is shown in Figure 6.3(c). Here the red color represents the lung material, the blue color represents the esophagus made of air material, the green color represents the bone material, specifically the rectangle is the sternum and the corona is the spine. Everything that is not colored is filled by water. This geometry is defined by a 16×16 cm^2 phantom.

6.2.3 Numerical parameters of simulations

In this section the parameters used in both the entropic model and Monte Carlo simulations are presented. These parameters concern the spatial discretization of the domain, the energy range and its discretization used in M_1 and the cut-off energy imposed in the PENELOPE code.

6.2.3.1 Entropic model parameters

In all simulations proposed in this chapter a uniform orthogonal spatial discretization is adopted with a square mesh of 0.25×0.25 mm^2. Such a small grid size is defined by the necessity to accurately discretize the source. With the future introduction of a non-uniform mesh, the number of cells may be consistently reduced.

The energy is discretized in 5 energy groups of equal width. The mean free path of secondary electrons is smaller than the mesh size and their transport is not considered. The energy lost in interaction of photons with the medium is locally deposited

without generating a secondary electron. Thanks to this approximation, we reduce the computational time and the needed memory allocation.

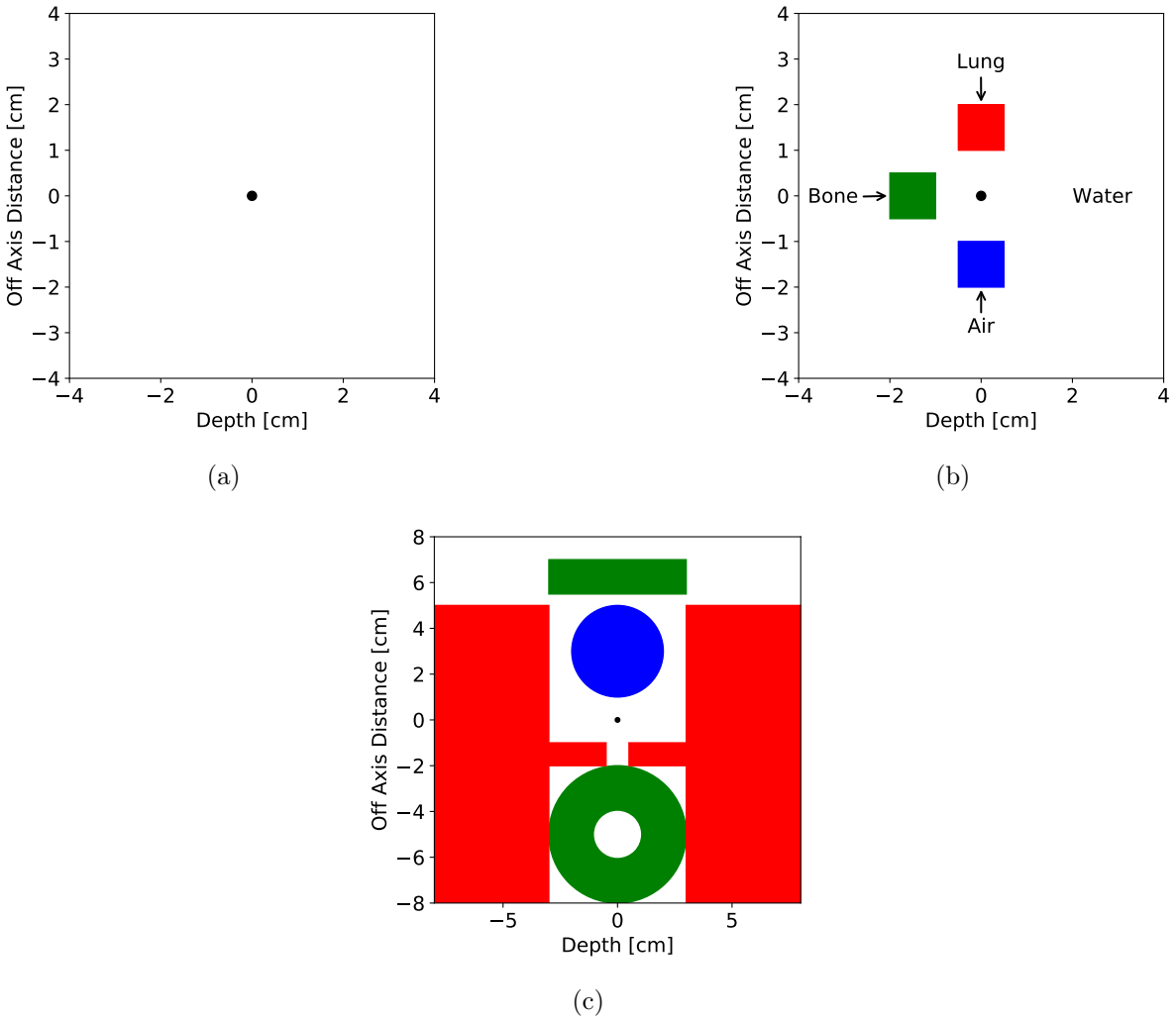

Figure 6.3: Geometries used for the brachytherapy validation:(a) homogeneous phantom, (b) heterogeneous phantom with inserts of different materials, (c) patient equivalent mathematical phantom for a thoracic brachytherapy treatment. The red color represents lung, green is bone, white is water and blue is air. Black point in the center indicates the source position.

6.2.3.2 PENELOPE parameters

The absorbed dose distributions in PENELOPE are tallied using a uniform orthogonal grid with $0.5 \times 0.5 \times 0.5$ mm^3 voxels. The two dimensional approximation is reached using a 30-cm-long cylindrical source. The typical number of tested particles in the Monte-Carlo calculations is 2×10^9, which allows us to obtain the deposited dose maps with a statistical uncertainty below the 1% in all voxels. Transport cut-off parameters

in all simulations are set to EABS(1, M) = EABS(3, M) = ∞ for electrons and positrons and EABS(2, M) = 0.001 MeV for photons.

6.3 Dose distribution in a homogeneous phantom

We begin the analysis of the brachitherapy simulations by calculating the dose distribution in a homogeneous domain. This case allows to evaluate the accuracy of our model in taking into account the physical interactions occuring in the low energy regime. Moreover, the dose calculation in a homogeneous domain is one of the principal approximations that is recommended in the TG-43 report [115].

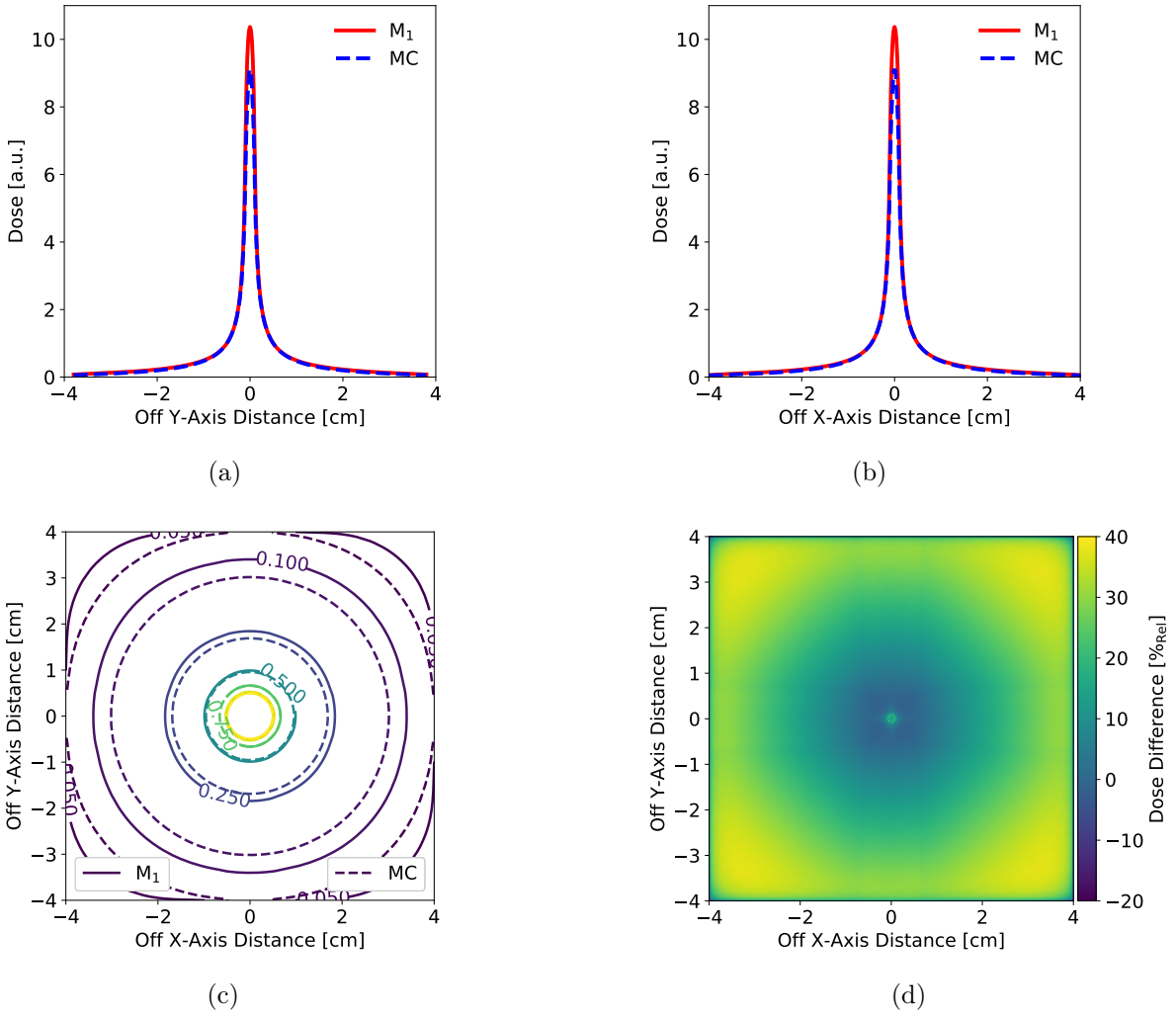

Figure 6.4: Dose distribution in a homogeneous phantom: (a) dose profile along $x = 0$, (b) dose profile along $y = 0$, (c) 2D isodose map in the xy plane and (d) spatial distribution of the dose differences between the Monte Carlo (dashed lines) and M_1 simulations (solid lines).

In Figure 6.4, we present the comparison between M_1 and PENELOPE results. The dose distributions for the Monte Carlo and M_1 results are normalized outside the source volume, as it is commonly done in the brachytherapy literature [104]. We chose a distance of 0.5 cm from the center of the source for the normalisation. As can be observed in Figure 6.4(c), the M_1 model is more diffusive compared to PENELOPE. The percentage dose difference shown in Figure 6.4(d) between the two simulations can reach 40% far away from the source. This difference is not acceptable in practice. However, one should be aware that such a big difference is calculated in a region where the absolute dose is very low.

Another important discrepancy between the two simulations can be noticed in Figures 6.4(a) and 6.4(b). These dose profiles are taken at $y = 0$ and $x = 0$ and show an overdose at the center of the source that corresponds to the maximum of the dose distribution. This difference can be explained by the incapacity of the M_1 model in treating the opposite fluxes of particles, as detailed in 3.3.3. In fact the initialization of an isotropic source implies that all the source cells produce particle fluxes exiting the edges. Consequently, at the edges of neighboring cells there are two opposite fluxes, as shown in Figure 6.5 . These fluxes are mutually cancelled. Thus, all the cells that are not on the border of the source are subject to the annhiliation of the fluxes and consequently to the local dose deposition of particles. This explains the higher dose deposition in the center of the source. The statistical analysis of the dose difference shows that the mean percentage dose difference between the two simulations is $23.36\% \pm 9.92\%$.

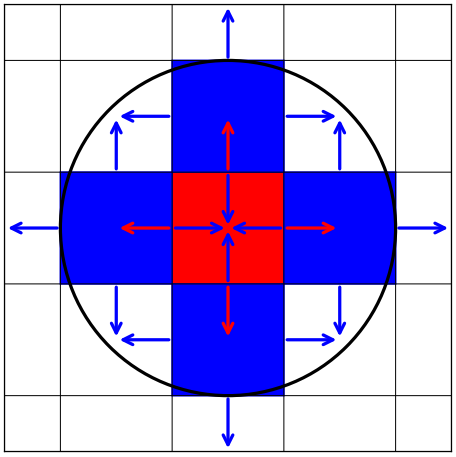

Figure 6.5: Scheme of cells initialization for an isotropic emission of a brachytherapy source. The cells inside the source are subject to the flux annihilation if treated with the M_1 model.

All these difficulties can be overcome by adopting the M_2 model introduced in Section 3.3.4. The M_2 model, shows some numerical issues, that need to be resolved before applying it for the external beam calculation. However, it can be successfully used in case of isotropic source such as in brachytherapy.

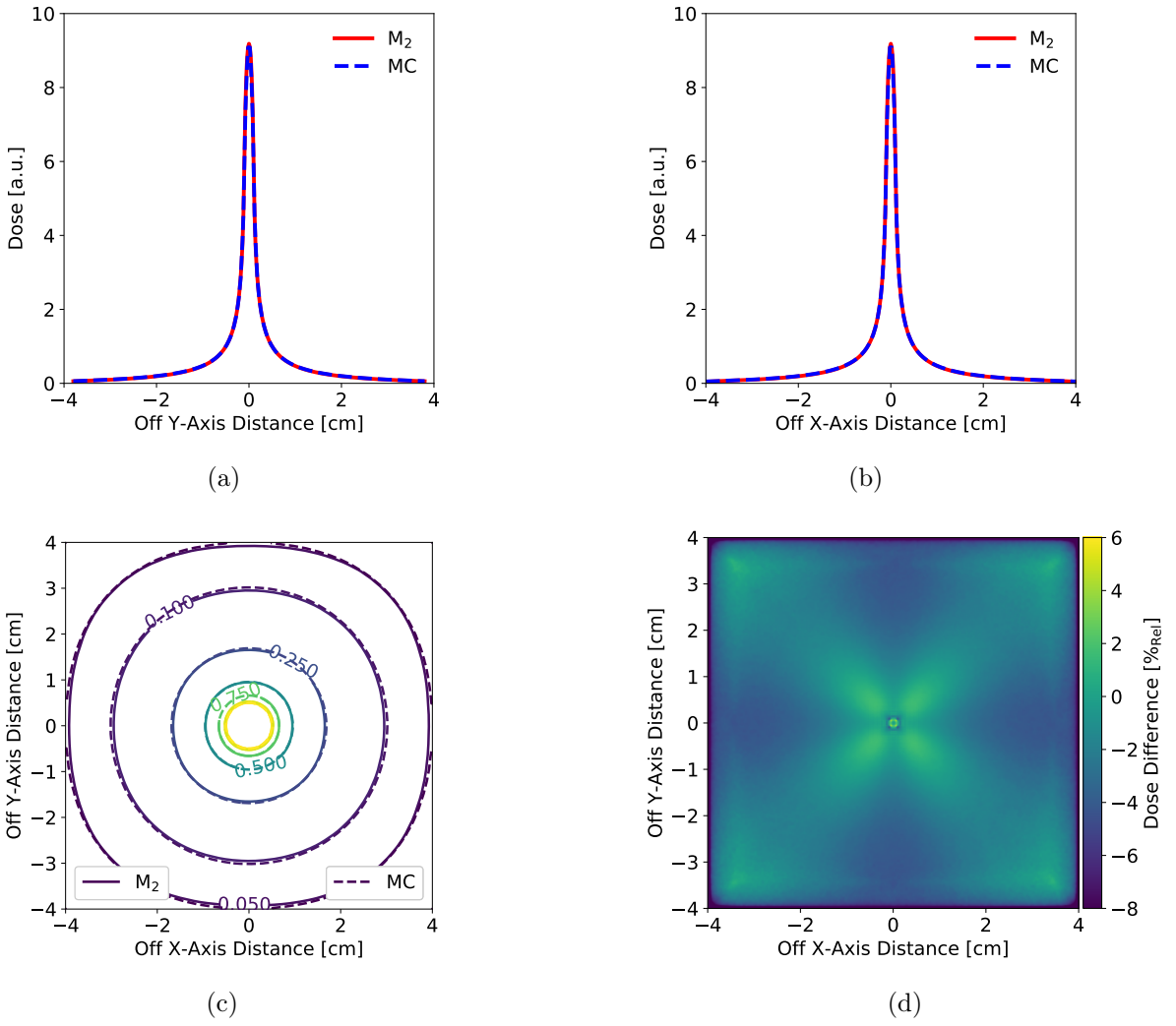

Figure 6.6: Dose distribution in a homogeneous phantom: (a) dose profile along $x = 0$, (b) dose profile along $y = 0$, (c) 2D isodose map in the xy plane and (d) spatial distribution of the dose differences between the Monte Carlo and M_2 simulations.

As shown in Figure 6.6, the M_2 model provides more accurate results compared to the M_1 simulations. The first improvement that can be observed in Figures 6.6(a) and 6.6(b) consists in the absence of overdose in the source volume. This result is consistent with the capacity of the M_2 model to treat opposite fluxes. Moreover, as shown in Figure 6.6(c), the M_2 simulation is less diffusive compared to M_1 and the dose difference between the M_2 and Monte Carlo simulations is less important. The statistical analysis of the percentage dose distribution shows that the discrepancy between the two simulations is $2.92\% \pm 1.18\%$. For these reasons in all the following tests, the M_2 model is adopted. In Figure 6.6(d) a characheristic pattern in the distribution of the dose difference can be observed. This is mainly due to the M_2 approximation and the Cartesian discretization of the domain. However, these oscillations remain small if compared to ray-effect shown by Papagiannis

et al. [104] comparing the Collapsed Cone Convolution method ONCENTRA (Elekta) with a Monte Carlo simulation.

6.4 Dose distribution in a heterogeneous phantom

In this section we propose a comparison between the M_2 model and PENELOPE in presence of heterogeneities, see Figure 6.3(b). We run our simulations firstly by taking into account only the density difference in the inserts and by using the water chemical composition everywhere. As a second step, we introduce the chemical composition of the different inserts in order to test the accuracy of our entropic model in taking into account the behaviour of the dose deposition due to the photoelectric effect.

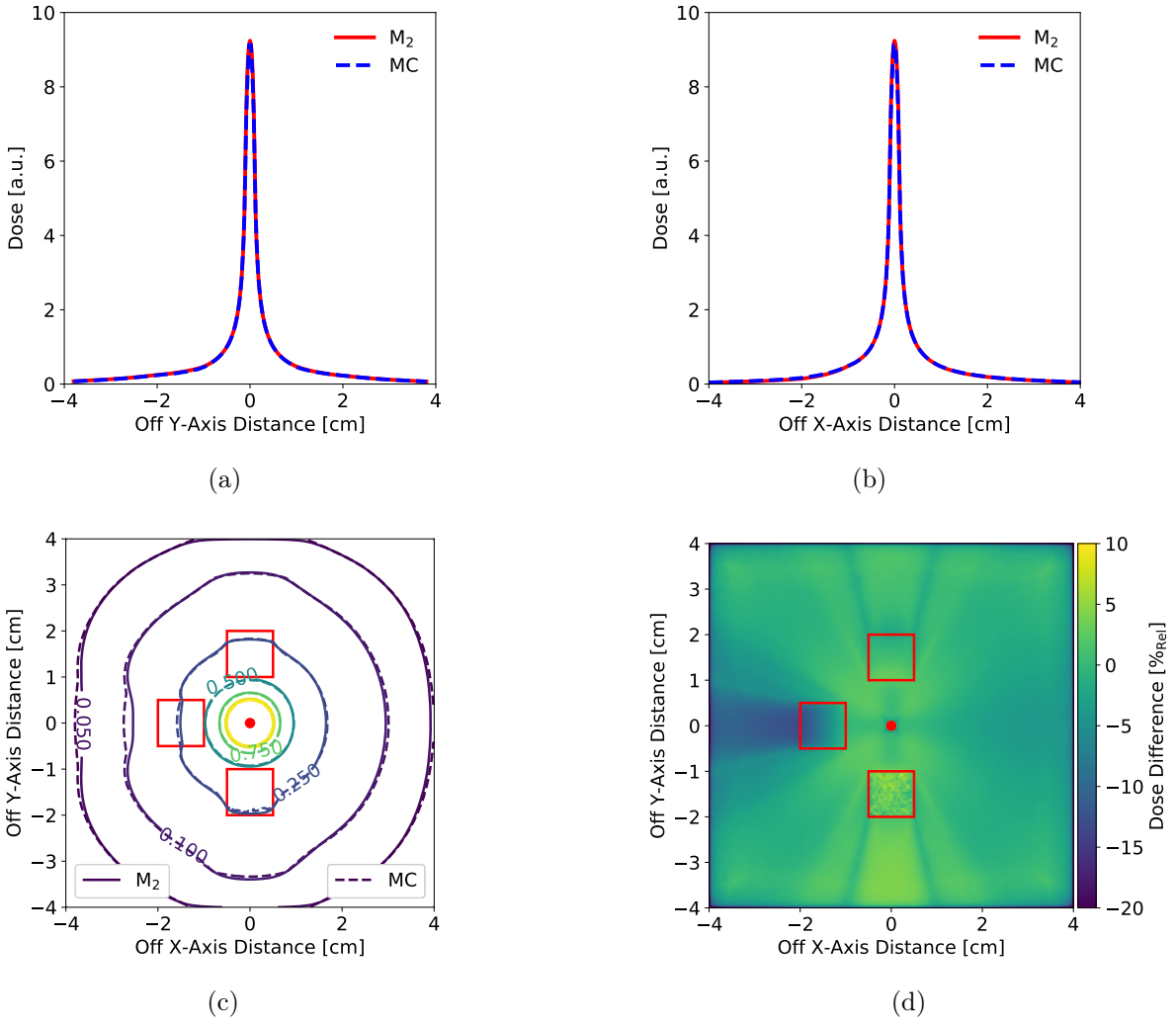

Figure 6.7: Dose distribution in the heterogeneous phantom while taking into account only the density of materials: (a) dose profile along $y = 0$, (b) dose profile along $x = 0$, (c) 2D isodose map in the xy plane and (d) spatial distribution of the dose differences between the Monte Carlo and M_2 simulations.

In Figure 6.7 the comparison between the M_2 and Monte Carlo simulations while taking into account only the density of the inserts is reported. In this case, we test the accuracy of our model in a realistic situation due to the fact that nowadays the CT scan of a patient does not include the information on the chemical composition of the tissues. Analysing the dose profiles in Figures 6.7(a) and 6.7(b), the contribution of the heterogeneities on the dose distribution for both the underdense and overdense materials is not very important. A small perturbation on the dose distribution can be noticed only on the isodose map shown in Figure 6.7(c). Small differences between the M_2 and Monte Carlo solutions are present only in the isodoses behind the bone insert. The percentage dose difference between the two simulations remains small with an accuracy of $2.49\% \pm 2.28\%$. In Figure 6.8 we show the comparison between the dose calculated while taking into account the density of the inserts and the dose in homogeneous domain. It can be observed that the two dose distributions do not strongly differ.

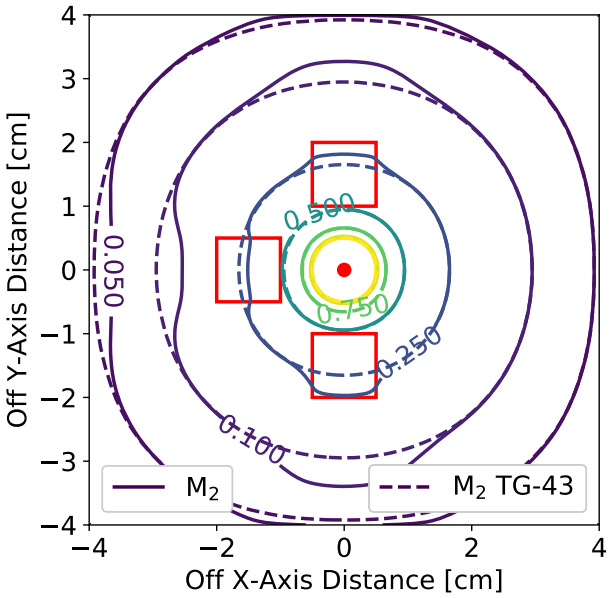

Figure 6.8: Comparison between the dose distribution calculated with the M_2 model following the recommendations of the TG-43 report, i.e. in homogeneous phantom (dashed lines), and in the heterogeneous phantom taking into account only the density of materials (solid line). The perturbation due to the density gradients remains small and the dose do not strongly differ from the TG-43 approximation.

We now test the accuracy of our model introducing the real chemical composition of the inserts in the same geometry. This case is of particular interest for the LDR brachytherapy, since in this energy range the photoelectric effect, which strongly depends on the atomic number, is the most probable interaction experienced by a photon propagating in the considered materials. Therefore, we expect to see a considerable effect on the dose deposition especially for bone.

As shown in Figure 6.9, the dose deposition changes considerably with respect to the

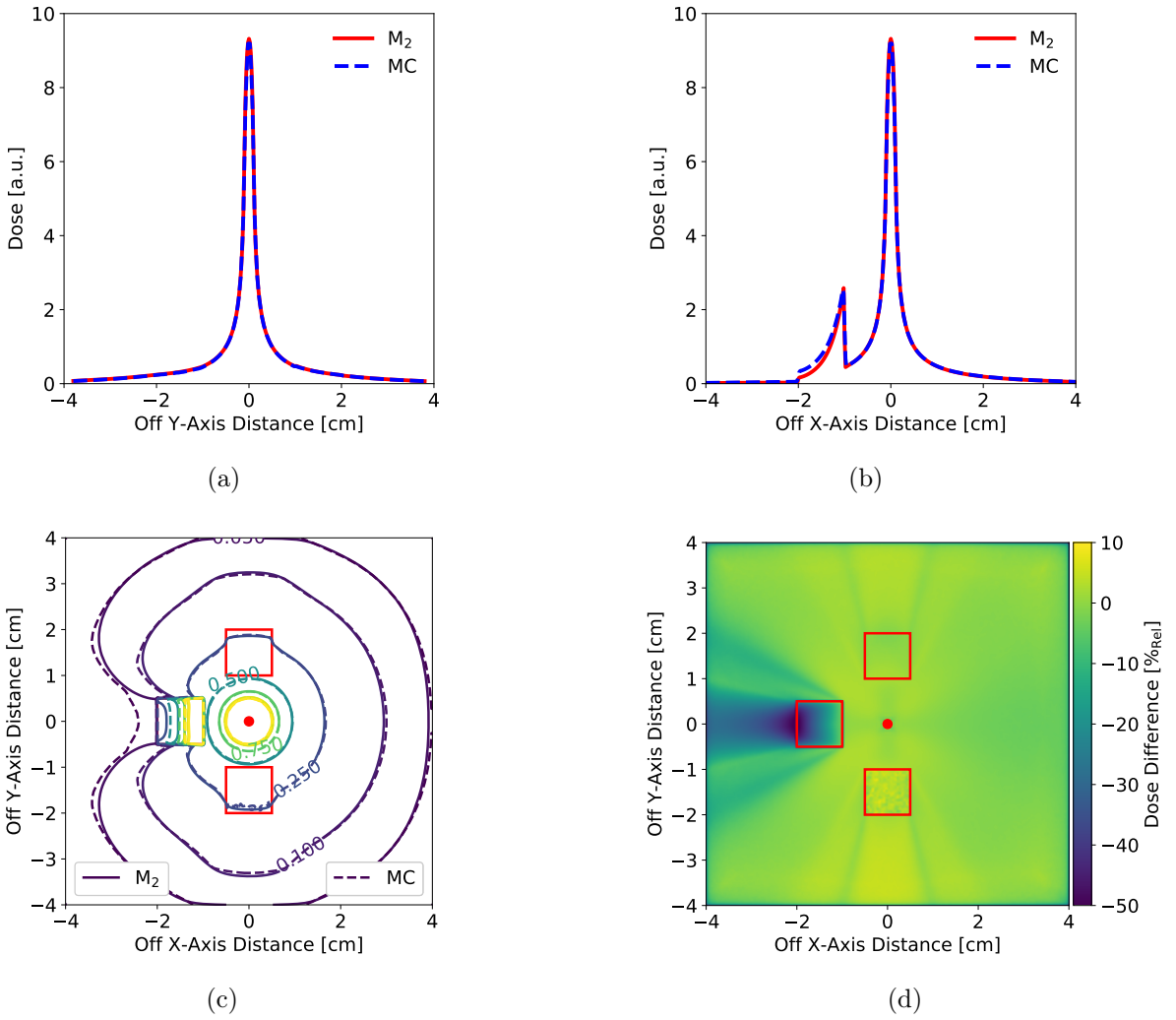

Figure 6.9: Dose distribution in the heterogeneous phantom taking into account also the chemical composition: (a) dose profile along $y = 0$, (b) dose profile along $x = 0$, (c) 2D isodose map in the xy plane and (d) spatial distribution of the dose differences between the Monte Carlo and M_2 simulations.

previous case. Of particular interest is the impact of the bone heterogeneity: Figure 6.9(b) shows a strong gradient of dose deposition appearing behind the bone interface. This is due to the fact that the photoelectric effect in bone material and for this energy range is largely predominant, see Figure 5.10. The percentage dose difference between the two simulations attains more than 50% in this particular zone, but in average it remains small with an accuracy of $4.13\% \pm 6.72\%$. In Figure 6.10 is shown the comparison between dose distributions calculated taking into account the chemical composition and in homogeneous phantom. Differently from the previous case, a strong difference between the real dose distribution and the TG-43 approximation can be oberved especially near the bone insert.

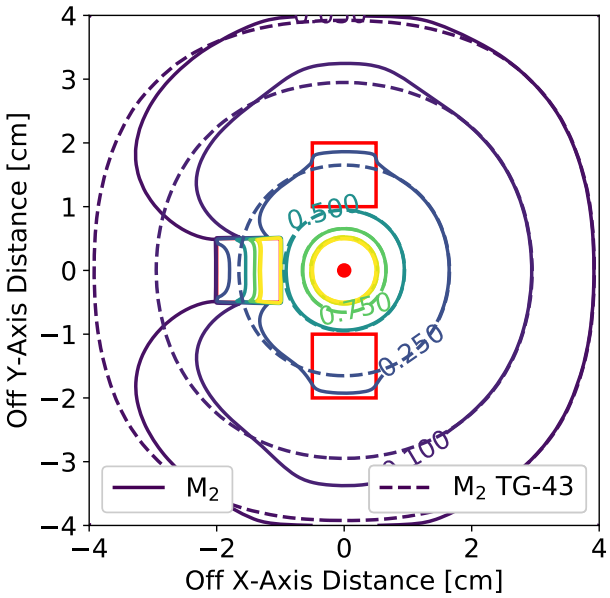

Figure 6.10: Comparison between the dose distribution calculated with the M_2 model following the recommendations of the TG-43 report, i.e. in homogeneous phantom (dashed lines), and in the heterogeneous phantom taking into account also the chemical composition of materials (solid line). The perturbation induced by the low density heterogeneities do not vary in an appreciable manner. However, the chemical composition of bone dramatically changes the dose distribution. This is due to the fact that the low density inserts atomic number is almost equivalent to the water one, while the difference with the equivalent atomic number of bone is higher.

6.5 Dose distribution in a patient-equivalent numerical phantom

As a last test, a more complex geometry is simulated, see Figure 6.3(c). This phantom has been used as a benchmark for the existing brachytherapy treatment planning dosimetry algorithms [5, 104]. It consists in a simplified numerical model of a esophageal scan and is composed by several heterogeneities with different densities, chemical compositions and shapes. This allows us to test the accuracy of our model in a more challenging situation. As in the previous section, we run our calculations in the two different approximations.

In Figure 6.11, we show the comparison between the M_2 and the Monte Carlo simulations, when accounting only for the difference in the inserts density. As shown in Figure 6.11(c), the M_2 model accurately reproduces the dose distribution calculated with PENELOPE. There are two main differences that do not have a great impact on the result: the first difference is between the isodoses representing the 5% of dose deposition in the lung to the right and to the left from the source. The difference between the two curves seems to be large mainly due to the very low gradient of the dose. Indeed, in this region the

percentage of dose difference is about 20%, which represents in absolute dose 1% of the dose normalized at 0.5 cm from the center of the source. The second difference that can be noticed between the two simulations is the treatment of the esophageal interface. In the Monte Carlo simulation a numerical artefact appears as shown in Figure 6.11(a) at 1 cm. This artefact is due to the presence of a dose diagnostic mesh lying on the interface. The statistical analysis of the percentage dose distribution shows that the discrepancy between the two simulations is $23.1\% \pm 13.6\%$. If we limit the statistical analysis at the region delimited by the 5% isodose curve the difference is $10.7\% \pm 12.04\%$.

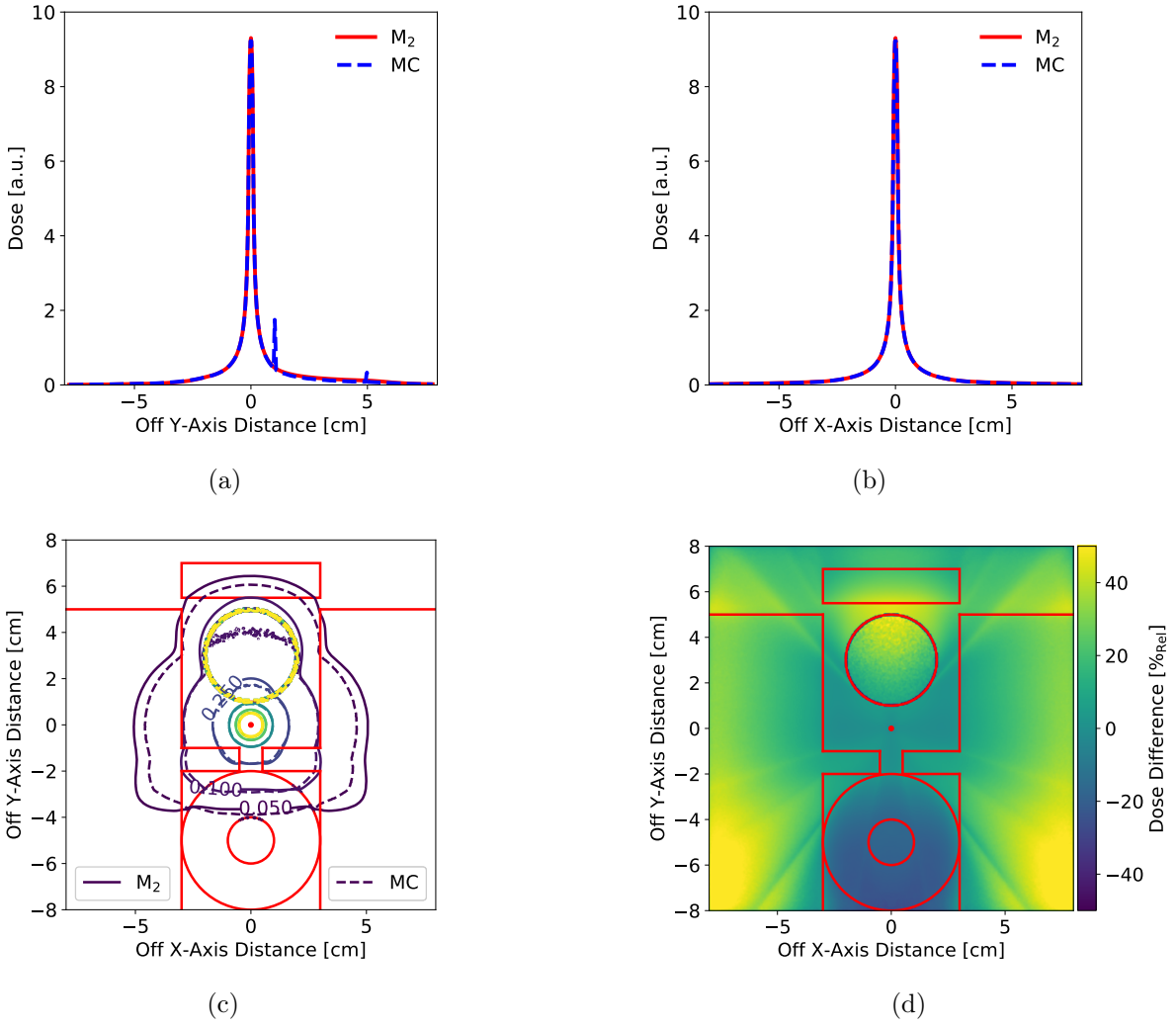

Figure 6.11: Dose distribution in a patient-equivalent numerical phantom: (a) dose profile along $y = 0$, (b) dose profile along $x = 0$, (c) 2D isodose map in the xy plane and (d) spatial distribution of the dose differences between the Monte Carlo and M_2 simulations.

In Figure 6.12, we show the comparison between the M_2 and the Monte Carlo simulations when also accounting for the chemical composition of the different tissues. In this case, the discrepancy calculated in the entire domain between the M_2 model and the

Monte Carlo simulation is $30.77\% \pm 19.66\%$. If we limit the statistical analysis at the region delimited by the 5% isodose curve the difference is $14.8\% \pm 16.16\%$. With respect to the previous simulation, a higher dose difference appears far from the source especially inside the spine. Even if the difference is high in percentage, it corresponds to a small value in absolute dose deposition.

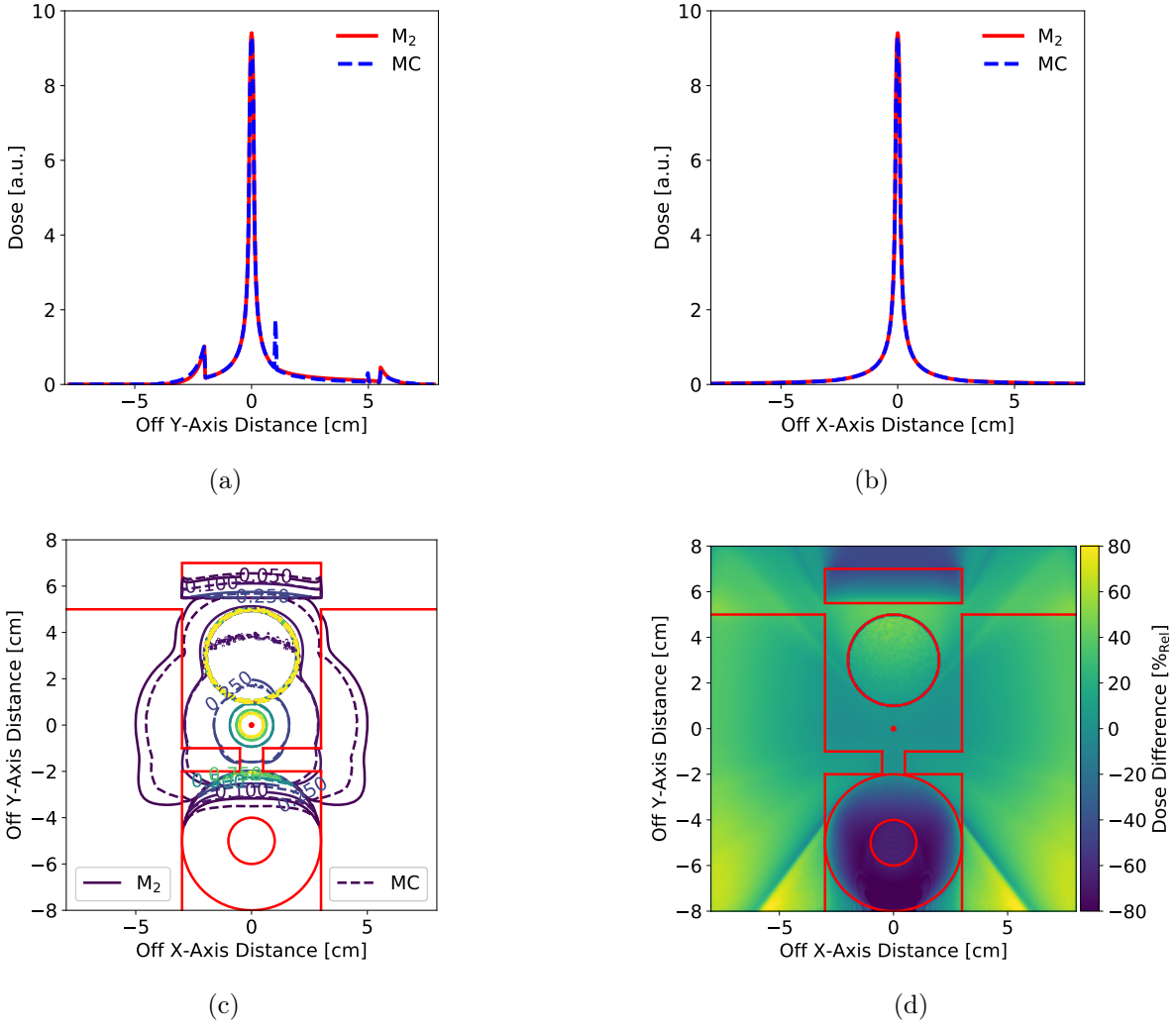

Figure 6.12: Dose distribution in a patient-equivalent numerical phantom: (a) dose profile along $y = 0$, (b) dose profile along $x = 0$, (c) 2D isodose map in the xy plane and (d) spatial distribution of the dose differences between the Monte Carlo and M_2 simulations.

6.6 An application to a I-125 prostate brachytherapy

After the validation of the M_2 model in numerical phantoms, we propose a simulation of a realistic prostate LDR brachytherapy. In this section, we analyze the impact on a

realistic dose calculation of the approximations previously described.

The calculation domain is represented by a CT image of a prostate. This image has been cut in order to treat only the region of interest and reducing the domain of the simulation. The conversion of CT Hounsfield units to mass density (g/cm^3) is achieved using a conversion curve defined by the tomograph calibration made at the Bergonié Hospital. The mass density conversion used in the M_2 model is plotted in Figure 6.13(a). The chemical composition of the different tissues is introduced by using rectangular windows in function of the density as shown in Figure 6.13(b). The source placement is not intended to be clinically accurate and is used only to investigate the differences of dose deposition in the different approximations.

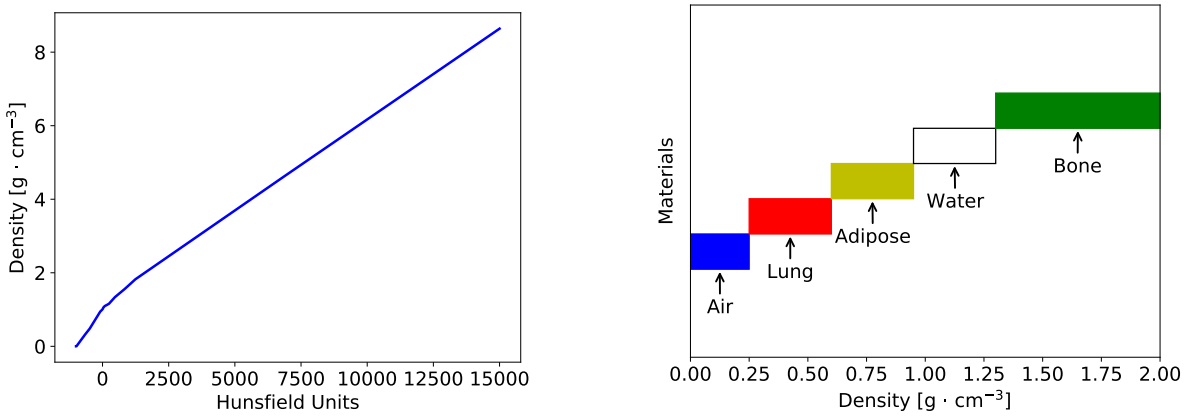

(a) (b)

Figure 6.13: Panel (a): CT Hounsfield unit to mass density conversions used in M_2 simulations. Panel (b): Mass-density-to-material assignments used in M2. The blue color represents the air, in red is represented the lung, in yellow is represented the adipose, in white is represented the water and in green is represented the bone.

In Figure 6.14, we show the results of the simulations run in the TG-43 approximation, i.e. in a homogeneous domain composed only by water, and while taking into account the difference in the tissues densities.

Analysing Figure 6.14(c), it is clear that small differences (in the range of 2%) occur if we take into account only the density difference of the tissues. Moreover, the dose in the surrounding pelvic bones seems to be very low. This result is consistent with the observations presented in the previous sections, where we have observed that the density of the different materials does not considerably affect the dose deposition.

In Figure 6.15 we compare the results of simulations performed while taking into account only the density difference of the tissues and while taking into account also the difference in the chemical composition.

Figure 6.15(c) shows that when the chemical composition is taken into account, the

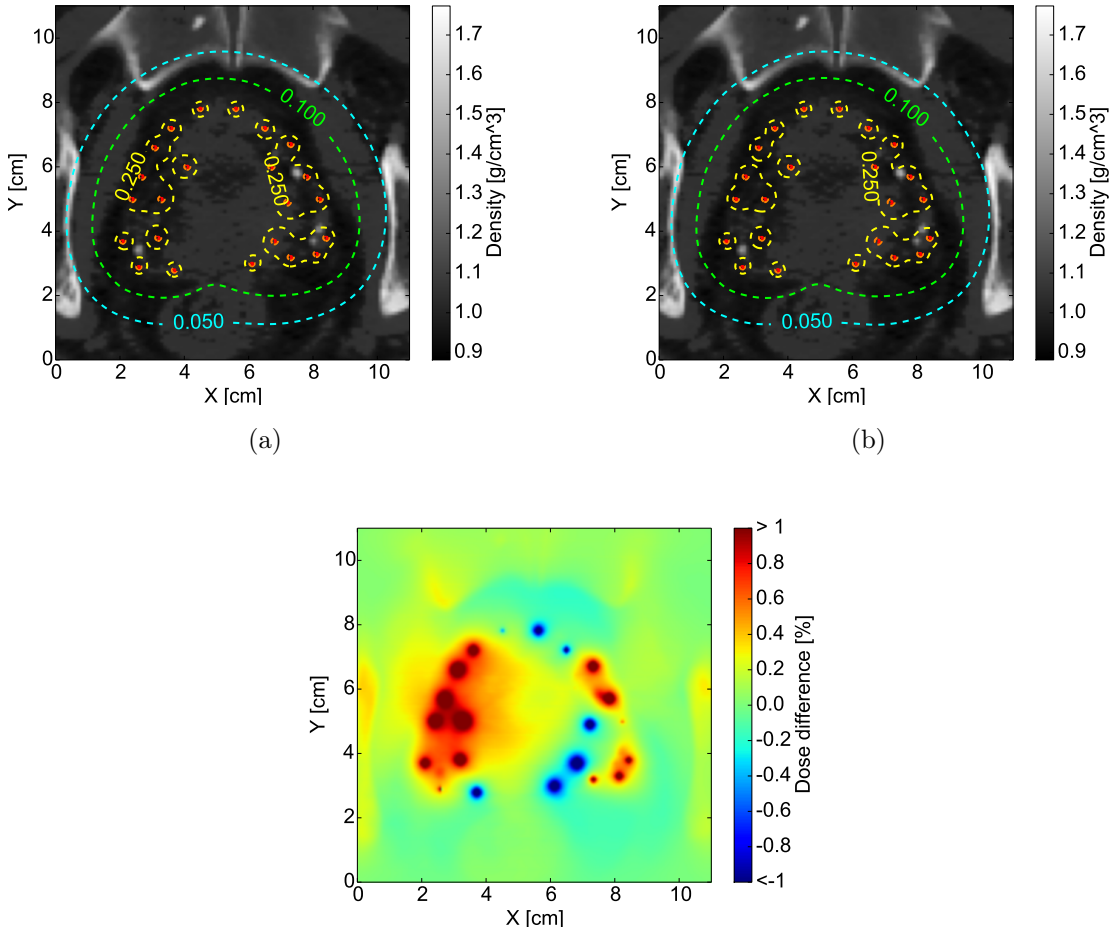

Figure 6.14: Dose distribution calculated with the M_2 model on a CT scan: (a) dose distribution calculated in the TG-43 approximation, (b) dose distribution calculated taking into account the density of the tissues, (c) percentage difference of dose between the two simulations.

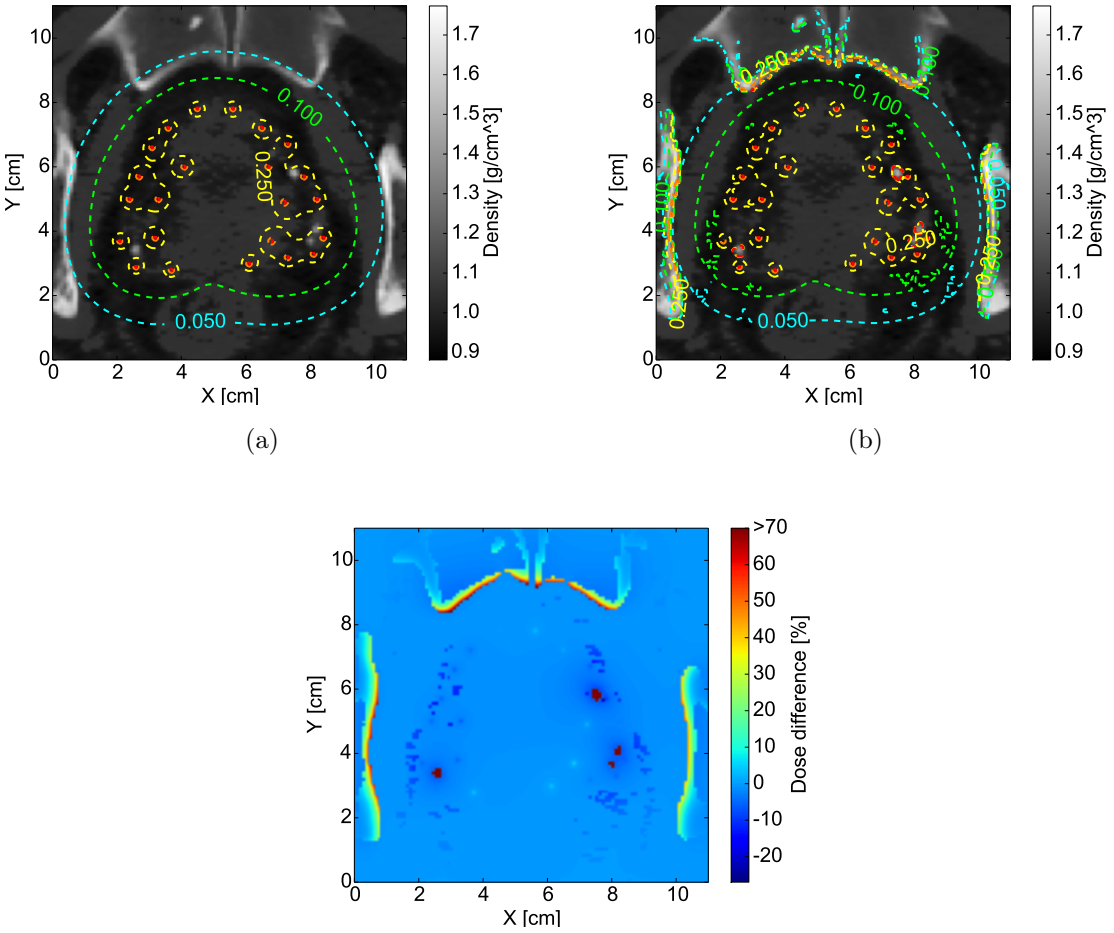

Figure 6.15: Dose distribution calculated with the M_2 model on a CT scan: (a) dose distribution calculated taking into account the density of the tissues, (b) dose distribution calculated taking into account the chemical composition of the different tissues, (c) percentage difference of dose between the two simulations.

dose distribution radically changes: the pelvic bones can receive more than 70% of the maximum dose calculated in the homogeneous case and the calcifications in the prostate can reach the 400%. A lack of dose (up to 20%) appears in pixels where adipose is present.

6.7 Conclusion

In this Chapter, the entropic model has been validated in a 2D geometry for the low dose rate brachytherapy applications. In the first part of the chapter, several tests on homogeneous domains have been presented. The source is not correctly resolved and the flux annihilation takes place inside the source volume. We conclude that the M_1 model is not sufficiently accurate for a reliable dose calculation. In order to overcome this problem, the same configuration has been tested with the M_2 model [108]. The results show a much better accuracy in the calculation of dose deposition. After this preliminary validation, the M_2 entropic model has been tested on heterogeneous domains, always providing an acceptable accuracy. We demonstrate that in the low energy range (10 - 50 keV) the chemical composition plays an important role in the dose distribution. Finally, we tested a dose calculation on a prostate CT scan. This simulation clearly demonstrates the impact of the chemical composition of human tissues in a realistic situation. However, this is encouraging but is still a preliminary test that does not provide the required clinical accuracy yet. The available in practice CT scan diagnostics does not provide the information about the chemical composition of the human tissues. The new technologies as the dual-energy computed tomography are promising to provide the needed information [91].

Conclusion and perspectives

Conclusion

This thesis is dedicated to application of entropic models for solution of the linear Boltzmann transport equation for radio-therapeutic applications. Our main result consists in the development of a numerical code to calculate the dose distribution in the tumor with practically acceptable level of accuracy and within a short computation time.

This thesis is built on several previous works that have been dedicated to that topic. The thesis by Caron [20] developed an application of the M1 model for the electron transport. Specifically only the Mott and Møller cross sections were taken into account. In the PhD work by Pichard [108] the moment model has been extended to on the second order moment equations, i.e. the M2 model. Moreover, the Compton effect has been introduced in order to model the propagation of a photon beam. In the present work it makes a further step. The first major improvement consists in the implementation of a complete description of all relevant physical interactions of electrons, photons and positrons. To this end the differential cross sections in the collisional operator of the LBTE have been developed in terms of Legendre polynomials and the soft and catastrophic parts have been treated separately by using the CEPXS library. This rigorous approach allows a higher accuracy of the model reducing consistently the number of energy groups used for the LBTE discretization with respect to the previous works.

The second major improvement consists in splitting the populations in the primary and the secondary particles as it is presented in Chapter 4. This approach allows to overcome the average in each energy group between the highly anisotropic primary particles and more isotropic secondaries. Since the previous works considered only monoenergetic particle beams, the secondary particles can be treated together with the primaries without loss of accuracy in the results. This is due to the fact that for a monoenergetic initial spectrum of photons, all secondary particles are produced in lower energy groups and do not mix with the primaries. However, this improvement is crucial to improve the accuracy of our model, in more realistic Bremsstrahlung initial spectrum.

The third important improvement is related to the initialization method of the parti-

cle beam. We developed an initialization technique based on a Monte Carlo phase space data file, as described in Chapter 3. Due to the mesoscopic nature of the M1 model, the injected beam is characterized by the anisotropy of each particle species and each energy group at the boundary of the domain or at the boundary of the source volume in brachytherapy applications. In the previous works the initial beam direction was specified by a single anisotropy value. This initialization is suitable for quasi-monodirectional beams but presents strong inaccuracies in a more realistic case of a divergent beam, as it has been shown in Chapter 4. The proposed method is general and it can be applied to both external beam radiotherapy and brachytherapy.

The model has been validated for both external beam radiotherapy and brachytherapy. External beam radiotherapy simulations are presented in Chapters 4 and 5 for the homogeneous domains and heterogeneous domains, respectively. The cross section description is improved by using a non uniform energy mesh. This technique allows to reduce the number of energy groups while decreasing the simulation time and preserving the accuracy of the model in the calculation of dose deposition. For the 6 MV spectrum only 21 energy groups were needed while for the 18 MV spectrum 39 energy groups were used. In the tests with a heterogeneous domain with different geometries and for the 6 MV spectrum the model shows an excellent level of accuracy in all considered cases. For the 18 MV spectrum some discrepancies are observed at interfaces with heterogeneities. Nevertheless the model demonstrates a practically acceptable level of accuracy in all considered geometries.

In Chapter 6 the entropic model has been validated for low dose rate brachytherapy applications. We demonstrate that the model can reach an acceptable level of accuracy but only with the second order moment equations. The M2 model is needed to overcome the flux annihilation effect inside the source volume. Partial annihilation of fluxes could be the origin of the dose discrepancies observed in the M1 model. The M2 model is validated in presence of heterogeneities. Due to the low energies of the propagating photons the chemical composition plays an important role in the dose distribution. The entropic algorithm is capable to reach a good accuracy in all tested cases. A simulation of a realistic prostate treatment demonstrates a potential of the moments models for a complete dose calculation in low dose rate brachytherapy. Further numerical improvements in the code will allow accelerate the simulations and improve its precision.

In this work we demonstrate that the entropic model can reach a high level of accuracy with less degrees of freedom with respect to the other deterministic methods. This type of models could be used in clinical practice as an alternative to the existing algorithms for the dose calculations in the treatment planning. Due to the reduced number of variables and after a mathematical optimization this numerical code will be capable to compute

dose distributions in few seconds with a precision comparable to the general purposes Monte Carlo codes.

Perspectives of developement

There are several perspectives and future developments which may significantly improve the performance of the entropic algorithm. Before a possible application in a clinical context, the code needs to be optimized in numerical aspects. In order to reduce the memory allocation and the computational effort, two strategies may be proposed. Moreover, a beam initialization that can model a real beam in presence of a multileaf collimator is needed.

Non-uniform discretization

As already anticipated in the conclusion of Chapter 4, the use of non uniform Cartesian grids can be a first step to reduce the number of cells for the domain discretization. Specifically, the non uniform discretization techinque consists in adapting the accuracy of the solution within certain regions of interest. This technique allows a strong reduction of the grid cells where the problem exhibits smooth behavior and a strongly localized increase of resolution in areas needing more accuracy. At the moment, due to the uniform discretization an excessive number of cells is required in order to have an accurate resolution.

In the external beam radiotherapy applications, the number of cells outside the beam can be reduced preserving the solution accuracy. Taking as example the domain used for the 18 MV calculations that has dimension of $6 \times 6 \times 20$ cm^3 (see Figure **??**), with the current discretization of cubic meshes of $0.5 \times 0.5 \times 0.5$ mm^3 we use 5.76×10^6 cells. Keeping the same meshing inside the beam and using a larger meshing of 1 mm^3 outside the beam the number of cells is reduced to 7.65×10^5 with a gain in the order of 10. This example is just a rough estimation of the gain that can be obtained by the introduction of a non-uniform meshing in external radiotherapy applications.

In brachytherapy applications the impact of the non-uniform discretization technique can be even more important. As explained in Chapter 6 at the moment we are forced to use a very fine meshing in order to well resolve the small source size. Introduction of a non-uniform grid will allow for very accurate resolution of the source geometry while strongly reducing the number of cells in the rest of the domain.

Higher order numerical schemes

Another complementary strategy that can be devised to reduce the number of mesh grids is introduction of higher order schemes for resolution of the LBTE. In this work the

entropic model is resolved with numerical schemes of first order, due to their simplicity and intrinsic stability. In the future, higher order schemes may be implemented for improving the accuracy of solution of the entropic model and for using of a less refined grid without any loss of precision. This would reduce the computational effort and a combination with the non uniform discretization technique could strongly reduce the calculation time to the order of a few seconds for a typical problem of dose deposition.

Real beam modelling

The beam initialization for both the external beam radiotherapy and brachytherapy applications proposed in this work needs to be further developed in order to meet the practical requirements. This method is now applied to the phase space data file generated with a point source placed at 100 cm from the phantom surface. This initialization is simple because the anisotropy distribution is the same for all the energies of the beam. Therefore it does not need to be calculated for all energy groups. On the contrary, in the case of a real beam exiting from the head of a LINAC once has to take into account the anisotropy distribution separately for each energy group.

Moreover, a suitable model for a real simulation has to describe with high precision the photon beam modified by any possible configuration of the multileaf collimator. In principle any phase space data file can be discretized and translated in anisotropy distribution but this technique in not suitable for a possible implementation in clinical practice. Alternatives methods that would preserve the accuracy reducing the calculation time for a real initialization are now under investigation.

Perspectives of applications

Intraoperative radiotherapy

In the present work we focus on application of the entropic model for external photon beam radiotherapy and brachytherapy. In the future the proposed model can be applied to other radiotherapy techniques, such as intraoperative radiotherapy (IORT). The main objective of IORT is to perform radiotherapy during surgery, directly after the removal of the tumor, with the aim of reducing the probability of recurrence. The Intrabeam (Carl Zeiss Meditec, Oberkochen, Germany) is a IORT device widely employed in medical practice, which is using a 50 kV x-ray beam. The M1 model could be used to produce fast and precise dose calculations during intraoperative radiotherapy.

Molecular radiotherapy

Another possible application can be the unsealed source radionuclide therapy, or molecular radiotherapy. In this technique a radionuclide or a radioactively labelled pharmaceutical substance is inoculated to the patient and it is fixed in the tumor cells. This way, the radiation dose is maximized in the tumour while minimized in the normal tissues. Apart from iodine-131 (^{131}I), in the molecular radiotherapy the lutetium-177 (^{177}Lu) isotope is mostly used. This isotope decays by β^- process to hafnium-177 (^{177}Hf), emitting electrons with a maximum energy of 498 keV and mainly gamma rays at 113 keV, 208 keV. This radionucleide has two main properties: the electrons have a range of few mm's and deposit their energy locally in the tumor, while the emitted photons can be detected by a single photon emission computed tomography (SPECT). Starting from the SPECT images of the patient, the entropic model can be used for inverse calculations, with the aim of calculating the activity of the source and the related deposited dose in the patient.

Hadrontherapy

This model can be also implemented for a hadron radiotherapy with a more complete physical description taking into account the cross sections for protons, alpha particles and carbon ions. This approach is currently the object of the thesis of E. Olivier at the CELIA laboratory. With the full implementation of the proton cross sections for elastic and inelastic scattering and of the fragmentation cross sections for the heavy ions, the entropic model will be applicable to dose calculations in hadrontherapy.

Perspectives of economic valorization

This work has been partially supported by the CEA Valorisation group in order to prepare an industrial valorization and to evaluate the potential interest of the market. A consistent amount of work regarding this perspective has been conducted in collaboration with the Aquitaine Science Transfer. This public society aims to help the reserch teams to bring on the market the results of their work.

Bibliography

[1] S. Agostinelli, J. Allison, K. Amako, J. Apostolakis, H. Araujo, P. Arce, M. Asai, D. Axen, S. Banerjee, G. Barrand, et al. Geant4—a simulation toolkit. *Nuclear instruments and methods in physics research section A: Accelerators, Spectrometers, Detectors and Associated Equipment*, 506(3):250–303, 2003. p. 17, 64

[2] A. Ahnesjö. Collapsed cone convolution of radiant energy for photon dose calculation in heterogeneous media. *Medical physics*, 16(4):577–592, 1989. p. 15, 16

[3] A. Ahnesjö and M. M. Aspradakis. Dose calculations for external photon beams in radiotherapy. *Physics in Medicine & Biology*, 44(11):R99, 1999. p. 14, 15

[4] M. Alber and F. Nüsslin. Optimization of intensity modulated radiotherapy under constraints for static and dynamic MLC delivery. *Physics in Medicine & Biology*, 46(12):3229, 2001. p. 8

[5] G. Anagnostopoulos, D. Baltas, E. Pantelis, P. Papagiannis, and L. Sakelliou. The effect of patient inhomogeneities in oesophageal 192Ir HDR brachytherapy: a Monte Carlo and analytical dosimetry study. *Physics in Medicine & Biology*, 49(12):2675, 2004. p. 138, 146

[6] J. St. Aubin, A. Keyvanloo, and B. G. Fallone. Discontinuous finite element space-angle treatment of the first order linear Boltzmann transport equation with magnetic fields: application to MRI-guided radiotherapy. *Medical physics*, 43(1):195–204, 2016. p. 18

[7] D. E. Bartine, R. G. Alsmiller Jr, F. R. Mynatt, W. W. Engle Jr, and J. Barish. Low-energy electron transport by the method of discrete ordinates. *Nuclear Science and Engineering*, 48(2):159–178, 1972. p. 40, 46

[8] G. Battistoni, F. Cerutti, A. Fasso, A. Ferrari, S. Muraro, J. Ranft, S. Roesler, and P. R. Sala. The FLUKA code: description and benchmarking. In *AIP Conference proceedings*, volume 896, pages 31–49. AIP, 2007. p. 17

[9] M. J. Berger, J. S. Coursey, M. A. Zucker, J. Chang, et al. *Stopping-power and range tables for electrons, protons, and helium ions*. NIST Physics Laboratory Gaithersburg, MD, 1998. p. 6

[10] H. Bethe and W. Heitler. On the stopping of fast particles and on the creation of positive electrons. *Proc. R. Soc. Lond. A*, 146(856):83–112, 1934. p. 21, 26, 36, 59

[11] H. J. Bhabha. The scattering of positrons by electrons with exchange on Dirac's theory of the positron. *Proc. R. Soc. Lond. A*, 154(881):195–206, 1936. p. 21, 24

[12] F. Biggs and R. Lighthill. Analytical approximations for photon–atom differential scattering cross sections including electron binding effects. Technical report, Sandia Labs., Albuquerque, N. Mex., 1972. p. 59

[13] E. Boman, J. Tervo, and M. Vauhkonen. Modelling the transport of ionizing radiation using the finite element method. *Physics in Medicine & Biology*, 50(2):265, 2005. p. 18

[14] J. M. Boone and J. A. Seibert. Monte Carlo simulation of the scattered radiation distribution in diagnostic radiology. *Medical physics*, 15(5):713–720, 1988. p. 17

[15] T. Bortfeld. IMRT: a review and preview. *Physics in Medicine & Biology*, 51(13):R363, 2006. p. 7

[16] H. Bouchard and J. Seuntjens. Ionization chamber-based reference dosimetry of intensity modulated radiation beams. *Medical physics*, 31(9):2454–2465, 2004. p. 17

[17] J. F. Briesmeister. MCNP: a general Monte Carlo code for neutron and photon transport. Version 3A. Revision 2. Technical report, Los Alamos National Lab., 1986. p. 17

[18] L. Brualla, F. Salvat, and R. Palanco-Zamora. Efficient Monte Carlo simulation of multileaf collimators using geometry-related variance-reduction techniques. *Physics in Medicine & Biology*, 54(13):4131, 2009. p. 64, 75

[19] K. Bush, I. M. Gagne, S. Zavgorodni, W. Ansbacher, and W. Beckham. Dosimetric validation of Acuros® XB with Monte Carlo methods for photon dose calculations. *Medical physics*, 38(4):2208–2221, 2011. p. 18, 19, 104

[20] J. Caron. *Etude et validation clinique d'un modèle aux moments entropique pour le transport de particules énergétiques: application aux faisceaux d'électrons pour la radiothérapie externe*. PhD thesis, Université de Bordeaux, 2016. p. 3, 47, 56, 57, 153

[21] C. Cercignani and G. M. Kremer. Relativistic Boltzmann equation: theory and applications. Springer, 2002. p. 40

[22] W. P. Chandler, C. L. Hartmann-Siantar, and J. A. Rathkopf. Calculation of radiation therapy dose using all particle Monte Carlo transport, February 9 1999. US Patent 5,870,697. p. 17

[23] S. Chandrasekhar. On the radiative equilibrium of a stellar atmosphere. *The Astrophysical Journal*, 99:180, 1944. p. 47

[24] S. Chandrasekhar. *Radiative transfer*. Courier Corporation, 2013. p. 47

[25] E. L. Chaney, T. J. Cullip, and T. A. Gabriel. A Monte Carlo study of accelerator head scatter. *Medical physics*, 21(9):1383–1390, 1994. p. 61

[26] D. Chassagne, A. Dutreix, P. Almond, J. Burgers, M. Busch, and C. Joslin. ICRU Report No. 38. Dose and volume specification for reporting intracavitary therapy in gynaecology. *Bethesda: International Commissioning on Radiation Units and Measurements*, 1985. p. 9

[27] J. Coleman, C. Park, J. E. Villarreal-Barajas, P. Petti, and B. Faddegon. A comparison of Monte Carlo and Fermi-Eyges-Hogstrom estimates of heart and lung dose from breast electron boost treatment. *International Journal of Radiation Oncology, Biology, Physics*, 61(2):621–628, 2005. p. 14

[28] J. Crook, M. McLean, I. Yeung, T. Williams, and G. Lockwood. MRI-CT fusion to assess postbrachytherapy prostate volume and the effects of prolonged edema on dosimetry following transperineal interstitial permanent prostate brachytherapy. *Brachytherapy*, 3(2):55–60, 2004. p. 11, 12

[29] J. E. Cygler, G. M. Daskalov, G. H. Chan, and G. X. Ding. Evaluation of the first commercial Monte Carlo dose calculation engine for electron beam treatment planning. *Medical physics*, 31(1):142–153, 2004. p. 17

[30] W. De Gersem, F. Claus, C. De Wagter, B. Van Duyse, and W. De Neve. Leaf position optimization for step-and-shoot IMRT. *International Journal of Radiation Oncology, Biology, Physics*, 51(5):1371–1388, 2001. p. 7

[31] D. Del Sorbo. *An entropic approach to magnetized nonlocal transport and other kinetic phenomena in high-energy-density plasmas*. PhD thesis, Université de Bordeaux, 2015. p. 47

[32] J. A. Doggett and L. V. Spencer. Elastic scattering of electrons and positrons by point nuclei. *Physical Review*, 103(6):1597, 1956. p. 29

[33] B. Dubroca and J.-L. Feugeas. Etude théorique et numérique d'une hiérarchie de modèles aux moments pour le transfert radiatif. *Comptes Rendus de l'Académie des Sciences-Series I-Mathematics*, 329(10):915–920, 1999. p. 39, 47, 48, 51

[34] R. Duclous, B. Dubroca, and M. Frank. A deterministic partial differential equation model for dose calculation in electron radiotherapy. *Physics in Medicine & Biology*, 55(13):3843, 2010. p. 3, 19, 48, 57

[35] G. A. Failla, T. Wareing, Y. Archambault, and S. Thompson. Acuros XB advanced dose calculation for the Eclipse treatment planning system. *Palo Alto, CA: Varian Medical Systems*, 20, 2010. p. 18

[36] M. Fippel, F. Haryanto, O. Dohm, F. Nüsslin, and S. Kriesen. A virtual photon energy fluence model for Monte Carlo dose calculation. *Medical Physics*, 30(3):301–311, 2003. p. 62

[37] M. K. Fix, P. J. Keall, K. Dawson, and J. V. Siebers. Monte Carlo source model for photon beam radiotherapy: photon source characteristics: Monte Carlo source model. *Medical physics*, 31(11):3106–3121, 2004. p. 62

[38] A. Fogliata, G. Nicolini, A. Clivio, E. Vanetti, and L. Cozzi. Accuracy of Acuros XB and AAA dose calculation for small fields with reference to Rapidarc® stereotactic treatments. *Medical physics*, 38(11):6228–6237, 2011. p. 19

[39] A. Fogliata, G. Nicolini, A. Clivio, E. Vanetti, and L. Cozzi. Dosimetric evaluation of Acuros XB advanced dose calculation algorithm in heterogeneous media. *Radiation oncology*, 6(1):82, 2011. p. 19

[40] A. Fogliata, G. Nicolini, A. Clivio, E. Vanetti, P. Mancosu, and L. Cozzi. Dosimetric validation of the Acuros XB advanced dose calculation algorithm: fundamental characterization in water. *Physics in Medicine & Biology*, 56(6):1879, 2011. p. 19

[41] A. Fogliata, E. Vanetti, D. Albers, C. Brink, A. Clivio, T. Knöös, G. Nicolini, and L. Cozzi. On the dosimetric behaviour of photon dose calculation algorithms in the presence of simple geometric heterogeneities: comparison with Monte Carlo calculations. *Physics in Medicine & Biology*, 52(5):1363, 2007. p. 14, 15, 103, 104

[42] D. Georg, J. Hopfgartner, J. Gòra, P. Kuess, G. Kragl, D. Berger, N. Hegazy, G. Goldner, and P. Georg. Dosimetric considerations to determine the optimal technique for localized prostate cancer among external photon, proton, or carbon-ion therapy and high-dose-rate or low-dose-rate brachytherapy. *International Journal of Radiation Oncology, Biology, Physics*, 88(3):715–722, 2014. p. 10, 11

[43] D. Georg, C. Kirisits, M. Hillbrand, J. Dimopoulos, and R. Pötter. Image-guided radiotherapy for cervix cancer: high-tech external beam therapy versus high-tech brachytherapy. *International Journal of Radiation Oncology, Biology, Physics*, 71(4):1272–1278, 2008. p. 10

[44] K. A. Gifford, J. L. Horton Jr, T. A. Wareing, G. Failla, and F. Mourtada. Comparison of a finite-element multigroup discrete-ordinates code with Monte Carlo for radiotherapy calculations. *Physics in Medicine & Biology*, 51(9):2253, 2006. p. 18, 55, 56, 57

[45] K. A. Gifford, M. J. Price, J. L. Horton Jr, T. A. Wareing, and F. Mourtada. Optimization of deterministic transport parameters for the calculation of the dose distribution around a high dose-rate brachytherapy source. *Medical physics*, 35(6Part1):2279–2285, 2008. p. 55, 56

[46] B. S. Gill, J. F. Lin, T. C. Krivak, P. Sukumvanich, R. A. Laskey, M. S. Ross, J. L. Lesnock, and S. Beriwal. National Cancer Data Base analysis of radiation therapy consolidation modality for cervical cancer: the impact of new technological advancements. *International Journal of Radiation Oncology, Biology, Physics*, 90(5):1083–1090, 2014. p. 1, 10

[47] F. Gobet, J. Caron, I. Bessieres, T. Bonnet, M. M. Aléonard, M. Antoine, P. Barberet, M. Comet, D. Denis-Petit, J.-L. Feugeas, et al. Experimental and Monte Carlo absolute characterization of a medical electron beam using a magnetic spectrometer. *Radiation Measurements*, 86:16–23, 2016. p. 40

[48] H. Grad. On the kinetic theory of rarefied gases. *Communications on pure and applied mathematics*, 2(4):331–407, 1949. p. 47

[49] M. Gryziński. Classical theory of atomic collisions. I. Theory of inelastic collisions. *Physical Review*, 138(2A):A336, 1965. p. 60

[50] F. Guedea, M. Ventura, J.-J. Mazeron, J. L. Torrecilla, P. Bilbao, and J. M. Borràs. Patterns of care for brachytherapy in Europe: facilities and resources in brachytherapy in the European area. *Brachytherapy*, 7(3):223–230, 2008. p. 10

[51] S. Guisset, S. Brull, B. Dubroca, E. d'Humières, S. Karpov, and I. Potapenko. Asymptotic-preserving scheme for the M1-Maxwell system in the quasi-neutral regime. *Communications in Computational Physics*, 19(2):301–328, 2016. p. 47

[52] A. Gustafsson, B. K. Lind, and A. Brahme. A generalized pencil beam algorithm for optimization of radiation therapy. *Medical physics*, 21(3):343–356, 1994. p. 14

[53] K. Han, M. Milosevic, A. Fyles, M. Pintilie, and A. N. Viswanathan. Trends in the utilization of brachytherapy in cervical cancer in the United States. *International Journal of Radiation Oncology, Biology, Physics*, 87(1):111–119, 2013. p. 1, 10

[54] A. Harten, P. D. Lax, and B. van Leer. On upstream differencing and Godunov-type schemes for hyperbolic conservation laws. *SIAM review*, 25(1):35–61, 1983. p. 56

[55] E. Heath, J. Seuntjens, and D. Sheikh-Bagheri. Dosimetric evaluation of the clinical implementation of the first commercial IMRT Monte Carlo treatment planning system at 6 MV. *Medical physics*, 31(10):2771–2779, 2004. p. 17

[56] W. Heitler. *The quantum theory of radiation*. Courier Corporation, 1984. p. 21, 29

[57] H. Hensel, R. Iza-Teran, and N. Siedow. Deterministic model for dose calculation in photon radiotherapy. *Physics in Medicine & Biology*, 51(3):675, 2006. p. 19

[58] L. Hoffmann, M.-B. K. Jørgensen, L. P. Muren, and J. B. B. Petersen. Clinical validation of the Acuros XB photon dose calculation algorithm, a grid-based Boltzmann equation solver. *Acta oncologica*, 51(3):376–385, 2012. p. 19

[59] K. Huang. *Introduction to statistical physics*. Chapman and Hall/CRC, 2009. p. 50

[60] D. A. Jaffray, M. C. Carlone, M. F. Milosevic, S. L. Breen, T. Stanescu, A. Rink, H. Alasti, A. Simeonov, M. C. Sweitzer, and J. D. Winter. A facility for magnetic resonance-guided radiation therapy. In *Seminars in radiation oncology*, volume 24, pages 193–195. Elsevier, 2014. p. 11

[61] S. Jan, G. Santin, D. Strul, S. Staelens, K. Assie, D. Autret, S. Avner, R. Barbier, M. Bardies, P. M. Bloomfield, et al. GATE: a simulation toolkit for PET and SPECT. *Physics in Medicine & Biology*, 49(19):4543, 2004. p. 17

[62] S. B. Jiang, A. L. Boyer, and C.-M. C. Ma. Modeling the extrafocal radiation and monitor chamber backscatter for photon beam dose calculation. *Medical physics*, 28(1):55–66, 2001. p. 62

[63] J. Katakura. Nuclear data sheets for A= 125. *Nuclear Data Sheets*, 112(3):495–705, 2011. p. 137

[64] I. Kawrakow and A. F. Bielajew. On the condensed history technique for electron transport. *Nuclear Instruments and Methods in Physics Research Section B: Beam Interactions with Materials and Atoms*, 142(3):253–280, 1998. p. 17

[65] I. Kawrakow and M. Fippel. Investigation of variance reduction techniques for Monte Carlo photon dose calculation using XVMC. *Physics in Medicine & Biology*, 45(8):2163, 2000. p. 17

[66] I. Kawrakow and M. Fippel. VMC++, a fast MC algorithm for radiation treatment planning. In *The Use of Computers in Radiation Therapy*, pages 126–128. Springer, 2000. p. 17

[67] I. Kawrakow, M. Fippel, and K. Friedrich. 3D electron dose calculation using a voxel based Monte Carlo algorithm (VMC). *Medical physics*, 23(4):445–457, 1996. p. 17

[68] I. Kawrakow and D. W. O. Rogers. The EGSnrc code system. *NRC Report PIRS-701, NRC, Ottawa*, 2000. p. 17, 64

[69] L. Kim, R. H. Pratt, S. M. Seltzer, and M. J. Berger. Ratio of positron to electron bremsstrahlung energy loss: an approximate scaling law. *Physical Review A*, 33(5):3002, 1986. p. 27

[70] C. Kirisits, M. J. Rivard, D. Baltas, F. Ballester, M. De Brabandere, R. van der Laarse, Y. Niatsetski, P. Papagiannis, T. P. Hellebust, J. Perez-Calatayud, et al. Review of clinical brachytherapy uncertainties: analysis guidelines of GEC-ESTRO and the AAPM. *Radiotherapy and oncology*, 110(1):199–212, 2014. p. 11

[71] B. L. Kirk. Overview of Monte Carlo radiation transport codes. *Radiation Measurements*, 45(10):1318–1322, 2010. p. 61

[72] O. Klein and Y. Nishina. Über die streuung von strahlung durch freie elektronen nach der neuen relativistischen quantendynamik von dirac. *Zeitschrift für Physik*, 52(11-12):853–868, 1929. p. 21, 35, 59

[73] H. W. Koch and J. W. Motz. Bremsstrahlung cross-section formulas and related data. *Rev. Mod. Phys.*, 31:920, 1959. p. 60

[74] P. Kolmonen, J. Tervo, and T. Lahtinen. Use of the Cimmino algorithm and continuous approximation for the dose deposition kernel in the inverse problem of radiation treatment planning. *Physics in Medicine & Biology*, 43(9):2539, 1998. p. 14

[75] R. O. Kornelsen and M. E. J. Young. Changes in the dose-profile of a 10 MV x-ray beam within and beyond low density material. *Medical physics*, 9(1):114–116, 1982. p. 106

[76] E. W. Larsen, M. M. Miften, B. A. Fraass, and I. A. D. Bruinvis. Electron dose calculations using the method of moments. *Medical physics*, 24(1):111–125, 1997. p. 19

[77] L. J. Lorence, J. E. Morel, and G. D. Valdez. Physics guide to CEPXS: a multigroup coupled electron-photon cross-section generating code. *SAND89-1685, Sandia National Laboratory*, 1989. p. 49, 59

[78] L. J. Lorence, W. E. Nelson, and J. E. Morel. Coupled electron-photon transport calculations using the method of discrete ordinates. *IEEE Transactions on Nuclear Science*, 32(6):4416–4420, 1985. p. 18

[79] D. A. Low and J. F. Dempsey. Evaluation of the gamma dose distribution comparison method. *Medical physics*, 30(9):2455–2464, 2003. p. 70

[80] C.-M. Ma, B. A. Faddegon, D. W. O. Rogers, and T. R. Mackie. Accurate characterization of Monte Carlo calculated electron beams for radiotherapy. *Medical physics*, 24(3):401–416, 1997. p. 62

[81] U. Mahmood, T. Pugh, S. Frank, L. Levy, G. Walker, W. Haque, M. Koshy, W. Graber, D. Swanson, K. Hoffman, et al. Declining use of brachytherapy for the treatment of prostate cancer. *Brachytherapy*, 13(2):157–162, 2014. p. 1, 10

[82] J. Mallet, S. Brull, and B. Dubroca. An entropic scheme for an angular moment model for the classical Fokker-Planck-Landau equation of electrons. *Communications in Computational Physics*, 15(2):422–450, 2014. p. 47

[83] J. Mallet, S. Brull, and B. Dubroca. General moment system for plasmas physics based on minimum entropy principle. *Kinetic and Related Models*, 8(3), 2015. p. 47

[84] C. Martens, W. De Gersem, W. De Neve, and C. De Wagter. Combining the advantages of step-and-shoot and dynamic delivery of intensity-modulated radiotherapy by interrupted dynamic sequences. *International Journal of Radiation Oncology, Biology, Physics*, 50(2):541–550, 2001. p. 8

[85] J. M. Martin, E. A. Handorf, A. Kutikov, R. G. Uzzo, J. E. Bekelman, E. M. Horwitz, and M. C. Smaldone. The rise and fall of prostate brachytherapy: use of brachytherapy for the treatment of localized prostate cancer in the National Cancer Data Base. *Cancer*, 120(14):2114–2121, 2014. p. 1, 10

[86] P. Mayles, A. E. Nahum, and J.-C. Rosenwald. *Handbook of radiotherapy physics: theory and practice*. CRC Press, 2007. p. 13, 62

[87] N. Metropolis and S. Ulam. The Monte Carlo method. *Journal of the American Statistical Association*, 44(247):335–341, 1949. p. 16

[88] M. Miften, M. Wiesmeyer, A. Kapur, and C.-M. C. Ma. Comparison of RTP dose distributions in heterogeneous phantoms with the BEAM Monte Carlo simulation system. *Journal of applied clinical medical physics*, 2(1):21–31, 2001. p. 106

[89] G. N. Minerbo. Maximum entropy Eddington factors. *Journal of Quantitative Spectroscopy and Radiative Transfer*, 20(6):541–545, 1978. p. 47

[90] R. Mohan, C. Chui, and L. Lidofsky. Differential pencil beam dose computation model for photons. *Medical Physics*, 13(1):64–73, 1986. p. 14

[91] C. Möhler, P. Wohlfahrt, C. Richter, and S. Greilich. On the equivalence of image-based dual-energy CT methods for the determination of electron density and effective atomic number in radiotherapy. *Physics and Imaging in Radiation Oncology*, 5:108–110, 2018. p. 152

[92] N. V. Mott and N. H. D. Bohr. The scattering of fast electrons by atomic nuclei. *Proceedings of the Royal Society of London. Series A, Containing Papers of a Mathematical and Physical Character*, 124(794):425–442, 1929. p. 21

[93] C. Møller. Zur theorie des durchgangs schneller elektronen durch materie. *Annalen der Physik*, 406(5):531–585, 1932. p. 21, 22

[94] R. Nath, L. L. Anderson, G. Luxton, K. A. Weaver, J. F. Williamson, and A. S. Meigooni. Dosimetry of interstitial brachytherapy sources: recommendations of the AAPM Radiation Therapy Committee Task Group No. 43. *Medical physics*, 22(2):209–234, 1995. p. 9

[95] W. R. Nelson, D. W. O. Rogers, and H. Hirayama. The EGS4 code system. Technical report, 1985. p. 29

[96] P. L. Nguyen, X. Gu, S. R. Lipsitz, T. K. Choueiri, W. W. Choi, Y. Lei, K. E. Hoffman, and J. C. Hu. Cost implications of the rapid adoption of newer technologies for treating prostate cancer. *Journal of Clinical Oncology*, 29(12):1517, 2011. p. 10

[97] D. W. Nigg, P. D. Randolph, and F. J. Wheeler. Demonstration of three-dimensional deterministic radiation transport theory dose distribution analysis for boron neutron capture therapy. *Medical physics*, 18(1):43–53, 1991. p. 18

[98] B. Nilsson and A. Brahme. Contamination of high-energy photon beams by scattered photons. *Strahlentherapie*, 157(3):181–186, 1981. p. 61

[99] B. Nilsson and A. Brahme. Electron contamination from photon beam collimators. *Radiotherapy and Oncology*, 5(3):235–244, 1986. p. 61

[100] International Bureau of Weights, Measures, B. N. Taylor, and A. Thompson. *The international system of units (SI)*. US Department of Commerce, Technology Administration, National Institute of Standards and Technology, 2001. p. 5

[101] E. Olbrant and M. Frank. Generalized Fokker–Planck theory for electron and photon transport in biological tissues: application to radiotherapy. *Computational and mathematical methods in medicine*, 11(4):313–339, 2010. p. 48

[102] J. Page. *Développement et validation de l'application de la force de Lorentz dans le modèle aux moments entropiques M1. Etude de l'effet du champ magnétique sur le dépôt de dose en radiothérapie externe*. PhD thesis, Université de Bordeaux, 2018. p. 47

[103] J. Page, Ph. Nicolaï, G. Birindelli, J. Caron, B. Dubroca, G. Kantor, V. Tikhonchuk, and J.-L. Feugeas. Introduction of external magnetic fields in entropic moment modelling for radiotherapy. *Physica Medica*, 42:313–318, 2017. p. 19, 20

[104] P. Papagiannis, E. Pantelis, and P. Karaiskos. Current state of the art brachytherapy treatment planning dosimetry algorithms. *The British journal of radiology*, 87(1041):20140163, 2014. p. 18, 138, 141, 143, 146

[105] J. P. Patau, C. E. Vernes, M. Terrissol, and M. Malbert. Calcul des caracteristiques qualitatives (TEL, FQ, equivalent de dose) d'un faisceau de photons de freinage a usage medical, par simulation de sa creation et de son transport. In *Proc. the 6th Symposium on Microdosimetry*, pages 579–88, 1978. p. 61

[106] D. G. Petereit, S. J. Frank, A. N. Viswanathan, B. Erickson, P. Eifel, P. L. Nguyen, and D. E. Wazer. Brachytherapy: where has it gone? *Journal of Clinical Oncology*, 33(9):980, 2015. p. 10

[107] L. Petrokokkinos, K. Zourari, E. Pantelis, A. Moutsatsos, P. Karaiskos, L. Sakelliou, I. Seimenis, E. Georgiou, and P. Papagiannis. Dosimetric accuracy of a deterministic radiation transport based brachytherapy treatment planning system. Part II: Monte Carlo and experimental verification of a multiple source dwell position plan employing a shielded applicator. *Medical physics*, 38(4):1981–1992, 2011. p. 18

[108] T. Pichard, G. W. Alldredge, S. Brull, B. Dubroca, and M. Frank. The M2 model for dose simulation in radiation therapy. *Journal of Computational and Theoretical Transport*, 45(3):174–183, 2016. p. 3, 19, 48, 55, 56, 57, 135, 152, 153

[109] G. C. Pomraning. *The equations of radiation hydrodynamics*. Courier Corporation, 2005. p. 47

[110] R. A. Price Jr, G. E. Hanks, S. W. McNeeley, E. M. Horwitz, and W. H. Pinover. Advantages of using noncoplanar vs. axial beam arrangements when treating prostate cancer with intensity-modulated radiation therapy and the step-and-shoot delivery method. *International Journal of Radiation Oncology, Biology, Physics*, 53(1):236–243, 2002. p. 7

[111] S. Rana. Clinical dosimetric impact of Acuros XB and analytical anisotropic algorithm (AAA) on real lung cancer treatment plans. *International Journal of Cancer Therapy and Oncology*, 2(1), 2014. p. 19

[112] C. Regan. Fast models for fast particles transport in the context of ICF. 2010. p. 47

[113] N. Reynaert, S. C. Van der Marck, D. R. Schaart, W. Van der Zee, C. Van Vliet-Vroegindeweij, M. Tomsej, J. Jansen, B. Heijmen, M. Coghe, and C. De Wagter. Monte Carlo treatment planning for photon and electron beams. *Radiation Physics and Chemistry*, 76(4):643–686, 2007. p. 61

[114] M. E. Riley, C. J. MacCallum, and F. Biggs. Theoretical electron-atom elastic scattering cross sections: selected elements, 1 keV to 256 keV. *Atomic Data and Nuclear Data Tables*, 15(5):443–476, 1975. p. 60

[115] M. J. Rivard, B. M. Coursey, L. A. DeWerd, W. F. Hanson, M. S. Huq, G. S. Ibbott, M. G. Mitch, R. Nath, and J. F. Williamson. Update of AAPM Task Group No. 43 report: a revised AAPM protocol for brachytherapy dose calculations. *Medical physics*, 31(3):633–674, 2004. p. 135, 140

[116] M. Rodriguez, J. Sempau, and L. Brualla. PRIMO: a graphical environment for the Monte Carlo simulation of Varian and Elekta linacs. *Strahlentherapie und Onkologie*, 189(10):881–886, 2013. p. 17

[117] D. W. O. Rogers, B. A. Faddegon, G. X. Ding, C.-M. Ma, J. We, and T. R. Mackie. BEAM: a Monte Carlo code to simulate radiotherapy treatment units. *Medical physics*, 22(5):503–524, 1995. p. 61

[118] D. W. O. Rogers and R. Mohan. Questions for comparison of clinical Monte Carlo codes. In *The Use of Computers in Radiation Therapy*, pages 120–122. Springer, 2000. p. 103, 104, 105

[119] D. W. O. Rogers, B. Walters, I. Kawrakow, et al. BEAMnrc users manual. *Nrc Report Pirs*, 509:12, 2009. p. 17

[120] J. J. Sakurai. *Advanced quantum mechanics*. Pearson Education India, 1967. p. 24

[121] F. Salvat. PENELOPE-2014: a code system for Monte Carlo simulation of electron and photon transport. Report NEA/NSC/DOC (2014). 2014. p. 17, 25, 26, 29, 37, 58, 64, 73, 74, 77, 111, 135, 136

[122] F. Salvat and J. M. Fernández-Varea. Semiempirical cross sections for the simulation of the energy loss of electrons and positrons in matter. *Nuclear Instruments and Methods in Physics Research Section B: Beam Interactions with Materials and Atoms*, 63(3):255–269, 1992. p. 26

[123] F. Sauter. Über den atomaren photoeffekt in der K-schale nach der relativistischen wellenmechanik diracs. *Annalen der Physik*, 403(4):454–488, 1931. p. 21, 31, 59

[124] A. E. Schach von Wittenau, L. J. Cox, P. M. Bergstrom Jr, W. P. Chandler, C. L. Hartmann Siantar, and R. Mohan. Correlated histogram representation of Monte Carlo derived medical accelerator photon-output phase space. *Medical physics*, 26(7):1196–1211, 1999. p. 62

[125] S. M. Seltzer. Electron-photon Monte Carlo calculations: the ETRAN code. *International Journal of Radiation Applications and Instrumentation. Part A. Applied Radiation and Isotopes*, 42(10):917–941, 1991. p. 17

[126] C. L. H. Siantar, R. S. Walling, T. P. Daly, B. Faddegon, N. Albright, P. Bergstrom, A. F. Bielajew, C. Chuang, D. Garrett, R. K. House, et al. Description and dosimetric verification of the PEREGRINE Monte Carlo dose calculation system for

photon beams incident on a water phantom. *Medical physics*, 28(7):1322–1337, 2001. p. 17

[127] J. St. Aubin, A. Keyvanloo, O. Vassiliev, and B. G. Fallone. A deterministic solution of the first order linear Boltzmann transport equation in the presence of external magnetic fields. *Medical physics*, 42(2):780–793, 2015. p. 18

[128] S. Stathakis, C. Esquivel, L. V. Quino, P. Myers, O. Calvo, P. Mavroidis, A. N. Gutiérrez, and N. Papanikolaou. Accuracy of the small field dosimetry using the Acuros XB dose calculation algorithm within and beyond heterogeneous media for 6 MV photon beams. *International Journal of Medical Physics, Clinical Engineering and Radiation Oncology*, 1(03):78, 2012. p. 104

[129] P. R. M. Storchi, L. J. Van Battum, and E. Woudstra. Calculation of a pencil beam kernel from measured photon beam data. *Physics in Medicine & Biology*, 44(12):2917, 1999. p. 14

[130] O. Tanaka, S. Hayashi, M. Matsuo, K. Sakurai, M. Nakano, S. Maeda, K. Kajita, T. Deguchi, and H. Hoshi. Comparison of MRI-based and CT/MRI fusion–based postimplant dosimetric analysis of prostate brachytherapy. *International Journal of Radiation Oncology, Biology, Physics*, 66(2):597–602, 2006. p. 11

[131] K. Tanderup, S. Beddar, C. E. Andersen, G. Kertzscher, and J. E. Cygler. In vivo dosimetry in brachytherapy. *Medical physics*, 40(7), 2013. p. 11

[132] K. Tanderup, C. Ménard, C. Polgar, J. C. Lindegaard, C. Kirisits, and R. Pötter. Advancements in brachytherapy. *Advanced drug delivery reviews*, 109:15–25, 2017. p. 9, 10, 11

[133] E. Tonkopi, M. R. McEwen, B. R. B. Walters, and I. Kawrakow. Influence of ion chamber response on in-air profile measurements in megavoltage photon beams. *Medical physics*, 32(9):2918–2927, 2005. p. 75

[134] M. Touati. *Fast Electron Transport Study for Inertial Confinement Fusion*. PhD thesis, Bordeaux, 2015. p. 47

[135] M. F. Tsiakalos, K. Theodorou, C. Kappas, S. Zefkili, and J.-C. Rosenwold. Analysis of the penumbra enlargement in lung versus the quality index of photon beams: a methodology to check the dose calculation algorithm. *Medical physics*, 31(4):943–949, 2004. p. 106

[136] O. N. Vassiliev, T. A. Wareing, I. M. Davis, J. McGhee, D. Barnett, J. L. Horton, K. Gifford, G. Failla, U. Titt, and F. Mourtada. Feasibility of a multigroup deterministic solution method for three-dimensional radiotherapy dose calculations.

International Journal of Radiation Oncology, Biology, Physics, 72(1):220–227, 2008. p. 18

[137] O. N. Vassiliev, T. A. Wareing, J. McGhee, G. Failla, M. R. Salehpour, and F. Mourtada. Validation of a new grid-based Boltzmann equation solver for dose calculation in radiotherapy with photon beams. *Physics in Medicine & Biology*, 55(3):581, 2010. p. 18

[138] B. R. B. İ Walters, I. Kawrakow, D. W. O. Rogers, et al. DOSXYZnrc users manual. *Nrc Report Pirs*, 794:31, 2005. p. 17

[139] F. Wang, Q. Tang, G. Lv, F. Zhao, X. Jiang, X. Zhu, X. Li, and S. Yan. Comparison of computed tomography and magnetic resonance imaging in cervical cancer brachytherapy: a systematic review. *Brachytherapy*, 16(2):353–365, 2017. p. 11

[140] T. A. Wareing, J. M. McGhee, J. E. Morel, and S. D. Pautz. Discontinuous finite element SN methods on three-dimensional unstructured grids. *Nuclear science and engineering*, 138(3):256–268, 2001. p. 18

[141] D. R. White, J. Booz, R. V. Griffith, J. J. Spokas, and I. J. Wilson. Report 44. *Journal of the International Commission on Radiation Units and Measurements*, os23(1):NP–NP, 04 2016. p. 105, 138

[142] J. F. Williamson and A. S. Meigooni. Quantitative dosimetry methods for brachytherapy. *Brachytherapy physics*, pages 87–134, 1995. p. 17

[143] L. Xing, B. Thorndyke, E. Schreibmann, Y. Yang, T.-F. Li, G.-Y. Kim, G. Luxton, and A. Koong. Overview of image-guided radiation therapy. *Medical Dosimetry*, 31(2):91–112, 2006. p. 8

[144] R. Yang, O. Zelyak, B. G. Fallone, and J. St. Aubin. A novel upwind stabilized discontinuous finite element angular framework for deterministic dose calculations in magnetic fields. *Physics in Medicine & Biology*, 63(3):035018, 2018. p. 18

[145] C.-Y. Yi, S.-H. Hah, and M. S. Yeom. Monte Carlo calculation of the ionization chamber response to beam using PENELOPE. *Medical physics*, 33(5):1213–1221, 2006. p. 17

[146] H. Zaidi. Relevance of accurate Monte Carlo modeling in nuclear medical imaging. *Medical physics*, 26(4):574–608, 1999. p. 17

[147] C. D. Zerby and F. L. Keller. Electron transport theory, calculations, and experiments. *Nuclear Science and Engineering*, 27(2):190–218, 1967. p. 29, 60

[148] T. Zhuang, T. Djemil, P. Qi, A. Magnelli, K. Stephans, G. Videtic, and P. Xia. Dose calculation differences between Monte Carlo and pencil beam depend on the tumor locations and volumes for lung stereotactic body radiation therapy. *Journal of applied clinical medical physics*, 14(2):38–51, 2013. p. 14

[149] K. Zourari, E. Pantelis, A. Moutsatsos, L. Petrokokkinos, P. Karaiskos, L. Sakelliou, E. Georgiou, and P. Papagiannis. Dosimetric accuracy of a deterministic radiation transport based brachytherapy treatment planning system. Part I: Single sources and bounded homogeneous geometries. *Medical physics*, 37(2):649–661, 2010. p. 18

[150] K. Zourari, E. Pantelis, A. Moutsatsos, L. Sakelliou, E. Georgiou, P. Karaiskos, and P. Papagiannis. Dosimetric accuracy of a deterministic radiation transport based 192Ir brachytherapy treatment planning system. Part III. comparison to Monte Carlo simulation in voxelized anatomical computational models. *Medical physics*, 40(1):011712, 2013. p. 18